Climate Change and Air Pollution Relationships. Lessons from a Subtropical Desert Region

Damián Oyarzún Valenzuela

A dissertation submitted in partial fulfillment

of the requirements for the degree of

Doctor of Philosophy

of

University College London.

Department of Geography

University College London

July 27, 2021

I, Damián Oyarzún Valenzuela, confirm that the work presented in this thesis is my own. Where information has been derived from other sources, I confirm that this has been indicated in the work.

Abstract

The Atacama Desert is the dryest desert on Earth. Atmospheric, ocean, and topographic forcings preserve an exceptional hyper-arid environment. As a product of anthropogenic and natural emissions, PM_{10} and $PM_{2.5}$ atmospheric concentrations have been observed to exceed international standards in urban areas where about 1.5 million people live. This research starts by describying the climate dynamics in northern Chile along with the primary anthropogenic emission sources of PM_{10}, $PM_{2.5}$, and gaseous precursor pollutants. Then, air quality levels across urban areas are evidenced. As a major source of natural PM, the unexplored mineral dust cycle of the Atacama desert is studied from satellite retrievals of aerosols properties. Two areas in the Antofagasta region are identified as predominant sources of dust, where links with reanalysed wind patterns are reported. This study is followed by the analysis of the relationship between PM_{10}-$PM_{2.5}$ levels and atmospheric ventilation from observational and modelled datasets. Because of the significant link found between both, especially in coastal areas, a wheater-driven model for PM events, with atmospheric ventilation as the most significant input variable, is proposed for the coastal city of Antofagasta. Finally, the future of the Atacama Desert, comprising atmospheric and oceanic regional forcings and future PM_{10}-$PM_{2.5}$ levels, is explored from the UKESM1 model.

The South Pacific Anticyclone is already extending and intensifying during the austral summertime. The above leads to increasing upwelling-favourable winds and coastal upwelling intensity of the Humboldt system at the surface ocean, enhancing atmospheric stability. However, a decline is simulated at deeper ocean layers. PM_{10}-$PM_{2.5}$ are both projected to increase under the SSP370 and SSP585

climate change experiments during the 21st Century. This increasing trend is more abrupt under the SSP370 than the SSP585 experiment due to increased SO_2 and dust emissions and the absence of mitigation measurements. Policy implications are discussed, and future academic research is proposed, including implications beyond academia.

Impact Statement

The climate of the Atacama Desert responds to a combination of atmospheric, oceanic and topographic factors that promote exceptional dry conditions. Along with being home for about 1.5 million people, several industrial facilities locate across this region which have historically emitted a vary of air pollutants. However, the understanding of natural emissions, such as mineral dust, the connection of air quality with atmospheric forcings, such as atmospheric ventilation, and the potential impacts of climate change on these processes has remained unexplored for this region of the world. This research focuses on understanding the mechanisms before mentioned, with direct impacts not only on future academic research in the field of air pollution and atmospheric science but also on future policy in Chile and applications beyond academia.

The mineral dust cycle of the Atacama had only been explored as part of global or continental studies, without providing insight into the local distribution of sources, their seasonality and frequency of events. The analysis performed provides evidence for future applications on air quality studies in remote areas in northern Chile. Also, it represents an opportunity for future studies on solar energy production, particularly about the potential effect of mineral dust on soiling and attenuation. Due to the exceptional conditions, solar power generation is a growing industry in northern Chile. Finally, the satellite-based dataset produced can be used for the validation of mineral dust forecasting schemes.

The quasi-permanent temperature inversion layer height (TILH) promoting high atmospheric stability along the northern Chilean coast has been explored to understand links between atmospheric ventilation and observed PM_{10}-$PM_{2.5}$ levels

in urban areas. Although the significance of the TILH for the climate of the desert has been discussed in the literature, their relationship with ventilation and air quality remained unexplored. The results obtained from both observational and modelling suggest a decline of the boundary layer height (BLH) not only along the coast (as previously reported) but also on inland regions during the last decades (1981-2010). This might have direct implication in future policy. Also, a prediction statistical model based on meteorological input variables has been able to predict over 70% of PM events in the city of Antofagasta. This represent a low-cost tool that could serve as basis for an operational forecasting model using ventilation conditions as predictor.

The future of the Atacama under climate change was explored by analysis outcomes of a state of the art earth system model (UKESM1) contributing to CMIP6. The results reveal enhanced atmospheric stability throughout the 21^{st} Century, including an accentuated decline of the BLH. This motivates the study of a potential climate penalty for PM_{10}, $PM_{2.5}$ and SO_2 over northern Chile with direct implications on future local policy and mitigation efforts. Also, this methodology could be further extended to other regions in South America.

Acknowledgements

I want to begin by acknowledging and thanking my supervisor, Dr Chris Brierley. I will always be deeply grateful for your guidance and support since the first day. Thank you for believing in the project and providing precise advice and help at every stage. You have pushed me beyond my limits and encourage me to be innovative and critical. Thank you for all the talks, academic opportunities and for always having your office open to provide help. I would also like to thank Prof. Neil Rose, my secondary supervisor, who supported the project since the first moment. Thank you for your valuable comments at the different stages and your assertive critical view. I am also grateful to Dr Steven Turnock from the Met Office, who kindly provide me with the PM data from UKESM1. Also, thanks to Dr Jesús Fernández from UCAN for providing me with the WRF-CORDEX datasets, Dr Deniz Bozkurt from CR2 for providing me with the RegCM4 simulations and Dr Nicolás Huneeus for the valuable critic to the air quality and satellite-based studies. Thanks to Dr José Gomez-Danz and PhD colleague Feng Yin for your advice on remote sensing analyses.

I could not be more grateful for my wife, Beatriz. You have travelled through this entire experience with me since far before it started, during all the ups and downs, being my source of love and energy. I am very fortunate that you have been an exceptional example in both personal and academic dimensions, supportive, comprehensive, loyal and the best companion on the road. Thank you for the infinite coffees, walks, travels and disinterested and honest help. You have encouraged me to believe in knowledge and be a better person. I am also endlessly grateful to my son Rafael. You came into our lives during this process to fulfil everything

with motivation and joy. You have been the most important source of strength and courage. Without you two, this couldn't have been possible.

Thanks to my parents, Clemencia and German, for your continued encouragement and support despite the long distance. Thank you to my brother German for believing in me. Also, thanks to my sister-in-law Claudia and my nephews and nieces for their support. Thanks to my in-laws, Patricia and Francisco, for their constant affection and interest, and Macarena and Franco for your help and company in many moments.

I would like to also thank Prof. Anson MacKay for the valuable advice before and during this research, Dr Clare Heaviside for providing help, academic opportunities, and assertive opinions at different stages of the process, and Dr Apostolos Voulgarakis for the endless talks on the first prospects of this research plan.

Thanks to the people at the Department of Geography of UCL, who have nurtured the PhD's long journey through enriching science meetings, seminars and teaching opportunities. Also thanks to the Art and Sciences department for allowing me to practice teaching on fascinating topics. Thank to my PhD colleagues for the excellent vibe at the lab and all the good moments that enriched the experience at UCL. Also, I am very grateful to the Center for Climate and Resilience Research (CR)2 for allowing me to join as an external doctorate researcher, which meant a valuable contribution to the research.

Thank you to my friends, who have provided valuable help in different aspects during this time, Tom, Marc, Felipe, Patricia, Christian, Francisca, Diego, Nicolás, Macarena, Ignacio, Jose Ignacio, Daniel, Yiya, Ciprian, Milena, Apostolos and Maria.

Finally, thanks to the National Research and Development Agency of Chile (ANID) for having granted the funding for fees and maintenance during this PhD.

Contents

List of Figures

List of Tables

Glossary

AERONET	Aerosol Robotic Network
AOGCM	Atmosphere-Ocean General Circulation Models (AOGCM)
ASI	Atmospheric Stagnation Index
BLH	Boundary layer height
CD	Coastal Desert (area, in Chapter 5.0)
CMIP5	Coupled Model Intercomparison Project Phase 5
CMIP6	Coupled Model Intercomparison Project Phase 6
CORDEX	Coordinated Regional Climate Downscaling Experiment
DB	Deep Blue
DMC	Meteorological Service of Chile (in spanish)
DN	Desert North (area, in Chapter 4.0)
DS	Desert South (area, in Chapter 4.0)
ESM	Earth System Model
ID	Inland Desert (area, in Chapter 5.0)
MAIAC	Multi-angle Implementation of Atmospheric Correction
MODIS	Moderate Resolution Imaging Spectroradiometer
RCM	Regional Circulation Model
SINCA	National Air Quality Information System of Chile (in spanish)
SPA	South Pacific anticylone
SST	Sea surface temperature
TIL	Temperature inversion layer
TILH	Temperature inversion layer height
VC	Ventilation coefficient

Chapter 1

Introduction

Air pollution is one of the most significant and challenging threats to human health. In 2016, over 4 million deaths were attributed to exposure to outdoor air pollutants around the globe (WHO, 2018). Although an impact on human health can be understood intuitively, poor air quality also leads to substantial economic costs (Horton et al., 2012), and the detriment of ecosystems (Incecik et al., 2014). Air pollution, especially atmospheric aerosols, can also significantly impact atmospheric circulation, radiative imbalance, and surface temperature (Qin et al., 2014).

Climate and air pollution are connected, as evidenced by the important amount of research focused on these interactions (Dickerson et al., 1997; Jacobson, 2000; Jacob and Winner, 2009; Lesins et al., 2002; Zhao et al., 2011b; Tai et al., 2012; Fiore et al., 2015). Usually, harmful air quality levels are linked to the simultaneous occurrence of both high pollutant emissions and unfavourable weather conditions (Jacob and Winner, 2009). As meteorology and air pollutants interact with each other, these feedbacks makes air quality highly sensitive to climate change (Tai et al., 2012). Therefore, the understanding of air quality at local scales is essential for adaptation, mitigation, and legislation of both local air quality and climate change.

The contribution of harmful indoor and outdoor air pollution levels on death rates are significant worldwide. Globally, air pollution contributed to an average of 9% of mortality in 2017, ranging between 2 and 15% depending on the individual country (Ritchie and Roser, 2017). In particular, Chile is one of the countries in the

Americas with the highest percentage of deaths linked to bad air quality, between 5 and 7.5 % of the total in 2017 (Fig. 1.1). Over the last two decades, attention has focused on the air pollution problems across the Central and Southern regions of the country (Kavouras et al., 2001; Gallardo et al., 2002; Jorquera et al., 2004; Mena-Carrasco et al., 2012; Jhun et al., 2013; Henriquez et al., 2015; Barraza et al., 2017). In Northern Chile, where the Atacama desert predominates, harmful pollution levels have also been linked to morbidity and mortality in urban areas (Ruiz-Rudolph et al., 2016).

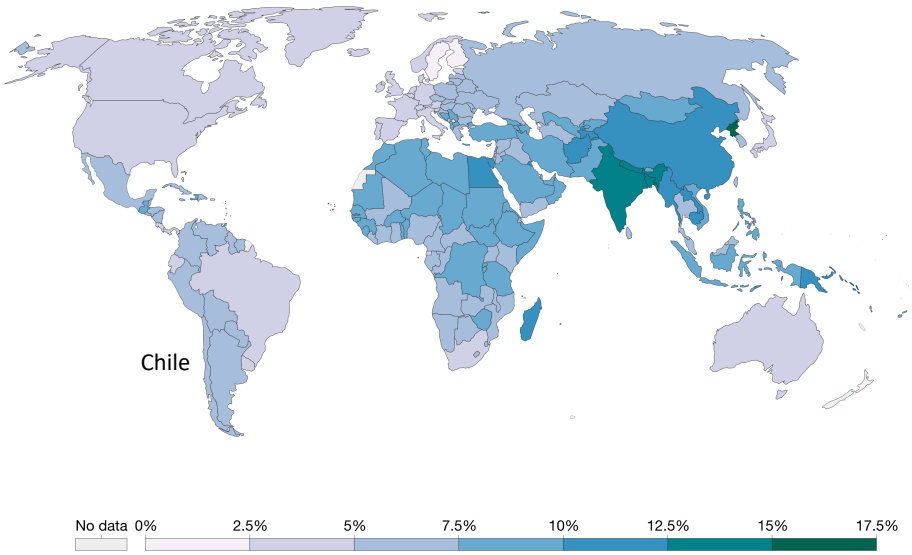

Figure 1.1: Global contribution of indoor and outdoor air pollution (as a risk factor) on deaths rates in 2017. Adapted from Ritchie and Roser (2017), based on IHME (2018) dataset.

The first section of this chapter comprises a general overview of air pollution, providing an introduction to particulate matter, gaseous compounds and policy implications. Then the Atacama Desert in Northern Chile is introduced as the study site for this research. The third section presents the purpose of the study and the research questions. Finally, section four provides an outline of this thesis.

1.1 Air Pollution

1.1.1 Particulate Matter (PM)

According to Tiwary and Colls (2010), anthropogenic particulate matter (PM) has a global production rate of 500 x $10^6 t$ annually, comprising of primary and secondary sources. This figure is about 10% of the natural production rate (around 4,900 $\times 10^6 t$). Naturally produced PM primarily arises from aeolian erosion of large bare soil areas, such as deserts, and sea salt evaporation (also called marine aerosols). Nonetheless anthropogenic PM has significant impacts due to the high density of the sources and the higher atmospheric residence of the finer particles.

Typically, PM levels and their composition vary between rural and urban areas (again mainly driven by the correlation between population and aerosol source density). In urban areas it is usual to find high concentrations of PM (both $PM_{2.5}$ and PM_{10}) along with nitric oxide (NO) and sulphur dioxide (SO_2) sourced from a combination of point sources, such as industrial chimneys, or linear sources, such as road traffic. On the other hand, in rural areas, it is common to observe higher emissions of ammonia scattered across large areas, promoting lower atmospheric concentrations.

PM is classified according to the particle aerodynamic diameter. Particles with an aerodynamic diameter equal to or less than 2.5 μm are known as $PM_{2.5}$, whilst PM_{10} refers to particles smaller than 10 μm. Because of the particulate size, PM_{10} and $PM_{2.5}$ are one of the atmospheric pollutants of major concern around the globe (Dreher and Costa, 2002; Jacob and Winner, 2009; Ji et al., 2012; Dawson et al., 2014). The above is because both PM_{10} and $PM_{2.5}$ can be inhaled by humans and deposited in the lungs (Kyung and Jeong, 2020). Based on epidemiological research, $PM_{2.5}$ has also been linked to adverse cardiovascular effects. Due to its size, PM_{10} deposits primarily in upper airways, whereas $PM_{2.5}$ can reach the smallest airways towards the alveolar-capillary membrane and eventually spread into the circulatory system (Du et al., 2016).

Due to the above, PM has been described as the air pollutant most strongly linked to human health detriment, impacting more population than any other (An-

derson et al., 2012; Li et al., 2015). In 2005, the World Health Organization (WHO) estimated that feasible reduction in particulate matter would lead to a decrease of 15% of related air pollution deaths. Inhaling airborne particles may lead to severe effects, such as chronic bronchitis, lung disease, irregular heartbeat and asthma (Pope et al., 2002; Sacks et al., 2010; Ruiz-Rudolph et al., 2016).

The effects of PM are related to both long-term and short-term exposure. For instance, long-term exposure to anthropogenic PM_{10} and $PM_{2.5}$ has been associated with about 29,000 deaths per year in the UK (Gowers et al., 2014). Also, a recent chemical transport modelling study suggests that about ten million premature deaths annually are attributable to fossil fuels components in $PM_{2.5}$ worldwide (Vohra et al., 2021). The higher mortality is consistent with the largest fossil fuel emitters in the present, namely China and India, along with other territories in Southern Asia, Europe and the USA. However, short-term exposure, such as a few days, is also linked to premature mortality. Macintyre et al. (2016) studied ten days of severe aerosol concentrations during the spring of 2014 in the UK and estimated around 600 deaths were exclusively attributable to this extreme event.

The capacity of PM to remain in the air is directly related to its size. PM_{10} settles down to the surface slower than coarser particles. Therefore they remain harmful for several days before being deposited back to the surface by sedimentation, diffusion or interception (Tiwary and Colls, 2010). PM is mainly composed of sulfate, nitrate, organic carbon, elemental carbon, soil dust and sea salt. The relative predominance of these components also varies with particle size. Whilst sulfate, nitrate, organic and elemental carbon are commonly found in $PM_{2.5}$, soil dust and sea salt are frequently components only of PM_{10} (Jacob and Winner, 2009). For example, a study conducted by Twigg et al. (2015) described sea salt as the main component, by 73%, of the coarse PM fraction (PM_{10}-$PM_{2.5}$) in a remote area in Southeast Scotland.

1.1.2 Gaseous emissions as drivers of PM pollution

The composition of PM is directly linked to gaseous emissions. Although particles are usually described based on their aerodynamic size, their constituents and toxic-

ity vary significantly among environments, depending on the nature of the sources. As reported by (Gonzáles et al., 2011) based on official data from the UK Environmental Agency, around three quarters of PM15 (particles with an aerodynamic diameter equal to or less than 15 μm) in the UK is carbonaceous matter from combustion, sulfates from SO_2 emissions and soluble minerals, such as mineral dust. In particular, this last group account for about 25% of the total. The remaining 25% mainly consist of ammonium from NH_3 emissions, nitrates from NO_x emissions, and chlorides from marine salt and coal emissions. $PM_{2.5}$ is constituted in about 50% by carbonaceous matter from combustion and around 20% by sulfates from SO_2 emissions. Unlike PM15, soluble minerals represent less than 5% of the total $PM_{2.5}$ across the UK. Minguillón et al. (2012) similarly find that in Zurich the coarse PM was primarily mineral matter and elements from tyre abrasion, whereas the fine PM fraction was dominated by compounds sourced from anthropogenic combustion processes. As exemplified above, atmospheric gas composition are an important source of understanding for PM levels and their composition when measured together, especially in the absence of chemical analysis from PM samples.

Due to their effects on the environment, human health, and the availability of data, Sulphur dioxide (SO_2), oxides of nitrogen (NO, NO_2 and NO_x) and ozone (O_3) have historically been recognised as the most significant gaseous pollutants. Whereas SO_2 and NO are primary pollutants, NO_2 and NO_x (NO + NO_2) may be either primary or secondary. Tropospheric ozone (O_3) is a secondary pollutant formed from NO_x and Volatile Organic Compounds ($VOCs$) in the presence of UV radiation. Its direct emissions are negligible.

Sulphur dioxide (SO_2) is usually a primary pollutant, although also most of the sulphur emissions oxidise to form gaseous SO_2 or sulphate aerosols. SO_2 is directly emitted from fossil fuels combustion, with electricity generation and heating being the most significant anthropogenic sources. 53% of UK SO_2 emissions were attributable to these activities in 2006 (Dore et al., 2008), although the subsequent phasing out of coal power plants will have reduced that proportion. Other anthropogenic sources of SO_2 identified were land use, metal melting and other industrial

processes. Emissions from transport were relatively low, accounting for about 2% of the total. Regarding natural sources of SO_2, these comprise volcanic activity, marine phytoplankton, soil and vegetation decay.

Similar to SO_2, oxides of nitrogen (NO_x) are primarily emitted from fossil fuel combustion linked to transport and power stations operations. Whereas over 90% of NO_x are directly emitted as nitric oxide (NO), most of the NO_2 is formed in the atmosphere as a secondary pollutant. Other important gaseous pollutants are ammonia (NH_3, mainly sourced from livestock farming, animal waste and fertilisation), volatile organic compounds emitted from solvents use and industrial processes, and carbon monoxide (CO). CO is a toxic gas emitted in small fractions with CO_2 emissions, primarily from fossil fuel combustion in transport, industrial processes and biomass burning (Tiwary and Colls, 2010).

1.1.3 Climate change and policy implications

The effect of air pollutants emissions on the atmosphere usually occurs across larger regions than the local environment into which the pollutants are emitted and where a specific air quality policy operates (Fiore et al., 2015). Therefore, a complex dilemma is that air quality and climate change are typically found in separate policy bodies, and the mitigation of one is not necessarily beneficial for the other (Maione et al., 2016). For example as will be discussed in Chapter 6, whereas a decrease of SO_2 concentrations has direct benefits for human health, the global effort for its reduction may pronounce atmospheric warming (Bedsworth, 2011). Nonetheless, measures to mitigate climate change, say through a reduction of fossil fuels emissions, also represent an opportunity to improve local air quality (West et al., 2004; Thambiran and Diab, 2011). Therefore climate change policy should consider local air quality standards. Additionally, future changes in meteorology may force additional mitigation efforts to meet air quality standards. The above is called the ”climate penalty”, which is already representing a challenging goal for the 21st Century (Junkermann et al., 2011; Bedsworth, 2011; Ravishankara et al., 2012).

As presented in more detail in the review on air quality and climate change relationships in Chapter 6 of this thesis, the study of long-term changes in the climate

system on air quality has mainly been developed around the understanding of potential changes on air quality meteorology. Therefore, atmospheric ventilation and the frequency of stagnation events have been inferred from climate change experiments at local and regional scales (Horton et al., 2014)

Results at regional and local scales have been reported from the application of regional climate models, such as the Weather Research and Forecasting (WRF) model (Trail et al., 2013; Zhao et al., 2011a). For instance, Zhao et al. (2011a) based on WRF outcomes, reported that air pollution episodes would be closely connected to stagnation events and ventilation conditions given by wind speed, sea breeze intensity and the planetary boundary layer height (PBLH).

During the last decades, air pollution from large urban areas has been accepted of playing a significant role in the atmospheric radiative balance due to the large transport of gases and airborne particles (aerosols) through continents and oceans. Indeed, satellite data reveals that air pollutants can travel trans-oceanic and trans-continent distances within a week (Ramanathan and Feng, 2009). Although the large-scale transport of aerosols is a direct threat to human (Samoli et al., 2011), the interaction of airborne particles in the atmosphere may lead to positive (warming) or negative (cooling) radiative forcing depending on their composition, as mentioned earlier (see §6.1).

The Atacama Desert in northern Chile, despite concentrating significant anthropogenic emissions of PM, and its natural exposition to mineral dust emissions (§3.3), has been unexplored in term of understanding air quality, mineral dust and their potential connections with the governing atmospheric forcings. Also, there an absence of studies about the potential impacts of climate change on these interactions, and their implications for air quality policy. The following section presents an overview of the Atacama Desert, which is the case study of this research and corresponds to the region that, due to its particular natural and anthropogenic configuration (Chapter 3) motivated the research questions presented in §1.3.

1.2 The Atacama Desert

The Atacama Desert is located in western South America stretching between central Chile all the way north into Peru (Fig. 1.2). Particularly, the extremely arid region of northern Chile spans between 18°S and 30°S (Schulz et al., 2011). The Pacific Ocean forms its western limit and to the east, it is flanked by the Andes Cordillera. The Atacama covers a surface area of 105,000 km^2 and ranges in altitude from sea level up to about 3,500 m a.s.l. (Houston and Hartley, 2003). This region is one of the driest places on the Earth, with registered annual precipitations between 1 and 80 mm in its northern and southern regions, respectively (Schulz et al., 2011; Sträter et al., 2010; Quade et al., 2008).

Four of the 15 administrative Chilean regions are fully contained within the desert (Fig. 1.2). These correspond to Arica and Parinacota (240,000 inhabitants), Tarapaca (340,000), Antofagasta (620,000) and Atacama (310,000) (INE, 2016). Also, the Northern margin of the Coquimbo region encompasses part of the hyper-arid area of the Atacama Desert (Fig. 1.2). Along the desert, several human settlements depend on fishing, shipping, energy. A major industry is mineral extraction, mainly based on the copper, iron, and gold reserves that are widely distributed throughout the Desert. The Atacama Desert plays a significant economic role for Chile. In addition to the roughly 1.5 million inhabitants living across this land, there is a large Chilean population depending directly or indirectly on the economic activities carried out in the Desert. For instance, mining employees often work in shifts and support families located in other regions of the country. The mining industry is a significant economic activity of Chile – for example Chile is the largest producer of copper globally (Lagos et al., 2020). According to the Chilean National Service of Geology and Mining (SERNAGEOMIN), about 69% of the overall copper production was produced in the Atacama Desert or close areas at those latitudes, such as the Andes Cordillera.

The energy sector is also significant across the Atacama Desert. In 2020 the total gross capacity installed in Chile was about 25,000 MW, from which 28% corresponded to hydroelectric, 9% wind, 11% solar, 1.8 biomass and 0.2% geothermal.

The remaining 50% corresponded to 19% natural gas, 20% coal and 11% petroleum derivatives (Bahamondez, 2020). By 2024 the 31% of this capacity will be withdrawn (Energy, 2020). Because of the natural geography, most hydropower production is located in the south and central regions of the country, whereas most of the solar and fossil fuels-based electricity generation is located in the North (Ruiz-Rudolph et al., 2016). In 2021, Chile has 70 times the capacity of solar energy generation than the current installed capacity (Energy, 2020). In the coming decades, the use of this capacity is aligned with political and environmental agreements undertaken by the Chilean government who has committed to phasing out coal-fired power energy generation by 2040 along with achieving carbon neutrality by 2050. By 2021, solar energy will account for 47% of the new capacity installed, almost 4,000 MW (Energy, 2020).

Figure 1.2: Regions of ”Arica y Parinacota”, ”Tarapaca”, ”Antofagasta”, ”Atacama” and ”Coquimbo”.

This intense anthropogenic activity has led to significant environmental impacts: especially on water resources and air quality. Some progress has been made around water resources, for example with seawater desalination. The impact on air quality in urban areas remains significant, especially from PM. Approaching

two-thirds of the Chilean population lives in areas exposed to harmful PM concentrations (Toro et al., 2015). In northern Chile, several areas in the Antofagasta and Atacama regions have been designated as "Saturated Zones" for PM_{10} and SO_2, which means that the concentration levels exceed Chilean standards. International air quality standards, such as those of the World Health Organization (WHO) are considerably stricter than Chilean standard levels, which have not changed since 1994 (Díaz-Robles et al., 2011). For instance, whereas the Chilean threshold for PM_{10} annual mean concentration is 50 μgm^{-3}, the WHO standard for the same indicator is 20 μgm^{-3}. Similar differences are found in the $PM_{2.5}$ legislation, despite the fact that the Chilean standard for $PM_{2.5}$ was enacted in 2011.

The main anthropogenic sources in the Atacama Desert have historically been industrial, such as mining extraction, copper foundries and energy production, and associated coal-burning power plants (Díaz-Robles et al., 2011; Ruiz-Rudolph et al., 2016). Anthropogenic sources from urban areas can also be significant. As reported in MMA (2015), urban PM pollution is exacerbated in Northern Chile due to the absence of effective mitigation measures, such as maintaining road networks, which lead to enhanced fugitive PM emissions by resuspension. The above has resulted in baselines studies reporting harmful PM_{10} and $PM_{2.5}$ (μgm^{-3} levels across urban settlements in the desert and coastal areas (MMA, 2015). A detailed and systematised description of PM_{10} and $PM_{2.5}$ levels in Northern Chile is presented in Chapter 3.

1.3 Purpose of the Study and Research Questions

This research aims to understand the relationship between particulate matter (PM_{10} and $PM_{2.5}$) levels and the climate and meteorological processes governing the hyper-arid nature of the Atacama Desert. There is a scarcity of studies on the topic in the existing literature, despite both the environmental vulnerability of the Atacama Desert and the important socio-economic role it plays for Chile. To achieve this aim, scientific understanding in several different topics must be advanced simultaneously. The natural mineral dust cycle has so far only been explored as part

of global studies, which is problematic given their resolution of the complex regional conditions. It is not yet clear whether insights about the role of atmospheric ventilation and stagnation on observed PM levels from elsewhere are pertinent for the Atacama desert. The intersection between climate and air quality projections the 21st Century has not yet been explored.

This work therefore aims to answer four related research questions.

1. What is the geographical and temporal distribution of mineral dust and its sources in the Atacama Desert?

2. What role do local atmospheric conditions play in episodes of dangerous particular matter levels in the Atacama Desert?

3. What are the mechanisms by which the climate of the hyper-arid environment in Northern Chile is projected to change over the coming century?

4. How would mineral dust, PM_{10} and $PM_{2.5}$ atmospheric concentrations respond under these future climate changes?

1.4 Outline of this Research

The rest of this thesis is structured in the six following chapters. Each of the four results chapters (chap. 3-6) start with a review of the existing literature and methodology specific to the analysis contained within that individual chapter. These are complemented by a chapter on common methods and data sources (chap. 2), as well as a chapter providing a synthesis and discussion of the entire thesis (chap. 7).

Chapter 2 describes the general methodology of the study as well as the fundamental methods used. It also contains a summary of the observational and modelled datasets used throughout the research and of the statistical analyses performed.

Chapter 3 analyses the climate dynamics of Northern Chile along with the elements of the climate system that promote the hyper-arid conditions of the Atacama Desert. Atmospheric concentrations of PM and gases are explored and discussed in the context of the Chilean standard as well as global guidelines. It does this through

analysis of observations from ground and upper-air weather stations and records of air pollution across Northern Chile.

Chapter 4 presents a satellite-based study of mineral dust characterisation over the Atacama Desert. Two MODIS algorithms retrieving aerosol optical depth (AOD) and Angstrom Coefficient are used. The primary mineral dust sources are identified, their variability is assessed and exceptional dust events across the area are detected. Winds patterns from the ERA5 reanalysis are analysed for the aeolian characterisation of mineral dust production and their role behind mineral dust events. Implications for air quality, solar power generation and future research are discussed.

Chapter 5 analyses meteorological forcers of PM_{10} and $PM_{2.5}$ variability and concentration levels. Atmospheric ventilation and stagnation were computed from observational and modelling datasets to analyse their spatial distribution and relationships with observed PM in the Atacama. The chapter concludes with the creation of a logistic regression model to aid in the prediction of severe PM events.

Chapter 6 explores historical and future simulations over Western South America under a set of standard scenarios from the UK Earth System Model Version I (UKESM1). Regional warming is studied through temperature and atmospheric moisture projections. Atmospheric stability is examined by analysing the South Pacific Anticyclone (SPA), atmospheric stratification and the planetary boundary layer. Then, the ocean forcing is studied by the governing Humboldt coastal upwelling system. Finally, future PM trends from UKESM1 are explored and discussed in the context of regional and local climate change impacts and their implications for local policy.

Chapter 7 synthesises the results from the previous research and places it in context. The limitations of the work are discussed along with suggestions for future research. The implications of the findings beyond academia are highlighted.

Chapter 2

Data and Methods

The four research questions proposed in Chapter 1 require different data and methods to answer them. This means that each of following chapters contains a method section describing the procedures followed for handling and processing the specific datasets used, as well as their nature and limitations. The four research chapters share similarities in their general approach, which will discussed in §2.1. The datasets they use are also generated using common methodologies - even if the datasets themselves are not shared. This chapter starts off by introducing and describing the general methodology of each portion of research (§2.1). There then follows a discussion of the observational datasets – ranging from ground-based measurements (§2.2), through satellites (§2.4.2), to reanalysis products (§2.7). The other main sources of information used to undertake this research comes from general circulation models, at either the regional (§2.6) or global scale (§2.5.1). It is important to mention that Chapters 3-6 provide the selection of data used, variables explored, period of study and statistical analyses performed in their respective methods sections.

2.1 General Methodology

The general methodology of this thesis considered the three stages shown in Fig. 2.1. First, a literature review was carried out to construct a critical theoretical framework on the climate and meteorological processes governing air pollution dynamic. This review had a particular focus on desert regions and particulate matter pollution,

the driving factors of the hyperarid environment of the Atacama Desert, natural and anthropogenic emission sources, and the potential effect of these processes under climate change over the coming century. As discussed in Chapter 1, and in the introductory sections of Chapters 3, 4, 5, and 6, there is a research gap with regards to the understanding of these processes in northern Chile. This first stage resulted in the set of research questions listed in Chapter 1 and provided the framework for methods selection, and the analyses of the results reported in Chapters 3, 4, 5, and 6.

The second stage comprised data collection, data processing and preliminary analyses (Fig. 2.1), which determined the scope of the following chapters and provided the basis for the analyses undertaken in each of them. The datasets collected comprise a wide range of observational and gridded datasets, including ground-based records of meteorology and air quality, upper-air meteorological observations, satellite retrieval of aerosols optical properties, reanalysis outcomes, regional climate modelling outcomes, and earth system modelling outcomes. These datasets and the institutions responsible for them are summarised in Tab. 2.1, and are described in more detail in the following sections. Tab. 2.1 shows the research questions (RQ1 to RQ4) addressed by each of the dataset, along with the thesis chapters where each dataset is used. The third stage consisted of developing each result chapter and analysing their findings to answer the proposed research question (Fig. 2.1).

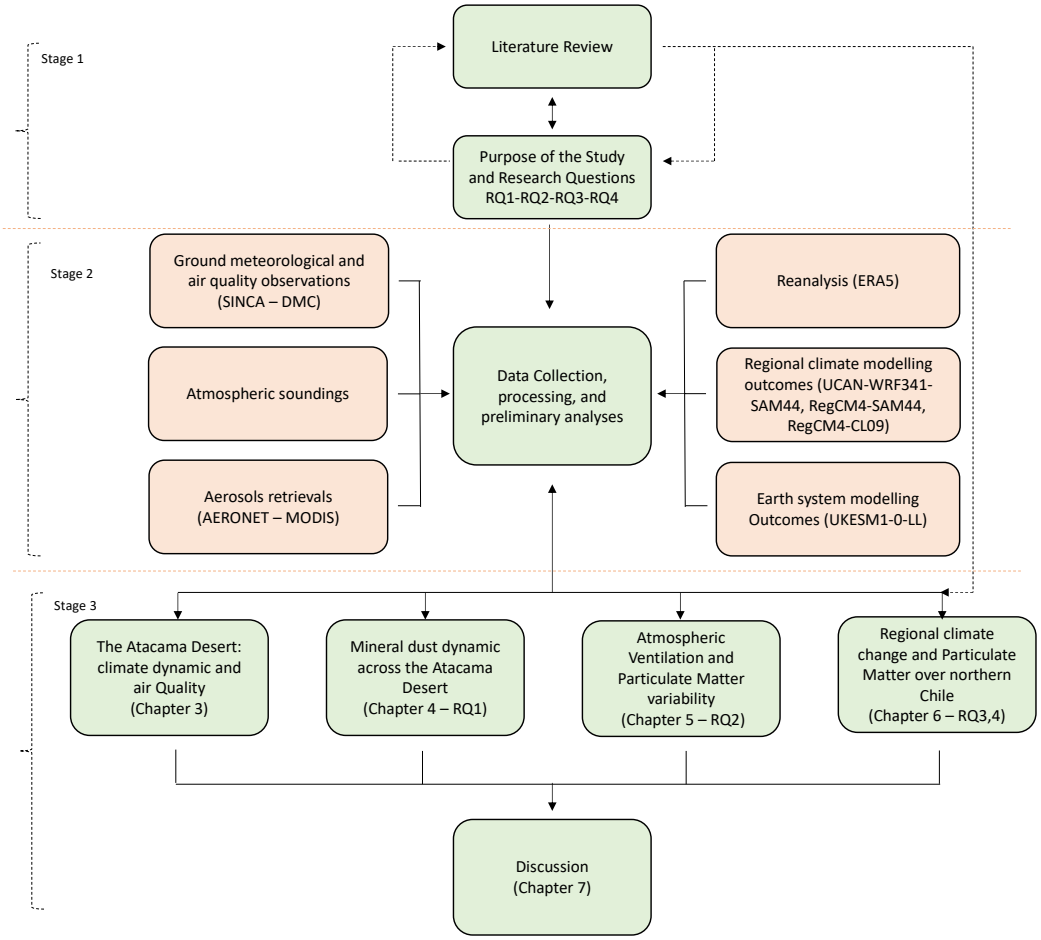

Figure 2.1: General Methodology. Salmon boxes depict data sources. Green boxes depict the different stages of this research.

Table 2.1: Primary datasets used in this research. RQ shows the research question addressed (§1.3)

Product-Dataset	**Institution**	**Product Type**	**Target characterisation**	**Chapt.**	**RQ**
National Air Quality Information System of Chile (SINCA)	Ministry of Environment of Chile (MMA)	Observational (ground-based)	Air quality and meteorology	3, 4, 5	RQ2
DMC Climate Services	Meteorological Service of Chile (DMC)	Observational (ground-based)	Meteorology	3, 5, 6	RQ2, RQ4
Cerro Moreno Atmospheric Sounding	University of Wyoming	Observational (atmospheric profiling)	Meteorology	3, 5, 6	RQ2, RQ4
Aerosol Robotic Network (AERONET)	National Aeronautics and Space Administration (NASA) and National Observatory For Aerosol (PHOTONS)	Observational (ground-based remote sensing)	Aerosols	4	RQ1
Moderate Resolution Imaging Spectroradiometer (MODIS)	National Aeronautics and Space Administration (NASA)	Observational (satellite-based remote sensing)	Aerosols	4	RQ1
UKESM1-0-LL	U.K.'s Met Office and the Natural Environment Research Council (NERC)	Earth System Model (ESM)	Climate	6	RQ3, RQ4
UCAN-WRF341I SAM44	Universidad de Cantabria (UCAN)	Regional Climate Model (RCM)	Climate and meteorology	5	RQ2
RegCM4-SAM44	Center for Climate and Resilience Research (CR2)	Regional Climate Model (RCM)	Climate and meteorology	5	RQ2
RegCM4-CL09	Center for Climate and Resilience Research (CR2)	Regional Climate Model (RCM)	Climate and meteorology	5	RQ2
ERA5 Reanalysis	European Centre for Medium-Range Weather Forecasts (ECMWF)	Reanalysis	Climate and meteorology	4, 5, 6	RQ1, RQ2, RQ4

The following subsections describe each dataset and its general usage. Following the structure in Tab. 2.1, the next section covers the ground-based meteorological and air quality observational datasets used (§2.2). The Cerro Moreno radiosonde is then described (§2.3), followed by aerosols retrieval products (§2.4), the description of earth system modelling and the UKESM1-0-LL model (§2.5), the regional climate models outcomes used (§2.6), and the ERA5 reanalysis (§2.7)

2.2 Ground-based meteorological and air quality observations

Ground-based meteorological and air quality observations provide observational evidence in Chapters 3, 4 and 5. The following subsections describe the National Air Quality Information System of Chile (SINCA), which provides meteorological and air quality data, and the climate services data source administrated by the Meteorological Service of Chile (DMC), which provides long-term meteorological observations.

2.2.1 National Air Quality Information System of Chile (SINCA)

The official Chilean air quality network SINCA[1] is a public dataset administrated by the Ministry of Environment of Chile, which provides real-time and historical observations of ground meteorology and air quality. SINCA comprises 216 monitoring sites across Chile and the 56 sites in the northern part of the country are used in this study. This observational dataset has been widely used for regular official Chilean reports concerning air quality (Toro et al., 2015) as well as scientific research (Mena-Carrasco et al., 2012; Jhun et al., 2013; Toro et al., 2015; Barraza et al., 2017).

The air pollutants monitored in SINCA include PM_{10}, $PM_{2.5}$, CO, O_3, NO_X, NO, NO_2, SO_2, Cu, Pb and As. The meteorological variables measured are solar radiation, atmospheric pressure, precipitation, relative humidity, surface temperature, wind direction and wind speed. Some sites suffer from significant gaps in their data

[1] http://sinca.mma.gob.cl

records and the monitoring periods can vary substantially between them.

Fig. 2.2 presents the location of the SINCA network sites in northern Chile. The full listing of the 56 sites and variables recorded is contained in the appendix. Fig. A1 summarises the air quality monitoring of the SINCA network, including sites location, period of operation, and the air pollutants recorded, whereas Fig. A2 summarises the meteorological monitoring.

Between the city of Arica (18.5°S) and Coquimbo (30.5°S) there are 56 monitoring sites contributing to SINCA (Fig. 2.2). Out of these, 36 sites have measured PM_{10}, and 27 stopped operation in 2010 or earlier. Eight are currently recording hourly real-time PM_{10} (see Fig. A1). Observations of $PM_{2.5}$ were incorporated later into the network, mainly only after 2015. Out of the 56 sites, 15 have measured $PM_{2.5}$, and nine sites are currently recording both PM_{10} and $PM_{2.5}$ hourly data (red crosses in 2.2). Seven of these sites are located in the Antofagasta region. Other pollutants (CO, O_3, NO_X, NO, NO_2, SO_2, Cu, Pb and As) are also monitored (Fig. A1). However, the number of sites monitoring these is considerably lower in comparison to PM_{10} observations with the exception of SO_2 (36 sites). Eight sites measure NO_x, NO and NO_2 or at least one of these, with two sites still taking measurements (Tocopilla and Calama, both in the Antofagasta region).

Meteorological observations are not taken at all SINCA sites (Fig. A2). Surface wind speed and direction have been recorded in 27 sites, with twelve of them still in operation. Unfortunately it is common that the observational periods of meteorological variables are shorter than those for the PM records. The detail of the data available for these and other meteorological variables monitored by SINCA is presented in Fig. A2.

For the purposes of this research, all the available data until December 2019 was downloaded and processed. The data selection from SINCA and the corresponding periods of analysis are detailed and justified in the methods section in Chapters 3, 4 and 5 in accordance with the purpose of each Chapter.

As a general approach for computing time averages from air quality and meteorological time series, daily means were calculated for days with at least 75% of

valid data, which means 18 or more hourly observations are available. Similarly, monthly means were calculated for months having at least 75% of valid data, which means at least 22 days available. Regarding air quality variables, daily mean data was directly obtained from the SINCA website. Monthly means were computed following the same criteria as meteorological data.

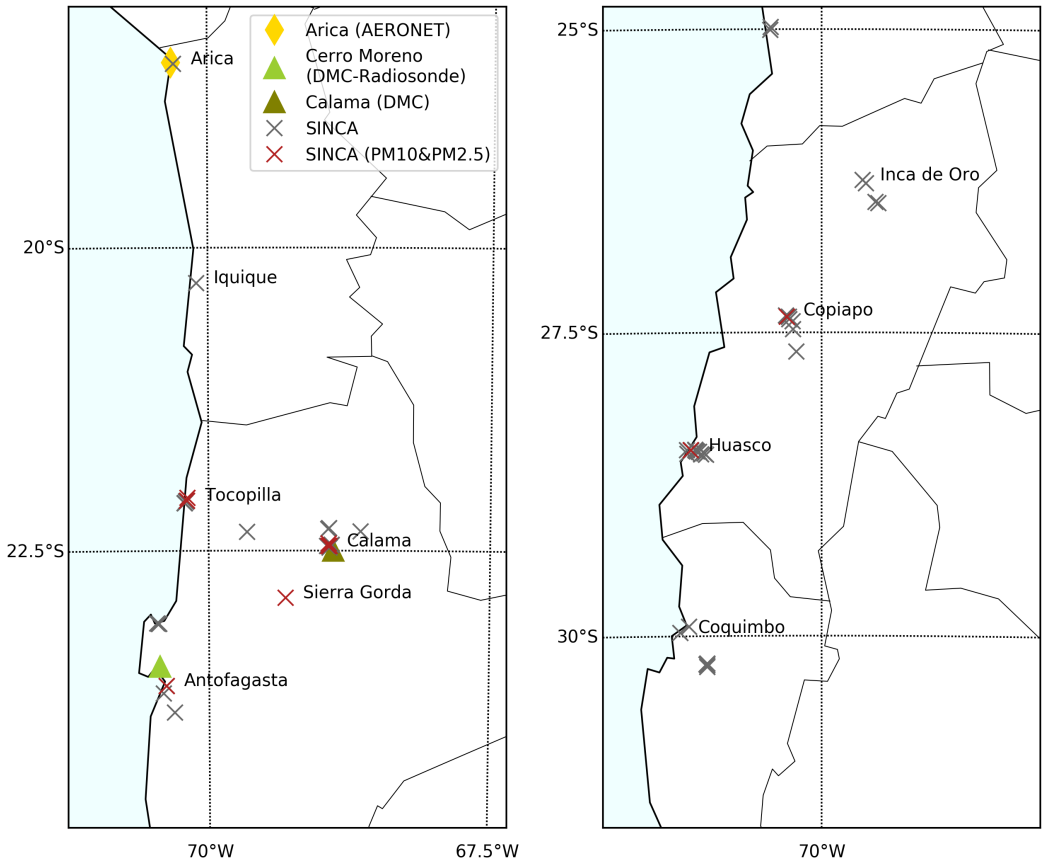

Figure 2.2: Meteorological and air quality observations sites from SINCA, DMC, AERONET and the Cerro Moreno radiosonde. Major cities are labelled with their locations demonstrated by the SINCA sites at the beginning of their names.

2.2.2 Meteorological Service of Chile (DMC)

The Meteorological Service of Chile (DMC) administers a national meteorological and climate observational network whose monitoring spans a range from a few years to several decades, starting in the mid-20th Century. This information is pub-

licly available on the DMC Climate Services website[2]. The monitoring includes measurements of surface temperature, precipitation, wind speed and wind direction. The location of DMC ground monitoring sites, Calama and Cerro Moreno (Antofagasta airport) considered in this study are plotted in Fig. 2.2. Both Cerro Moreno and Calama sites from DMC have surface records to the date of wind speed and wind direction (10 m height), temperature, relative humidity, and surface atmospheric pressure since 1950. As the data is provided at an hourly frequency, temporal averages were computed following the same criteria as the SINCA dataset.

2.3 Cerro Moreno atmospheric sounding

Radiosondes have been launched at Cerro Moreno (Antofagasta airport) since 1957. For most of the period only a single sounding was taken 12:00 UTC (08:00 or 09:00 am local time), although an additional 00:00 UTC sounding is now routine. The variables measured throughout the atmospheric column correspond to the standard list for atmospheric sounding datasets: atmospheric pressure, height, temperature, dew point, relative humidity, wind direction, and wind speed. The number of pressure levels has varied significantly over the years, from roughly 15 in the first decades to more than 100 levels at present, spanning from the surface to the mid-stratosphere, at about 30 km height.

The data is officially available from the Department of Atmospheric Science of the Wisconsin University[3], which has been widely used for scientific research as a data source for atmospheric soundings around the globe. Although launching started in 1957, the Wisconsin dataset reports data since 1973. However, this is appropriate for the purposes of this research. As shown in Fig. 2.2, Cerro Moreno (Antofagasta airport) corresponds to a shared location of both the Cerro Moreno radiosonde launching site and the DMC meteorological monitoring site.

[2]https://climatologia.meteochile.gob.cl/
[3]http://weather.uwyo.edu/upperair/sounding.html

2.4 Remote sensing of aerosols

Two sources of data are used for aerosol characterisation in northern Chile and analysed in Chapter 4. These correspond to the Aerosol Robotic Network (AERONET) and the Moderate Resolution Imaging Spectroradiometer (MODIS) dataset. The satellite-based study of mineral dust dynamics over the Atacama Desert in Chapter 4 is primarily based on MODIS satellite products of aerosols optical features. The AERONET data from the Arica site (Fig. 2.2) was used for validation purposes of the MODIS satellite products. Both data sources are described in the following subsections.

2.4.1 Aerosol Robotic Network (AERONET)

The Aerosol Robotic Network (AERONET)[4] comprises a global observational network equipped with Sun and sky scanning ground-based radiometers, and was developed to measure optical and microphysical properties of aerosols around the globe (Holben et al., 1998). It is administrated by the National Aeronautics and Space Administration (NASA) and the National Observatory for Aerosol (PHOTONS).

From a few sites when started in 1992, there are currently about 500 sites distributed worldwide that perform Sun measurements at 340, 380, 440, 500, 675, 870, 940, 1020 and 1640 nm wavelengths, which are used to compute total column Aerosol Optical Depth (AOD) (Jethva et al., 2019; Sinyuk et al., 2020). The AERONET network has extensively been used by the research community either for local aerosol characterisation and climatology, or satellite product validation (Holben et al., 1998; Zhang et al., 2005; Schuster et al., 2006; Kaskaoutis et al., 2007; Russell et al., 2010; Martins et al., 2017; Xu, 2018; Jethva et al., 2019). In this work, data from the AERONET site located in the northern city of Arica (Fig. 2.2) is used. The data correspond to AERONET Version 3 Level 2 product (cloud-cleared and quality-assured, Giles et al. (2019)). The data selection from the AERONET site in Arica and the collocation method used for validation of the satellite MODIS products are detailed in Chapter 4's method (§4.2).

[4] https://aeronet.gsfc.nasa.gov/

2.4.2 Moderate Resolution Imaging Spectroradiometer (MODIS)

The Moderate Resolution Imaging Spectroradiometer (MODIS) instrument is onboard the Terra and Aqua satellites operated by the National Aeronautics and Space Administration (NASA). It is the most widely validated remote sensing instrument, or sensor, for aerosols retrieval (Levy et al., 2013; Bilal and Nichol, 2015; Mhawish et al., 2017; Tao et al., 2017; Mhawish et al., 2019). MODIS sensors measure the reflected and emitted radiance of the Earth-atmospheric system with 36 bands between 0.4 and 14.4 μm (Tao et al., 2017). The two satellites pass overhead at different times: Terra provides aerosols retrievals at morning and noon local time, whereas Aqua provides aerosols retrievals at afternoon local times. MODIS products are widely used for studying aerosols properties around the globe over the oceans and multiple land categories. Four independent algorithms have been developed to retrieval of aerosols properties: dark target (DT) over ocean (Levy et al., 2013), dark target for dark land and vegetated regions (Tanré et al., 1997), deep blue (DB) for bright surfaces (Hsu et al., 2004), currently operational over the entire globe (Hsu et al., 2013), and the Multi-angle Implementation of Atmospheric Correction (MAIAC) for global application (Lyapustin et al., 2011a,c). The MAIAC algorithms has only recently become an operational product (Lyapustin et al., 2018).

The quality of aerosols retrievals from satellite sensors relies on four fundamental factors; determination of the surface reflectance, identification of surface snow and ice, detection of clouds, and the microphysical & optical model (Hsu et al., 2013).The relative importance of these four factors varies with aerosol load. The correct determination of the surface reflectance becomes more important as the aerosol load decreases, and it is a key factor for aerosol properties retrieval over land (Mi et al., 2007). On the other hand as the aerosols load increases, the accurate determination of the microphysical and optical properties becomes key (Jeong and Li, 2005). Over the land the surface reflectance influences the top-of-atmosphere reflectance signal at red and near-infrared wavelengths, which introduces uncertainty in the determination of aerosol properties. This is significantly enhanced in areas

with high surface reflectance, such as deserts – sometimes to the point that remote sensors struggle to separate both signals adequately (Hsu et al., 2013). The deep blue (DB) algorithm was developed to get around this issue, by using the 412 nm wavelength, at which surface reflectance is less, to allow the discrimation of the top-of-atmosphere signal over bright areas (Hsu et al., 2004; Jethva et al., 2019). Since its formulation, Deep Blue has been widely used for dust characterisation over arid and semiarid regions (Ginoux et al., 2012; Sayer et al., 2014; Tao et al., 2017; Jethva et al., 2019). The second generation of the DB algorithm, described in detail in Hsu et al. (2013), detects mineral dust based on the difference of brightness temperature in the infrared bands $8.6\mu m$, where dust absorption is stronger, and 11 μm. DB retrieval operates at 1 km horizontal resolution, which is aggregated at 10 km horizontal resolution in the level two products MOD04L2 (Terra) and MYD04L2 (Aqua)[5].

The Multiangle Implementation of Atmospheric Correction (MAIAC) (Lyapustin et al., 2011a,c) is a relatively new operational algorithm from MODIS. After significant improvements for aerosols retrieval over bright land surfaces, such as deserts, and smoke detection (Lyapustin et al., 2012), Lyapustin et al. (2018) introduced the latest version of MAIAC for processing the MODIS Collection 6 data record. MAIAC retrieves aerosols properties at 1 km resolution, as a final product, over both dark and bright surfaces on a sinusoidal grid (see Fig. 2.3). This allows fine-scale variability characterisation which is useful for local mineral dust and air pollution studies (Lyapustin et al., 2012; Kloog et al., 2015; Martins et al., 2017). MAIAC gridded products are currently available for the entire time that the MODIS satellites have been operating since 2000 for Terra and since 2002 for Aqua.

MAIAC uses a time series approach and multi-angle observations for dynamically deriving the surface bidirectional reflectance factors between 0.47 (blue) and 2.1 μm. In particular, MAIAC derives the spectral surface bidirectional reflectance distribution function (BRDF), favouring smoke and dust detection, and atmospheric correction. This method delivers a significant advantage in comparison to other al-

[5]https://modis.gsfc.nasa.gov/data/dataprod/mod04.php

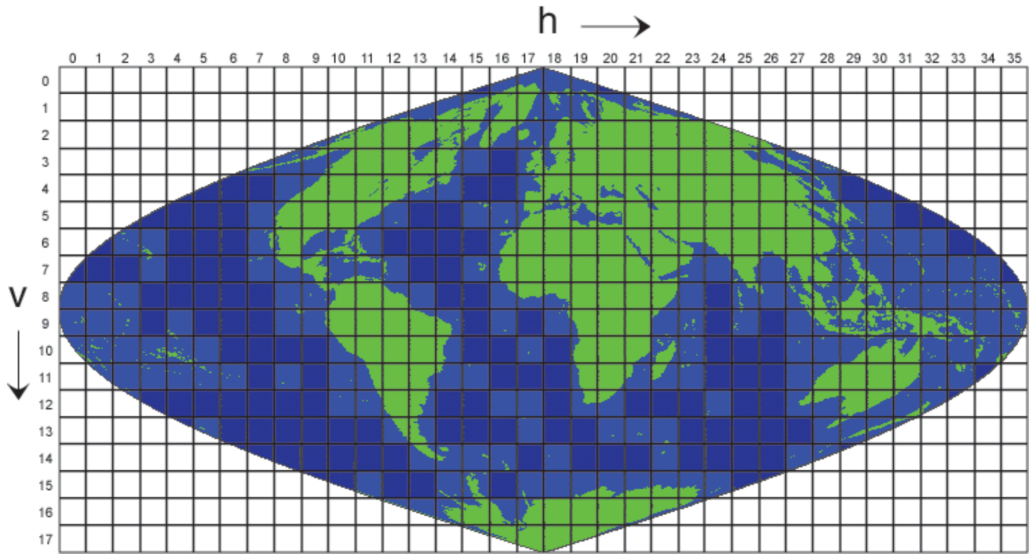

Figure 2.3: MODIS sinusoidal grid used by MAIAC algorithm. MAIAC process data over green (land) and light blue (ocean-land-containing) tiles (Lyapustin et al., 2018)

gorithms such as Dark Target (Levy et al., 2013) and VIIRS (Jackson et al., 2013) that are based on empirical assumptions for deriving surface properties (Martins et al., 2017). Those products use swath-based processing meaning that the satellite footprint is orbit-dependant and varies according to the scan angle. This requires aerosols retrievals to be based on prescribed spectral surface reflectance ratios (Martins et al., 2017; Lyapustin et al., 2018). MAIAC, however, uses physical atmosphere-surface model whose parameters are determined from surface observations (Lyapustin et al., 2012) resulting in significantly fewer prescribed properties. This is possible due to the multi-angle implementation in MAIAC over the regular sinusoidal 1km-resolution grid (see Fig. 2.5). The algorithm also applies time series accumulation over a 16-day period with a sliding window, as well as image-based processing. This means that MAIAC can retrieve aerosol properties and the bidirectional surface reflectance simultaneously (Lyapustin et al., 2018). These variables, provided at fine 1 km resolution, have led to the use of MAIAC product in several air quality studies (e.g. Chudnovsky et al., 2013; Kloog et al., 2014, 2015; Di et al., 2016; Stafoggia et al., 2017; Tang et al., 2017; He et al., 2020).

Both DB (MOD04L2 and MYD04L2) and MAIAC (MCD19A2) datasets were

downloaded from the Level-1 and Atmosphere Archive and Distribution System Distributed Active Archive Center (LAADS DAAC) website[6]. The selection of aerosols optical features from MODIS MOD04L2, MYD04L2 and MCD19A2 products, and the time and spatial coverages from the satellite retrievals are described in the method section in Chapter 4.

2.5 Earth system modelling outcomes

Earth system modelling outcomes from the UKESM1 Earth System Model (UKESM1-0-LL) are explored in detail in Chapter 6 in order to provide modelled evidence throughout the 20th and 21st centuries regarding climate change impacts over southern South America and the eastern South Pacific and future trends of PM_{10} and $PM_{2.5}$ across northern Chile. Here earth system models are described as a state-of-the-art family of fully coupled climate models, and then the UKESM1-0-LL model used in this study is described.

2.5.1 Earth System Models (ESMs)

Coupled atmosphere-ocean models simulate the physical processes of the climate system, such as the conservation of momentum, equation of state, temperature equation, continuity equation, conservation of mass, moist dynamic and equations governing the cryosphere. These computations have been at the core of the so-called coupled Atmosphere-Ocean General Circulation Models (AOGCM). Additionally, AOGCMs commonly include a land surface model to capture the land surface temperature, soil moisture, snow cover and vegetation. This module can be a subcomponent of the atmospheric model due to the short time feedback between both (Neelin, 2011).

Recent endeavours in modelling science, especially during the last decade, have been focused on incorporating the chemical and biological elements of the climate system to the modelling scheme. A widely accepted term for this family of models is Earth System Models (ESMs), although the terminology has not been without controversy (Neelin, 2011). ESMs still use an AOGCM for simulation of

[6]https://ladsweb.modaps.eosdis.nasa.gov/

the physical aspects of the climate system. However, complexity is added by coupling the AOGCM with the modelling of ecosystem processes, atmospheric chemistry, aerosols and biogeochemical cycles (e.g. carbon and nitrogen cycles), among others (Neelin, 2011; Flato et al., 2013b; Heavens et al., 2013; Bonan and Doney, 2018). A significant advantage of the ESM approach is not only the physical understanding of the ecosystem (such as the alteration of energy and mass balance by marine and terrestrial feedbacks) but also the opportunity of better measures of direct impacts on society (such as marine biological production and air quality(Bonan and Doney, 2018)). On the other hand, ESMs represent a significant challenge in terms of measuring uncertainty due to the inclusion of Earth system components that are difficult or even impossible to observe (Sellar et al., 2019) (Fig. 2.4).

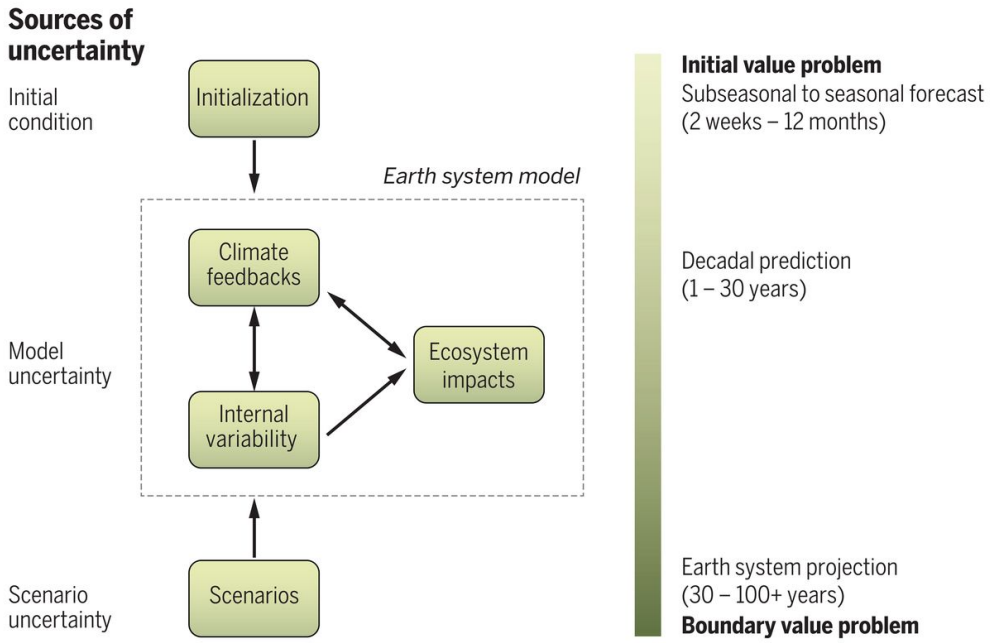

Figure 2.4: Sources of uncertainty in Earth System Models (ESMs). Model outcomes are given by climate feedback, the internal variability and ecosystem impacts. These elements, along with initial conditions and scenarios formulation, contribute to final models uncertainty. (From Bonan and Doney, 2018) .

The atmosphere and ocean modelling components in a climate model are coupled, which means they regularly transfer information between themselves. Generally speaking, the entire system is discretised into grid cells representing a portion

of atmosphere or ocean which defines the spatial resolution of the model (Neelin, 2011). However, grid systems differ between the atmosphere and ocean module. In the atmosphere, hybrid vertical coordinates are often used. These are essentially pressure coordinates aloft, but transition to heights nearer the surface. The horizontal resolution of both meridional and zonal grids may vary from the Equator to the poles (Sellar et al., 2019). The vertical grid is finer at the lower troposphere, to capture boundary layer dynamics, and tends to decrease significantly from the mid-Troposphere (Neelin, 2011).

Ocean grids tend to present similar characteristics, although their formulations respond to different approaches accordingly to the portion of the ocean basin to simulate. In ocean models, the depth coordinate of distance is used for the representation of the boundary layer, that is the shallow layer of seawater. Models can use terrain-following sigma coordinates (useful for ocean boundaries) or isopycnic coordinates (useful for interior ocean representation). However, both these grids must be interpolated onto depth coordinates prior to upload onto the Earth System Grid Federation (ESGF; Griffies, 2004). Similarly to atmosphere grids, the vertical resolution is considerably finer near the surface due to the complex ocean-atmosphere interchange taking place in the mixing layer and the thermocline (Griffies, 2004; Neelin, 2011).

2.5.2 UKESM1-0-LL

The first version of the UK Earth System Model UKESM1[7] (Sellar et al., 2019), is the successor of the HadGEM-2-ES model (Bellouin et al., 2011a). It represents a joint effort of the U.K.'s Met Office and the Natural Environment Research Council (NERC) which also contributes to the Coupled Model Intercomparison Project Phase 6 (CMIP6). UKESM1 uses the HadGEM3-GC3.1 model (Kuhlbrodt et al., 2018; Williams et al., 2018) as the physical core for the representation of the physical climate system, which has shown significant improvements in comparison with its predecessor (Kuhlbrodt et al., 2018; Sellar et al., 2019). The atmosphere in UKESM1 is represented by 85 vertical levels on a hybrid following-terrain coordi-

[7] https://ukesm.ac.uk/

nate scheme from the surface up to 85 km height. The analysis undertaken in this thesis uses the low horizontal resolution of the model, formally called UKESM1-0-LL. Both land and atmosphere are discretised through a regular grid with 1.25° latitude and 1.87° longitude of horizontal resolution (Sellar et al., 2019; Walters et al., 2019). On the other hand, the ocean grid (Storkey et al., 2018) comprises a common vertical grid of 75 levels on an isotropic Mercator grid with a hierarchical resolution scheme from three different model configurations of 1, 1/4 and 1/12 ° resolution at the Equator. The thickness of the vertical levels ranges from 1 m near the surface to 200 m in the deep ocean to focus resolution within the mixing layer.

The Earth system components coupled to HadGEM3-GC3.1 constitute models in themselves. This coupling between components is particularly relevant since it allows dynamic feedback between them and provides the scope for the model's practical applications (Sellar et al., 2019). The set of system modelling components includes terrestrial carbon and nitrogen cycles, ocean biogeochemistry and an atmospheric chemistry model (encompassing both the troposphere and stratosphere), coupled with a multi-species aerosol scheme. The aerosol scheme includes sea salt, black carbon (BC), sulphate, particulate organic matter and dust aerosol species (Sellar et al., 2019; Mulcahy et al., 2020). Several benefits arise from the atmospheric chemistry coupling, which has direct applications on policies along with the opportunity of addressing a wide range of scientific questions not possible to answer solely through its physical core model. For instance, the prognostic atmospheric chemistry allows the inference of particulate matter concentrations from chemical species outcomes and the analysis of air quality trends globally or regionally under given global emissions pathways and future climate change scenarios. Also, mitigation strategies can be assessed from short-lived pollutants and climate forcers, such as tropospheric ozone or methane (Stohl et al., 2015; Sellar et al., 2019). The main components of UKESM1 and their corresponding references are listed in table Table 2.2. A full description of UKESM1 components is available in Sellar et al. (2019).

Table 2.2: UKESM1 Component Models

Component Model	Description	Reference
Physical core model	HadGEM3-GC3.1: atmosphere-land-ocean-sea ice coupled model	Kuhlbrodt et al. (2018); Williams et al. (2018)
Terrestrial biogeochemistry	Joint UK Land Environment Simulator (JULES). Plants physiology and funcional types, and nitrogen cycle. Land use model, dynamic vegetation and agricultural land use change	Clark et al. (2011); Harper et al. (2016, 2018)
Ocean biogeochemistry	Model of Ecosystem Dynamics, nutrient Utilisation, Sequestrationand Acidification (MEDUSA). Submodel (diagnostic) for Dimethylsulfide (DMS) surface sea water concentration	Yool et al. (2013); Anderson et al. (2001)
Atmospheric chemistry, composition	United Kingdom Chemistry and Aerosol model (UKCA). Unified stratospheric-tropospheric chemistry, aerosols-chemistry coupling	Archibald et al. (2020); Mulcahy et al. (2018)

The aerosol scheme in UKESM1 corresponds to the GLOMAP modal aerosol microphysics scheme (Mann et al., 2010, 2012; Mulcahy et al., 2020). The term modal refers to the aerosol species computation through the aerosol mass and number estimation for five size classes (or modes) of particle. For black carbon (BC), organic matter (OM), sulphate and sea salt, there are four soluble modes (with radius boundaries between the modes at 5, 50 and 250 nm) as well as one insoluble mode. The aerosol composition is computed separately for each mode from microphysical representations during the model simulation (Mulcahy et al., 2020). The anthropogenic emissions of SO_2, BC and OM taken from the Community Emissions Data System (CEDS, Hoesly et al., 2018). The anthropogenic biomass burning emissions were compiled by van Marle et al. (2017) from the Global Fire Emissions Database, the interactive fire and emissions algorithm for natural environments (INFERNO), and fire modelling. Whereas all anthropogenic emissions are prescribed, natural aerosols emissions are dynamically computed in UKESM1. This is possible due to the full coupling of ESM components, including biochemical processes and vegetation dynamics. This interactive simulation capacity allows the dynamical estimation

of emission for sea salt aerosols, dimethyl sulfide (DMS), primary organic aerosols, and biogenic volatile organic compounds (BVOCs) (Sellar et al., 2019; Mulcahy et al., 2020).

Dust aerosol emissions are computed independently through the 'CLASSIC' dust scheme (Bellouin et al., 2011b). As mineral dust production is simulated from the bare soil fraction in the land-use module, the bias in emissions is strongly sensitive to vegetation representation in the land-use model, especially in arid or semi-arid regions (Sellar et al., 2019). Once the dust is emitted, the horizontal flux is computed for nine bins between 0.064 and 2000 μm diameter, and the vertical flux is derived for six bins from 0.064 to 64 μm diameter (Mulcahy et al., 2020).

Regarding optical properties of mineral dust and its wavelength-dependent refractive response, these are parameterised following Balkanski et al. (2007). The refractive indices proposed by Balkanski et al. (2007) are based on mineralogical databases comprising abundances of iron oxides (main absorber in the visible spectrum). Therefore, the optically active mineral components of dust are first considered for refractive indices computation according to the range of minerals constituents over a given region.

In the 'CLASSIC' mineral dust scheme, from all aerosol species, both mineral dust and FFBC (fossil fuel black carbon) are considered non-hydrophilic. This means that during simulations, mineral dust particles do not experience hygroscopic growth. Therefore, they do not experience changes in specific extinction due to increasing relative humidity (Bellouin et al., 2011b). Regarding to the other aerosols species, the parameterization for hygroscopic growth follow the schemes by Fitzgerald (1975) (sulphate, sea-salt, and nitrate aerosols), Haywood et al. (2003) (biomass burning aerosols, fossil fuel organic carbon aerosols), and Varutbangkul et al. (2006) (biogenic aerosols).

2.6 Regional climate modelling outcomes

Regional climate models (RCMs) were developed for downscaling climate fields produced by GCMs to provide simulations at finer scales, usually more suitable

for regional analyses, including applications on impact assessments and adaptation (Giorgi, 2019).

Nowadays, RCMs are usually forced by an AOGCM, ESM or reanalysis products and hence provide dynamical downscaling. This is particularly useful for analysing short-term phenomena and for the development of predictions and forecasting tools, such as air quality forecasting services. This is the reason why RCMs usually force chemical transport models (CTM) for air quality simulation. Although dynamical downscaling represent a suitable alternative to minimise topographic biases from forcing global models or reanalyses, the success depends on the regional model's formulation and the domain (Manzanas et al., 2018). Such uncertainties, along with any other from climate models, add additional sources of uncertainty for air quality analyses (Menut et al., 2013).

Regional climate modelling outcomes from the UCAN-WRF341I SAM44, RegCM4-SAM44 and RegCM4-CL09 models provide modelled evidence for the atmospheric ventilation study over northern Chile carried out in Chapter 5. In the following subsections, each modelling dataset is described.

2.6.1 UCAN-WRF341I SAM44

The Weather Research and Forecasting (WRF) model (Skamarock et al., 2008) is a numerical weather prediction (NWP) and atmospheric simulation system widely used by the scientific community for both operational applications and weather-climate scientific research. Its use as an open-source community model allows its extensive application for research, including regional climate simulations and air quality.

The UCAN-WRF341I SAM44 model (Manzanas et al., 2018) corresponds to WRF model, version 3.4.1, configured by the University of Cantabria (UCAN), as a contribution to the Coordinated Regional Climate Downscaling Experiment (CORDEX) for the South American domain[8] (Fig. 2.5). UCAN-WRF341I SAM44 is one of the few RCMs contributing to CORDEX over this region.

The South American domain in CORDEX (SAM-44) is set to 0.44° horizontal

[8]https://cordex.org/

resolution with a rotated pole system over an equatorial domain (Fig. 2.5). This reproduces a quasi-uniform resolution equivalent to about 50 km across the domain. The experiment explored was the evaluation period (1979-2011) forced by the ECMWF ERA-Interim reanalysis (a precursor to the ERA5 reanalysis, at a 0.75° horizontal resolution) .

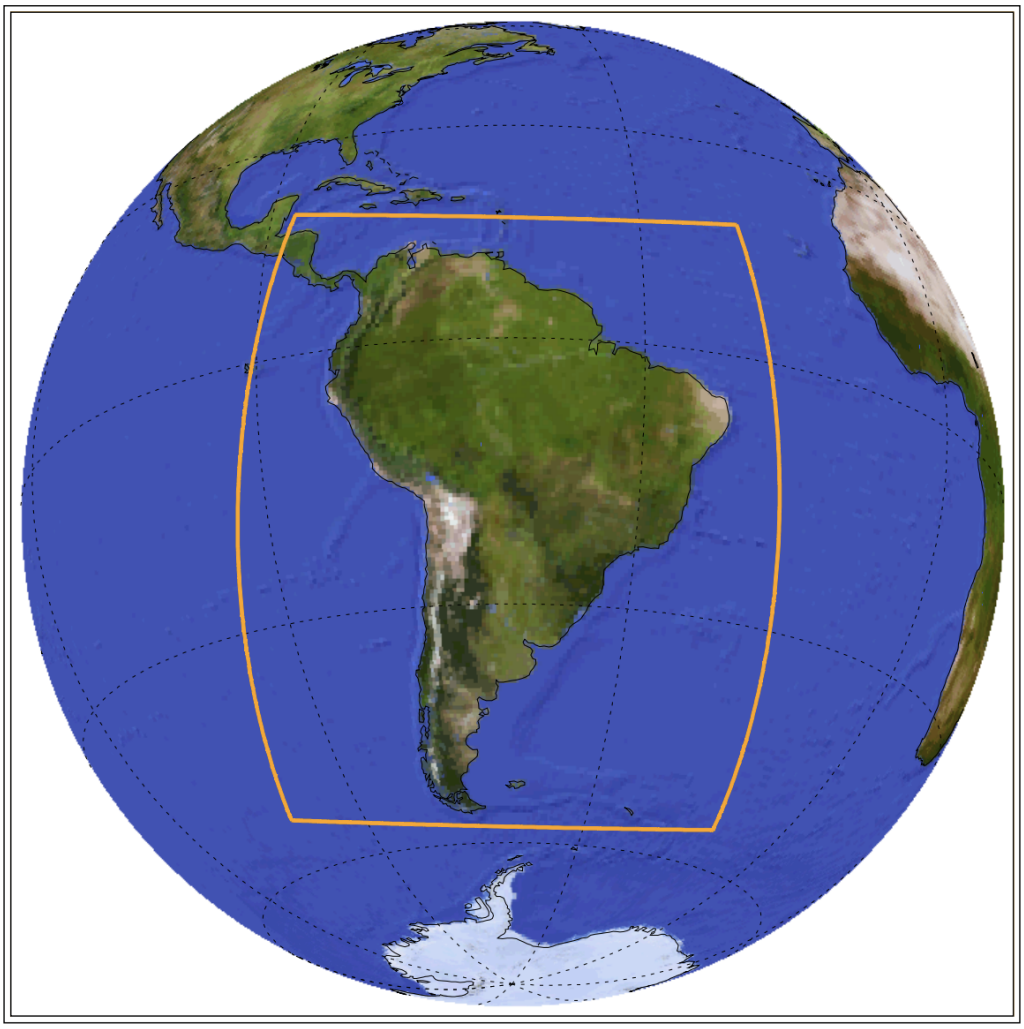

Figure 2.5: South American Domain SAM-44 defined by CORDEX and used in UCAN-WRF341I SAM44 and RegCM4-SAM44 models (CORDEX, 2015).

The UCAN configuration of WRF for CORDEX comprises 30 vertical levels along with the physical parameterisations summarised in Tab 2.3 as described by Manzanas et al. (2018). Daily output was downloaded for the evaluation experiment. A complete list of variables as well as the analyses performed are detailed in

the method section in Chapter 5.

Table 2.3: UCAN-WRF341I SAM-44 physical parameterisations

Physical Param.	Scheme	Reference
Long and short wave radiation	NCAR Community Atmosphere Model	Collins et al. (2004)
Non-local closure planetary boundary layer (PBL) scheme	Yonsei University (YSU)	Hong et al. (2006)
Land surface model	Noah land surface model	Chen and Dudhia (2001)
Moist processes	single-moment scheme with 5 microphysics species (WSM5)	Hong et al. (2006)
Unresolved convection	Kain-Fritsch cumulus scheme	Kain (2004)

2.6.2 RegCM4-SAM44 and RegCM4-CL09

The RegCM4-SAM44 and RegCM4-CL09 (Bozkurt et al., 2019) are two simulations over Chile of the hydrostatic Regional Climate Model version 4 (RegCM4) developed by the International Centre for Theoretical Physics (ICTP) (Giorgi et al., 2012). RegCM4 is the latest version of RegCM which was first published by Giorgi et al. (1993). Its dynamical core is based on the Penn State/NCAR Mesoscale Model (MM5) (Grell et al., 1994). RegCM has been widely used for simulations of the climate system at regional scale on domains governed by complex topography, such as complex land regions across the European Alps, (Giorgi et al., 2016), Asia (Marcella and Eltahir, 2012; Xue-Jie et al., 2013; Oh et al., 2014), and the poles (Grassi et al., 2013; Bozkurt et al., 2018) and northern Chile (Bozkurt et al., 2016).

RegCM4-SAM44 and RegCM4-CL09 datasets are the product of a set of simulations on two nested domains coupled with a one-way nesting approach (Bozkurt et al., 2019). The coarser domain corresponds to SAM-44, as defined by CORDEX (0.44°horizontal resolution, 50 km), and its outcomes are reported as RegCM4-SAM44. The outcomes from the finer domain (0.09°horizontal resolution, 10 km) forced by RegCM4-SAM44, are reported as the RegCM4-CL09 (Fig. 2.6).

The simulation was performed for an evaluation experiment (hindcast simulation) spanning the period 1980-2015 (1979 spin-up), whose driving global dataset was the ERA-Interim reanalysis (0.75°horizontal resolution) which provides boundaries condition for the coarser domain SAM-44 (Bozkurt et al., 2019).

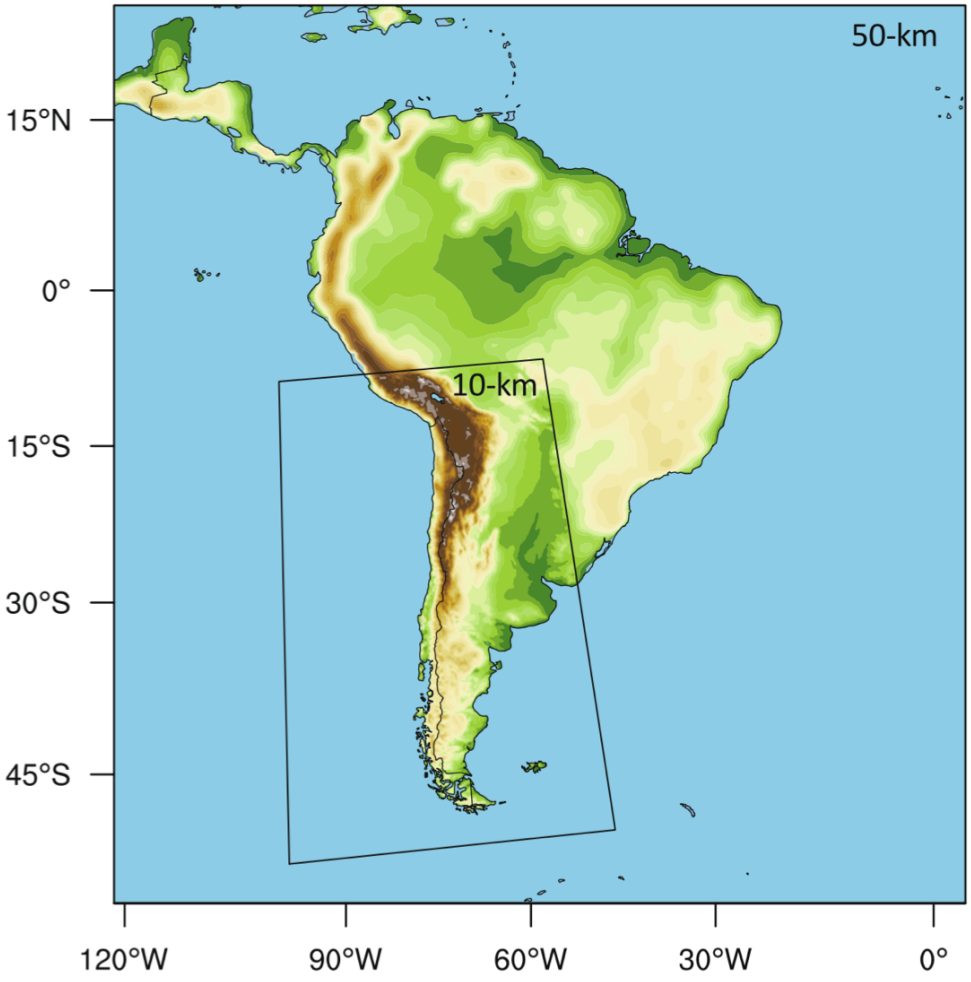

Figure 2.6: South American Domain SAM-44 defined by CORDEX used by RegCM4-SAM44 (coarse, 50 km), and CL09 domain over Chile used by RegCM4-CL09 (fine, 10 km). *Adapted from Bozkurt et al. (2019)*

The configuration of RegCM4 for both domains (SAM-44 and CL-09) comprises 27 vertical levels along with the physical parameterisations summarised in Tab 2.4 as described by Bozkurt et al. (2019). Daily outcomes from both RegCM4-

SAM44 and RegCM4-CL09 were downloaded from the CR2 server[9].

Table 2.4: RegCM4-SAM-44 and RegCM4-CL09 Physical Parameterisations

Physical Param.	Scheme	Reference
Land surface model	Biosphere-Atmosphere Transfer Scheme (BATS)	Dickinson (1993)
Planetary Boundary layer	-	Holtslag et al. (1990)
Radiative scheme	NCAR Community Climate System Model Version 3 (CCSM3)	Kiehl et al. (1996)
Ocean ux parameterization	-	Zeng et al. (1998)
Resolvable precipitation	-	Pal et al. (2000)
Cumulus convection	Grell	Grell (1993)
Cumulus closure scheme	Fritsch and Chappell	Fritsch and Chappell (1980)

2.7 ERA5 reanalysis outcomes

The ERA5 reanalysis is used in multiple chapters to provide reanalysed meteorological data as support for a satellite-based mineral dust analysis (Chap. 4), the computation of atmospheric ventilation indexes (Chap. 5) and the characterisation of current meteorology in the analysis of future climate change impacts over the Atacama Desert (Chap. 6).

The ERA5 reanalysis[10], developed by the European Centre for Medium-Range Weather Forecasts (ECMWF), replaced the ERA-Interim reanalysis, which ended production in 2019. Several improvements were performed in ERA5 in comparison with its predecessor (ERA-Interim). These include hourly resolution outcomes for a wide range of climate, land and oceanic variables on single and by pressure levels since 1979. The dataset is public access in the Climate Data Store (CDS)[11].

[9] http://www.cr2.cl/simulaciones-regionales-regcm4/
[10] https://www.ecmwf.int/en/forecasts/datasets/reanalysis-datasets/era5
[11] https://cds.climate.copernicus.eu

A preliminary version for the period 1950-1978 is also currently available. The reanalysis comprises 137 vertical levels up to roughly 80 km height (a substantial improvement compared to the 60 levels in ERA-Interim). ERA5 is provided on a Gaussian N160 grid, with a resolution of approximately 31 km.

The ERA5 dataset used in this research comprises hourly outputs of zonal and meridional wind at surface and 500 hPa, surface temperature, and boundary layer height across northern Chile and over the eastern Pacific. The data was downloaded from the CDS website. The specific variables selection and period of analyses are detailed in the method sections in Chapters 4, 5, and 6 in accordance with the objectives defined in each chapter.

2.8 Summary

This chapter has outlined a range of datasets that are used in the subsequent analyses as well as an overarching methodology through which the research has been performed. The datasets come from sources rooted in instrumental observations and model simulations, or a blend both.

Observational datasets comprise air quality and meteorological ground level records from the National Air Quality Information System of Chile (SINCA) and meteorological observations from the Meteorological Service of Chile (DMC). Also, upper-air meteorological observations from the last decades have been explored from the Cerro Moreno atmospheric sounding. Satellite aerosols retrievals comprise DB (MOD04L2-MYD04L2) and MAIAC (MCD19A2) aerosols products at 10 and 1 km resolution, respectively, over northern Chile for 2010-2019. Also, aerosols properties have been obtained from the Aerosol Robotic Network (AERONET) site located in Arica for the same period.

Regarding the regional climate models explored, these correspond to the UCAN-WRF341I SAM44 model contributing to CORDEX, and the RegCM4-SAM44 and RegCM4-CL09 modelling experiments developed by the Center for Climate and Resilience Research (CR2). Also, reanalysed data from ERA5 have been used. Finally, historical (20^{th} Century) and climate change (21^{st} Century)

analyses had been carried out by exploring the outcomes from the UK earth system model (UKESM1) contributing to CMIP6.

At their heart, the model simulations used in this dissertation are often built upon general circulation models. Given the finite computer resources, there is a necessary trade-off between resolution, complexity and size of the domain. Simulation output from regional climate models is used to investigate boundary layer meteorology in Chap. 5, which requires information at fine temporal and spatial scale. Meanwhile, Chap. 6 on future climate and air quality change requires a fully coupled Earth System Model, with its additional complexity and components. This chapter has focused on aspects of the methodology that span several chapters. Further specifics on each of the datasets and analyses used for each individual study are included in the relevant chapters.

Chapter 3

The Atacama Desert: Climate Dynamics and Air Quality

The Atacama Desert is located along the western coast of South America between 15°S and 30°S, meaning it includes southern Peru and the bulk of northern Chile (Houston and Hartley, 2003). The hyper-arid region of northern Chile, which is the subject of this research, spans between 18°S and 30°S (Schulz et al., 2011). As introduced in Chapter 1, this region plays a crucial role in the socio-economic development of Chile, and it is home to about 1.5 million people concentrated in several major urban areas.

This chapter describes the Atacama Desert in detail with a particular focus on its climate, current anthropogenic and natural emissions, and concentration levels of particulate matter (PM_{10} and $PM_{2.5}$). The understanding of these three elements provides the basis for the studies presented in the Chapters 4-6 of this thesis. It starts with a review of the climate dynamics of the Atacama Desert (§3.1). Data from upper-air observations are then analysed to compute the height of the temperature inversion layer, which dominates the northern Chilean coast (§3.2). Third, a public dataset of air pollutants emissions is explored to characterise primary emitter activities. Finally, air quality levels, focusing on particulate matter, are examined, followed by the final remarks. It is important to highlight that this chapter does not intend to do source attribution but reflects on the observed air pollution levels as a characterisation of the study area.

3.1 Climate Dynamics in the Atacama Desert

The Atacama Desert is bounded in the west by the Pacific Ocean, whereas to the east, it is flanked by the Andes Cordillera that reaches altitudes up to about 3,500 m above sea level (Houston and Hartley, 2003). This region is one of the driest places on the Earth, with mean annual precipitations ranging between 1 and 80 mm in its northern and southern regions, respectively (Quade et al., 2008; Sträter et al., 2010; Schulz et al., 2011).

The extremely arid conditions of the Atacama Desert are the result of several interactions between the ocean, atmosphere and land surface occurring on multiple temporal and spatial scales (Fig. 3.1). These hyper-arid conditions are directly related to this regions location under the high-pressure system associated with the subsidence of the Hadley cell at the southern tropical latitudes (Houston and Hartley, 2003; Sträter et al., 2010; Muñoz et al., 2011; Schulz et al., 2011). As well as large-scale atmospheric subsidence, the South Pacific Anticyclone leads to a constant southerly airflow driving active coastal upwelling of the Humboldt current along the Northern Chilean and Southern Peruvian coasts (Oyarzún and Brierley, 2019). Because of the Humboldt upwelling, surface waters in the Southeast margin of the Pacific Ocean exhibit remarkably cool temperatures in comparison to the zonal mean (Schulz et al., 2011). Both the stable subsidence system (zonal forcing) and the persistent cold sea surface water along the coast (ocean forcing) lead to strong atmospheric stability and the formation of a very persistent temperature inversion layer (TIL) at roughly 1 km above sea level (Sträter et al., 2010). This inhibits convection and hence precipitation (Houston and Hartley, 2003; Sträter et al., 2010; Muñoz et al., 2011; Schulz et al., 2011). Additionally, the upwind slope of the Andes Cordillera acts as a natural barrier for mixing and convection processes of moist easterly air masses, which leads to a rainshadow effect on the leeward side of the Andes (Houston and Hartley, 2003; Schulz et al., 2011). Finally, a disconnection with the Amazonia-Atlantic source of moisture provides a continental forcing of the extremely arid conditions in the region (Ortlieb, 1995; Houston and Hartley, 2003).

The Andes have a substantial effect on the climate of the Atacama Desert, since they acts as a vertical barrier for easterly atmospheric flows. At the lower latitudes over the Andes, between roughly 15°S and 22°S, intense precipitation can occur as a result of convective systems associated with a north-easterly humid-warm upper airflow from Amazonia (Garreaud et al., 2003; Schulz et al., 2011). In this Andean region, known as the 'Altiplano', the zonal summertime airflow is linked to a latitudinal expansion of the equatorial easterlies in the middle and upper troposphere. Therefore, this abundance of moisture is the product of a large-scale moisture transport rather than changes in local moisture sources (Vuille, 1999; Garreaud et al., 2003). In wintertime, the primary source of moisture in the Atacama is associated with the north-easterly extratropical cold fronts, leading to frontal precipitations systems (Garreaud and Rutllant, 1996; Vuille and Ammann, 1997; Schulz et al., 2011). Also, cut-off lows that usually hit central Chile can reach lower latitudes and trigger rainfall in northern Chile (Fuenzalida et al., 2005; Schulz et al., 2011). Therefore, two primary sources of moisture are identified for the Atacama Desert, depending on the season and location. In the Altiplano, convective rainfall usually occurs in summer, whereas in coastal areas and lower altitudes, frontal precipitations occur in winter, with occasional contributions of cut-off low-pressure systems that migrate from higher latitudes. Due to the zonal dependence of these phenomena, the boundary between both areas is described as a diagonal limit over the Andes Cordillera at the Altiplano latitudes (Houston and Hartley, 2003).

Surface local wind patterns are seasonally modulated the South Pacific Anticyclone (SPA), especially along the coast. The land-ocean thermal contrast enhanced by the equatorward winds that promote coastal upwelling reaches their maximum during the afternoon of the austral summertime (Rutllant et al., 2003; Oyarzún and Brierley, 2019). The varying land-ocean pressure gradients over the course of the day combines with topographic factors modulates the daily wind speed and direction cycles along the coast and over the inner Atacama Desert. This results in a distinctive wind pattern over the desert (Garreaud and Falvey, 2009; Rutllant et al., 2013). Within the planetary boundary layer, the ocean-land gradient results in pre-

vailing strong south-westerlies during the afternoon, contrasting with light north easterlies during the night and early morning. This cycle is enhanced by an intensification of the coastal subsidence during the afternoon, which results in the clearing of the stratocumulus cloud deck (Garreaud and Falvey, 2009; Schulz et al., 2011; Rutllant et al., 2013). As reported by Muñoz et al. (2013) from two years of multilevel observational records, there are some differences between the central region desert and the region closer to the Andes. This cycle provides a significant zonal wind component in the central desert region, with intense westerlies dominating during the daytime and weaker easterlies governing nighttime and the early morning. However, in Calama, and influenced by topography, south-westerlies predominate during the daytime, and down-valley north easterlies govern during the night and early morning (Rutllant et al., 2013).

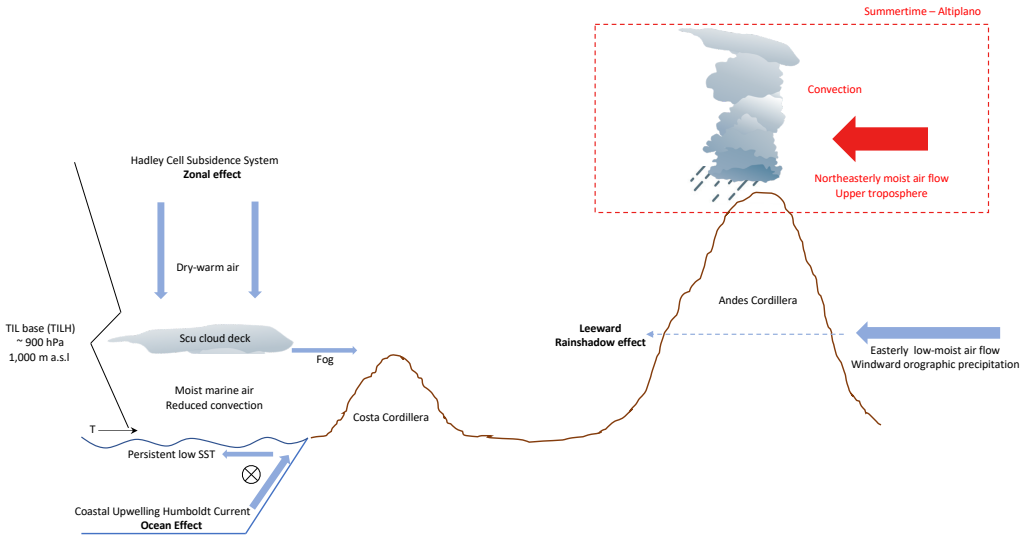

Figure 3.1: A schematic of the climate dynamics in Northern Chile. This cross-section is looking equatorwards and highlight the three important contributors: the zonal, ocean and rainshadow effects. *TIL means 'temperature inversion layer' and Scu means 'stratocumulus'.*

Along the coast of Northern Chile, the planetary boundary layer is capped by a persistent Temperature Inversion Layer (TIL). Under the inversion, the lower troposphere is characterised by cold and humid marine air, whereas the subsiding

air above is warm and dry (Rutllant et al., 2003; Muñoz et al., 2011; Schulz et al., 2011). The inversion leads to a persistent low-level stratocumulus cloud deck over the coast along the desert, with the consequent radiative impacts and its influence on the large-scale climate (Muñoz et al., 2011). Under the inversion and the quasi-persistent stratocumulus cloud deck, a westerly fog, also known as "Camachaca", develops during wintertime. This represents an additional source of moisture of the Desert (Houston and Hartley, 2003), which the local ecosystem has evolved to harvest.

Previous studies have reported that the height of the inversion has consistently increased during ENSO events during the 20^{th} Century (Rutllant et al., 2003; Schulz et al., 2011), as might be expected from the increasing sea surface temperatures. Also, the daily and weekly cycles of the boundary layer height and cloud cover variability have been strongly linked to synoptic-scale forcings (Garreaud et al., 2002; Muñoz et al., 2011).

The many factors governing the hyper-arid core of the Atacama Desert, along with the intricate topography, impose a significant challenge for climate models. Models usually underestimate the temperature inversion layer height and contain biases in the cloud fraction estimation, both essential in setting the hyper-arid conditions (Garreaud and Muñoz, 2005; Hannay et al., 2009; Muñoz et al., 2011). The ocean components of climate model fail often smear out the coastal upwelling, resulting in offshore SSTs that are too warm (Oyarzún and Brierley, 2019). Winds patterns suffer from inconsistencies in simulations especially in the inner desert, because they only coarsely resolve the complex local geography (Bozkurt et al., 2019).

3.2 Temperature inversion layer height

This section presents an analysis of the radiosonde records from the Cerro Moreno launching site. This site at Antofagasta's airport is the only upper-air monitoring site in Northern Chile, with sufficient coverage over the relevant period. Further details about the records can be found in §2.3. First, a subsection describes the methods

used to compute the temperature inversion layer height (TILH), and second, the calculated TILH is analysed. This time series is later used in Chapter 5.

3.2.1 Methods

The height of the base of the extremely stable temperature inversion layer along the coast of the Antofagasta Region can be considered as an approximation of observed PBLH in the area (Schulz et al., 2011). The TILH was inferred from radiosonde observations launched daily since 1957 at 8:00 local time (12:00 UTC) and 20:00 local time (00:00 UTC) from the Cerro Moreno station, north of the city of Antofagasta.

The number of pressure levels on which data is available varies from roughly 15 in the early decades to over 100 in the present day. Vertically, these span from the surface to the mid-Stratosphere. Only data from 1973 until 2018 is analysed, because several gaps and the reduced number of vertical levels prior to this. The number of vertical levels has increased from 50 (in 1973) to about 125 in the last decade (Figure 3.2). Only the 12:00 UTC soundings are analysed, becuase data recorded at 00:00 UTC is scarce and mainly available before 1987. These data selection criteria result in a dataset of 15,009 records from 12:00 UTC launches spanning 1973 and 2018.

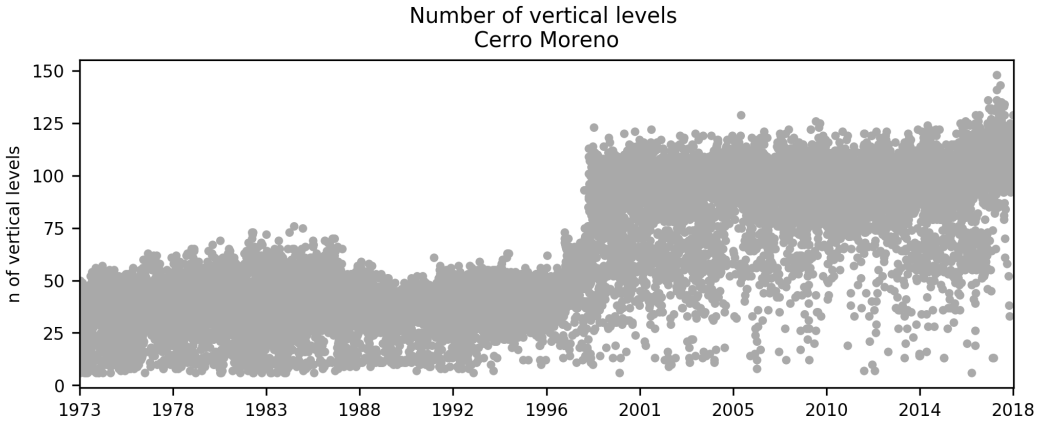

Figure 3.2: Number of vertical levels of the radiosonde records from Cerro Moreno between 1973 and 2018.

A temperature inversion was identified when a pronounced and coincident divergence of the dew point (decrease) and temperature (increase) was observed oc-

curred within a sounding (Fig. 3.3). The pressure level (hPa) and recorded height (m) at its base was registered as the TILH for that day. This deviation between temperature and dew point is also associated with a decrease of humidity, which characterises the overlying air mass (Fig. 3.3).

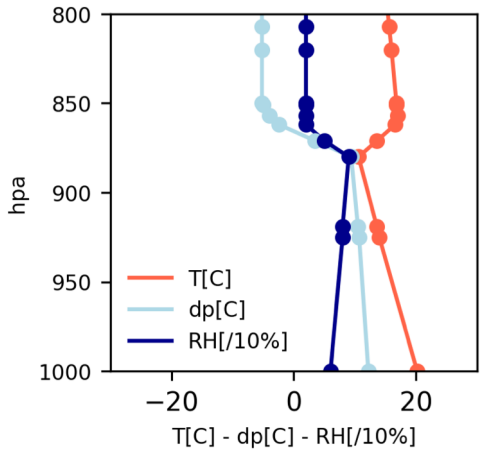

Figure 3.3: Example vertical profile for 21st Dec 2016 showing the temperature inversion layer base height. The profile contains 110 vertical levels in total, although only the lowest levels are shown. The inversion occurs at 880 hpa.

One limitation of computing inversion base heights from radiosonde records is the potential scarcity of observations where the inversion occurs. In the case of Cerro Moreno, the number of vertical levels in the soundings has increased considerably after 1997 (Fig. 3.2). When no inversion is detected, the number of pressure levels between 600 and 1,400 m height was explored to ensure that the absence of inversion responded to an atmospheric condition rather than an absence of measurements. These two heights were used since they have been reported as usual bottom and upper limits of the TILH in the area (Schulz et al., 2011). 880 soundings (therefore days) had less than three observations between 600 and 1,400 m. This is insufficient to detect a turning point, and therefore these soundings were excluded from subsequent analysis. From the 14,129 valid daily records between 1973 and 2018, 277 days did not experience an inversion layer – representing less than 2% of the period analysed.

For the elaboration of Figure 3.4, temperature observations from each profile were interpolated into a common regular vertical grid between 0–1,005 hPa with

201 equally-spaced levels. This is necessary for the creation of temporal averages and climatologies. The interpolation method used was linear in pressure. The TILH values analysed and presented subsequently in this dissertation are derived from using the raw levels profiles of each measurement. Although the density of vertical levels introduces some level of uncertainty regarding the exact height of the TIL base (TILH), using vertically-interpolated data does not minimise this uncertainty.

3.2.2 Temperature inversion layer height (TILH)

The Cerro Moreno radiosonde data shows that a quasi-permanent inversion is observed, in agreement with Schulz et al. (2011). There is a clear seasonal cycle in the inversion layer height, although it remains around 900 hPa throughout the period (Fig. 3.4).

Higher altitudes of the TIL base are observed in summer (Fig. 3.5). January and February also show greater variability in TILH. Single daily records have reached up to about 1900 m height in summer, whereas in winter, the TILH reaches up to about 1650 m height. This computed TILH time series is later used in Chapter 5 for characterising the atmospheric ventilation conditions in this area.

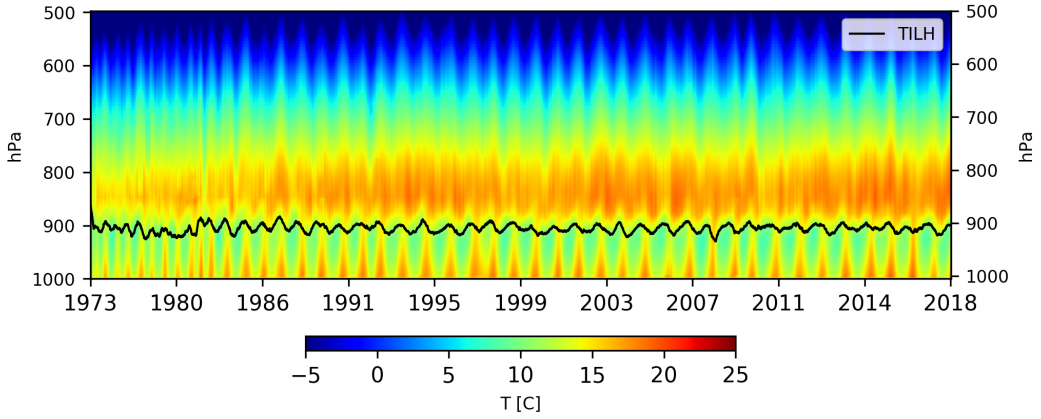

Figure 3.4: Vertical profile of temperatures from the Cerro Moreno radiosonde dataset.The black line depicts the computed TILH..

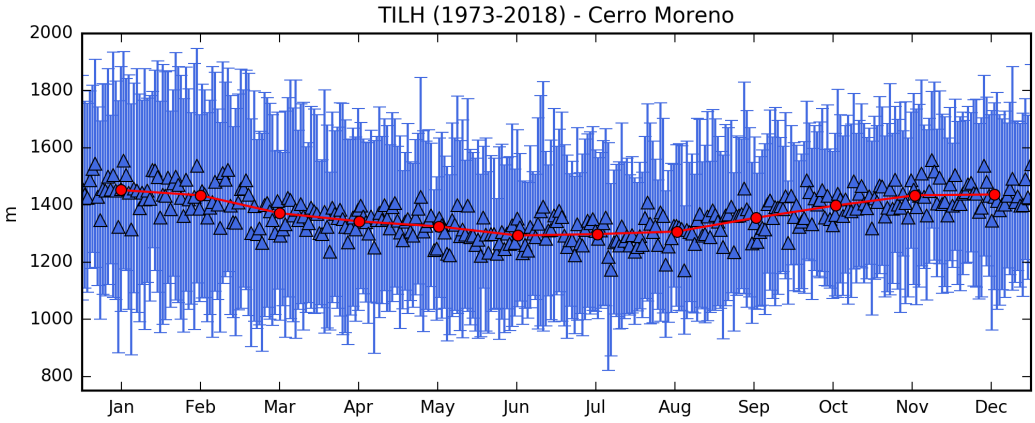

Figure 3.5: The annual cycle of the TILH computed from the radiosonde dataset from Cerro Moreno in 1973-2018. Blue bars depict the range of one standard deviation of the observations of each day during 1973-2018. Blue triangles represent daily averages, and red circles correspond to the monthly mean during the period of analysis.

3.3 Air pollutant emissions in northern Chile

Air pollutant emission sources in northern Chile are the result of both the geographical conditions and the economic development experienced in the country during the last decades. The latter has led to the installation of large-scale facilities, which comprise of mainly smelters, mineral extraction operations, and coal- and oil-fired power plants to supply the industrial operations as well as the local population. Both energy generation and the mining industry are of major concern regarding air pollutants emissions (PM and gaseous species) in northern Chile (Ruiz-Rudolph et al., 2016).

Between 2004 and 2009, there was a sharp rise in coal- and oil-fired power plants as a response to the expansion of the copper mining industry and subsequent energy demand (Díaz-Robles et al., 2011). These industrial facilities all emit a significant amount of the so-called 'criteria pollutants' (PM_{10}, $PM_{2.5}$, NO_x, SO_2 and CO) as well as lead and arsenic. In addition, coal-and oil-fired power plants are responsible for mercury emissions and mining operations lead to large amounts of coarse particulate matter (CPM, or PM_{coarse}) entering the atmosphere (Ruiz-Rudolph et al., 2016).

Anthropogenic emissions reach even remote areas of the desert, as demonstrated by fog samples collected 70 km away from the city of Iquique (20.2°S) (Sträter et al., 2010). Evidence of sulphates and heavy metals was found, which the authors suggest originated from populated cities, power plants, mining and steel industry using back trajectories. The aridity of the Atacama Desert means that there is a minimal amount of vegetation and high levels of natural dust emissions occur from the bare soil. Sträter et al. (2010) suggest that about 50% of the ionic concentrations in their samples were associated with sea salt. They also associate the high acidity of the fog with metals from bare soil-sourced particulate matter.

The emission rates (t per year) of a range of air pollutants across Chile are systematically collected through the Emissions and Transfer Registry (RETC in Spanish) database[1]. This is an official and public access initiative designed to collect, organise, analyse and disseminate information regarding emissions and transfers of air pollutants harmful to human health and the environment. The database comprises of council-level yearly data, which is updated every year with emissions to the atmosphere by point and diffuse sources from both industrial and non-industrial activities across the whole country. The data of emissions are solicited every year and regulated by the health authority (MINSAL, 2005). This statutory body obliges all polluters to declare their emissions.

A summary of the 2018 version of the RECT dataset for point sources is given in Table 3.1. Energy generation dominates the emissions for all pollutants tabulated, except for SO_2 which is dominated by metal production. Mineral extraction makes a significant contribution to NO_x and CO emissions. Construction makes notable contributions to both the SO_2 and NO_x emissions. Nearly all the $PM_{2.5}$ emissions (93.7%) comes from energy generation, dwarfing all other contributors by nearly 2 orders of magnitude. It is important to mention that these statistics do not consider diffuse emissions, which comprise wildfires, urban fires, and urban-rural residential firewood combustion. These emissions are very scarce or even nil in the dry environment of the Atacama Desert (MMA, 2018).

[1] https://datosretc.mma.gob.cl/dataset/

Table 3.1: Combined emissions for the regions of Arica & Parinacota, Tarapaca, Antofagasta and Atacama from the RECT dataset. *Sectorial contributions over 5% are noted.*

Industry	PM_{10}	$PM_{2.5}$	SO_2	NO_x	CO
Manufacturing	0.7	0.2	2.1	20.8	4.5
Mineral extraction	113.4	46.0	1286.5	2297.7 (13%)	547.9 (22%)
Fishing	52.3	34.6	704.6	435.4	73.5
Metal production	860.4 (30%)	13.4	63,699.8 (72%)	945.3 (5%)	149.1 (6%)
Construction	70	6.8	4410.2 (5%)	849.8 (5%)	50.6
Energy generation	1746.5 (61%)	1582.4 (94%)	17866.9 (20%)	13182.2 (72%)	1602.1 (64%)
Water supply	2.0	0.5	3.1	57.9	12.5
Energy trans^n & dist^n	0.2	0.1	0.4	6.9	1.5
Agricultural and forestry	0.1	0.0	0.1	1.8	0.4
Others	10.0	5.0	59.9	390.8	74.2
Total	2,855.7	1,689	88,033.5	18,440.0	2,516.3

The largest point sources, categorised by sectors, are mapped in Fig. 3.6. Across the Desert, there are 75 power energy facilities (Fig. 3.6b) and 107 mineral extraction facilities (Fig. 3.6d). Meanwhile, there are 20 metal production facilities (Fig. 3.6c), whose SO_2 emission account for 72% of the total.

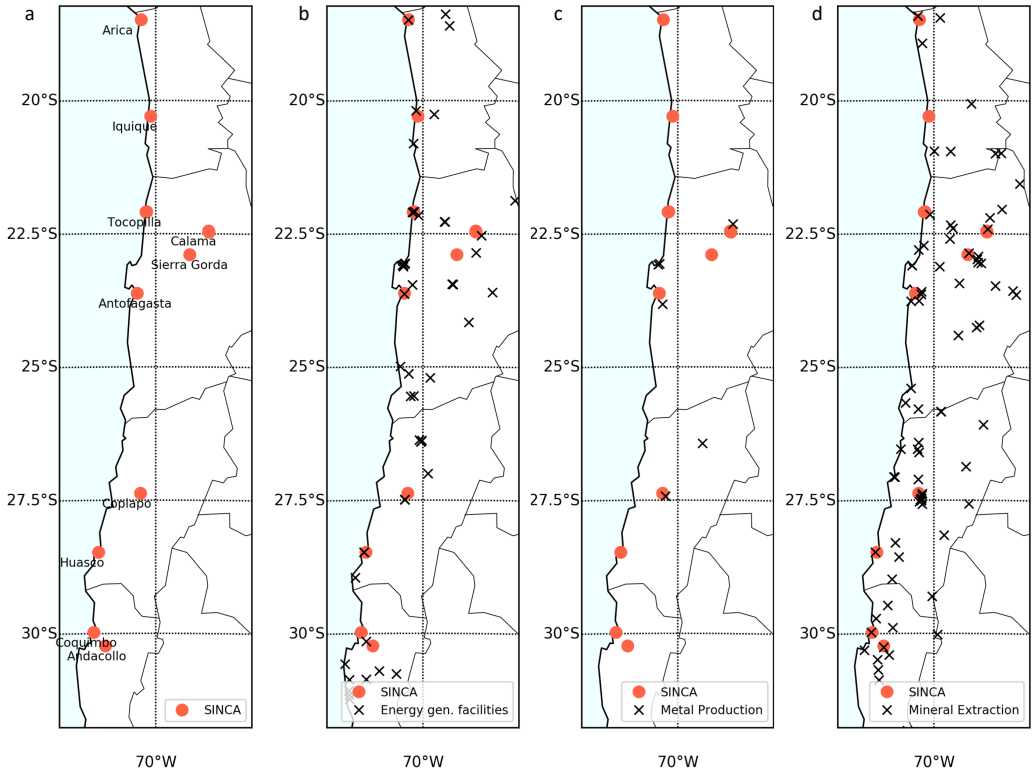

Figure 3.6: The relative location of emissions sources to the observing network. (a) The SINCA network, labelled by their cities. Vehicle emissions data is available for Antofagasta, Arica and Calama (Tab. 3.2). (b) Energy generation facilities. (C) Metal production facilities. (d) mines and other mineral extraction facilities.

The RECT treats vehicle emission data separately to point sources, and breaks it down to the city level (Tab. 3.2). For PM_{10} and $PM_{2.5}$, these comprise emissions from tyre wear, brake wear, and exhaust emissions. Only exhaust emissions contribute to SO_2 and NO_x emissions. For northern Chile, the RECT database contains information for the cities of Arica (230,000 inhabitants), Antofagasta (390,000 inhabitants) and Calama (180,000 inhabitants). The urban transport emissions of SO_2 and NO_x are small compared to other sectors (Tab. 3.2). $PM_{2.5}$ and PM_{10} are roughly the same magnitude to each other, because of the nature of the emission

where the fine fraction of particles predominates. Vehicle emissions of $PM_{2.5}$ are larger than all point sources for but the energy generation sector.

Table 3.2: Transport emissions (t) by pollutant in 2018 for the 3 largest cities in Northern Chile. Computed from the RECT dataset

City	PM_{10}	$PM_{2.5}$	SO_2	NO_x
Arica	75.0	70.0	1.5	746.5
Antofagasta	105.2	92.9	4.1	1,545.2
Calama	21.2	18.5	0.7	240.1

3.4 Particulate Matter in Northern Chile

The Chilean air quality standard for PM_{10} is enshrined in law by the National Environmental Commission and the Ministry General Secretariat of the Presidency of Chile through DS-59-1998 (59th Supreme Decree during 1998, CONAMA, 1998). The standard for PM25 is underpinned by DS-12-2011 and the later-established Ministry of Environment of Chile (MMA, 2011). Both decrees define air quality thresholds, whose exceedance represents a threat to human health. An area is categorised as "latent" non-attainment when the air pollutant concentrations lie between 80 and 100% of the threshold value, and an area is classified as "saturated" non-attainment when the threshold value is equalled or exceeded. According to Chilean legislation, when the area is latent, an atmospheric prevention plan has to be implemented. When the area is saturated, an atmospheric decontamination plan has to be carried out. Until 2010, the latent and saturated areas in northern Chile were mostly related to dangerous concentrations of SO_2 and PM_{10}, and primarily associated with coal-based energy generation and copper foundries (Díaz-Robles et al., 2011). Although mitigation efforts during the last decade have had some success, the air quality in northern Chile still represents a challenge (Ruiz-Rudolph et al., 2016). The threshold levels defined in both acts (DS-59-1998 and DS-12-2011) have not been modified since their enactment, which has resulted in a substantial discrepancies from the WHO guidelines (Tab. 3.3).

Table 3.3: Chilean standards for annual and 24-hours means of PM_{10} (CONAMA, 1998), $PM_{2.5}$ (MMA, 2011), and the equivalent WHO guidelines (WHO, 2006)

Pollutant	Chilean standard (μgm^{-3})		WHO standard (μgm^{-3})	
	annual	24h	annual	24h
PM_{10}	50	150	20	50
$PM_{2.5}$	20	50	10	25

SINCA contains nine sites contributing to SINCA are measuring PM_{10} and twelve are measuring $PM_{2.5}$. These sites are mapped in Fig. 3.6 and described further in §2.2.1. The recent air quality measured at these SINCA sites are given in Tab. 3.4 and categorised in Fig. 3.7. Chilean legislation requires the average of three consecutive years to identify the exceedance of annual mean thresholds, so 2017-2019 are used. The sites must also have at least nine months of valid data to compute an annual mean (§2.2.1), although this is a practical rather than legal consideration. The WHO does not set a latent range (WHO, 2006), though a similar approach to the Chilean definition (i.e. 80–100% of the threshold) has been adopted. SINCA contains several sites in close proximity to each other. There are three sites in Calama (Calama-PVK, Calama-CD and Calama) and two sites in Tocopilla (Gobernacion and Tocopilla (Escuela E-10)). However, for mapping purposes, only the worst case is plotted in the case of each pollutant.

There is a substantial contrast between the impressions of northern Chilean air quality depending on whether national or international standards are used (Fig. 3.7). For PM_{10}, all the sites exceed the WHO standard of 20 μgm^{-3} for the annual mean. When considering the Chilean standard though, the sites of Gobernacion, Copiapo and Calama-PVK qualify as latent and only Sierra Gorda qualifies as saturated (Fig. 3.7a,b). The contrast is more stark for $PM_{2.5}$ – all sites present good air quality under Chilean standards, yet all of them are either latent or saturated under the WHO guidelines (Fig. 3.7c,d). A particularly interesting case is the city of Antofagasta. This city presented reasonably good levels of PM_{10} and $PM_{2.5}$ under the national guidelines. However, under WHO standards, this urban centre exceeds the threshold for PM_{10} and lies in the latent range for $PM_{2.5}$.

Since under Chilean normative, this distinction triggers the implementation of

mitigation plans, either an atmospheric prevention plan or an atmospheric decontamination plan, the definition of what level of annual concentration is defined as a threat for human health directly impacts the actions that the central government will or will not undertake.

The annual mean values computed for all the sites measuring both PM_{10} (9) and $PM_{2.5}$ (12) are summarised in Table 3.4. Regarding PM_{10}, it is relevant to note that all the sites exceed at least by 50% (30 μgm^{-3}) the WHO threshold (20 μgm^{-3}).

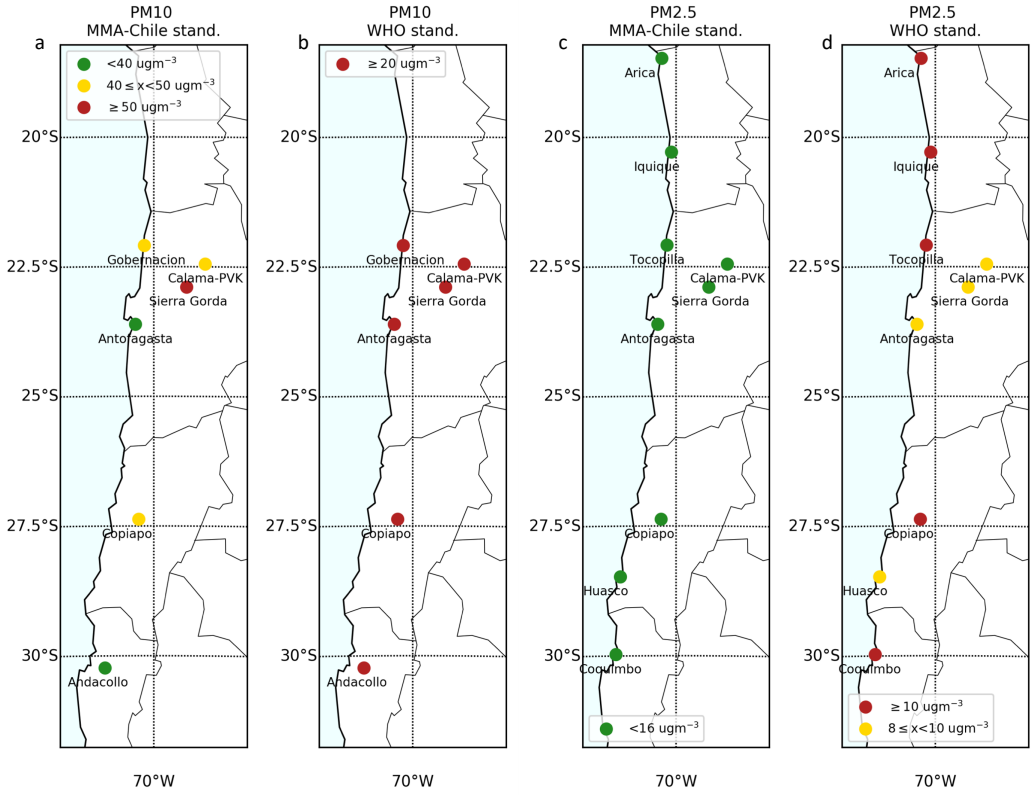

Figure 3.7: The annual mean of PM_{10} and $PM_{2.5}$ for 2017-2019. Colours indicate the concentrations that exceed (red), lie in latent range (yellow) or are under (green) the standards defined by national legislation (a,c) and international guidelines (b,d)..

Table 3.4: The annual mean of PM_{10} and $PM_{2.5}$ for SINCA sites (averaged over 2017-2019)

Site	PM_{10} (μgm^{-3})	$PM_{2.5}$ (μgm^{-3})
Arica	-	12.0
Iquique	-	11.8
Gobernacion	41.3	-
Tocopilla	38.4	11.4
Antofagasta	33.9	9.9
Sierra Gorda	56.6	9.4
Calama	31.6	6.5
Calama-CD	41.0	7.6
Calama-PVK	45.5	9.8
Copiapo	41.9	13.6
Huasco	-	9.9
Coquimbo	-	13.1
La Serena	-	14.0
Andacollo	39.0	-

A closer look at the daily mean PM_{10} time series from each site during the last two decades reveals a mix of trends between them (Fig. 3.8). These time series has not been filtered to preserve daily mean values and visually contrast with national and international standards. First, in all sites, it is evident that most of the daily records exceed the WHO standard for the annual mean (dashed red line), hence the high yearly levels in Tab. 3.4. A decreasing trend is observed at Tocopilla, Calama-PVK and Andacollo; with most days since 2015 between the two thresholds. This might be related to ongoing mitigation atmospheric decontamination plans in these locations. Tocopilla, the Chuquicamata Foundry area (which lies 21 km north of Calama), and Andacollo were designated as saturated under Chilean legislation in 2007 (for PM_{10}), 1991 (for PM_{10} and SO_2), and 2009 (for PM_{10}) respectively (Díaz-Robles et al., 2011). The area around Chuquicamata has a long history of air pollution incidents starting well before DS-59-1998 legislation was enacted. Several mitigation efforts in the area taken place and are still ongoing, whose results are evidenced from the observations. Despite this, all the sites are still largely exceeding international standards (Fig. 3.7c).

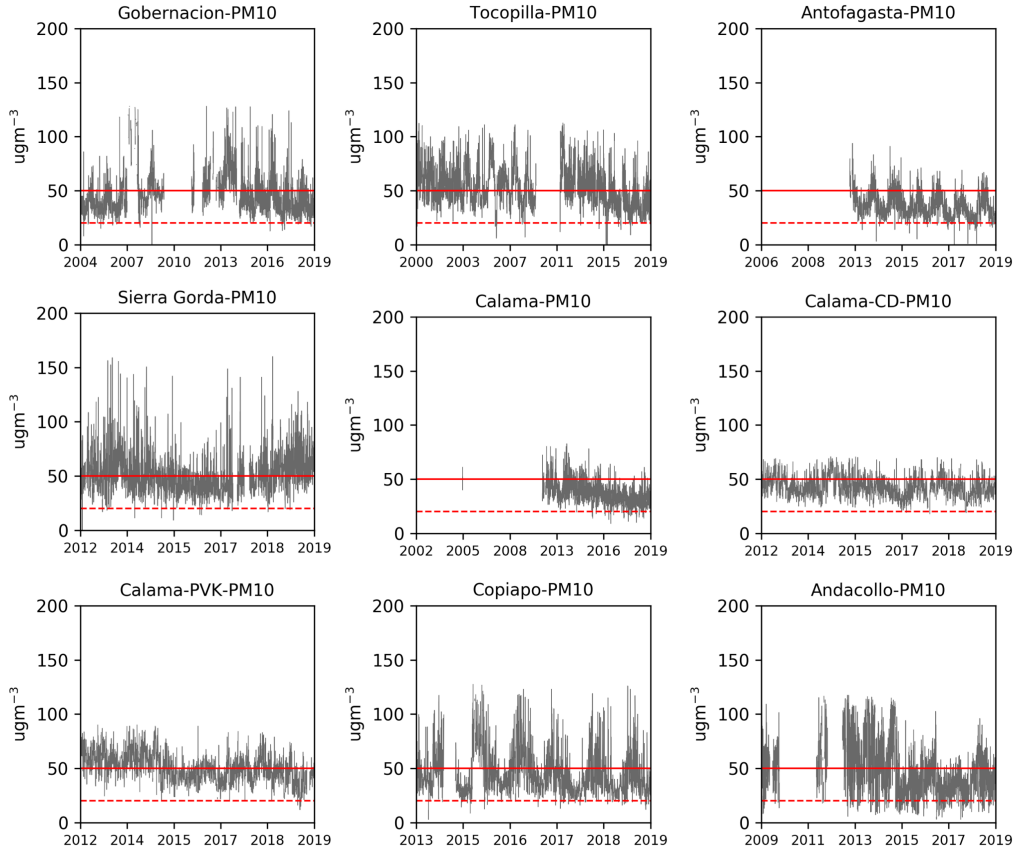

Figure 3.8: Daily mean PM_{10} time series at each location. Gaps of data have been preserved in order to evidence missing records. Outliers have been removed with 99% confidence to focus on the general trends without missing the raw data. The data has not been temporally filtered. The solid red line indicates the Chilean standard of 50 μgm^{-3}. The dashed red line indicates the WHO standard of 20 μgm^{-3}.

$PM_{2.5}$ observations at most of the sites do not show clear trends (Fig. 3.9). The exception is Calama, where daily $PM_{2.5}$ concentrations have tended to lie below the WHO standard since 2018 (dashed red line). This trend is also observable, but less evident, in Calama-PVK. In general term all the sites lie between the national and international standard values during the entire period of record, with some seasonal exceptions when more intense $PM_{2.5}$ events took place (Fig. 3.9). The exception is Tocopilla, where the first half of the last decade suffered considerably from dangerously high $PM_{2.5}$ levels, which have thankfully decreased since 2015. This may be a consequence of the atmospheric decontamination plan required by the city in

2010 as response of the saturated levels of PM_{10}. A comparison with Andacollo, whose atmospheric decontamination plan for PM_{10} began in 2015, unfortunately cannot be made as there are no $PM_{2.5}$ data available for this SINCA site.

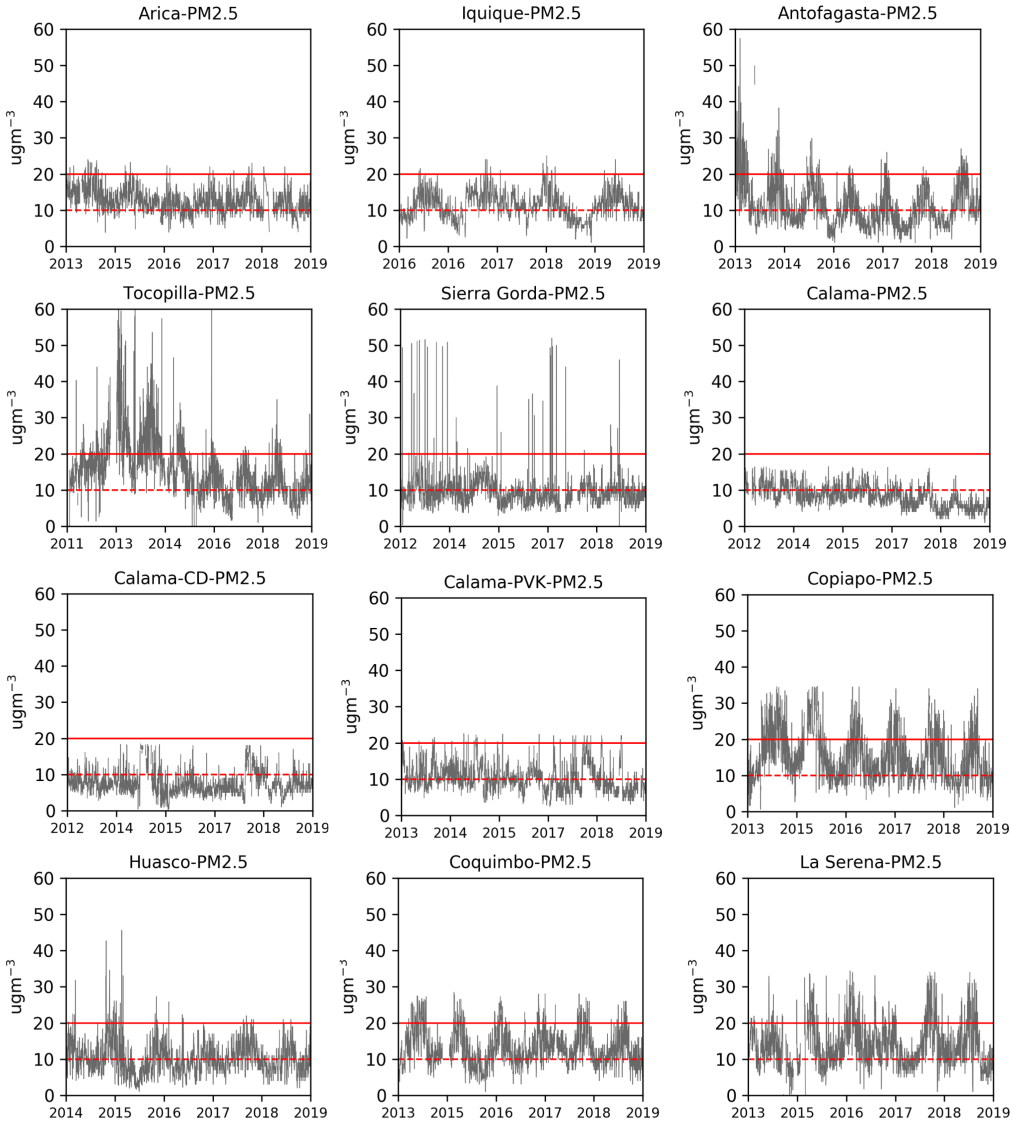

Figure 3.9: Daily mean $PM_{2.5}$ concentration at SINCA sites in northern Chile. Gaps of data have been preserved in order to evidence missing records. Outliers have been removed with 99% confidence to focus on the general trends without missing the raw data. The data has not been filtered. The solid red line indicates the Chilean standard of 20 μgm^{-3}. The dashed red line indicates the WHO standard of 10 μgm^{-3}.

When PM_{10} is dominated by fine-particles, such as would happen for concentrations arising from exhaust emissions (Tab. 3.2), PM_{10} and $PM_{2.5}$ levels tend to be

similar. However, when a coarse-particle emission source dominates a given area, PM_{10} will be considerably higher than $PM_{2.5}$. The amount of coarse particulate matter (PM_{coarse}) can be calculated as the difference between both pollutants concentrations (PM_{10}-$PM_{2.5}$). The following Figures present the scatter plots between daily means of PM_{10} and $PM_{2.5}$ (Fig. 3.10), and between PM_{coarse} and PM_{10} (Fig. 3.11), respectively, for the SINCA monitoring sites measuring both pollutants.

Positive linear relationships are observed for all sites between PM_{10} and $PM_{2.5}$. In Tocopilla, Antofagasta, and Sierra Gorda, correlations are weaker, partially explained by the absence of relationships during higher PM_{10} episodes. In these three locations, PM_{10} events over about 200 μgm^{-3} seem to be exclusively related to an intrusion of PM_{coarse}, such as mineral dust anthropogenic dust from blasting, which increases PM_{10} without rising $PM_{2.5}$ concentrations. On the contrary, higher values of $PM_{2.5}$ are not necessarily linked to an increase in PM_{10}. This suggest that $PM_{2.5}$ event are dominated by fine-fraction particle sources, such as nitrogen species from exhaust emissions or sulphate compound from power energy plants. In the case of Calama (Calama-PVK, Calama-CD and Calama) higher correlations are observed. However, this is because of the absence of events of PM_{10} exceeding 200 μgm^{-3} (as daily average). Finally, Copiapo presents a high correlation (r=0.69), suggesting a lower frequency of events dominated by PM_{coarse}, with some exceptions of high PM_{10} episodes reaching around 400 μgm^{-3}.

In Fig. 3.11 the strong connection of PM_{10} and PM_{coarse}, and their similar magnitudes, evidences the high presence of PM_{coarse} associated with increments in PM_{10}. In environments dominated by fine fractions ($PM_{2.5}$), PM_{coarse} tends to remain constant due to a joint variability of PM_{10} and $PM_{2.5}$. However, in environments dominated by a coarse fraction of particles, it is reasonable to expect PM_{coarse} values closer to PM_{10} levels and highly correlated, like this case.

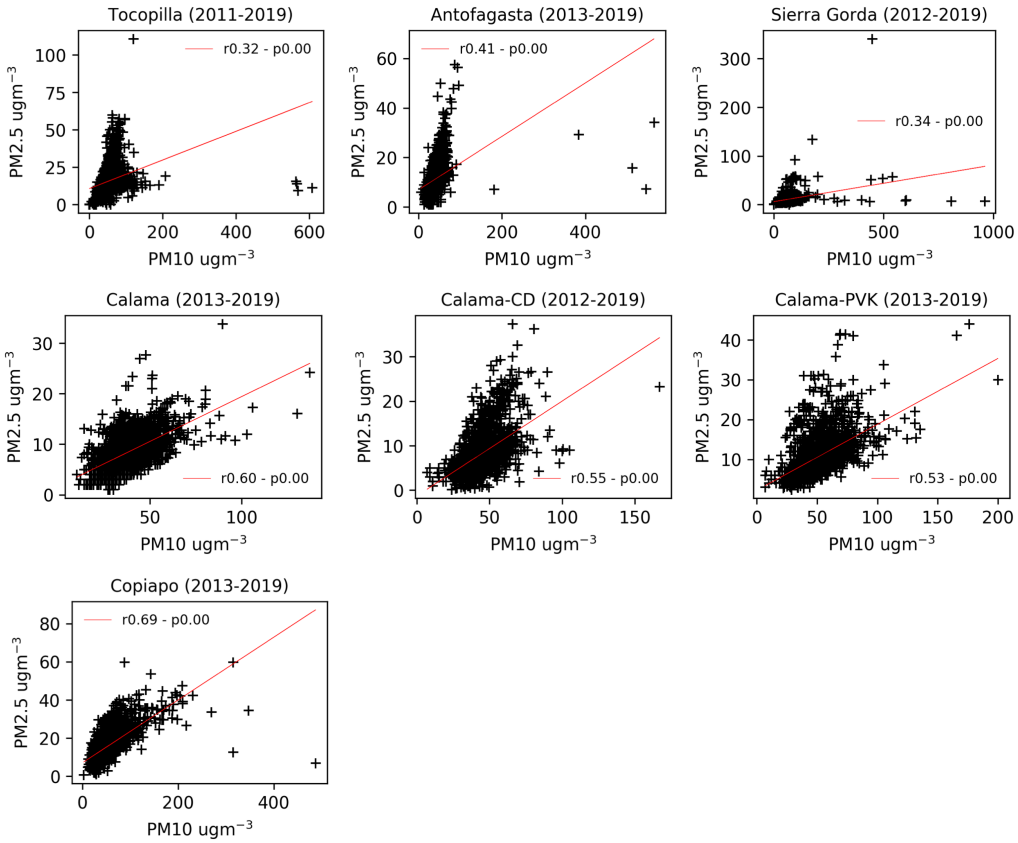

Figure 3.10: Scatter plots between daily mean PM_{10} and $PM_{2.5}$ concentrations. These are computed from all available coincident daily records from SINCA dataset. The location and length of each sites data is given above each plot.

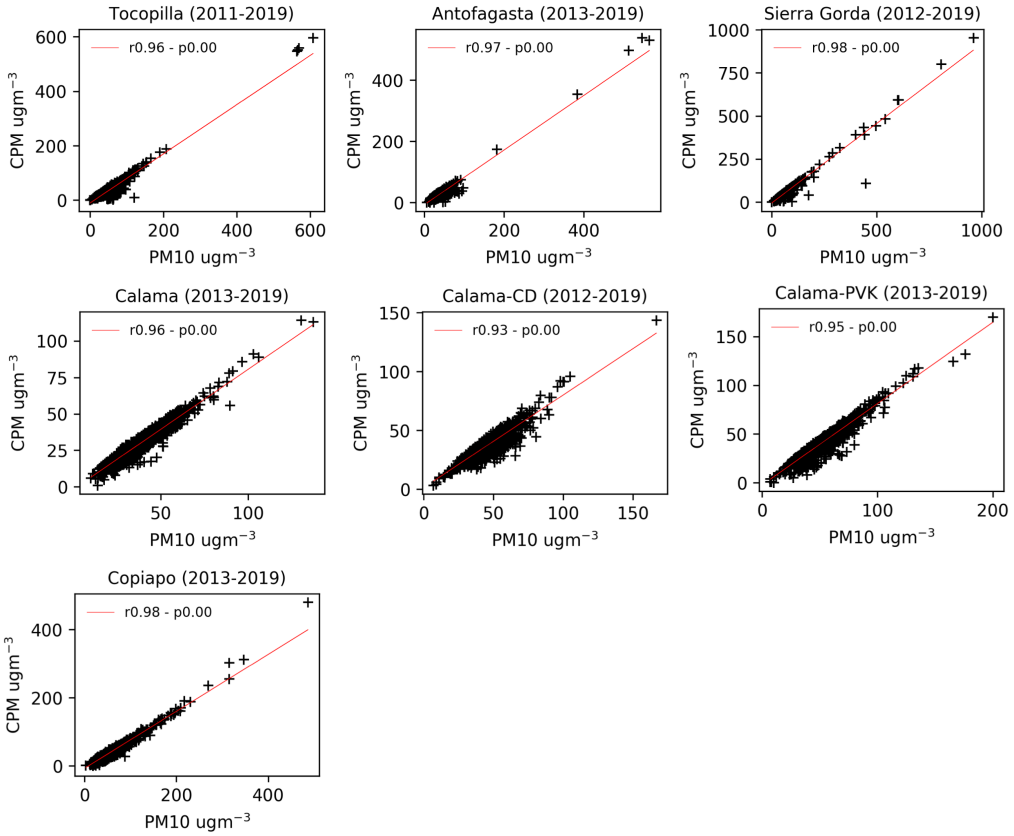

Figure 3.11: Scatter plots between daily mean PM_{coarse} and PM_{10} for the period indicated. Computed from daily records from SINCA database..

Daily cycles of particulate matter can be computed from the hourly records at each location. PM_{10} peaks between 8–10 am at all sites (Fig. 3.12), which is typically associated with traffic rush hours in urban centres (Tiwary and Colls, 2010). In many locations, such as Antofagasta, Copiapo and Sierra Gorda there is also a morning peak in $PM_{2.5}$ (Fig. 3.13) for the same reason. However in Calama (Calama-PVK, Calama-CD and Calama) no prominent morning peak of $PM_{2.5}$ is observed, which instead sees increasing levels of both PM_{10} and $PM_{2.5}$ during the afternoon and evening. An important factor to consider in the urban centres in northern Chile is the high amount of dust deposited on roads, which are not usually cleaned as required (MMA, 2015). The resuspension of PM from vehicles circulation is another anthropogenic source of PM_{10} and $PM_{2.5}$, dominated by the PM_{coarse} fraction.

An interesting pattern is observed in the $PM_{2.5}$ daily cycle in Iquique, Tocopilla and Huasco (Fig. 3.13). The three sites show little no daily variability, except a slight peak during the morning rush hour. There is no significant variation during the afternoon in these locations, and the peak present during the evening at other sites is not observed. This suggests the contribution, and dominance, of fine particles sourced from sources other than traffic. On the other hand, Arica, Sierra Gorda, Copiapo, Coquimbo, and La Serena show a decrease of $PM_{2.5}$ concentration during the 'afternoon valley', between around 12:00 to 17:00 hours, with an increase again towards the evening. In the case of Calama, a clear increase of $PM_{2.5}$ levels during daytime and the evening is evidenced. Regarding nocturnal levels, and with similar behaviour of PM_{10} (Fig. 3.12), there is no significant decrease of concentrations during night-time. This is likely associated with the low radiative boundary layer and lower wind speeds during the night, as is seen in the Santiago Valley in California (Gramsch et al., 2006). Regardless of the local anthropogenic activity of cities, the primary emissions of PM_{10} at the regional level are energy generation and mining, especially copper foundries (§3.3). Both operate continuously during day and night.

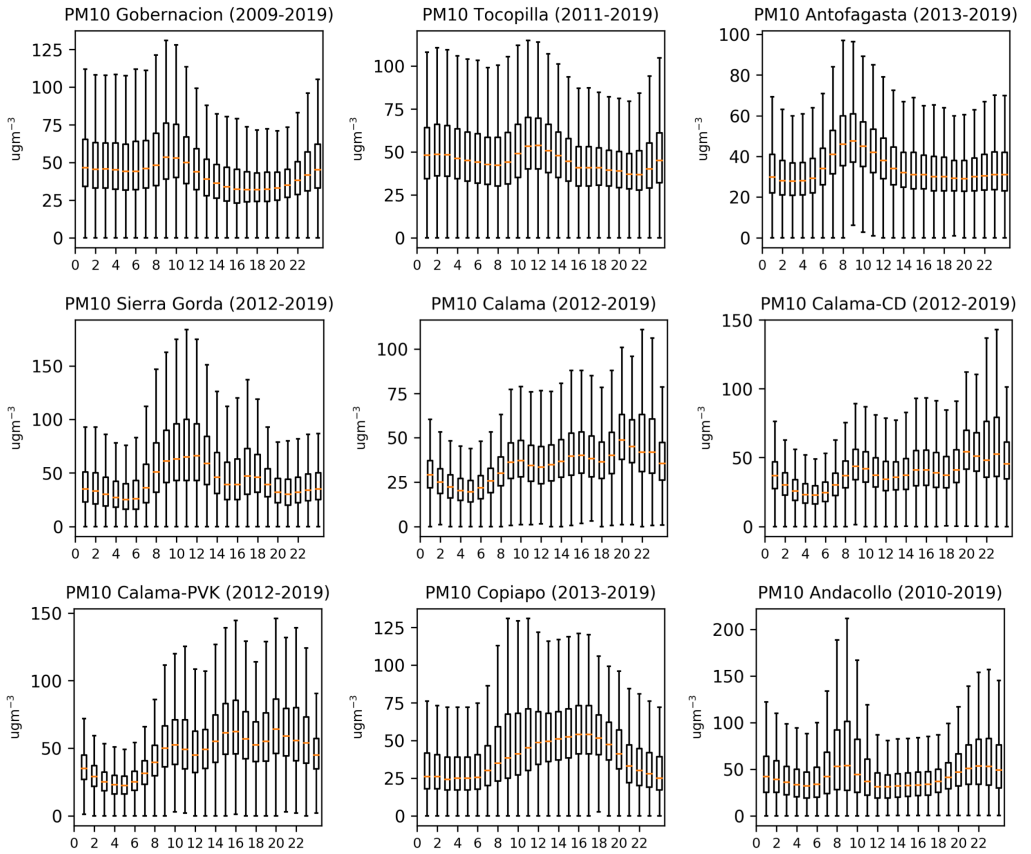

Figure 3.12: The daily cycle of PM_{10} concentrations computed using all available data in SINCA. Each sites is considered separately with the location and observing period indicated above each plot. The central box depicts the interquartile (IQR) range, whilst the whiskers represent the range between Q1-1.5xIQR and Q3+1.5xIQR, minimum and maximum limits, respectively. Orange lines connect the hourly medians. Note: the vertical axes are not constant between all panels..

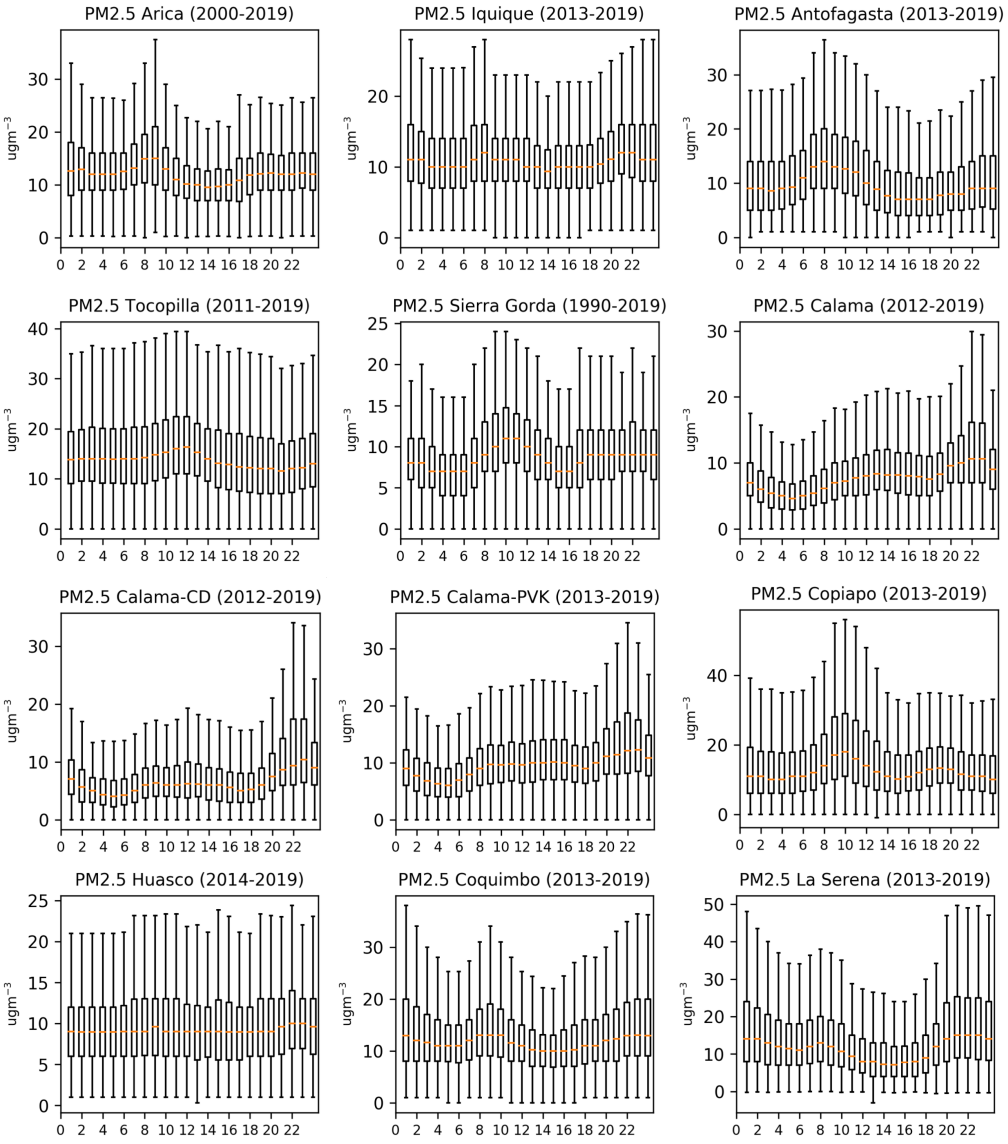

Figure 3.13: The daily cycle of $PM_{2.5}$ concentrations computed using all available data in SINCA. Each sites is considered separately with the location and observing period indicated above each plot. The central box depicts the interquartile (IQR) range, whilst the whiskers represent the range between Q1-1.5xIQR and Q3+1.5xIQR, minimum and maximum limits, respectively. Orange lines connect the hourly medians. Note: the vertical axes are not constant between all panels..

3.4.1 Gaseous emissions contributing to PM levels

Several studies have gleaned insights into PM sources by analysing nitrogen and sulphate precusor species during the same period of monitoring (Gramsch et al., 2006; Sträter et al., 2010; Díaz-Robles et al., 2011; Lu et al., 2013; Jorquera and Barraza, 2013; Ruiz-Rudolph et al., 2016; Barraza et al., 2017). Analysing NO and SO_2 daily cycles along with PM_{10} and $PM_{2.5}$ in northern Chile can therefore shed a light on potential PM sources. Two sites contributing to SINCA measure simultaneously PM_{10}, $PM_{2.5}$, NO, and SO_2: Calama and Tocopilla (Escuela E-10). Both cities are close to energy generation facilities (Fig. 3.6), and Calama is also close (21 km) to the Chuquicamata mining complex, which comprises both the open-pit mines of Chuquicamata and Ministro Hales and a copper smelting facility.

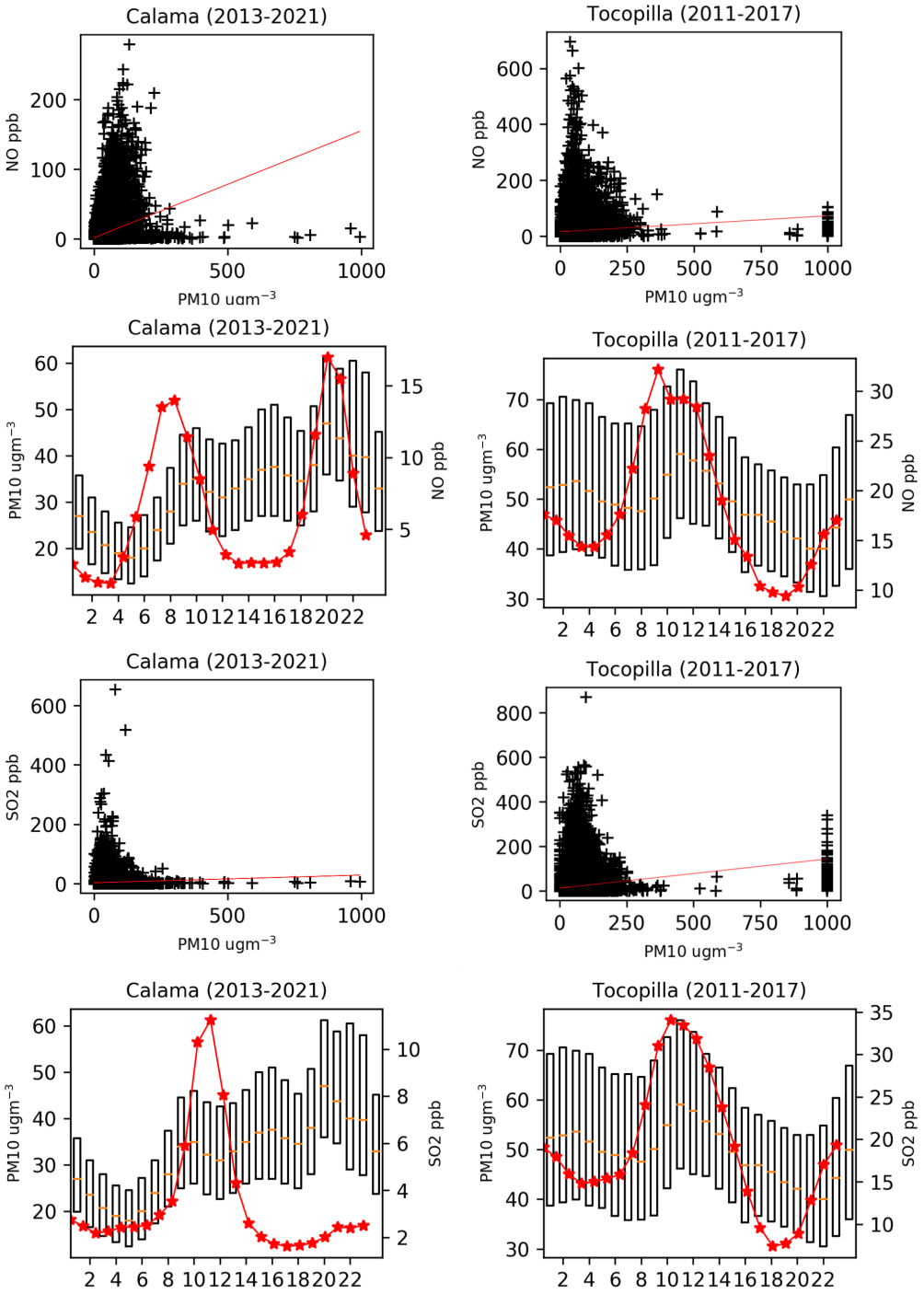

Figure 3.14: Relationship of PM_{10} to NO and SO_2 emissions in Calama and Tocopilla. The top four panels focus on NO, whilst the bottom four focus on SO_2. Scatter plots of daily values shows the covariation of PM_{10} (horizontal axes) and NO or SO_2 (vertical axes). Daily cycles show the hourly average PM_{10} conditions (after Fig. 3.8) along with the median NO or SO_2 concentrations (red). Only the central box depicting the interquartile range and medians (orange) of the daily PM_{10} cycle are shown. Plots are computed using all available hourly observations from the SINCA database – the site and observing years are given in the panel title.

PM_{10} events observed in Calama and Tocopilla do not coincide with either NO or SO_2 events (Fig. 3.14). This is consistent with Fig. 3.11, which suggests that coarse particulate matter drives PM_{10} events. This seems reasonable considering the exposure of open-pit copper extraction projects located nearby (Fig 3.6). The resuspension of dust and other PM from the road network probably also contributes. Similarly there is a disconnect between $PM_{2.5}$ events and both NO and SO_2 (Fig. 3.15). In the case of Calama, as observed for the three sites of this city (Calama-PVK, Calama-CD and Calama) in Figure 3.10 the reasonably good correlation between PM_{10} and $PM_{2.5}$ contributes to argue that $PM_{2.5}$ is, at some extent, modulated by PM_{10}, and therefore coarse material.

Figures 3.14 and 3.15 present the daily cycle of PM_{10}-$PM_{2.5}$ and NO-SO_2. The null correlation observed in the scatter plots corresponds nicely with the different daily cycles observed between PM_{10} (Figure 3.14) and $PM_{2.5}$ (Figure 3.15) and both gases. Two peaks in NO (morning and evening) are observed in Calama, which are expected during rush hours in a city of about 180,000 inhabitants. Therefore, both PM_{10} and $PM_{2.5}$ levels could certainly be influenced by NO at these hours, but not during the rest of the day.

In the case of Calama, an important aspect to consider is that the Chuquicamata complex is located northeast of the city. As described by Rutllant et al. (2013), there is a predominance of north westerlies during the afternoon and evening. Therefore, potential gas emissions from the copper melting facility might not be able to reach the city at these hours, suggesting that the gases trends in Calama (Fig. 3.14) would be primarily modulated by inner-city gaseous sources, such as traffic or other industries. Aeolian mineral dust exposure from the central area of the Antofagasta region (see Chapter 4) during the afternoon, when westerlies predominate, seems to contribute to the levels observed in Calama. In fact Salvador et al. (2016) estimated a contribution by 23% of natural mineral dust on PM_{10} levels on Calama, further breaking the relationship between PM and precursor emissions. Regarding SO_2, only a morning peak is observed in Calama. In the absence of a peak during the afternoon or evenings when westerlies dominate, morning SO_2 concentrations

from the copper melting facility seems a plausible explanation, considering that easterlies dominate the area during night and morning hours. A chemical transport model would be needed to further explore the role of the Chuquicamata complex on Calama's air quality.

Tocopilla similarly shows a lack of relationship of PM to both NO and SO_2 and different daily cycles (Fig. 3.14) – similar to Calama. Unlike Calama, there is no evening peak of NO though. This is consistent with a city considerably smaller than Calama (25,000 versus 180,000 inhabitants) whose transport activity is considerably lower. Tocopilla experiences a regular daily cycle in wind climatology, with an intense ocean-land flow during the afternoon and the early evening that brings marine aerosols and enhances the suspension local dust. Combined with existence of a single, morning peak in both NO and SO_2 (Fig. 3.15), this suggests the daily cycles in gaseous pollutants are associated with the operation of nearby energy production facilities (Figure 3.6b) in hours when winds are weak and the boundary layer height is lower.

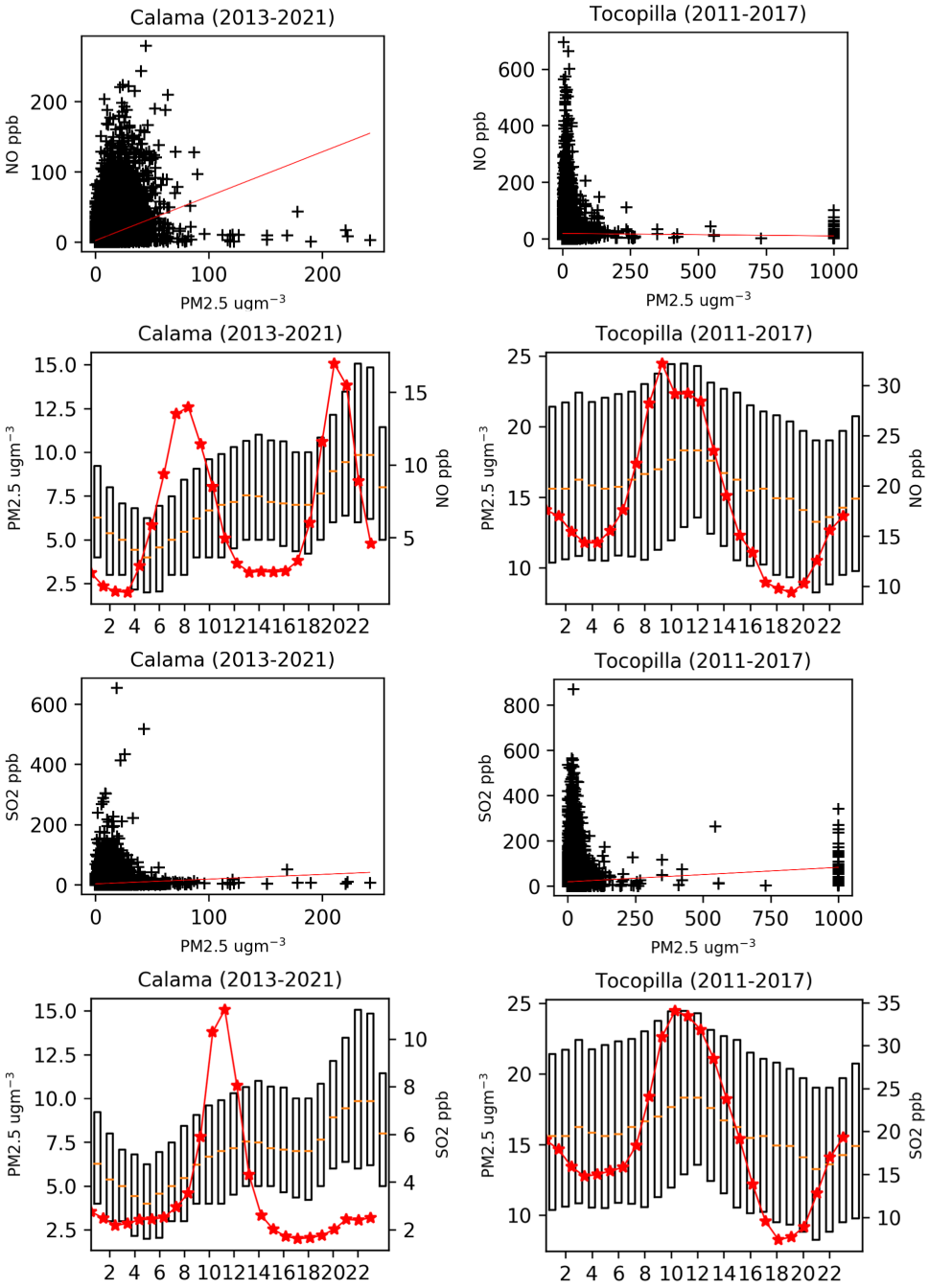

Figure 3.15: Relationship of $PM_{2.5}$ to NO and SO_2 emissions in Calama and Tocopilla.The top four panels focus on NO, whilst the bottom four focus on SO_2 Scatter plots of daily values shows the covariation of $PM_{2.5}$ (horizontal axes) and NO or SO_2 (vertical axes). Daily cycles show the hourly average $PM_{2.5}$ conditions (after Fig. 3.8) along with the median NO or SO_2 concentrations (red). Only the central box depicting the interquartile range and medians (orange) of the daily $PM_{2.5}$ cycle are shown. Plots are computed using all available hourly observations from the SINCA database – the site and observing years are given in the panel title.

3.5 Final Remarks

The Atacama desert is one of the driest places on earth and the driest desert in the world. Its existence relies on coexisting atmospheric, oceanic and topographic factors that promote extremely stable and dry conditions, with almost no precipitation. In this environment, around 1.5 million people live along with intense mining and coal-and oil-based energy production activities. This leads to significant emissions of particular matter (PM_{10} and $PM_{2.5}$) and gases (NOx and SO_2). Additionally, mineral dust contributes to particulate matter levels in both rural and urban areas.

Historically, urban centres have exceeded the Chilean standard for outdoor air pollution exposure, in particular the cities of Tocopilla (PM_{10}), Copiapo (SO_2), Andacollo (PM_{10}) and the Chuquicamata area, next to Calama (PM_{10} and SO_2). Most of these areas have since seen some improvement in air quality, because of the application of mitigation plans imposed by the air quality statutory body. However, those efforts today are still not sufficient in comparison to international criteria, particularly the WHO guidance.

Observed air quality data from the SINCA network suggests that PM_{10} and $PM_{2.5}$ are mostly linked to particulate matter-exclusive emissions, such as natural or anthropogenic dust. The contribution from primary (precursor) gases sources, such as power plants operations seems limited, something that is also supported by PM_{10} and $PM_{2.5}$ events occurring independently from peaks in NOx and SO_2.

This characterisation provides context for the following chapters of this thesis. Chapter 4 explores the annual cycle of mineral dust concentrations of the Atacama Desert and it mineral dust sources, which are highly influenced by the complex topography. Then, chapter 3 analyses air quality data from SINCA and its potential links with atmospheric factors, such as atmospheric ventilation and their joint variability at seasonal a scale. Finally, chapter 6 analyses the atmospheric and oceanic forcings on the Atacama Desert's climate and future particulate matter trends under climate change. The research in this chapter improving our understanding of the different contributors towards the dangerously high PM concentrations in the Atacama can hopefully assist with designing measures to reduce and combat them -

which is discussed in Chap 7.

Chapter 4

Mineral dust dynamics across the Atacama Desert

The term 'mineral dust' refers to the coarse fraction (usually greater than 1 μm) of material formed by mechanical processes, such as material eroded from the Earth's surface (Tiwary and Colls, 2010). Globally, desert regions are the dominant sources of natural mineral dust (Tanaka and Chiba, 2006; Florence et al., 2010). Previous studies have attempted to estimate the various contribution of natural dust sources based on modelling approaches. However, the resulting contributions are highly variable due to differences in model formulations and source specifications (Huneeus et al., 2011). A significant factor to consider is the distinctive seasonal behaviour of each emission source (Engelstaedter and Washington, 2007; Florence et al., 2010). An early study estimated the global production of mineral dust to be $3,000 \times 10^6 tyr^{-1}$ (Tegen and Fung, 1994). However, more recent studies place production rates between 1,019 x $10^6 tyr^{-1}$ (Miller et al., 2004) and 2,073 x $10^6 tyr^{-1}$ (Ginoux et al., 2004). Despite the differences in global total emissions, all studies analysing the relative size of possible sources identify North Africa (Sahara Desert) as the largest contributor of natural mineral dust on the globe, ranging between 51 and 69 % of the total production rate (Werner et al., 2002; Zender et al., 2003; Luo et al., 2003; Ginoux et al., 2004; Miller et al., 2004; Tanaka and Chiba, 2006).

In South America, whose primary source is the Atacama Desert, the production rate has been estimated to be about $35 - 55 \times 10^6 tyr^{-1}$ (Tanaka and Chiba, 2006).

This represents 2.3-2.6% of global mineral dust production, which is a similar order of magnitude of production rates computed for Australia (2.9 to 5.7%) and one order of mangitude higher than North America (0.1-0.4%) (Zender et al., 2003; Ginoux et al., 2004; Tanaka and Chiba, 2006). As befits their relative contributions to the global dust budget, historically most research studies so far have focused on Asia and the Sahara Desert (Florence et al., 2010). The Atacama Desert has received scarce attention, despite its potential for developing intense dust storms and becoming a major dust source Reyers et al. (2019).

Particulate Matter (PM) can be transported long distances in the atmosphere. Samoli et al. (2011) identified PM pollution from the Sahara Desert travelling across the Mediterranean Sea. Tanaka and Chiba (2006) used the MASINGAR Chemistry-Transport Model (CTM) to compute global transport and PM concentrations from the major dust emission sources around the globe, finding peaks values of dust concentration in South America over Patagonia and the Atacama Desert. The lifetime of aerosol dust was calculated to be around 1.7 to 3.2 days from permanent sources with evident seasonal cycles. For instance, in the Atacama Desert, the simulated emission peaks were identified in summer, with lower emissions in winter (Tanaka and Chiba, 2006). This was directly associated with the seasonal pattern of precipitation, and the natural dynamics of dry and wet deposition affecting the original dust emission flux for coarse and fine particles respectively. Similar seasonality has been reported by other global-scale modelling studies (Ginoux et al., 2001; Miller et al., 2004; Ginoux et al., 2012). Global models have severe difficulties dealing with rough terrain, and topography plays a crucial role in particles transport and dispersion (Tiwary and Colls, 2010). Therefore, finer resolution products are required to analyse airborne particles dynamic over areas with complex topography, such as the Atacama.

Dust production depends on both soil properties and meteorological conditions, specifically by the momentum transfer from winds to the surface (Marticorena and Bergametti, 1995; Shao, 2001; Xu, 2018). Therefore, a wind speed threshold for dust production can be established for a given area (Ginoux et al., 2001; Tegen

et al., 2002; Xu, 2018). That threshold refers to the wind speed value over which the momentum transfer activates, and dust is produced. In this sense, wind speed is crucial not only for dust production, but also for transport. Therefore, accurate simulation of surface winds is fundamental for reliable dust production and transport computations.

This chapter focuses on identifying the variability and magnitude of mineral dust over the Atacama desert, including characterising individual events – particularly over the Antofagasta region. Firstly, the chapter introduces remote sensing techniques used for aerosol and mineral dust characterisation (§4.1). §4.2 summarises the methods and datasets used in this research. Then the results of the mineral aerosol load over Atacama desert throughout the decade 2010-2019 are presented (§4.3), followed by the results on coarse aerosols detection and mineral dust dynamics (§4.4). Mineral dust events are then identified and analysed (§4.5) to assess their variability and magnitude as well as the role that wind plays in their occurrence. Finally, a discussion of the implications of the study is carried out (§4.6). Although the connection of mineral dust and air quality is not a primary objective of this study, the results are discussed in term of their applicability for future research in this regards, including future climate change, their utility for validation of chemical transport modelling, and their implications on the solar power industry in Northern Chile.

Part of the literature review on remote sensing retrieval, the methods and the results from satellite retrievals are part of a first author article which is expected to be submitted in 2021 (Oyarzun et al. 2021) in a joint effort with a research team based in the Center for Climate and Resilience Research (CR2), Chile. The implications of mineral dust on the solar power industry in Northern Chile are part of a co-authored article titled ”Human and Environmental Health and Safety Effects of Soil Dust in the Americas: A Review” by Tong, D et al. (2021), expected for submission during 2021.

4.1 Remote Sensing Aerosol Retrieval

Aerosols are solid and liquid particles suspended in the air whose sizes range between sub-micron to several microns in aerodynamic diameter (Tiwary and Colls, 2010). These airborne particles can exhibit a wide range of physical, chemical and optical properties, and are emitted from natural and anthropogenic sources (Lee et al., 2011; Mhawish et al., 2019). These features depend on meteorological factors (Altaratz et al., 2013), strength of the emissions (Banerjee et al., 2015; Singh et al., 2017), and their geological origin (Ramanathan and Ramana, 2005). The study of aerosols is relevant for our understanding of the climate system, as well as environmental pollution. The former comprises of aerosol-cloud interactions and the effects of aerosol on the energy budget of the Earth (see Chap. 6). The latter is associated with the direct incidence of aerosol load on air quality, such as the presence in the atmosphere of significant amounts of PM_{10} or $PM_{2.5}$ (Lee et al., 2011) (see Chap. 3). In some areas, such as Southern Asia, high aerosol loads have been found to compromise food security due to their impacts modifying the hydrological cycle, the monsoon season, and agriculture (Ramanathan et al., 2001; Kumar et al., 2017; Burney and Ramanathan, 2014; Mhawish et al., 2019).

The use of satellite observations for aerosol research has increased significantly during the recent decades (Martins et al., 2017). This arises from a growing interest in understanding the spatial distribution of aerosols, which is challenging to determine from a sparse network of monitoring sites (Van Donkelaar et al., 2010). Remote sensing has been widely used for studying aerosol dynamics and their implications for air quality, especially in remote areas where ground observations are scarce or do not exist (Al-Saadi et al., 2005; Di Nicolantonio et al., 2009; Van Donkelaar et al., 2010; Lee et al., 2011; Huang et al., 2018; Kim et al., 2019). A widely used measure for the content of aerosols in the atmosphere is the Aerosol Optical Depth (AOD), which quantifies the total content of aerosols in the atmospheric column. This is calculated by computing the light extinction due to particles scattering or absorption (Lee et al., 2011). The study of ground-level air quality from satellite AOD has led to satisfactory results in the recent past (Li et al., 2015). However, a

recurrent issue arises from the discrepancy between the observed aerosol content in the atmospheric column and the PM concentration measured in ground-level monitoring sites. Surface observations of PM often occur in drier conditions compared with the wide range of humidities at which satellites provide AOD data (Schäfer et al., 2008; Collaud Coen et al., 2013). This discrepancy is pronounced by aerosols' response to increased relative humidity (Van Donkelaar et al., 2010; Altaratz et al., 2013; Crumeyrolle et al., 2014), which along with the daily variation of aerosol vertical structure may condition AOD-PM relationships to a day-to-day basis (Lee et al., 2011; Nordio et al., 2013). In fact, aerosols modify their properties in humid environments due to hygroscopic growth associated with water vapour capture – leading to changes in their optical properties (Michel Flores et al., 2012; Chen et al., 2019). This effect is mainly observed in the vicinity of low-level clouds (up to 2 km height in the troposphere). Such clouds are a feature of the climate in Northern Chile (§3.1) and include very high concentrations of aerosols (Blanchard and Woodcock, 1980; Pringle et al., 2010; Altaratz et al., 2013).

As Li et al. (2015) point out, the relationship between AOD and PM has to be assessed considering the seasonal cycle of both metrics in a given location. Seasonal variations in the aerosol vertical distribution, relative humidity and cloud fraction, lead to variations of the surface reflectance and particle properties, which add complexity to the retrieval of aerosol data (Mhawish et al., 2019). For instance, Li et al. (2015) found a reasonable agreement of interannual variability between AOD and ground observations of $PM_{2.5}$. The seasonality between both metrics agreed only over the Eastern US, opposite cycles were computed elsewhere in United States. The primary factor postulated by Li et al. (2015) was the seasonality of the mixing layer height, which led to reduced AOD but increased $PM_{2.5}$ during wintertime. Indeed, an increasing aerosol load is linked to stable planetary boundary layer (PBL) as reduction of surface solar radiation promotes higher air pollutant concentrations (Chen et al., 2019).

Noise from measurements occurs in all satellite datasets and at ground-level monitoring sites, which may result in poor agreement between them. Removing the

noise from the signal, for instance by averaging over whole months, can go some way to reconciling different measurements of aerosol data (Liu and Mishchenko, 2008; Li et al., 2013a). However long-term averaging can restrict the study of other air quality phenomena, such as pollution events occurring at daily or even hourly time scales. In this sense, a multi-sensor approach that avoids relying upon one single satellite dataset reduce uncertainty by focusing on common features of all the available sources of data (Li et al., 2015).

Aerosols' radiative effects on clouds have widely been described in terms of their implications for the Earth's radiative balance and its perturbation under climate change (see Chapter 6). Aerosols tend to have a weak optical signal which can make their detection challenging using remote sensing sensors (Altaratz et al., 2013). Aerosol-cloud interactions add even more complexity. In the vicinity of clouds, it can be difficult to discriminate between water droplets and aerosols, meaning clouds can infect the aerosol signal (Zhang et al., 2005; Koren et al., 2007; Altaratz et al., 2013). Clouds can also confuse AOD signals due to their illumination effect on aerosols – the so-called 3D radiative effect (Marshak et al., 2006). Thus, AOD products incorporate cloud masking which discards AOD pixels over clouds and their vicinity (often indicated as quality flags in the released product). Overall these aerosol-cloud issues provide a limitation on AOD data from satellite sensors, especially in cloudy regions or seasons.

Aerosol optical depths ranges from nearly zero up to about 1.0 or higher. Usually, aerosols sources are classified into three main groups; Urban-Industrial & mixed, Biomass Burning, and Desert dust & oceanic. Dubovik et al. (2002) summarised several observations during the 1990's from the Aerosol Robotic Network (AERONET, Holben et al., 1998) to derive typical AOD ranges for the three groups mentioned above. Values for urban-industrial and mixed areas range between 0.1 and 1.8 (mean 0.43, for Mexico City); biomass burning ranges between 0.1 and 1.5 (mean 0.38, for African savanna); and desert dust & oceanic ranged between 0.1 and 1.5 (mean 0.17, for Saudi Arabia). These ranges correspond to illustrative regions that are extreme cases, and so the ranges may differ in other areas accord-

ing to the nature of emission sources. The seasonality and temporal evolution of aerosols, including dust variability, has been studied over several locations globally either from observational data from satellite sensors or ground-based scanning radiometers (e.g. Engelstaedter and Washington, 2007; Di Nicolantonio et al., 2009; Ginoux et al., 2012; Li et al., 2013a; Nordio et al., 2013; Li et al., 2015; Martins et al., 2017) or modelling studies (e.g. Tegen and Fung, 1994; Ginoux et al., 2001; Tegen et al., 2002; Werner et al., 2002; Zender et al., 2003; Huneeus et al., 2011; Konsta et al., 2018). Tegen and Fung (1994) and (Zender et al., 2003) distinguish an annual cycle over desert regions that governed by higher dust production during summertime. As reported by Zender et al. (2003), emissions are higher in Asia and Northern Africa during the Northern Hemisphere summer, whereas in Australia, emissions peak during the Southern Hemisphere summertime. Satellite-based research over the Western Sahara supports this, finding a peak of dust production in June, which coincides with the southward crossing of the Inter-Tropical Convergence Zone (ITCZ) over dust emission hot spots. Engelstaedter and Washington (2007) reported a lack of studies based on either modelled or observational evidence for the Atacama Desert. Later, Martins et al. (2017) suggested that a spring and summer peak in aerosol emissions appears to also exist over South America in the Moderate Resolution Imaging Spectroradiometer (MODIS) dataset. These results focused on the validation of the Multi-angle Implementation of Atmospheric Correction (MAIAC) from MODIS (see §2.4.2). At a regional scale, South America is dominated by the aerosols sourced from biomass burning in the Amazonia – no specific results for mineral dust production in the Atacama are reported by Martins et al. (2017). However, the authors argue that aerosols emissions over Patagonia and Northern chile are governed by dust plumes, unlike other regions where industrial emissions (megacities) and biomass burning (Brazilian savanna) predominate.

Since aerosols comprise particles with a wide range of aerodynamic diameter sizes, an issue when looking at AOD data is the discrimination of aerosol type. AOD gives only an estimation of the total amount of airborne particles with no information about particle size. For instance, mineral dust and sea salt are coarse particles,

whilst smoke and suburban particles are much finer. Therefore, when looking at AOD data, there is a mixture of particles sizes with different optical properties and particles sources with their underlying emission profiles. Ångström (1929) postulated the spectral dependence of the aerosol optical depth, or extinction by airborne particles, which has been useful for multiple applications within aerosols research such as the modelling of aerosols radiative properties and their effects on the atmospheric system, and methodologies for sources identification (Eck et al., 1999). A key parameter is the Ångström wavelength exponent, α (sometimes referred to simply the Ångström Exponent, AE; Eq. 4.1), which provides information about particle size based on the different response of aerosols to wavelengths (Fig. 4.1).

$$\tau_a = \beta\lambda^{-\alpha} \tag{4.1}$$

In Eq. 4.1, τ_a is the Aerosol Optical Depth (AOD) at the wavelength, λ. β is the Ångström turbidity coefficient which represents the approximated AOD at a wavelength of 1 μm. As presented in Eck et al. (1999), α can be calculated by comparing two specific wavelengths (λ_1 and λ_2) with their respective AOD values (τ_{a_1} and τ_{a_2}), and then taking the logarithm. α usually range from jsut below 0 until values greater than 2.0. Values less than 1.0 indicates size distributions dominated by coarse aerosol particles ($radii > 0.5\mu m$), such as sea salt and mineral dust, and values greater than 2.0 are associated to fine airborne particles dominance ($radii < 0.5\mu m$), such as biomass burning and combustion-sourced particles (see Fig. 4.1 Kaufman et al., 1992; Eck et al., 1999; Schuster et al., 2006). In particular, dusty environments are typically found to present α values between -0.5 to 0.5 (Eck et al., 1999; Ginoux et al., 2012). For instance, values ranging from -0.2 to 0.04 have been computed over dust events in Niger (Osborne et al., 2008), and negative α values were computed for several dust events during summer in Birdsville, Australia (Radhi et al., 2010).

The Ångström Exponent has been widely used along with AOD data for inferring aerosols composition and emission sources (Nakajima and Higurashi, 1998; Eck et al., 1999; Schuster et al., 2006; Kaskaoutis et al., 2007; Russell et al., 2010;

Soni et al., 2011; Ginoux et al., 2012), and specifically for characterisation of mineral dust (Wang et al., 2004; Pandithurai et al., 2008; Kalashnikova and Kahn, 2008; Osborne et al., 2008; Radhi et al., 2010; Valenzuela et al., 2015; Ealo et al., 2016). However, all these studies have focused on desert areas either in Asia, Europe or Africa, and there is a lack of research on the understanding of mineral dust dynamics over the Atacama Desert in South America. Often research over the Atacama Desert is only included as part of a large-scale regional (Martins et al., 2017) or global (Nakajima and Higurashi, 1998; Ginoux et al., 2012) analyses. Nakajima and Higurashi (1998) used satellite products to show coarse aerosols dominate over oceans and subtropical arid regions, whereas fine particles were mostly found over industrial areas on mid-latitude regions and biomass burning areas in the tropics. Later, Ginoux et al. (2012) estimated that natural dust contributes to about 75% of global mineral dust emissions.

The seasonal variation of aerosols particles size can also be explored using α satellite retrievals from ground-based radiometers. From hand-held measurements in Delhi, Soni et al. (2011) detected a marked seasonal cycle of α primary attributed to the dust seasonality. Lower values of α were computed in summer, in contrast with the higher values observed in the winter season.

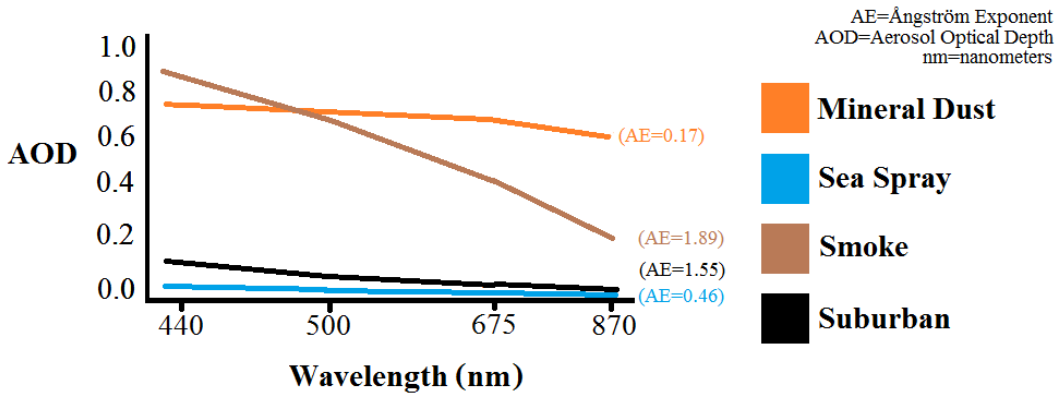

Figure 4.1: Wavelength dependence of AOD for different aerosols types. AOD tends to be lower at longer wavelengths, which directly impacts the α value. Coarser aerosols (such as sea spray and mineral dust) have a more constant response through the spectral range, leading to lower α values (from Chen et al., 2015).

4.1.1 AOD Retrievals from the Moderate Resolution Imaging Spectroradiometer (MODIS) Dataset

As described in Section 2.4.2, the Moderate Resolution Imaging Spectroradiometer (MODIS) instrument is onboard the Terra and Aqua satellites operated by the National Aeronautics and Space Administration (NASA), and it is the most widely validated remote sensing instrument, or sensor, for aerosols retrieval (Levy et al., 2013; Bilal and Nichol, 2015; Mhawish et al., 2017; Tao et al., 2017; Mhawish et al., 2019). These two satellites pass overhead at different times: Terra at morning and noon local time, whereas Aqua at afternoon local times. From the four independent algorithms that have been developed for retrieving aerosols properties (dark target for ocean (Levy et al., 2013), dark target for dark land and vegetated regions (Tanré et al., 1997), deep blue (DB) (Hsu et al., 2004, 2013), and MAIAC (Lyapustin et al., 2018)), two operational products were developed and optimised for retrieving aerosols properties over bright surfaces. These correspond to the Multi-Angle Implementation of Atmospheric Correction (MAIAC) and the deep blue (DB) algorithms (see 2.4.2).

Lyapustin et al. (2011b) compared the MAIAC (first version) and DB algorithms for four AERONET locations in the Saharan region. The AOD derived from both algorithms was similar in the Bodélé depression and western downwind transport region. However, MAIAC was able to identify more of the mineral dust events seen in other independent datasets. The authors concluded that MAIAC presented a strong potential for dust characterisation over the Sahara Desert (Lyapustin et al., 2011b). Similarly, a recent study comparing the accuracy of the MAIAC, DB and DT algorithms for 171 AERONET sites in North America found that the three algorithms performed equally well over dark regions, whereas MAIAC performed relatively better over regions dominated by brighter surfaces and more intricate topography (Jethva et al., 2019). These latter regions bear the most similarly to conditions over the Atacama Desert.

4.2 Methods

Table 4.1 summarise the satellite dataset used for aerosols load characterisation over the Atacama Desert as well as the AERONET observations for AOD validation at the Arica site, and the ERA5 reanalysis product from which wind patterns were analysed. Regarding MODIS data, as indicated above, the two operational products that have been optimised for retrieving aerosols properties over bright surfaces are MAIAC and DB (see 2.4.2). The MCD19A2 is the MAIAC algorithm-based product at 1 km resolution from which AOD land (550nm) data was used (Table 4.1). Additionally, MOD04L2 (Terra) and MYD04L2 (Aqua) are DB-based products at 10 km resolution from which AOD land 550nm and Ångström Exponent (α) Land 470-670 nm retrievals were analysed. All datasets span the period 2010-2019, except for the ERA5 Reanalysis which only had data available to 2018 when the analysis was performed.

All products were sampled daily at Terra and Aqua times separately. For the case of MODIS products (MCD19A2, MOD04L2 and MYD04L2), the retrievals at morning-noon hours from the Terra dataset were directly averaged on a daily basis. Similarly, the data at afternoon hours from the Terra dataset were averaged daily. Therefore a single averaged value was representative of either Aqua or Terra observations for each day. Terra overpasses the Atacama Desert mostly between 11:00 and 12:00 hours local time (Fig. 4.2a) whereas Aqua retrieves data mostly between 14:00 and 16:00 hours local time (Fig. 4.2b). In the case of AERONET and ERA5 datasets, the data was collected for the corresponding Aqua and Terra times available from the satellite observations each day during the 2010-2019 decade. Area-averaged time series and other areal statistics were computed when at least 50% of the area had valid records available each time step.

Some form of regridding it required to bring all the datasets onto a common grid to allow differences to be computed. Here the "Ångström Exponent Land 470-670 nm" (α) was bilinearly interpolated from the original 10 km resolution of the MOD04L2 and MYD04L2 products up to the 1 km resolution grid of the MCD19A2. As MCD19A2 is available in a fixed sinusoidal grid subdivided by

Table 4.1: Observational datasets used in this chapter. **# Retr.** gives the number of satellite retrievals used, or the temporal resolution in the case of ERA5. **Res** gives the horizontal resolution. **surface meridional and zonal velocities. †Hourly data is needed so that velocity data can be sampled only at the overpass times of the Terra or Aqua satellites.*

Product	Algorithm	Platform	Parameter	# Retr.	Res. (km)
MCD19A2	MAIAC	Terra	AOD (Land, 550nm)	10199	1
MCD19A2	MAIAC	Aqua	AOD (Land, 550nm)	11807	1
MOD04L2	DB	Terra	α (Land, 470-670nm), AOD (Land, 550nm)	5254	10
MYD04L2	DB	Aqua	α (Land, 470-670nm), AOD (Land, 550nm)	5575	10
AERONET	Version 3	Arica	AOD 500nm	-	-
ERA5 Re-analysis	-	-	us,vs*	hourly†	$\sim$31

tiles (Fig. 2.3), the first step comprises of warping the MCD19A2 file through a GeoJSON geographical element of a given area of interest. Then, swath-based MOD04L2 and MYD04L2 products were reformated and reprojected to the above resultant grid of 1 km resolution. Two GeoJSON files were used, one for the Atacama desert region spanning from 18.0-29.0°S and 68.0-71.5°W, and the second one focused over the Antofagasta region spanning 21.0-24.0°S and 68.0-72.0 °W. These files were used to produce both spatial analyses of AOD and α retrievals, and for the computation of areal statistics over time.

For satellite data, quality assurance was carried out by exclusively selecting highest-quality observations. In MOD04L2 and MYD04L2 datasets, this was

achieved by selecting data flagged as QA Confidence (QAC) = 3, which comprises cloud-free and snow-free masks. For the MCD19A2 product, only data flagged as 'bit 8-11 = 0000' was considered. This corresponds to the best quality pixels selection by comprising the cloud-free, cloud-adjacency, water sediments, and AOD within +-2km from the coastline masks (Lyapustin et al., 2018). The amount of data as a result of this operation varies spatially. This is discussed in the following section.

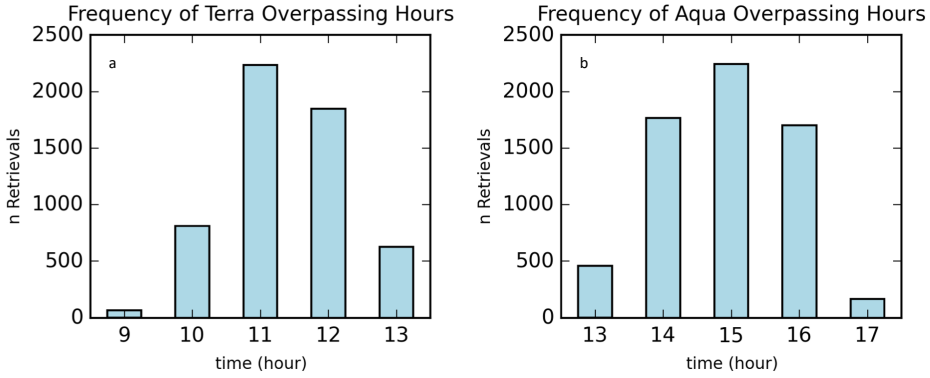

Figure 4.2: The number of retrievals for each overpass hour (local time) of the Aqua and Terra satellites for the Atacama Desert in 2010-2019 (computed from the MCD19A2 dataset.)

4.3 Aerosols Load over the Atacama Desert

The extremely arid region of the Atacama Desert in Northern Chile spans from approximately 18°S to 30°S (§3.1, Schulz et al., 2011). This region is governed by complex topography, resulting in a heterogeneous spatial distribution of aeolian roughness lengths ($z0$). Aeolian surface roughness (characterised by its length) is a crucial parameter for surface-atmosphere exchanges of mass and energy. The roughness components of the surface partially absorb the stress resulting from the wind shear, which leads to an increase in the eolian erosion threshold. When the surface roughness length increases, the soil losses are usually observed to decrease (Marticorena et al., 2006). Therefore, aeolian roughness plays a fundamental role in mineral dust emissions. It is an input variable for the friction velocity computation

($\mu*$), which triggers aeolian dust production (Alfaro et al., 2011). Higher values of $z0$ lead to higher values of $\mu*$ resulting in higher wind speeds being required to raise dust. Fig. 4.3 presents the values of $z0$ for the Atacama Desert obtained from Prigent et al. (2012) compared to the aerosol distribution.

On-site measurements of $z0$ have only been carried out in the Mejjillones Peninsula, north of Antofagasta (Ant, 23°S) (Flores-Aqueveque et al., 2010; Alfaro et al., 2011; Flores-Aqueveque et al., 2014) where an average $z0$ equal to 0.03 cm was computed. This is one order of magnitude lower than the closest pixel of the Prigent et al. (2012) satellite-derived dataset (0.3 cm), whose western boundary by the Coast Cordillera does not provide data over the flat terrain of the peninsula. Also, the 10 km resolution of the Prigent et al. (2012) data might not adequately capture specific sites measurements. Despite the above, $z0$ plotted in Fig. 4.3 (left) match the complex topography governed by the Andes Cordillera and the transversal valleys to the East Antofagasta, which become more intricate southwards of 26 °S.

The decadal-mean AOD pattern (Fig. 4.3, computed from MCD19A2) shows the largest aerosol loads occur along the coast between 18°S and 20°S and the central desert region between 21°S and 23°S. This bears a similarity with the $z0$ distribution (Fig. 4.3), although some inconsistencies are observed around Calama (Cal), and between 24.5°S and 26°S where AOD is low. These differences may arise from several other factors, such as wind patterns and the influence of anthropogenic aerosol sources. For instance, the Chuquicamata mining operation is located to the north of Calama and is the largest open-pit mining on Earth (§3.3). A high AOD decadal mean was computed over this area, as well as a particularly high aeolian roughness length (0.5 cm, may be expected for such a mountainous region).

In order to focus the analysis in areas where natural mineral dust production is predominant, this Chapter analyses the Antofagasta region, denoted with the black square in Fig. 4.3, where the decadal mean is notably higher in almost the entire area from both satellite observations (Terra and Aqua). This region is of particular interest in terms of future significance of these results, due to the higher availabil-

ity of surface Particulate Matter data (PM_{10} and $PM_{2.5}$) and wind pattern observations in the sites located in Calama (Cal), Sierra Gorda (SG), Antofagasta (Ant) and Tocopilla (Toc). In all these sites, the annual mean value of PM_{10} exceeds the Chilean normative threshold (see Chapter 3). Also, As argued by Rondanelli et al. (2015) and Molina et al. (2017), this area in the Atacama Desert in Northern Chile houses the site with the highest solar irradiance on the planet. The above has led to increased investment in solar power projects (Cordero et al., 2018). Therefore, understanding the unexplored dust cycle in the region also contributes to targeting mitigation plans for soiling (dust deposition) on Photovoltaics (PV) panels. Indeed, cleaning and mitigation methods have become a fundamental component of the solar industry due to its dramatic impact in degrading energy production (Gupta et al., 2019).

The only AERONET site in the northern section of Chile is located in Arica (18.4°S, Fig. 4.3). This site is used to assess MAIAC accuracy of Aqua and Terra AOD retrievals in the region (Fig. 4.4). Whilst this study focuses on mineral dust from the MAIAC dataset, it seems sensible to contrast its performance with the AOD data from the MODIS Deep Blue algorithm due to its nature as an optimised aerosol product over bright areas. As suggested by Ichoku et al. (2002) and later by Martins et al. (2017), a spatial-temporal collocation was performed applying a pertinent spatial window and temporal interval. This assumes that aerosol plumes behave homogeneously within certain time-space boundaries, which seem justifiable in this situation (Anderson et al., 2003). The results in Fig. 4.4 were computed using a temporal window of 60 min centred on satellite data and a 50x50 km^2 spatial area centred on the location of the Arica AERONET site from the satellite products. These criteria sit comfortably in the middle of the parameters applied by Martins et al. (2017), who used temporal intervals in the range 30-120 min and spatial windows between 3x3 km^2 and 125x125 km^2 across several AERONET sites in South America.

The MAIAC data better captures the variability observed in the AERONET dataset for both Terra and Aqua satellites compared to the Deep Blue data (Fig. 4.4)

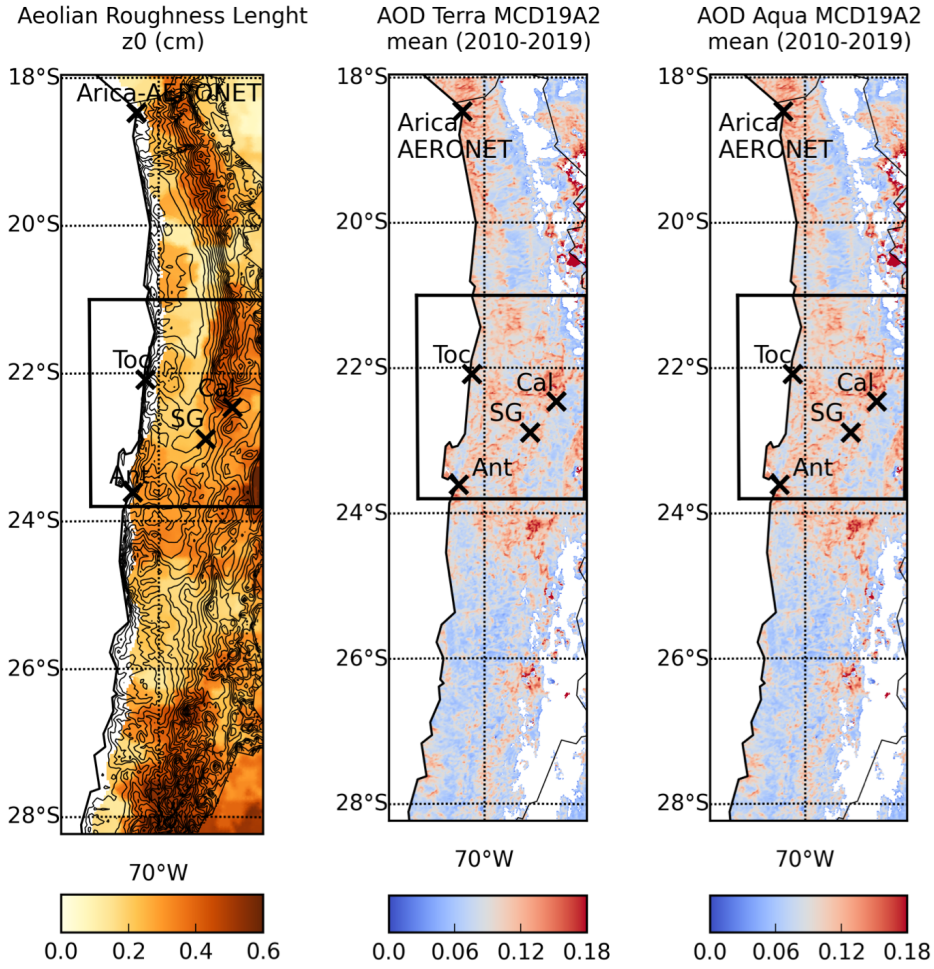

Figure 4.3: Left: Roughness length (z0) over the Atacama Desert from the GARLAP dataset with 6 km horizontal resolution. Black contour lines represent topography at 250 m vertical resolution. Centre: AOD decadal mean computed for 2010-2019 from the MCD19A2 Terra dataset. Right: AOD decadal mean computed for 2010-2019 from the MCD19A2 Aqua dataset. Black crosses indicate the location of the Arica AERONET site and mayor urban areas in the Antofagasta region. Ant: Antofagasta, Toc: Tocopilla, SG: Sierra Gorda and Cal: Calama.

– with r-values of 0.52 (Terra) and 0.45 (Aqua). This finding is similar to the results reported by Jethva et al. (2019) over bright surface regions with complex topography in Western North America. In agreement with (Lyapustin et al., 2011b), MAIAC shows higher sensitivity for reproducing atmospheric aerosols load. For MA-

IAC Terra retrievals (n=404), the mean bias in 2010-2019 reaches -0.09 (std=0.06) whereas the mean bias from MAIAC Aqua data (n=774) is -0.05 (std=0.07), with a recognisable decline between 2016-2019. These results are also in agreement with the results of the Deep Blue validation analyses over East Asia by Tao et al. (2017), where the authors argued a significant underestimation of Deep Blue AOD over deserts regions.

In the case of DB, the number of MODIS-AERONET matchups for both Terra and Aqua is considerably lower due to the lower amount of valid high quality data available. Also, in agreement with the results by Lyapustin et al. (2011b) over the Saharan region and Mhawish et al. (2019) over South Asia, DB AOD magnitudes are significantly lower in comparison with MAIAC results. DB Terra retrievals (n=161), reproduce a bias mean by -0.16 (std=0.05) whereas the bias mean from DB Aqua (n=224) is -0.11 (std=0.06). Since MAIAC retrievals better fit AERONET observations and, as discussed in detail later, the amount of valid data is considerable higher in comparison to DB in terms of both temporal and spatial coverture (.1 panels in Figs. 4.5, 4.6, 4.7, 4.8), the seasonal and spatial distribution of AOD over the Antofagasta region is analysed from the MCD19A2-MAIAC dataset (Figs. 4.5 and 4.6). It is important to note that the Arica AERONET site, as well as the large coastal margin of the Atacama Desert, is a transitional land-ocean area. As pointed out by Martins et al. (2017) in their MAIAC algorithm assessment over South America, this product represents an accurate alternative for characterising atmospheric aerosols load along heterogeneous surfaces and transitional coastal regions without available routine observations.

4.3.1 Aerosols Load over the Antofagasta Region

MAIAC presents noticeable seasonal cycle with both higher AOD and spatial coverage in summer (DJF) and spring (SON) (Figs. 4.5a,d & 4.6a,d). These observations confirm the seasonality reported by Tanaka and Chiba (2006) from simulated emission outcomes. During Terra overpasses, the highest seasonal-mean AOD occurs in central locations of the Antofagasta region – reaching 0.27 for the DJF mean (Fig. 4.5a.2) and 0.25 in SON (Fig. 4.5d.2). Also in this area, the maximum AOD is

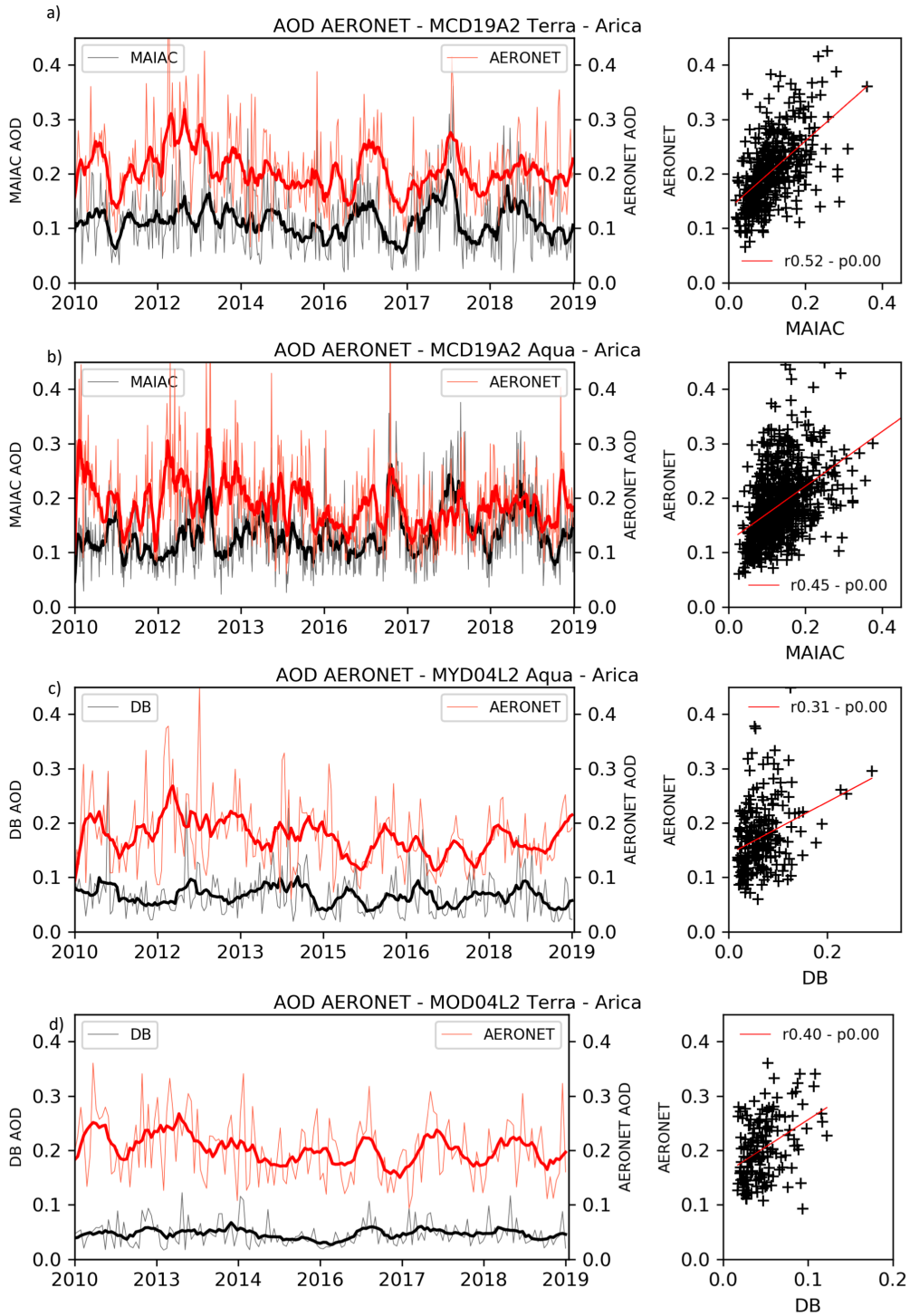

Figure 4.4: Correlation of AOD 500 nm measured at the AERONET Arica site with AOD 550 nm from MCD10A2 Aqua (a) and Terra (b), and AOD from MOD04L2 Terra (c) and MYD04L2 Aqua (d).

found. This was computed taking average over 2000-2019 of the maximum daily AOD per season. This value reaches 0.69 in summertime (Fig. 4.5 a.3) and 0.62 in spring (Fig. 4.5d.3).

In the afternoon (Aqua-times), AOD magnitudes are in similar order than late morning (Terra-times) during the active aerosol season. This is especially noticeable during summer, when the maximum Aqua seasonal AOD mean in DJF reaches 0.59 (Fig. 4.6a.2, c.f. 0.27 for Terra-times). Similar to Terra retrievals, maximum seasonal AOD during 2010-2019 also takes place during summer and spring, when reaches 0.59 (Fig. 4.6, a.3) and 0.55 (Fig. 4.6, d.3), respectively.

As expected from the described AOD seasonality, the highest frequencies of AOD events greater than 0.25 are also observed during summer and springtime from both retrieval groups (Figs. 4.5 and 4.6). Using a threshold of 0.25 to define for AOD events seems reasonable to detect potential mineral dust sources in the absence of geostationary satellites retrievals, where back-trajectories analyses can be performed. Tao et al. (2017) use a threshold of 0.3 over Asia, but that region presents higher AOD values and frequency of dust events than the Atacama. The selected threshold lies within the range of AOD mean values (0.17-0.39) reported by Dubovik et al. (2002) for desert regions. Terra retrievals from MAIAC reproduce frequencies over 15 days per season during summer over several Antofagasta region areas, including the Northeast of the Calama city (Cal), the Northwest of Sierra Gorda (SG) and the central desert region above 22°S (Fig. 4.6a.4). A similar pattern is detected during spring, and sources are similarly distributed, although frequencies tend to decline slightly (Fig. 4.6d.4). Similar locations are determined using the Aqua retrievals, although a more substantial decline is observed over spring (Fig. 4.6).

As observable, and consistent with the strong seasonality, in both retrievals groups, the central desert region does not present significant activity during autumn and wintertime (b panels in Figs. 4.5 and 4.6). An exception to the above is the northern area from Calama city (Cal) where the Chuquicamata open mining operation is located. This seems reasonable as the mine does not cease activity during

these seasons, and its anthropogenic emissions remain mostly stable throughout the year.

4.4 Coarse Aerosols Detection and Mineral Dust over the Antofagasta Region

The Ångström Exponent (α) has been used as a proxy for particles size (Ginoux et al., 2012), especially for mineral dust detection in desert areas where α values below 1.0 dominate. α from MODIS Deep Blue datasets (Terra MOD04L2 and Aqua MYD04L2) was computed for 2010-2019 during the aerosol active season (DJF and SON) over the Antofagasta region (Figs. 4.7 and 4.8 for Terra and Aqua respectively).

α over land using the Deep Blue algorithm unsurprisingly suffers from the same data gaps as AOD for the Atacama (Figs. 4.7a.1,b.1 and 4.8a.1,b.1). Despite this a noticeable pattern is distinguishable over the Antofagasta region, which does not appear to be influenced by the cloud cover. In both Aqua and Terra products, lower values of α (coarser particles) are located in the central region of the desert where the topography is relatively flat (this region generally also has some of the best data coverage). The daily seasonal minimum is predominantly less than 0.3 (4.7a.3,b.3 and 4.8a.3,b.3), although this increases over the complex topography along the Andes Cordillera where data coverage is sparse. The highest frequencies of days with α less than 1.0 is also detectable over this central desert zone (Figs. 4.7a.4,b.4 and 4.8a.4,b.4), further supporting a predominance of coarse aerosols. Along the coastline (the Coast Cordillera) and the eastern margin of the Andes Cordillera, both mean α and the frequency of low α day suggest fewer coarse particles – although this information comes from a considerably lower number of retrievals.

Although summer (DJF) exhibits higher values of α in both the Terra and Aqua datasets, the spatial distribution of α remains consistent during both active seasons (Figs. 4.7 and 4.8). During Terra retrievals in 2010-2019, the minimum α mean reached -0.28 and the maximum frequency (days with $\alpha < 1.0$) reached 33 days,

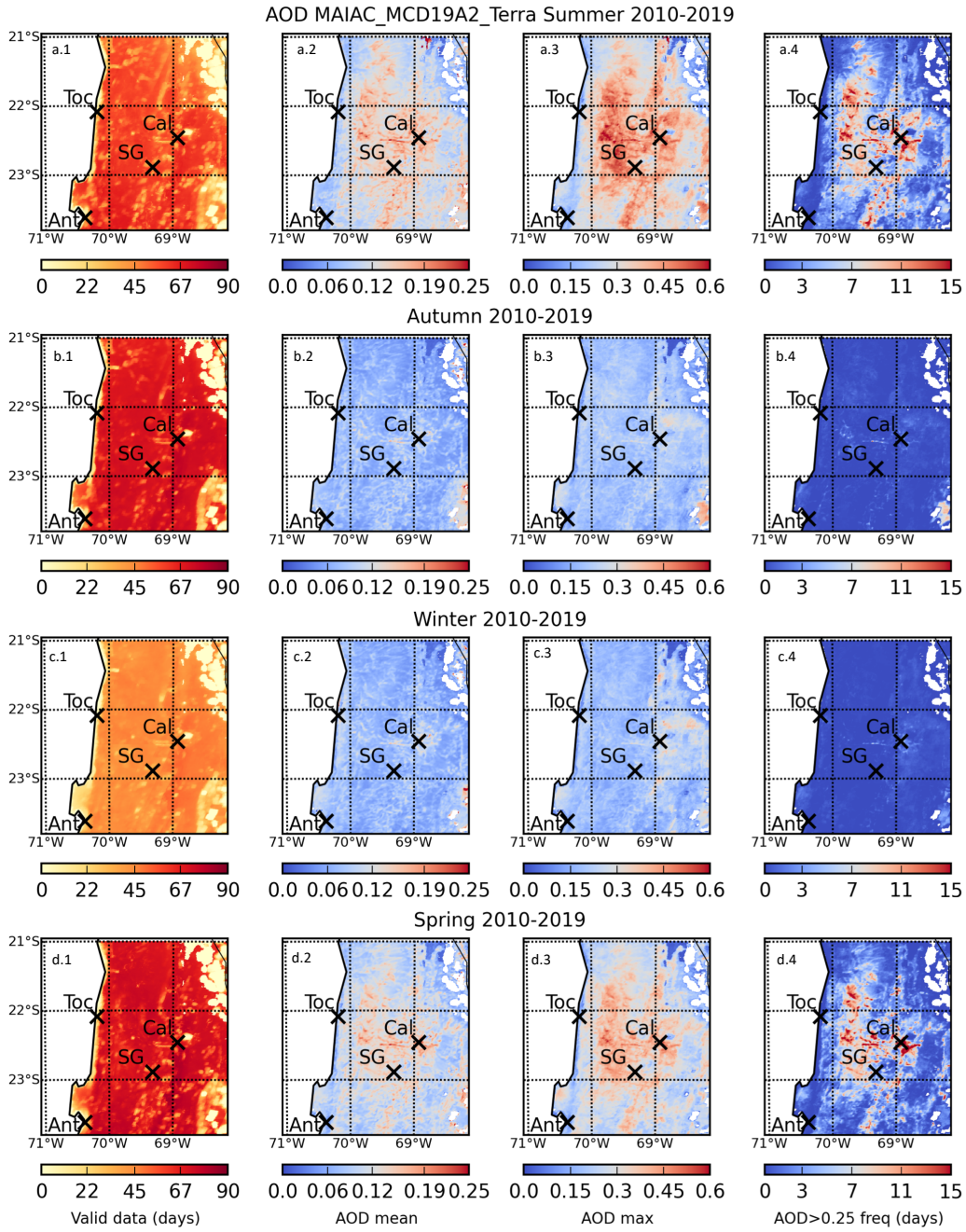

Figure 4.5: Seasonal spatial distribution of AOD Terra over the Antofagasta Region. MCD19A2 dataset. Panels a1-b1: valid number of AOD data. Panels a2-b2: decadal mean. Panels a3-b3: decadal mean of yearly max AOD values. Panels a4-b4: decadal mean of the frequency of days per year when AOD greater than 1.0.

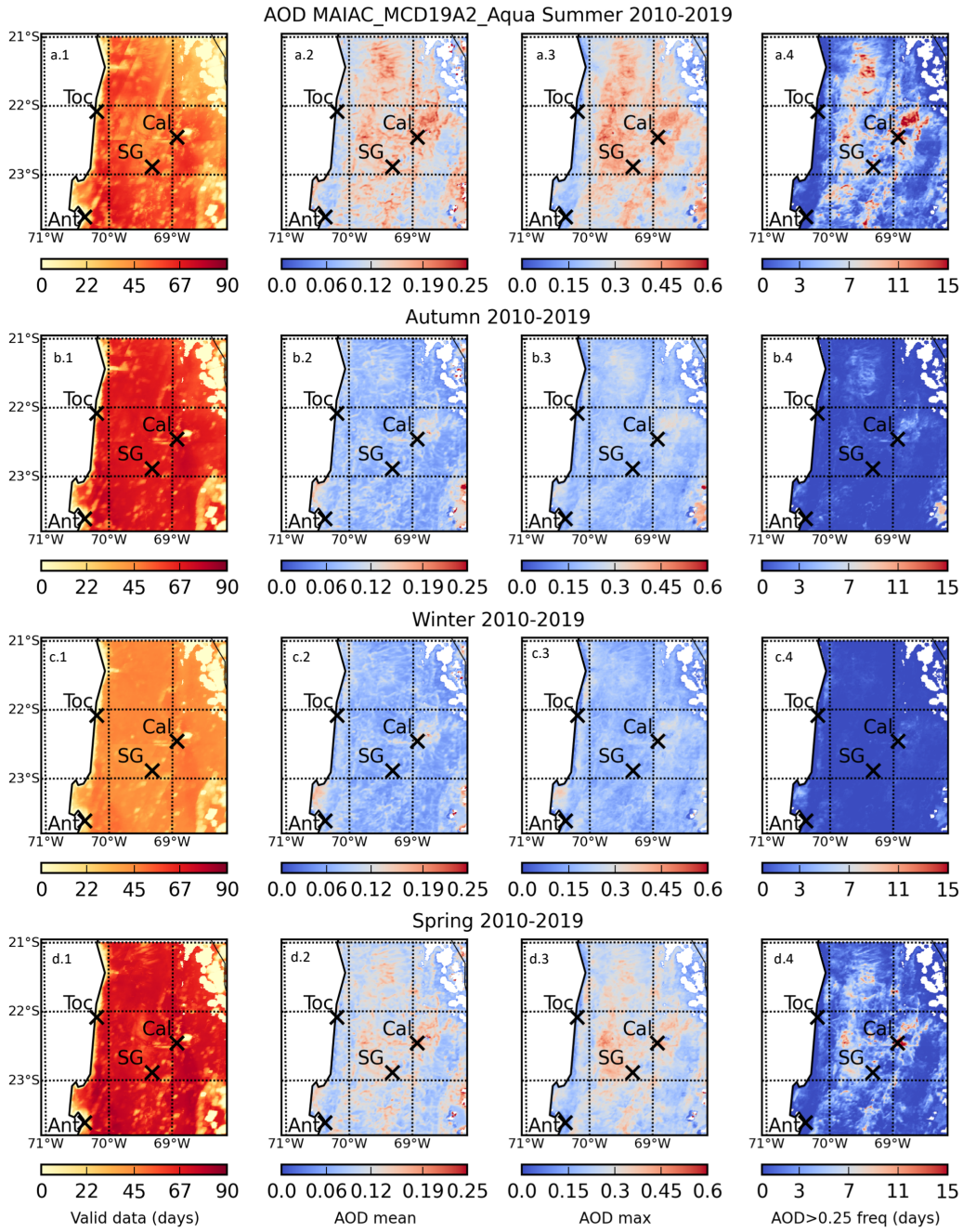

Figure 4.6: Seasonal spatial distribution of AOD Aqua over the Antofagasta Region. MCD19A2 dataset. Panels a1-b1: valid number of AOD data. Panels a2-b2: decadal mean. Panels a3-b3: decadal mean of yearly max AOD values. Panels a4-b4: decadal mean of the frequency of days per year when AOD greater than 1.0.

this means areas where about 75% of the observations were less than 1.0. On the other hand, during spring, the minimum seasonal mean was -0.39, yet the maximum frequency remains the same. Analysis of Aqua retrievals gives fundamentally identical conclusions. DJF exhibits higher values. The minimum seasonal mean during summer was +0.22, with a maximum frequency of 34.7. During spring at Aqua times, α means reached -0.37 with zones presenting frequencies until 38.7 days per season with α values less than 1.0.

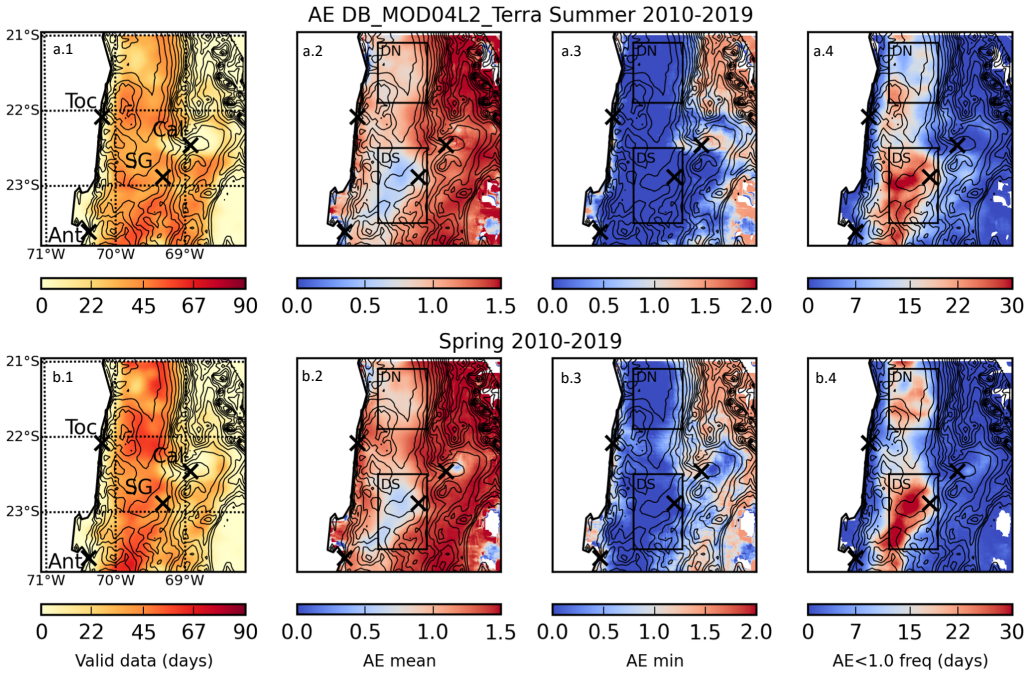

Figure 4.7: Seasonal spatial distribution of AE (α) Terra over the Antofagasta Region during the active mineral dust season, DJF (summer) and SON (spring). MOD04L2 dataset. Panels a1-b1: valid number of AE (α) data. Panels a2-b2: decadal mean. Panels a3-b3: decadal mean of yearly min α values. Panels a4-b4: decadal mean of the frequency of days per year when α less than 1.0.

In order to expand the analysis and explore the temporal variability of both AOD and α together throughout the decade, area-averaged time series of two locations of interest were computed (Fig. 4.9a,b and Fig. 4.10a,b). The selected areas, henceforth Desert North (DN - 21.1°S to 21.9°S and 69.2°W to 69.9°W) and Desert South (DS - 22.5°S to 23.5°S and 69.2°W to 69.9°W) are plotted in Figs. 4.7 and 4.8. Both areas are located in desert zones where the topography is relatively flat.

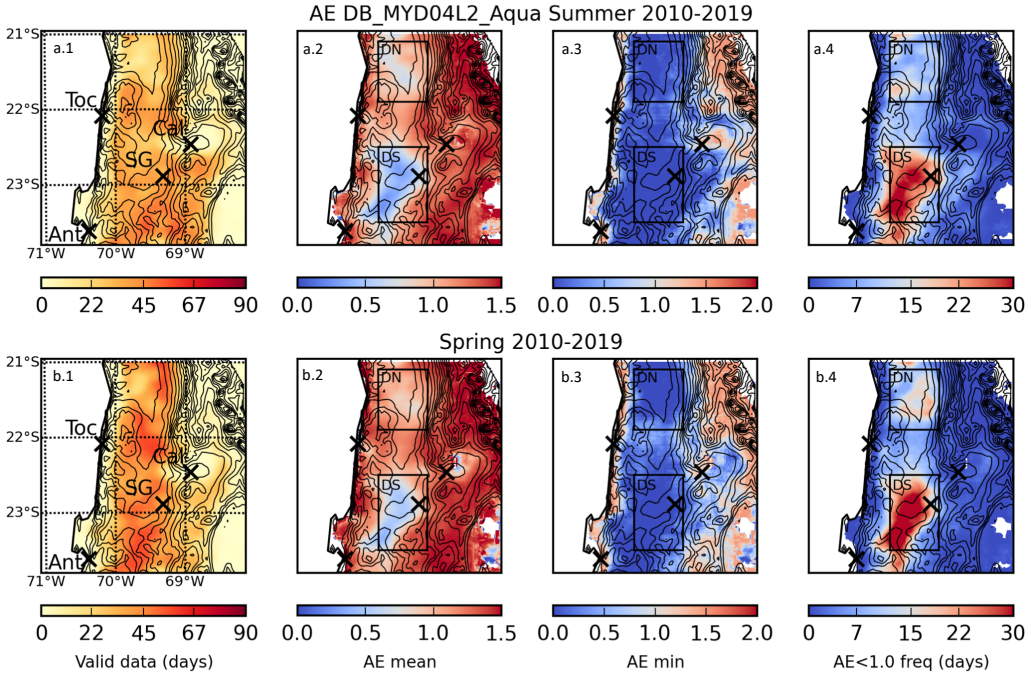

Figure 4.8: Seasonal spatial distribution of AE (α) Aqua over the Antofagasta Region during the active mineral dust season, DJF (summer) and SON (spring). MYD04L2 dataset. Panels a1-b1: valid number of AE (α) data. Panels a2-b2: decadal mean. Panels a3-b3: decadal mean of yearly min α values. Panels a4-b4: decadal mean of the frequency of days per year when α less than 1.0.

Both are also flanked by the Coastal Cordillera to the west and the Andes Cordillera to the east. These are selected to explore the strong signals that suggest exceptionally low values of α and significantly higher frequencies of days with α lower than 1.0. These two areas also have a higher number of retrievals in both seasons compared to the rest of the region, especially in spring, providing a reasonable number of observations to collocate α data with MAIAC AOD retrievals. Both AOD and α exhibit a consistent annual cycle with higher AOD and lower α values during spring and summer. This implies a strong dust production during these seasons as the aerosol load is high and the particulates are predominantly coarse. This seasonality is observed in both satellite retrievals from Terra and Aqua and over both the Desert North and South areas (Fig. 4.9c,d & Fig. 4.10c,d).

In the Desert North area, AOD and α correlate higher in Terra retrievals than Aqua data, implying a stronger seasonality of coarse-dominant particles production

(Fig. 4.9 a and b). Notably, during Aqua times, an increase of AOD is observed during 2015-2019 along with a weaker rise of α values. This might be greater anthropogenic emissions dominated by finer particles. The increase of AOD effects the correlation between both variables, although the seasonality is still consistent during these years. In the following subsection (§4.5), this phenomenon is analysed along with the wind patterns that might also be associated with the observed aerosols load variability.

There is higher variability in both AOD and α during the active aerosol season (DJF-SON) throughout the decade (2010-2019). In summer, the Terra AOD monthly mean ranges between an lower quartile 0.07 and an upper quartile of 0.20. However, these drop to 0.03-0.09 in winter (blue box plots in Fig. 4.9). On the other hand, for α the lower & upper quartiles are 0.32 and 1.35 in summer, but only 1.18 and 1.44 in winter (grey thin boxes in Fig. 4.9). This variability implies that the active season comprises a higher load of aerosols consisting of mostly coarse particles, with few fine particles present. Yet for most of the autumn and winter, a low aerosol load is governed by fine particles.

Aqua retrievals exhibit a clear seasonal cycle with higher variability in the active aerosol season (Fig. 4.9). The values are slightly more constrained than those observed for Terra. The observed AOD monthly means concentrates the 50% (p25 to p75) of the observations between 0.09 and 0.20 in summer, compared to 0.05 and 0.09 in winter. On the other hand, α concentrates the central 50% of retrievals in the range 0.48-1.10 during summer, and 1.21-1.43 in winter. This implies a slightly higher load of coarse aerosols during the active season, in comparison to Terra retrievals.

In the Desert South area (DS), AOD and α reproduce higher correlations in Terra than Aqua retrievals (Fig. 4.10a,b). However, both satellite datasets present higher correlations in this area (DS) than those computed for DN. An increase in AOD after 2015 is observed at Aqua times in the Desert South area, as in the Desert North area. Both AOD and α exhibit a clear seasonality in Desert South (Fig. 4.10). α variability is significantly higher than the observed over the DN area, and there is

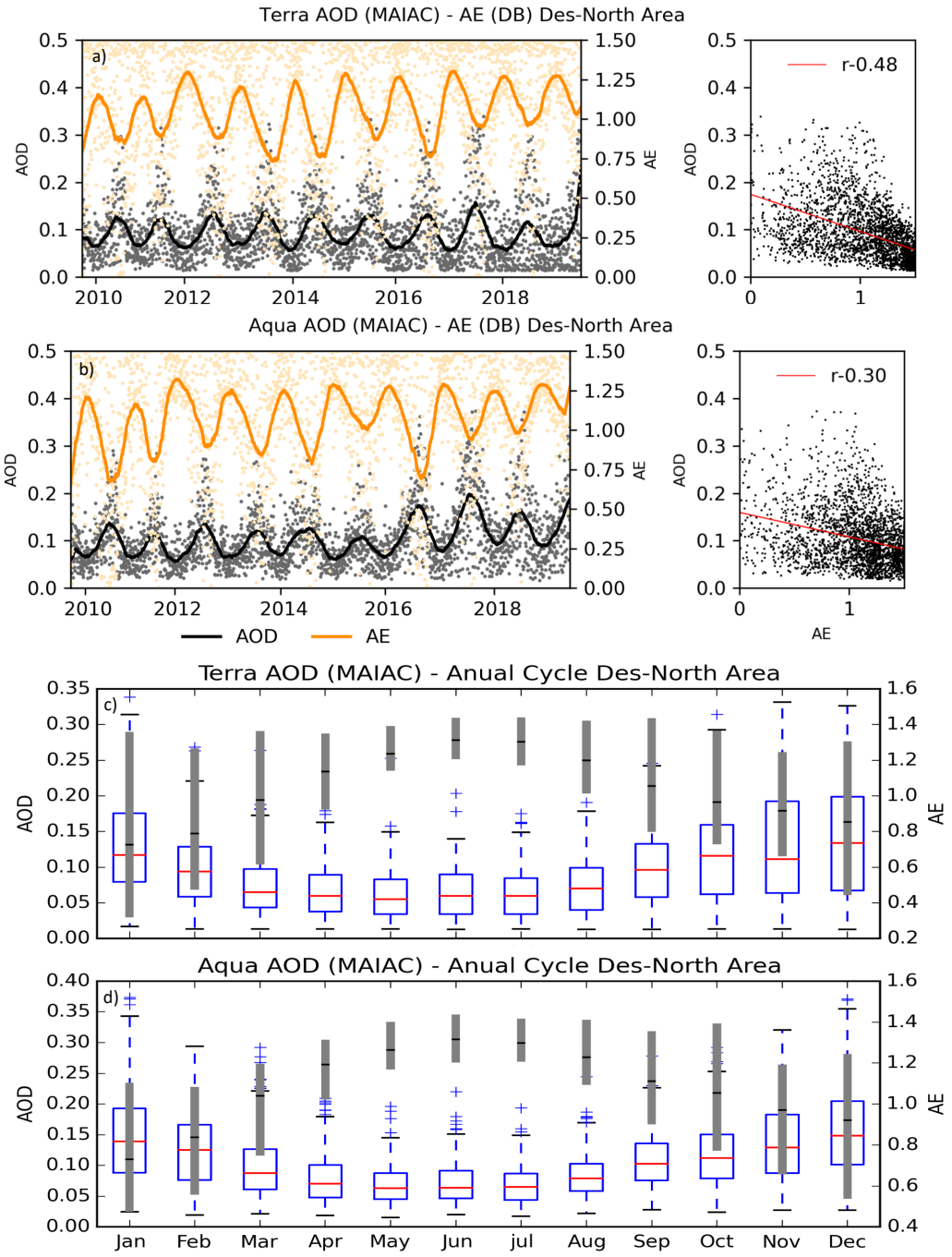

Figure 4.9: AOD (MCD19A2) and α (MOD04L2 and MYD04L2) area-averaged time series over the Desert-North area throughout 2010-2019 for Terra (a) and Aqua (b) retrievals. c: AOD and α seasonality from Terra. d: AOD and α seasonality from Aqua. In c and d, grey bars depict the interquartile range (p25-p75) of the α monthly data in 2010-2019

considerably lower values of α reproduced in the summertime, especially in Aqua retrievals (Fig. 4.10 d). Both AOD and α presents higher variability during the active aerosol season. In Terra retrievals, the central quartiles of AOD monthly means sit between 0.09 and 0.23 in summer, whereas they decline to 0.04 - 0.10 in winter (blue box plots in Fig. 4.10). These are slightly higher values of AOD in comparison to DN area observations (Fig. 4.9). On the other hand, α concentrates the central quartile values in summer between 0.25 and 1.08, whereas in winter it varies between 1.15 and 1.50 (thin grey boxes in Fig. 4.10). The described variability over the DS area implies that the active season is governed by coarse particles with most of the observations consistently reproducing low α values (< 1.0). On the contrary, most of the autumn and winter season there is a predominancy of a low aerosol load and fine particles.

Aqua datasets exhibit a clear seasonal cycle with higher variability in the active aerosol season for both AOD and α in the Desert South area. However, similar than the observations in DN, values are constrained (Fig. 4.10, d). The central half of the distribution of AOD monthly-mean value is observed between 0.09 and 0.18 in summer, whereas in winter they sit within the range 0.05 - 0.09. Regarding α, the interquartile range in summer is comprised between 0.36 and 1.00, and between 1.01 and 1.50 in winter. This implies that summer emissions consist mostly of coarse particulates attributable to mineral dust. Similar to what has been observed over both areas and satellite groups during autumn and winter, the lower aerosol load at Aqua times in DS is dominated by fine particles, presumably mainly anthropogenic emissions.

4.5 Mineral Dust Events

Selection of dust events was assessed based on different seasonal thresholds of AOD, as the atmospheric aerosol load over the Atacama exhibits a consistent seasonal cycle. The threshold for each season was computed as the value of one standard deviation above the decadal mean (Tab. 4.2). Unsurprisingly higher AOD thresholds are calculated for DJF and SON, with slightly higher seasonal ranges in

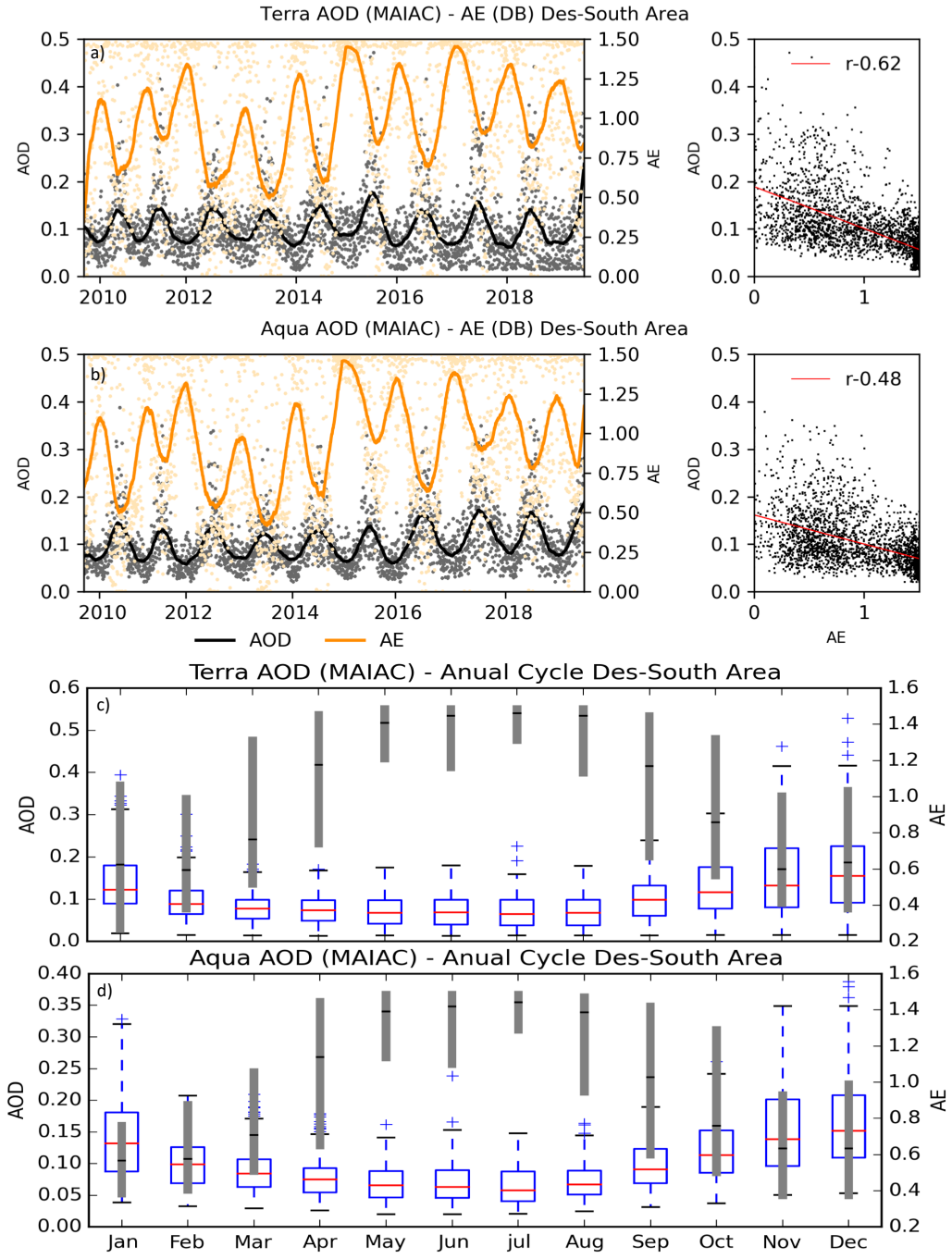

Figure 4.10: AOD (MCD19A2) and α (MOD04L2 and MYD04L2) area-averaged time series over the Desert-South area throughout 2010-2019 for Terra (a) and Aqua (b) retrievals. c: AOD and α seasonality from Terra. d: AOD and α seasonality from Aqua. In c and d, grey bars depict the interquartile range (p25-p75) of the α monthly data in 2010-2019

the Desert North compared to the South area. Having a higher threshold implies greater variability and more intense AOD events. The number of events and their magnitude for each season during 2010-2019 is presented in Figs. 4.11 (DN) and 4.12 (DS). An event was identified when it simultaneously presented both the AOD exceeding the respective seasonal threshold and the α was lower than one. In histograms, the amount of valid data for the decade, its annual mean and its standard deviation (between years) have also been indicated to contextualise the number of events within the actual amount of data (days) available from the MAIAC dataset. As mentioned in the methods (§4.2), area-averaged time series for DN and DS were computed only when at least the 50% of the cells presented maximum quality data, retaining over 2/3 of the days within each year.

Table 4.2: AOD seasonal thresholds for dust events computation, computed as the standard deviation of over the decade

Area-Sat	DJF (Su)	MAM (Au)	JJA (Wi)	SON (Sp)
DN-Terra	0.20	0.10	0.10	0.18
DN-Aqua	0.22	0.13	0.11	0.18
DS-Terra	0.22	0.11	0.11	0.20
DS-Aqua	0.21	0.11	0.10	0.18

Over the Desert North area in 2010-2019, AOD events occur more at Terra-times than at Aqua-times except in the last three years of the decade (Fig. 4.11). This may arise as a function of the threshold method being determined from a trending dataset. As expected from the described seasonality, these events reached a higher intensity during the active season – with maximum individual grid-cell AOD values (red star) regularly exceeded 0.5. Dust events, with an area-average AOD greater than 0.20 in DJF and 0.18 in SON (Tab. 4.2), increased slightly towards the end of the decade, reaching 15 days per season during the summers of 2017 and 2019. The highest number of events were 18 days, which occured in both the spring 2014 and autumn 2019. It is important to note, that valid data is restricted to the best quality available in the satellite product, therefore these 18 events as well as other computed could feasible be more. Although more extreme events are expected to occur in spring, the strongest event during the autumn of 2019 was particularly ex-

treme. Although the seasonal threshold is equal to 0.10 (Tab. 4.2), this reached a maximum single-cell AOD value of 0.5, similar to those observed during the active season in summer and spring. Regarding the afternoon Aqua retrievals (Fig. 4.11a), an exceptional trend was identified. Dust events had a low occurrence until 2016. However, between 2017 and 2020 these increased dramatically. This accompanied a slight increase in the area-averaged AOD computed for the maximum event in each season (black stars). Large AOD events took place with a considerably higher frequency towards the end of the decade with exceptional raises during the summer of 2017 (area-averaged $AOD > 0.22$ during 22 days) and during the autumn of 2018 when the area-averaged AOD exceeded 0.13 during 30 days.

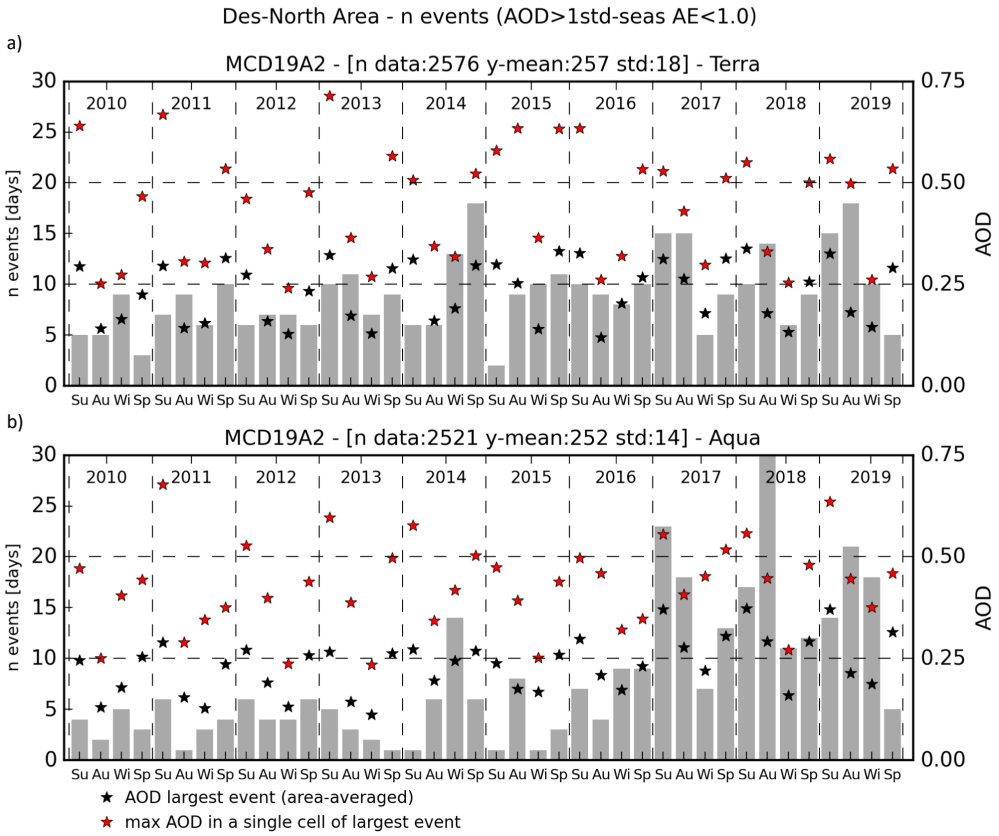

Figure 4.11: Seasonal AOD events computed in 2010-2019 from the MCD19A2 dataset over the Desert-North area from Terra (a) and Aqua (b) retrievals. Above each panel are given the total amount of valid retrievals data over the entire decade (n data), the average number of valid retrievals per year (y-mean) and the standard deviation of the amount of valid data available between years.

In the Desert South area, AOD events were more frequent at Terra-times than at Aqua-times, similar to the observed over the Desert North area (Fig. 4.12). Also in this area particularly intense events took place in DJF, such as the maximum single-cell AOD values (red star) exceeding 1.4 (Terra) and 1.2 (Aqua) in the summer of 2013. Indeed, all events with AOD above 0.75 occured during summer from both Terra and Aqua retrievals. It is interesting to note that the event in summer 2013 was also observed over the Desert North area, although in this area it was less intense reaching maximum single-cell AOD values of about 0.7 (Terra) and 0.6 (Aqua) (Fig. 4.11).

At Aqua-times in Desert South, there is strong trend of increasing frequencies toward the end of the decade, as seen also in the Desert North area. Season with more than 10 days exceeding the threshold occur much more in 2017-2019 than in the rest of the decade (Fig. 4.12b). This coincides with an increase of the seasonal mean atmospheric dust load compared with the rest of the decade (Fig. 4.10). However, at Terra-times events are not unprecedented and remain within the range of the observed AOD throughout the rest of the decade (Fig. 4.10a). At Aqua-times, there is not an evident increase in the area-averaged AOD computed for largest events compared to the rest of the decade (Fig. 4.12b), unlike in the desert North area (Fig. 4.11b). Despite this, large AOD events during the active season took place with a considerably higher frequency towards the end of the decade starting in the spring of 2017 (area-averaged $AOD > 0.18$ during 18 days). Like Aqua retrievals over DN, the autumn of 2018 exhibited an unusual activity, reaching 30 events exceeding the AOD season threshold of 0.11 (Fig. 4.12b and Tab. 4.2). However, as expected for the described AOD seasonality, these events were considerably weaker (area-averaged AOD of largest event equal to 0.2) than those observed during summer or spring, where the area-averaged AOD frequently reached 0.3 or 0.4, and the maximum single-cell AOD exceeded 0.5 most of the decade.

4.5.1 Wind Forcing and Dust events: Desert-North Area

As argued by Alfaro et al. (2011), the aeolian roughness directly contributes to dust production as the crucial soil property that either facilitates or difficult the aeolian

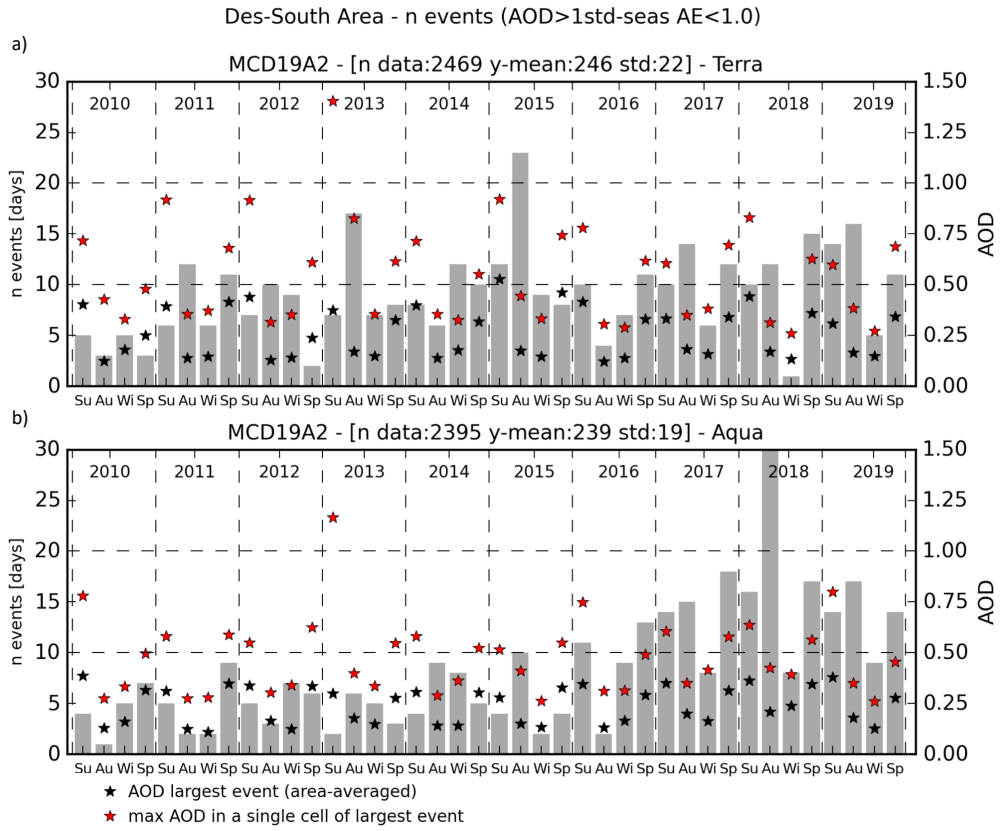

Figure 4.12: Seasonal AOD events computed in 2010-2019 from the MCD19A2 dataset over the Desert-South area from Terra (a) and Aqua (b) retrievals. Above each panel are given the total amount of valid retrievals data over the entire decade (n data), the average number of valid retrievals per year (y-mean) and the standard deviation of the amount of valid data available between years.

transport of dust particles from the ground. Higher roughness required higher wind speeds for particles lifting; on the contrary, lower roughness requires lower wind speed for dust generation. The predominant wind mode governing dust events was assessed by analysing the zonal (*us*) and meridional (*vs*) components of the wind from the ERA5 reanalysis for both areas of interest in the Antofagasta region (DN and DS) in 2010-2018. This period was selected according to the temporal extension of the ERA5 dataset used as described in the methods section. This subsection aims to identify the governing wind condition of both the observed seasonality of mineral dust and the occurrence of the extraordinary events in the Desert North area.

The area-averaged time series of wind speed computed from the ERA5 dataset

exhibits a distinctive seasonality, qualitatively similar to the observed AOD annual cycle in the Desert-North area at Terra-times (Fig. 4.13c). Higher wind speeds are seen in summer and lower wind speeds during winter. As argued in §3.1 and §6.5 of this Thesis, the annual cycle of wind speed over the Atacama Desert, with maximums in summer, is regionally modulated by the South Pacific Anticyclone. As presented in §5.3, ERA5 reasonably reproduce the observed (2000-2018) wind speed seasonality at both coastal (Antofagasta) and inner desert areas (Calama).

Although the resultant wind speed vector correlates positively with AOD, opposite trends are observed for zonal and meridional winds. Whereas the eastward wind (us) presents a weak positive correlation with AOD (+0.21) (Fig. 4.13a), the northward component of wind (vs) correlates negatively (-0.19) (Fig. 4.13b). Consistent with the described daily cycle of wind speed for this region (§3.1), Aqua winds (afternoon) (Fig. 4.14) are stronger with a larger variability than those at Terra-times (morning-noon) (Fig. 4.13).

Windspeed does not significantly correlate with AOD data when there is very low α ($\alpha < 0.5$, red stars in Fig. 4.13d). However, coarse aerosols tend to be associated with more intense eastward winds and more intense southward winds (negative *vs*). For the subgroup containing coarse particles ($AE < 0.5$) the mean zonal wind speed increases from 0.55 ms^{-1} (black dashed line) to 0.68 ms^{-1} (blue solid vertical line). This results in an increase of the wind speed between the two groups (all aerosols - coarse aerosols) from 0.7 ms^{-1} to 0.82 ms^{-1}.

In the case of Aqua retrievals (Fig. 4.14), the relationship between AOD and wind patterns is qualitatively similar to Terra datasets. However, the relationships in the Aqua retrievals are stronger. Here similar to Terra retrievals, wind speed seasonality is correlated to the observed AOD annual cycle, with maximum wind speeds in DJF and minimum in JJA (Fig. 4.14c). The resultant wind speed vector correlates positively with AOD (r=0.47), with similar positive correlation with the zonal component (r=0.42). Conversely, meridional winds correlate negatively with AOD retrievals (r=-0.46) (Fig. 4.14 d). Coarse aerosols (red stars in Fig. 4.14d) show a similar behaviour as in the Terra retrievals, though with a more robust pattern

being observed in comparison with its Terra counterpart. AOD observations with α less than 0.5 are aligned with intense eastward winds and intense southward winds (negative *vs*). The area-averaged DN zonal wind mean (black dashed vertical line in Fig. 4.14d, left panel) reached 1.7 ms^{-1} whereas for the subgroup containing coarse particles only ($AE < 0.5$) this increased to 2.09 ms^{-1} (blue solid vertical line). On the other hand, the meridional mean (black dashed vertical line in Fig. 4.14d, central panel), reached -0.5 ms^{-1} whereas for coarse particles ($AE < 0.5$) this was computed equal to -1.03 ms^{-1} (blue solid vertical line). This results an average windspeed in the coarse particle subgroup of 2.37 ms^{-1} compared to 1.7 ms^{-1} for the entire dataset (Fig. 4.14d right).

The analysis above, describing that zonal and meridional winds correspond with AOD, can be used to infer the governing wind directions during coarse aerosols events (Fig. 4.15). For Terra retrievals, consistent with Fig. 4.13, coarse and high aerosol observations are predominately aligned to positive zonal winds (Fig. 4.15b), which results in winds directions mostly between SW and NW (Fig. 4.15a). The wind directions also contain a less-frequent east component during Terra-times, which is not seen during the Aqua retrievals (Fig. 4.15c). These eastward flows are observed during the morning in the desert when the land-ocean flows that govern the nocturnal wind trajectories still occur (see Chapter 3). Meanwhile Aqua retrievals exhibit a predominant western component with a few southern winds observations, which is consistent with the governing afternoon ocean-land flows over the Atacama region.

In the afternoon (Aqua times), most of the coarse events take place when wind flows from the WNW with eastward component values (positive *us*) from about 1.8 ms^{-1} and negative meridional winds (southward) (Fig. 4.15d).

As described in §3.1, the westerly sea breeze along northern Chile dominates during the daytime with peaks during the afternoon. However, this well-studied pattern of surface winds across the desert (Garreaud and Falvey, 2009; Schulz et al., 2011; Rutllant et al., 2013; Muñoz et al., 2013) has not been previously described as a driver of mineral dust production. The results here exposed suggest a strong

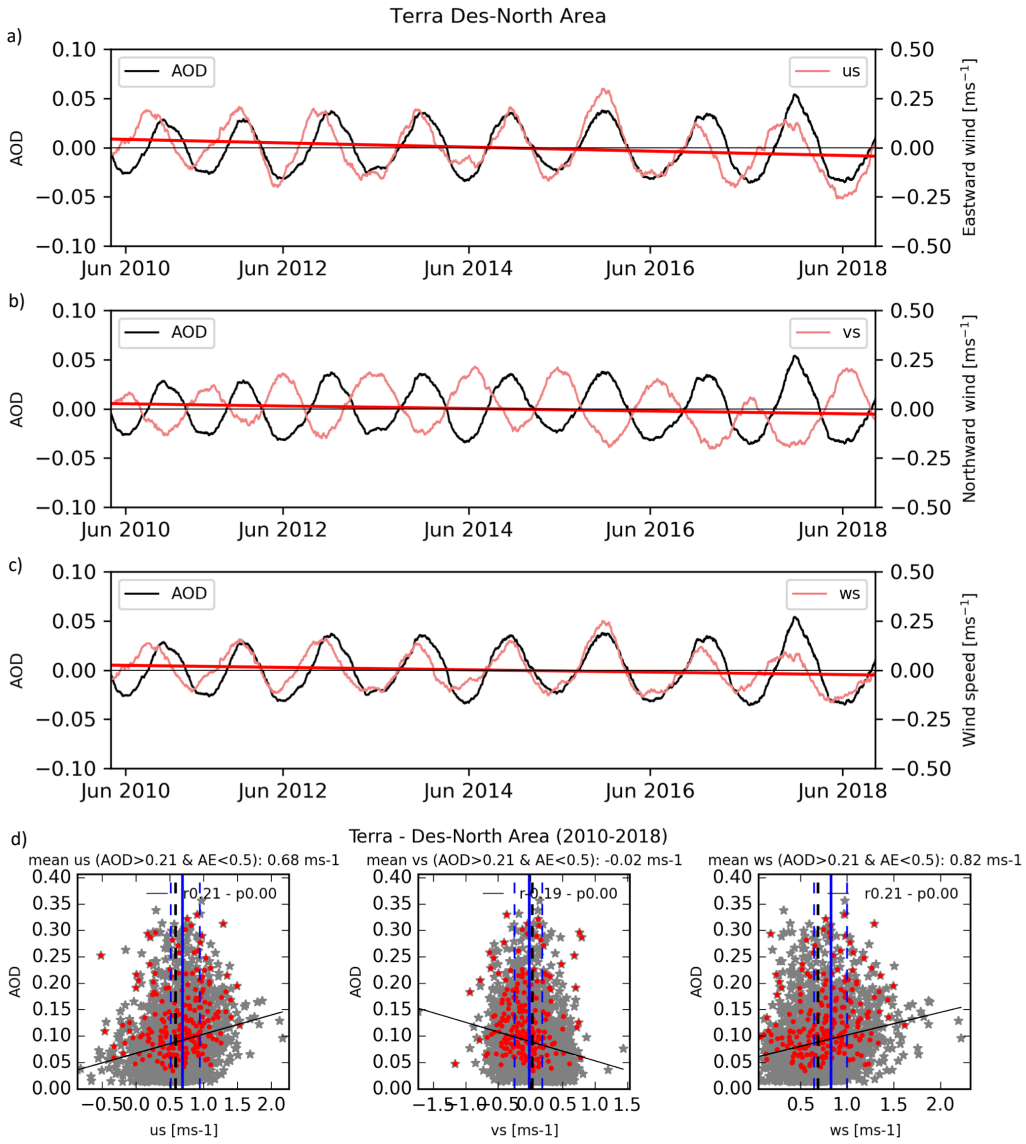

Figure 4.13: AOD (MCD19A2) and wind speed time series (ERA5) at Terra times over the Desert-North area during 2010-2018; a: Eastward wind component (*us*), b: Northward component (*vs*), and c: surface wind speed. The bottom row (d) contains scatter plot between AOD and *us* (left), *vs* (centre) and wind speed (right). Vertical dashed black lines indicate the wind component means for the entire dataset. Vertical solid (dashed) blue lines indicate the wind component means (interquartile ranges) for the subset of data with $AOD > 0.2$ and $\alpha < 0.5$ (red stars).

connection between the sea breeze and higher mineral dust production. As expected by the daily cycle of wind direction and intensity during Aqua retrievals (maximum

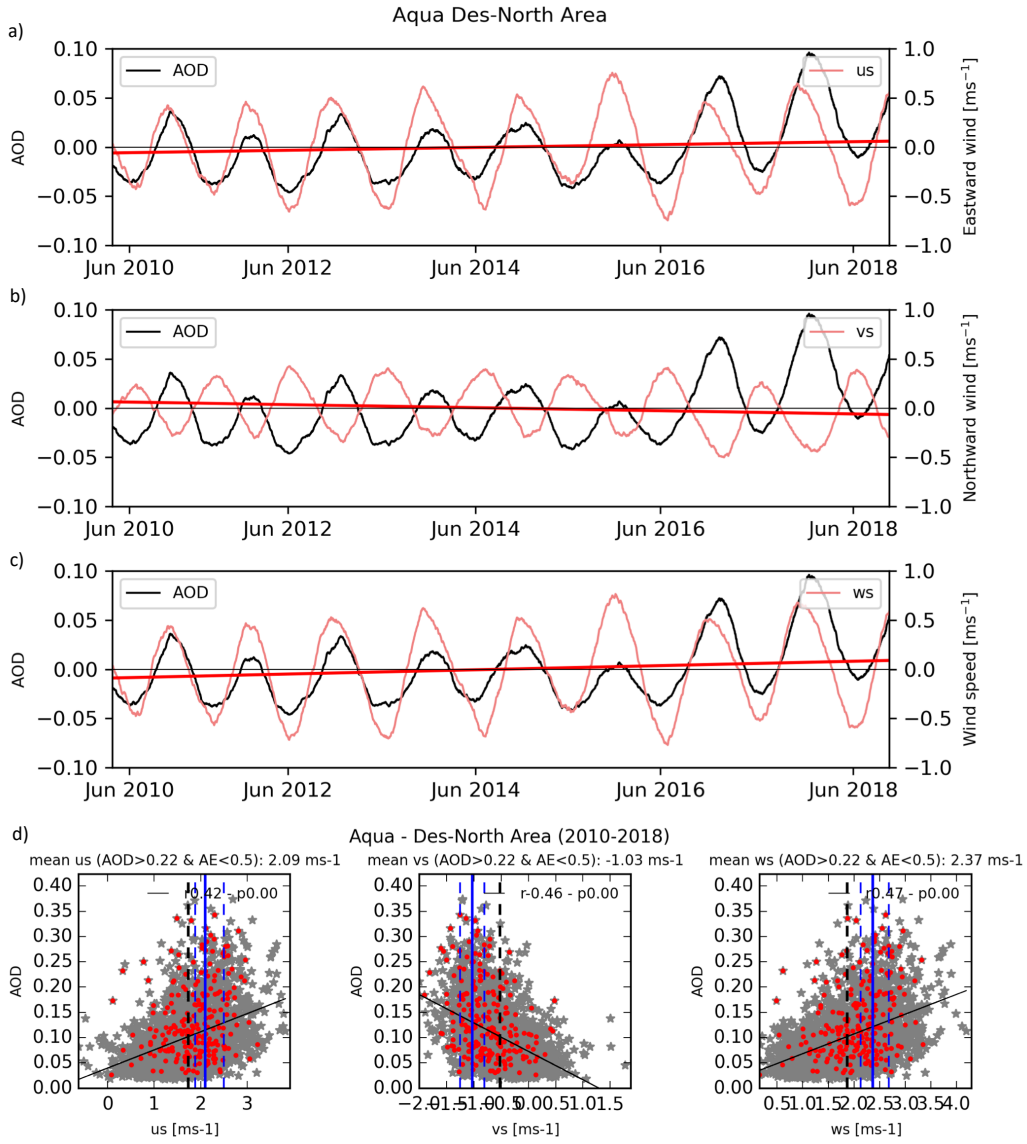

Figure 4.14: AOD (MCD19A2) and wind speed time series (ERA5) at Aqua times over the Desert-North area during 2010-2018; a: Eastward wind component (us), b: Northward component (vs), and c: wind speed vector. d: Scatter plot between AOD and us (left), vs (centre) and ws (right). Vertical dashed black lines indicate the wind component means for the entire dataset. Vertical solid (dashed) blue lines indicate the wind component means (interquartile ranges) for the subset of data with $AOD > 0.2$ and $\alpha < 0.5$ (red stars).

westerlies during the afternoon), the sea breeze exerts a less dominant effect, as this has not yet fully developed (Fig. 4.15, top). On the other hand, during Terra retrievals (afternoon), a clear link of the fully developed sea breeze with higher dust

emissions is evidenced Fig. 4.15, bottom).

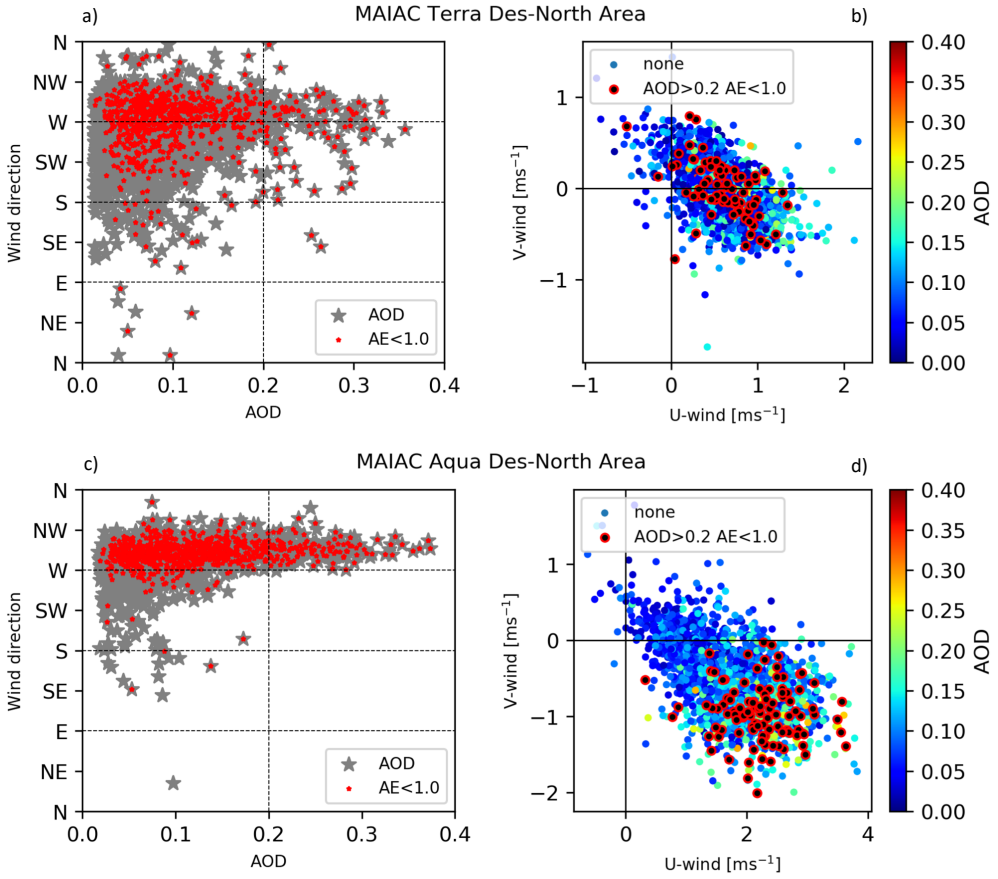

Figure 4.15: MAIAC AOD and ERA5 wind pattern DN. (a) AOD from MCD19A2 and wind direction scatter plot of area-averaged time series over the Desert-North area from Terra retrievals during 2010-2018. Red stars depict AOD observations with $\alpha < 1.0$. (b) Wind component scatter plots from Terra with red circles highlighting data with $AOD > 0.2$ and $\alpha < 1.0$. (b) and (d) repeat figures (a) and (c) respectively with Aqua retrievals.

The axis x in Fig. 4.16 corresponds to the lower thresholds of AOD used for selecting the respective dataset from which the winds plotted in the axes y were computed. For instance, in the panel b-left of Fig. 4.16, for a subset of data with AOD values equal o greater than 0.2 (vertical black dashed line), the correspondent mean wind speed computed from this subset is equal to 0.72 (solid red line). Similarly, right panels in Fig. 4.16 summarise the results for AE. However, in this case, the subset is given by the data less than the upper threshold values plotted in the x axes.

Wind speed in Desert North tends to be dominated by the zonal component, where land-sea breeze develops, which is one order of magnitude higher than the meridional component (Fig. 4.16). Regarding Terra retrievals, there is no consistent trend of windspeed with AOD (Fig. 4.16a). This is consistent with Fig. 4.15b where AOD values greater than 0.2 does not clearly differentiate from those with α greater than one. For Terra, wind speed follows a weak decline as α increases (Fig. 4.16b). Indeed, α greater than one (fine aerosols) are associated to lower wind speeds (mean $< 0.7 ms^{-1}$) in contrast with coarser particles ($\alpha < 0.5$) observation which take place at a wind speed mean of about 0.8 ms^{-1}.

A more evident pattern is found for both AOD and α observations within Aqua retrievals in the DN area (Fig. 4.15b,d). AOD consistently increases as wind speed rises. Subsets with AOD values greater than 0.2 exhibit winds speeds exceeding 2.4 ms^{-1} with a standard deviation range between 1.8 and 3.1 m s^{-1}. This in contrast with lower AOD subsets (< 0.1) where wind speed declines to less than 2.0 ms^{-1} (mean) and a standard deviation range of 1.1 to 2.6 ms^{-1}. Here the influence of zonal (solid grey line) and meridional (dashed grey line) is robust. Whereas zonal wind aligns with wind speed, the (mean) meridional wind decreases abruptly for $AOD > 0.2$ reaching -1.0 ms $^{-1}$ (Fig. 4.15b). In respect with α (Fig. 4.15d), mean wind speed remains at about 2.1 ms $^{-1}$ for coarse particles ($\alpha < 1.0$). For fine particles ($\alpha > 1.0$) mean wind speed drops to 1.8 ms $^{-1}$, with similar behaviour of zonal winds (u-wind), along with an increase of the northward component (v-wind).

4.5.2 Wind Forcing and Dust events: Desert-South Area

In the Desert-South area, the wind speeds from ERA5 at Terra times also exhibit a distinctive seasonality with a summer peak and low in winter (Fig. 4.17c). This seasonality is similar to that observed for the Desert-North area. However unlike Terra-time records for the DN area, in DS the AOD correlates negatively with the wind speed (r=-0.27). This AOD correlation extends to the meridional wind component (r=-0.21) yet is opposite to the zonal wind component (r=+0.37, Fig. 4.17d). Aqua Afternoon winds (as sampled by the Aqua retrievals) (Fig. 4.17) are stronger and with more considerable variability than those at Terra-times (morning-noon)

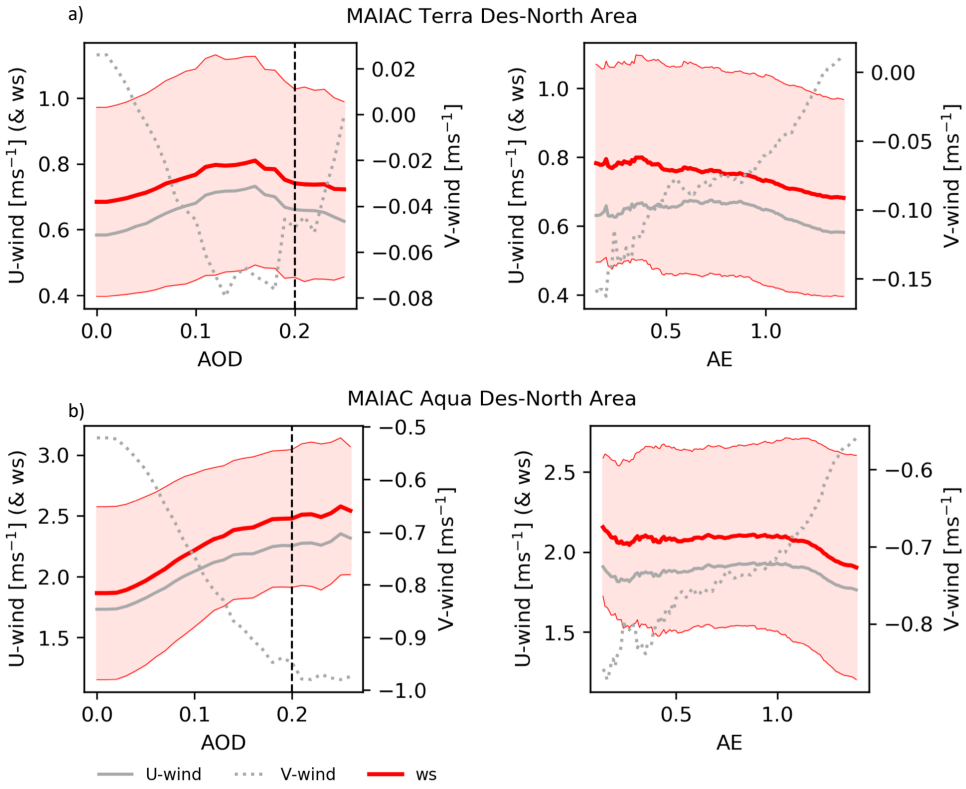

Figure 4.16: Subsets of AOD (left) and α (right) data and wind components over the Desert-North area for Terra (a) and Aqua (b) times. X-axes correspond to lower (AOD) and upper (AE) thresholds used to select the respective datasets from which the winds plotted in axis y were computed.The light red area depicts the one-standard-deviation range from the mean (solid red line) of the wind speed

(Fig. 4.18). Again this behaviour is consistent with the described daily cycle of wind speed for this region (§3.1). However, in this area (DS) winds are more intense at both times (Terra and Aqua) than those observed along the Desert North area (Figs. 4.13 and 4.14).

The subset of AOD with low α (< 0.5) shows a distinguishable pattern when plotted against zonal winds (red stars in Fig. 4.17 d-left). Coarse aerosols tend to be associated with slower westward winds, in comparison with AOD records governed by finer particles. Also, high dust loads (AOD greater than 0.5) are also coincident with the few and weak eastern flows. Indeed, the zonal wind mean (black dashed vertical line), as area-average in the DS area, reached -1.2 ms^{-1} whereas for the

coarse particles subgroup ($\alpha < 0.5$) this decreased to -0.34 ms^{-1} (blue solid vertical line). This indicates a certain predominance of eastward winds ($us > 0$) of the coarse aerosol subgroup in comparison with the entire dataset. Despite the above, it is interesting to note that the westward winds are still predominant at Terra times in the Desert-South area, in contrast to the Desert-North area, where the zonal wind component is mostly governed by weak eastwards (Fig. 4.13).

High AOD values tend to take place at low magnitudes of wind (Fig. 4.17) and large events are at velocities less than 2.0 ms^{-1} (Fig. 4.13 d right). This might be unexpected, as the AOD load in this area is larger at Terra times than the observed on the DN area. However, AOD load does not seem to be associated with predominant strong wind flows, at least when analysing the area-averaged winds. The assumption of averaging both AOD and α can lead to misleading interpretations in areas of complex topography. Although both areas were selected considering their less intricate orography, they are surrounded by two mountain ranges. At hours when the dominant wind direction is still transitioning, complex local winds patterns comprising both easterlies and westerlies within the area of interest may cancel each other, leading to small net magnitudes and hence masking the existing local effects on dust production.

In the case of Aqua retrievals, AOD and wind speed exhibit a similar annual cycle with highs in DJF and lows in JJA (Fig. 4.18c). As a result wind speed correlates positively with AOD (r=0.40), although the zonal component alone shows stronger positive correlation (r=0.52, Fig. 4.18a)). On the other hand, no correlation is observed with the relatively weak meridional wind component (r=-0.01 and p=0.58) (Fig. 4.18b). AOD observations with α less than 0.5 are aligned with intense eastward winds (red stars in Fig. 4.18d). The zonal wind mean is 1.1 ms^{-1} whereas for the coarse particles subgroup (those with $AE < 0.5$) this increased significantly until 2.45 ms^{-1}. As the winds are predominantly east-west, a similar behaviour is seen for surface wind speed (1.1 ms^{-1} vs 2.90 ms^{-1} for the coarse particles, Fig. 4.18d).

For Terra retrievals, coarse ($\alpha < 1.0$) and high aerosol load ($AOD > 0.2$) are mostly found at negative zonal and meridional winds values (Fig. 4.19b). This re-

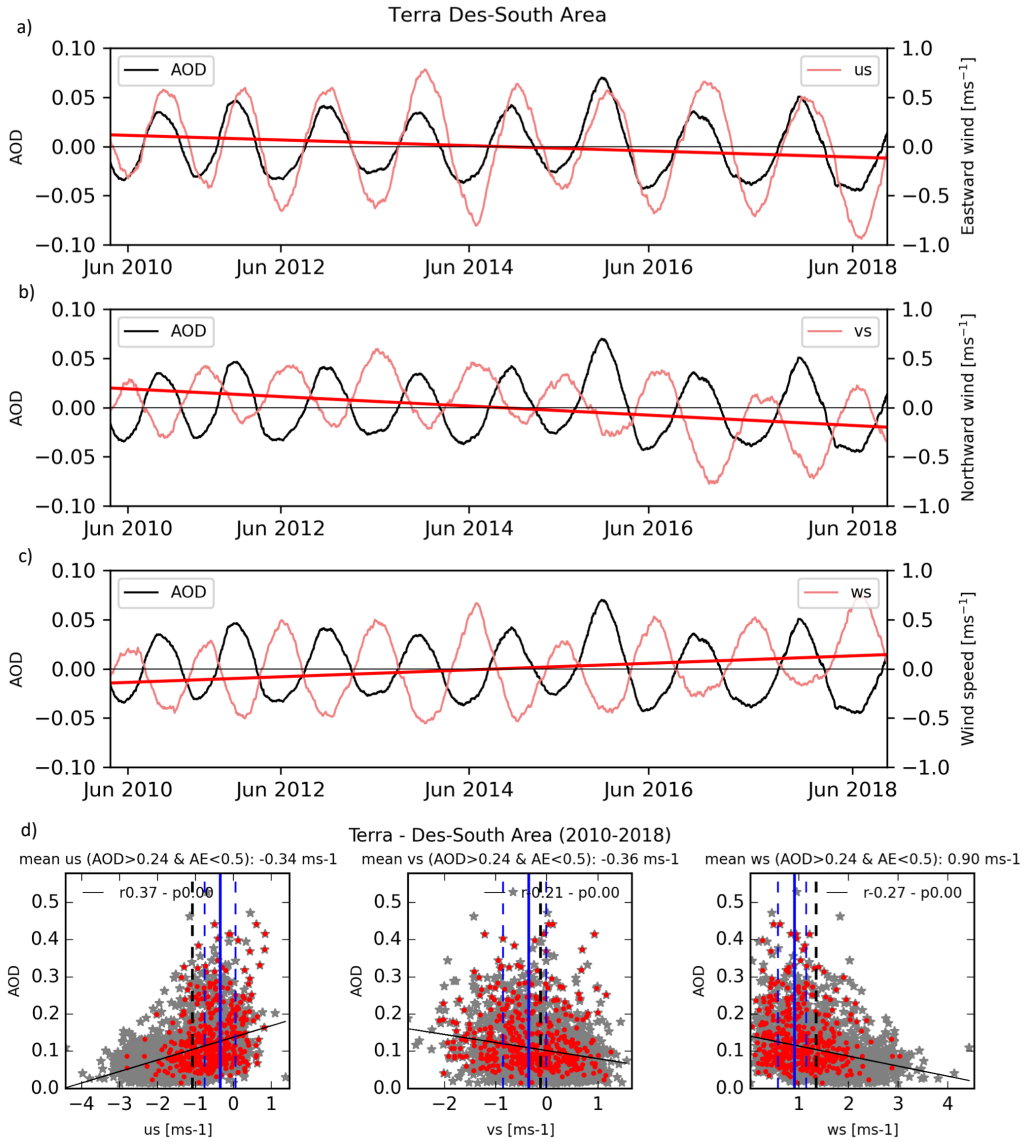

Figure 4.17: AOD from the MCD19A2 dataset compared and wind speed time series sampled from ERA5 at Terra times over the Desert-South area during 2010-2018. (a) Eastward wind component, *us*, (b) Northward component, *vs*, and (c) surface wind speed. The bottom row shows scatter plots between AOD and *us* (left), *vs* (centre) and wind speed (right). Vertical dashed black lines indicate the wind component means for the entire dataset. Vertical solid (dashed) blue lines indicate the wind component means (upper and lower quartiles) for the subset of data with $AOD > 0.2$ and $\alpha < 0.5$ (red stars).

sults in a predominance of E and NE winds ranging from north to south (Fig. 4.19a). However, wind directions at Terra times also show a less frequent west component

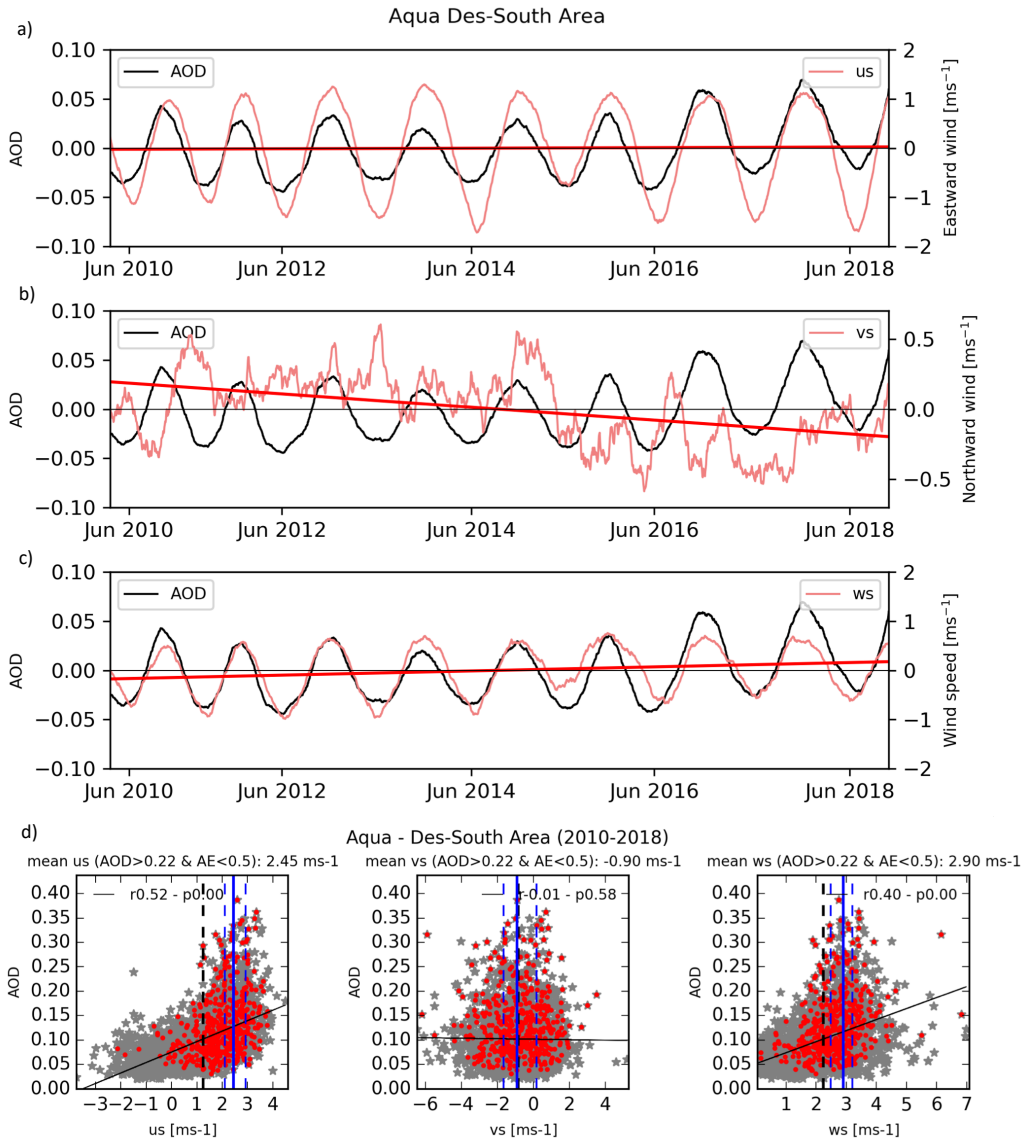

Figure 4.18: AOD from the MCD19A2 dataset compared and wind speed time series sampled from ERA5 at Aqua times over the Desert-South area during 2010-2018. (a) Eastward wind component, *us*, (b) Northward component, *vs*, and (c) surface wind speed. The bottom row shows scatter plots between AOD and *us* (left), *vs* (centre) and wind speed (right). Vertical dashed black lines indicate the wind component means for the entire dataset. Vertical solid (dashed) blue lines indicate the wind component means (upper and lower quartiles) for the subset of data with $AOD > 0.2$ and $\alpha < 0.5$ (red stars).

which also occurs high-AOD events. Conversely, Aqua retrievals exhibit a predominant WNW component with a few observations of NE winds, which is consistent

with the governing afternoon ocean-land flows over the Atacama region and similar to DN area. At Aqua times, coarse events occur predominantly with wind flowing from the NNW with a zonal intensity from 1.5 ms^{-1} and a meridional wind component ranging between 2.0 and -4.0 ms^{-1} (Fig. 4.19,d).

Similar to the results reported for the DN area in Fig. 4.15, at Terra times, the sea breeze effect on mineral dust production is evidenced (Fig. 4.19, bottom). However, no clear evidence is observed during Aqua times of a sea breeze intrusion driving mineral dust production (Fig. 4.19, top). As described in §3.1 the above can be expected as at Aqua times (morning-noon), the sea breeze has not yet fully developed. Unlike the DN area, westerlies from the eastern South Pacific Ocean seem to have an almost null effect on mineral dust production on the DS. The above might be enhanced by local scales cancellations of the positive (eastward) and negative (westward) zonal components when an area average is computed at times when both are present. As described by (Rutllant et al., 2013), late morning and noon are transitional hours from a land breeze to a sea breeze dominance. Also, the more intricate topography in comparison with the DN area (see Fig. 4.7) contributes to a more complex identification of the role that the Sea breeze is playing on dust production at Aqua times in this area (DS).

Consistent with AOD and winds records at Terra times, increasing winds speeds are associated with a decreasing trend of AOD (Fig. 4.20a) and an increasing trend of α (Fig. 4.20b). For the case of AOD subsets in Fig. 4.20, higher aerosols loads are associated to decreasing meridional winds (southward strengthening) and increasing zonal winds (westward weakening). Yet above 0.15 values, AOD does not exhibit a clear trend. Similarly, for α values greater than 0.3, increasing α (from coarse to fine particles predominance) is associated to an increasing of the meridional wind component intensity (southward weakening) and a decreasing of the zonal component (westward strengthening).

For Aqua times in the DS area, the wind speed (solid red line) tend to be modulated mainly by the zonal component (solid grey line) which is one order of magnitude higher than the meridional component (Fig. 4.20b). AOD consistently

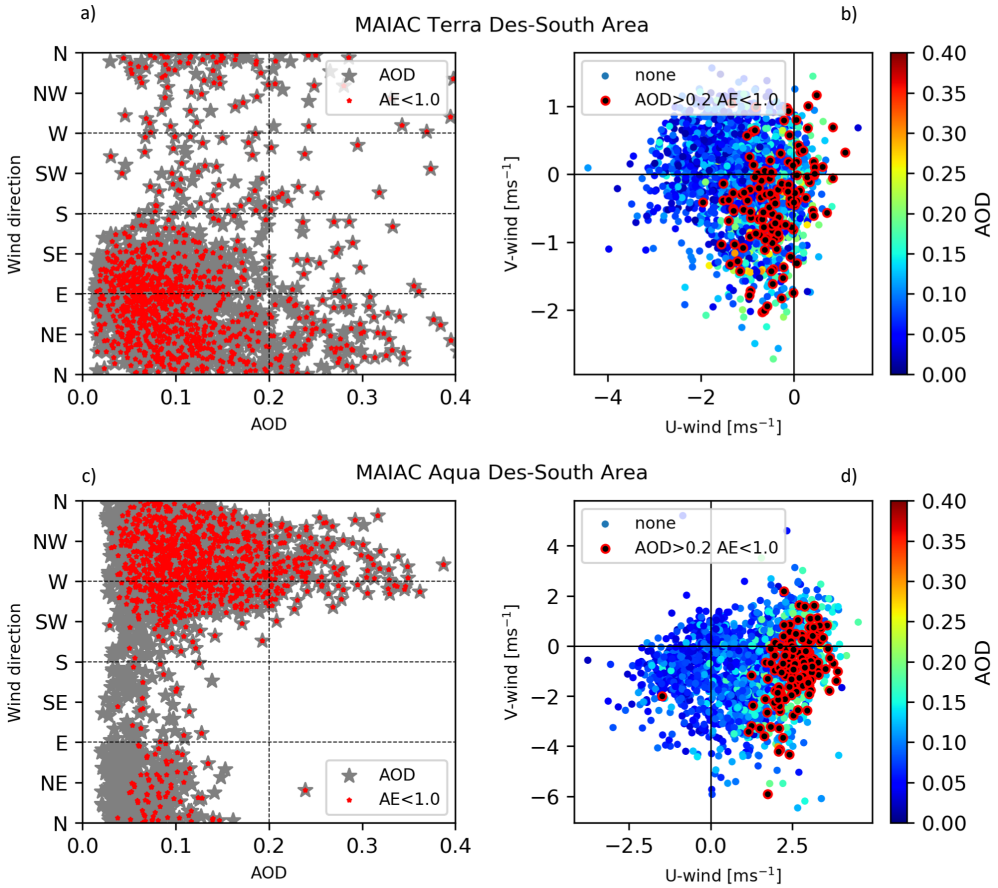

Figure 4.19: MAIAC AOD and ERA5 wind pattern DS. (a) AOD from MCD19A2 and wind direction scatter plot of area-averaged time series over the Desert South area from Terra retrievals during 2010-2018. Red stars depict AOD observations with $\alpha < 1.0$. (b) Wind component scatter plots from Terra with red circles highlighting data with $AOD > 0.2$ and $\alpha < 1.0$. (b) and (d) repeat figures (a) and (c) respectively with Aqua retrievals.

increases as wind speed rises. This is similar to the Aqua times in the DN area (Fig. 4.16). Subsets comprising AOD values greater than 0.2 reproduce higher winds speeds exceeding 2.9 ms^{-1} with a standard deviation range between 2.2 and 3.6 ms^{-1} (Fig. 4.20c). This in contrast with lower AOD subsets (< 0.1) where the mean wind speed declines until values less than 2.2 ms^{-1}. Here, the influence of zonal (solid grey line) and meridional (dashed grey line) is also robust. Whereas zonal wind aligns with wind speed, the meridional wind decreases abruptly for AOD greater than 0.2, reaching values between -0.95 and -1.05 ms $^{-1}$ (Fig. 4.19 b left). The mean wind speed declines progressively as α increases, from coarse to fine dominant

particles distributions (Fig. 4.20b). It ranges between 2.75 and 2.5 ms^{-1} for coarse particles ($\alpha < 1.0$) and between 2.5 and 2.4 ms^{-1} for fine particles ($AE > 1.0$). For the subgroups with the finest average particles the standard deviation range expands considerably towards lower wind speeds, reaching a minimum of 1.5 ms^{-1} ((Fig. 4.20d).

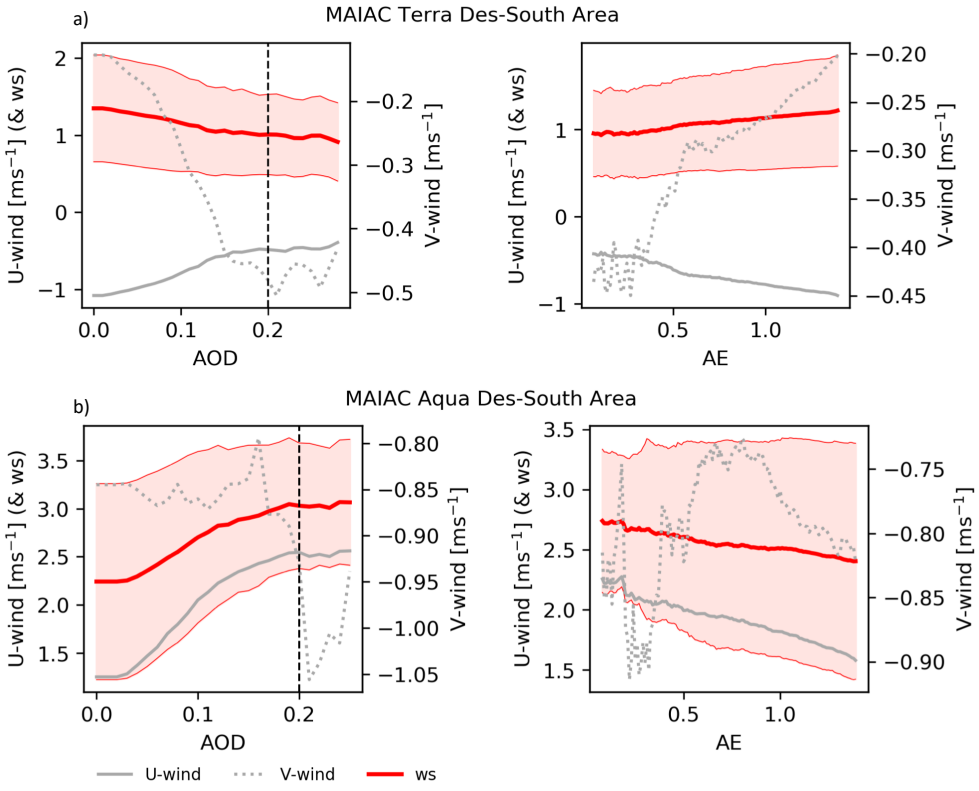

Figure 4.20: Subsets of AOD (left) and α (right) data and wind components over the Desert-South area for Terra (a) and Aqua (b) times. X-axes correspond to lower (AOD) and upper (AE) thresholds used to select the respective datasets from which the winds plotted in axis y were computed. Note the different scales for the zonal (left axes) and meridional winds (right axes). The light red area depicts the one-standard-deviation range from the mean (solid red line) of the wind speed

4.6 Summary and Discussion of Implications

The seasonality of mineral dust and the occurrence of dust events over the Atacama Desert has implications in a range of dimensions such as air quality, solar power generation, and radiative feedback. An increasing trend might provide some theo-

retical counter-balance to the radiative effects of increasing greenhouse gas concentrations, although its actual effect would need to be explored through a modelling approach with a special focus on aerosols composition. In this sense, the results here reported will contribute for future modelling validation and the selection of specific temporal-spatial modelling experiments of interest, such as the study of the events of the summer of 2013 or the unusual activity detected in autumn 2018 (Figs 4.11 and 4.12).

To explore the trends and event characteristics over the past decade, two desert regions were select. Both the desert north and desert south regions showed similar AOD climatologies, but exhibited rather different α values (Fig. 4.5, Tab. 4.3). Although between Terra and Aqua times AOD reached similar magnitudes in both areas, its decadal trend in 2010-2019 varied significantly. At both areas, Aqua retrievals reproduced an increasing trend of AOD, and specially AOD events with lower α values.

The spatial effect of the Eastward and Northward wind components on mineral dust events has been analysed (Figs. 4.15 and 4.19), evidencing a strong link between the diurnal sea breeze and the development of mineral dust events, especially during afternoon hours. As reported in Oyarzún and Brierley (2019), wind speed along the coastal margin of the Atacama Desert is expected to intensify during the 21st Century, which, as discussed in Chapter 6, is connected to an intensification of the South Pacific Anticyclone during the Southern Hemisphere summer. Future work should also explore the impact of considering climatological anomalies.

Table 4.3: AOD mean computed for DN and DS areas

Area-Sat	Annual mean	std	DJF (Su)	MAM (Au)	JJA (Wi)	SON (Sp)
DN-Terra	0.09	0.06	0.13	0.07	0.07	0.12
DN-Aqua	0.10	0.06	0.15	0.08	0.07	0.10
DS-Terra	0.10	0.07	0.14	0.08	0.07	0.13
DS-Aqua	0.10	0.06	0.14	0.08	0.07	0.13

The mineral dust dynamics over the Atacama Desert described in this chapter play a role in determining air quality. It has been suggested that the daily varia-

tion of aerosol vertical structure (Van Donkelaar et al., 2010; Altaratz et al., 2013; Crumeyrolle et al., 2014) and the influence of increased relative humidity at a day-to-day basis (Lee et al., 2011; Nordio et al., 2013) also play roles. Observations from Calama city (Cal in Fig. 4.3) can be used to explore these factors relative importance. Coarse particulate matter concentration has been computed as the difference between PM_{10} and $PM_{2.5}$ levels (Fig. 4.21). The Calama site is described in Section 3.4 and is compared to the satellite derived aerosol optical depths. It is noticeable that at Terra times there is little match between both datasets (Fig. 4.21a), but there is a moderate correlation (r=0.49) at Aqua times (Fig. 4.21b). This seems reasonable as at Terra times eastward winds are less intense, and easterlies are sometimes also present. Therefore, there is no predominant wind flow to Calama from the major mineral dust sources detected in the central desert zone of the Antofagasta region (Fig. 4.3). Also, the more significant urban signal might not be properly captured by the coarse-resolution of the satellite, which might contribute to the discrepancy. Also, at Terra times, relative humidity is higher, and the hygroscopic growth might play a more significant role than during the dryer hours of the afternoon (Aqua).

Even though natural dust represents a severe threat to air quality and human health at local scales (Sassen et al., 2003), quantitative studies analysing the connection between natural mineral dust and a worsening of air quality are scarce, even for the major sources worldwide (Florence et al., 2010). Therefore, a logical future extension of this research would be to carry out experiments with a chemical transport model to assess the anthropogenic forcing and expand the analysis to the entire daily cycle. At a larger time scale, the implications of climate change on both natural dust and PM_{10}-$PM_{2.5}$ over the Atacama Desert are discussed in Chapter 6.

Finally, South America contains some excellent sites for solar energy production. The Atacama Desert is particularly suited to generation, because of the extremely high solar irradiance reaching the surface. In fact, the Atacama Desert houses the site with the highest solar irradiance on Earth (Rondanelli et al., 2015; Molina et al., 2017). In this region, photovoltaic (PV) power capacity increased

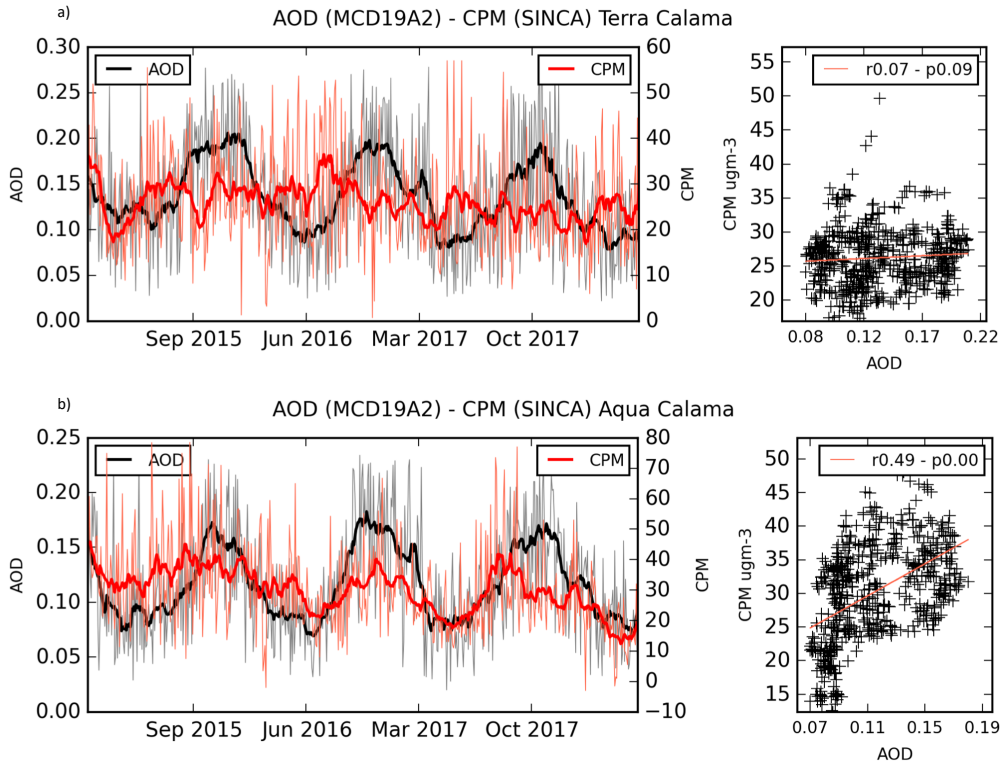

Figure 4.21: Coarse PM observed at Calama and AOD from the MCD19A2 dataset for Terra (upper) and Aqua (lower) times.

from 3.6 MWp in 2012 to 1.8 GWp in 2017 (Cordero et al., 2018) – comprising about the 70% of PV plants installed in South America Gil et al. (2020). Dust accumulation on photovoltaic panels, or 'soiling', leads to reflectance degradation and reduces the lifespan of PV cells due to overheating and shading (Sarver et al., 2013; Shi et al., 2020). Most research during the 20th Century considers exposure length as a fundamental factor reducing output power (Sarver et al., 2013). However, laboratory experiments by El-Shobokshy and Hussein (1993) revealed that dust nature, such as dust composition and particle size distribution, significantly impact energy production from PV cells. Wind tunnel experiments (Goossens et al., 1993) suggested that wind speed and the orientation on a PV cell impact dust deposition and distribution, a finding later supported in the field (Hammond et al., 1997). Also, changes in dust optical properties (Michel Flores et al., 2012; Chen et al., 2019) lead to increasing dry deposition rates (Mohan, 2016). Given current and massive

future deployment of solar power generation combined the impact dust has on its efficiency, understanding the dynamics of mineral dust in the Atacama Desert is an important subject and this chapter provides some of the first insight into it.

Chapter 5

Atmospheric Ventilation and Particulate Matter Variability

Poor air quality is usually associated with high emissions, either natural or anthropogenic, and weather conditions promoting increasing levels of air pollutants (Jacob and Winner, 2009). Once pollutants are emitted to the atmosphere, their transport, dilution and concentration are directly conditioned by the meteorological conditions they experience. Depending on the nature of the contaminant, the environmental conditions may force it to rapidly settle out or remain aloft for a long time. Among the several aspects that have to be taken into account to understand the meteorological conditions governing air pollution, it is fundamental to consider the temporal and spatial scales involved (Appelhans et al., 2013).

This chapter introduces the fundamentals of climate and meteorology that impact particulate matter concentration and its transport by providing a review of the relevant academic literature. Following a description of the relevant methods, the atmospheric ventilation over the Atacama Desert is analysed from ground-level and upper observational records and four gridded datasets. The fourth section analyses the relationship between the ventilation conditions and observed surface levels of particulate matter ($PM_{2.5}$ and PM_{10}). The role of atmospheric stagnation and its connection is then discussed in relation to both atmospheric ventilation and particulate matter events. Finally, a statistical model is created that has potential to predcit extreme PM events in the coastal city of Antofagasta.

5.1 Boundary Layer Meteorology

5.1.1 The Planetary Boundary Layer

The Planetary Boundary Layer (PBL) is the lower layer in the Troposphere directly influenced by the earth's surface, and it responds to earth forcings such as evaporation and transpiration, heat transfer, air pollution, and topography (Stull, 1988). The PBL is a transition region between the earth's surface and the free Troposphere. In this layer, the atmospheric flow is governed by strong turbulence, which leads to small-scale exchanges of momentum, heat and moisture (Deardorff, 1972; Beljaars, 1992; Zhang et al., 2015). This usually turbulent layer is also considered the mixed layer where air pollutants are vertically dispersed (Benkley and Schulman, 1979; Garrat, 1992).

Due to the small spatial scale, or sub-grid scale, where these phenomena occur, the PBL is usually parametrised and diagnosed in climate models through the so-called PBL schemes. As described by Zhang et al. (2015), PBL schemes are classified into two categories: local and non-local schemes. In local schemes, the vertical fluxes are linked to local parameters, such as potential temperature or wind gradients. Due to their nature, they fail to capture non-local transport (Stull, 1988). On the other hand, non-local schemes take into account large-scale non-local motions that develop, for instance, under strong convective conditions. Also, these last schemes are more suitable for simulating wind shear turbulence under stable conditions (Xie et al., 2012).

A typical parameter to characterise the PBL is the Richardson number (R_i), an indicator of both atmospheric turbulence and stability. This number is the ratio between an stability parameter s (rate at which stability suppresses turbulence) and the turbulence generated by mechanical shear forces at a rate proportional to $(\partial\bar{u}/\partial z)^2$ (Schnelle, 2003) (Eq. 5.1).

$$R_i = \frac{s}{(\partial\bar{u}/\partial z)^2} \tag{5.1}$$

A strong negative Richardson number indicates strong vertical motion and un-

stable atmospheric conditions. On the contrary, strong positive values indicate stable conditions where convection is weak, and mixing ceases. Neutral conditions are given by a Richardson number close or equal to zero. The height of the PBL (PBLH) varies significantly in time and space, from hundreds of meters to a few kilometres (Stull, 1988). PBLH is usually computed through the bulk Richardson number, which corresponds to the Richardson number of an atmospheric layer from the surface to a given height (Holtslag and Boville, 1993; Zhang et al., 2015).

5.1.2 The Ventilation Coefficient

Temperature inversions play an important role in pollutant dispersion, because they result in stable atmospheric conditions that prevent mixing penetrating through them. One type of inversion, normally taking place at a few hundred meters height, is produced by the radiative cooling of the surface during nighttime associated with slow wind speeds (Benkley and Schulman, 1979; Marshall and Plumb, 2008). For instance, Ji et al. (2012) found a close relationship between PM_{10} and $PM_{2.5}$ concentrations with both low wind speeds and low heights of the temperature inversion over Beijing. Several atmospheric pollution episodes were reported in the San Joaquin Valley in California associated with a shallow mixed layer tapped by a temperature inversion (Zhao et al., 2011b,a). Another type of temperature inversion is the so-called ”trade-wind” inversions, which is common in subtropical regions in the Northern and Southern hemispheres (Marshall and Plumb, 2008), such as California (Zhao et al., 2011b), and the coast of the Atacama Desert in Northern Chile (Schulz et al., 2011; Muñoz et al., 2011; Rutllant et al., 2013; Muñoz et al., 2016). The base of these inversions are often found between 0.4 and 2.0 km height, being usually persistent due to the descending Hadley Cell warmed adiabatically – see §3.1 for more details. The strong role of subsidence associated with the global meridional overturning circulation results in many subtropical areas experiencing high pollution levels (Marshall and Plumb, 2008).

Variations in the mixed layer combine with the impacts of winds (as analysed in Chap. 4) to influence air quality. To quantify these influences, Kassomenos et al. (1995) defined a ventilation coefficient (VC, m^2/s) as a proxy of the efficiency of

the atmosphere to disperse pollutants. VC is computed as the product between wind speed within the mixing layer and mixing height. As argued by Zhao et al. (2011a) for their application of VC, a sensible simplification is to consider the product of surface wind speed (ws,m/s), commonly at 10 m height above the surface, and the boundary layer height (BLH,m). This simplification has benefits arising from the sparsity of reliable upper observations across an area of interest and models' vertical resolutions.

$$VC = ws \times PBLH \tag{5.2}$$

Higher values of VC indicate more ventilation capacity of the lower Troposphere. Therefore, lower wind speeds reduces the ventilation of the atmosphere, as does lowering boundary layer height. The ventilation coefficient was conceived to track the temporal behaviour of ventilation over a given area (Kassomenos et al., 1995). Pielke et al. (1991) extend this by showing that a single hour can be considered as unvented when the resultant VC value is less than $6,000 m^2 s^{-1}$, as originally suggested by Holzworth (1972). This threshold has been applied in a variety of global settings, such as the United States (Trail et al., 2013) and China (Huang et al., 2018).

Zhao et al. (2011a) calculated the VC throughout the pollution season in California (summer and spring) - a coastal climate environment sharing some similarities with the situation of the Atacama Desert (§3.1). They found air pollution levels are strongly linked to stagnant conditions and low boundary layer heights. In addition to the complex topography, a key factor influencing the poor air quality in California is the marine boundary layer given by a temperature inversion layer along shore formed by the subsiding hot air linked to the Pacific Subtropical High (PSH). Additionally, the cold Sea Surface Temperature (SST) associated with coastal upwelling inhibits convection, enhancing this atmospheric dynamics (Zhao et al., 2011b). Similar coastal dynamics influencing air pollution events were described for the Attica Peninsula, Greece, by Nester (1995) and Melas et al. (1995). Also, for the northern coast of Chile, along the Atacama Desert, similar ocean-

atmosphere interactions have been described (Schulz et al., 2011; Muñoz et al., 2011; Rutllant et al., 2013; Oyarzún and Brierley, 2019). Despite the similarity in prevailing ocean-atmospheric conditions, it has not yet been explored whether similar the connections between the boundary layer meteorology and pollution levels measured in several urban settlements occur in the Atacama Desert.

Atmospheric ventilation also has direct implications on the radiative balance (Yang et al., 2019). The anomalous atmospheric composition changes observed in the upper troposphere and lower stratosphere (UTLS) region over South Asia is directly connected to the time of residence of air masses and their transport from the Iranian and Tibetan Plateaus. This is itself primarily driven by the ventilation conditions over these two emission sources (Yang et al., 2019).

5.1.3 Atmospheric Stagnation

Several studies argue that wind speed, wind direction, temperature, precipitation, humidity, sea breeze, cloud cover, convection and mixed layer height directly impact air pollution levels (Holzworth, 1967; Kassomenos et al., 1995; Nester, 1995; Melas et al., 1995; Jacob and Winner, 2009; Tai et al., 2010; Zhao et al., 2011b; Dawson et al., 2014). Some variables may predominate over others in certain areas due to multiple factors. High pollution episodes have often been associated with atmospheric stagnation, especially for Particulate Matter (PM) and ozone (O_3) pollution events (Jacob and Winner, 2009; Horton et al., 2012; Trail et al., 2013). A stagnation event occurs when the lack of atmospheric ventilation and reduced dispersion given by low wind speeds at the low troposphere is combined with low precipitation rates (Horton et al., 2012). An established indicator for atmospheric stagnation is the daily-basis National Climatic Data Center (NCDC) Air Stagnation Index (ASI) based on the thresholds defined by Wang and Angell (1999). ASI defines stagnation events if; 1) the daily mean of both wind speed at 500 hPa and 10 m above the ground is less than 13.0 m/s and 3.2m/s, respectively, and 2) the total precipitation during the day is less than 1.0 mm. In addition, Wang and Angell (1999) proposed a stagnation episode if these conditions occur for four consecutive days. This consideration can be relaxed by 10 % if a temperature inversion layer

is present below 850 hPa. However, Dawson et al. (2014) discarded this last criterion considering it only appropriate for multi-day warm weather stagnation events. Pollution events in Chicago take place during cold days in the presence of stagnation and low mixed and temperature inversion heights. However, in Birmingham (Alabama), the relationship with surface temperature is not evident, and pollution events are mostly attributed to stagnant conditions under the presence of a low-temperature inversion layer (Dawson et al., 2014). In addition to its application in understanding air quality levels, ASI has also been used as a measure of potential air quality in areas with significant emissions and absence of monitoring, usually with a low density of population (Horton et al., 2014).

The meteorological dependence of air pollution is not trivial to describe. This since the varied response of the different air pollutants to meteorological conditions (Horton et al., 2014). Tai et al. (2010) applied multiple linear regression (MLR) methods to deseasonalised $PM_{2.5}$ and meteorological time series across the USA. Although temperature, precipitation, circulation and relative humidity explained about the 50% of $PM_{2.5}$, different signs of correlation were computed for different places and particles components, namely nitrate, sulfate, and organic and elemental carbon. Precipitation was the only variable negatively correlated with all the components. However stagnation events led consistently to higher $PM_{2.5}$ concentrations, in agreement with Jacob and Winner (2009) and Horton et al. (2014). Despite Tai et al. (2010) and other studies demonstrating the potential of using ASI, its application is still scarce. Horton et al. (2014) estimated ASI at a global scale from the CMIP5 dataset. However, as the authors pointed out, this index excludes fundamental air pollutant dispersion factors, such as temperature inversions and topography. These factors are of particular relevance when analysing areas where natural emissions are important. The Atacama desert, where mineral dust production is associated with higher wind speeds (§4.6) is one such potential region. Nonetheless in urban areas (where pollution monitoring stations are often sited), stagnation driven by low wind speeds might lead to enhanced accumulation of pollutants other than dust which are emitted by anthropogenic sources.

The analysis of stagnation events based on ASI is a measure of stagnation episodes at synoptic scales (Horton et al., 2012). Therefore, this approach has been mainly applied at continental (Wang and Angell, 1999; Leibensperger et al., 2008; Tai et al., 2010) or global scale and coarse spatial resolutions from General Circulation Model (GCM) simulations (Horton et al., 2012). Horton et al. (2014) used ASI to analyse the response of stagnation events under global warming globally. The study concluded that the frequency of stagnations events would increase by 55% in populated areas, with the highest increments in the tropics and subtropics, where stagnation days may rise in 40 days per year (Horton et al., 2014). Despite the coarse resolution of that analysis potenitally missing the influence of local-scale factors like topography, the connection between synoptic climate and air pollution events in populated areas highlight the possibility of changing air quality under climate change.

5.1.4 The Role of Anticyclones and Climate Modelling

The causes of worsening air pollution can be non-trivial to determine as they can arise from increased anthropogenic emissions, unfavourable climate-meteorological factors and/or interactions feedbacks between them (Ji et al., 2012). Several studies have analysed synoptic influences, particularly pressure systems, to learn more about air quality (McGregor and Bamzelis, 1995; Makra et al., 2006; Cheng et al., 2007; Chen et al., 2008; Kuo et al., 2008; Appelhans et al., 2013; Ji et al., 2012; Tai et al., 2012). High-pressure systems promote stagnant conditions because of their weaker winds (especially at the edges), associated atmospheric stability, and their longer residence over a given area. In contrast with low-pressure systems lead to more turbulence and instability. Chen et al. (2008) found strong correlations between PM_{10} pollution events in Northern China and synoptic pressure patterns. Appelhans et al. (2013) found that anticyclones over New Zealand are a dominant control factor of air pollution using classification and regression tree techniques. McGregor and Bamzelis (1995) applied principal component analysis to identify strong connections between continental anticyclonic air masses and high pollution episodes over the UK, whilst marine cyclones were associated with low pollution

events. Tai et al. (2012), also using principal components and multiple linear regression, identified a strong positive correlation between less frequent frontal ventilation and $PM_{2.5}$ concentrations in the eastern USA. Makra et al. (2006) applying statistical analysis identified a connection of the anticyclone over the Carpathian Basin with phases of high pollution in Hungary. Combined, these studies suggest that reduced atmospheric ventilation linked to the influence of a high pressure system, such as the South Pacific Anticyclone (SPA), are expected to exert a negative effect (increase) on PM concentration levels. The above has been unexplored for northern Chile.

The study of anticyclones is usually carried out using General Circulation Models (GCM, see §2.5.1 for a description). However, GCMs and their coarse resolution have difficulties representing local dynamics, especially over complex terrains. Regional Climate Models (RCM, see §2.6) have been described as a suitable tool for simulating processes at these scales (Bozkurt et al., 2019). Trail et al. (2013) used the WRF model to dynamically downscale the NASA GISS model E2 earth system to a $12x12km$ horizontal resolution for a better representation of atmospheric stagnation, ventilation and precipitation conditions linked to increasing ozone concentrations. Precipitation is one of the fundamental meteorological variables governing air pollution levels and directly impacts the stagnation conditions of a given area (Horton et al., 2012). However, coarse climate models can exhibit systematic biases on precipitation arising of poor representation of topography, especially at coarse scales (Rojas, 2006).

5.2 Methods

5.2.1 Modelled Atmospheric Ventilation

The Ventilation Coefficient (Kassomenos et al., 1995) and the Air Stagnation Index (ASI), based on Wang and Angell (1999) thresholds, were computed from modelling (modelled VC and ASI) and observational datasets (observed VC and ASI) on a daily basis. In the case of modelled VC and ASI these were computed from the gridded outcomes summarised in Tab. 5.1 throughout the Evaluation simu-

lation experiment (1981-2010). These datasets correspond to outcomes from three Regional Climate Models (WRF341lI-SAM44, RegCM4-SAM44, RegCM4-CL09) forced by the ERA-Interim reanalysis and gridded data from the ERA5 reanalysis (Copernicus, 2017). These datasets, as well as the selected Evaluation experiment, are described in Chapter 2.

Table 5.1: Gridded (RCMs and reanalysis) Datasets Used in this Study

Dataset	Institution	Driving Dataset	Horizontal. Res. (°Lat x °Lon)	Experiment	t freq.	Ref.
WRF341I-SAM44	Universidad de Cantabria (UCAN). Contributing to CORDEX dataset	ERA-Interim	0.44 X 0.44	Evaluation (1979-2011)	daily	Skamarock et al. (2008); Katragkou et al. (2015); Manzanas et al. (2018)
RegCM4-SAM44	Center for Climate and Resilience Research (CR)2	ERA-Interim	0.44 X 0.44	Evaluation (1980-2015)	daily	Bozkurt et al. (2019)
RegCM4-CL09	Center for Climate and Resilience Research (CR)2	RegCM4-SAM44	0.09 X 0.09	Evaluation (1980-2015)	daily	Bozkurt et al. (2019)
ERA5 Reanalysis	European Centre for Medium-Range Weather Forecasts (ECMWF)	-	0.28 X 0.28	(1980-2018)	hourly	Copernicus (2017)

5.2.2 Observed Atmospheric Ventilation and Particulate Matter

Observed VC and ASI index were computed from the observational records summarised in Tab. 5.2. These comprise of observations of meteorology and air quality (PM_{10}, $PM_{2.5}$) from Chile's National Air Quality Information System (SINCA). Three ground monitoring sites exist along the coast of Northern Chile (Iquique, To-

copilla and Antofagasta) and a further two situated on inland at Sierra Gorda and Calama (§2.2.1). Since meteorological records in the SINCA network usually have a shorter temporal coverage than particulate matter (PM_{10} and $PM_{2.5}$), these have been supplemented with meteorological observations from two ground monitoring sites (Antofagasta and Calama) operated by Chile's Meteorological Service (DMC).

Upper air observations of wind speed at 500 hPa, as well as the height of the base of Temperature Inversion Layer (TILH) along the coast of Northern Chile were computed from radiosondes launched daily at 12:00 UTC from the Cerro Moreno station, north of Antofagasta city. When calculating the ventilation coefficient, the inferred TILH was used as an approximation of BLH over the area (as suggested by Schulz et al., 2011). More details of the TILH estimation and the radiosonde dataset employed are presented in Chapter 3, where its variability and its significance for the climate dynamic of the Atacama Desert are discussed.

Table 5.2: Observational datasets used in this study. ws: surface wind speed, wd: surface wind direction, T: surface temperature, AP: surface atmospheric pressure, RH: relative humidity, ws500: wind speed measured at 500 hPa, TILH: temperature inversion layer height computed as described in §3.2. Wind speed (ws) was computed from the native variables us (zonal component of the wind) and vs (meridional component of the wind) in each gridded dataset. SINCA, DMC and Cerro Moreno datasets are described in §2.2 and §2.3.

Dataset	Variable	Site	Period
Chile's National Air Quality Information System (SINCA)	PM_{10}	Antofagasta (Ant)	2013-2019
		Escuela E-10 (Toc)	2011-2019
		Estacion Centro (Cal)	2013-2019
		Sierra Gorda (SG)	2012-2019
	$PM_{2.5}$	Antofagasta (Ant)	2013-2019
		Escuela E-10 (Toc)	2011-2019
		Calama (Cal)	2012-2019
		Sierra Gorda (SG)	2012-2019
		Alto Hospicio (Iqu)	2016-2019
	ws	Escuela E-10 (Toc)	2011-2019
		Sierra Gorda (SG)	2012-2019
		Alto Hospicio (Iqu)	2016-2019
Chile's Meteorological Service (DMC)	ws,wd,T,RH,AP	Cerro Moreno (Ant)	1950-2018
		Calama	1950-2018
Atmospheric Soundings, Uni. Wyoming	ws500, TILH,	Cerro Moreno (Ant) (12:00 UTC)	1973-2018

All meteorological datasets from SINCA and DMC were obtained at hourly time-frequency, from which the daily means were computed. The calculation of VC and ASI index, both daily metrics, were calculated from the daily averaged observations. Daily means were only calculated for days with at least 75% valid data (i.e. with at least 18 hours of data available). Similarly, monthly means computed for the analysis of long-term relationships between particulate matter and VC were calculated for months having at least 75% of valid data (at least 22 days available). Particulate Matter observations (PM_{10}, $PM_{2.5}$) were obtained from the SINCA website as daily means.

Two areas were defined for area-averaged time series computation in order to analyse atmospheric ventilation and BLH temporal trends from gridded datasets – coastal and inland desert regions (Fig. 5.1). As the atmospheric boundary layer height governs ventilation along with wind speed these two areas may be expected to experience different conditions. The areas contain the three coastal and two inland ground monitoring sites of particulate matter from SINCA and DMC indicated in Tab. 5.2.In the case of the Coastal desert area (CD) (19.5°S to 45.5°S and 69.8°W to 70.8°W), the atmospheric boundary layer is directly influenced by the TILH, and wind patterns are primarily modulated by the direct effect of the South Pacific Anticyclone (SPA). On the other hand, in the Inland Desert area (ID) (19.5°S to 45.5°S and 68.8°W to 69.8°W), temperature inversions are governed by radiative effects and the orography, which also modulates local winds patterns..

5.2.3 Logistic Regression

Classification methods are a fundamental subgroup of techniques within machine learning and data analysis. Logistic regressions allow for the targeting of two-class classification problems from multiple independent variables. Therefore the outcome is dichotomous and numerically correspond to a probability of occurrence of a binary event, p. Its mathematical expression is based on the Sigmod function (Eq. 5.3) applied on a multiple linear regression (Eq. 5.4).

$$p = \frac{1}{1 + e^{-y}} \tag{5.3}$$

$$p = \frac{1}{1 + e^{-(\beta_0 + \beta_1 X_1 + \beta_2 X_2 ... + \beta_n X_n)}} \tag{5.4}$$

Due to its nature, the dependant (target) variable in the logistic regression follows the Bernoulli distribution, and its parameters can be calculated by the Maximum Likelihood Estimation (MLE) method. Therefore, there is no fitness assessment through r values. If the outcome from the logistic function (Eq. 5.3) is greater than 0.5 (probability equal to 50%), the result can be classified as 1 (True), otherwise is 0 (False).

The logistic regression method was applied to pollution events in the city of Antofagasta based on observational meteorological and PM data. An extreme event was defined as the daily mean of PM ($PM_{2.5}$ or PM_{10}) exceeded the 80^{th} percentile. This limit seems reasonable since the values obtained for both $PM_{2.5}$ (16 μgm^{-3}) and PM_{10} (46 μgm^{-3}) lies within the latent range for the annual mean policy for both contaminants. As explained in 3, the term 'latent' in Chilean normative means the range between 80 and 100% of the normative threshold, meaning a potential risk for human health. Additionally, a sensitivity test was performed considering thresholds between percentiles 60 to 95.

Three experiments were carried out using different sets of input variables, as presented in Tab. 5.3. The first one (Exp1) considers the VC as part of the independent variable list along with other meteorological variables. The second one (Exp2) considers VC and ASI index as independent variables. The third experiment (Exp3) comprises only the meteorological variables listed in Tab. 5.3. The models were fitted using a training dataset corresponding to 75% of the data, with the performance of the resulting model assessed using the remaining 25% of the data. The models were assessed using the metrics of accuracy, precision and recall, as well as plotting the Receiver Operating Characteristic (ROC) (depicting true positive against the false positive rates), and the confusion matrix (which summarises true and false

positives along with true and false negatives). ROC curve is a measure of the classification performance, and the area under this curve (AUC-ROC) is used to measure the performance of the prediction (Marzban, 2004).

A regularisation technique was carried out, which penalises large weight coefficients to reduce overfit and peculiarities from the training dataset. This technique is known to improve performance on unseen data. Initially, all models were fitted without regularisation and then the method was applied. In all cases, a better fit to the evaluation data were achieved.

Table 5.3: Observational datasets used for logistic regression experiments (Exp1, Exp2 and Exp3). wd: surface wind direction, T: surface temperature, AP: surface atmospheric pressure, RH: relative humidity

Experiment	Atmospheric Ventilation Features	Other Meteorological Features
Exp1	VC	T,RH,AP,wd
Exp2	VC,ASI	T,RH,AP,wd
Exp3	-	T,RH,AP,wd

Wind direction was discretised to the four cardinal points. Also stagnation days were included as dummy variables, set as 1 when a day was stagnant under ASI criteria or 0 when not. Additionally, weekdays and weekend days were also incorporated as dummy variables to indirectly distinguish behaviours potentially linked to non-natural emissions and governed by intra-weekly cycles, such as urban transport. All variables were normalised prior to computation.

5.3 Atmospheric Ventilation over the Atacama Desert

The daily Ventilation Coefficient (VC) was computed from surface wind speed and boundary layer height for the ERA5 reanalysis and the three RCMs (Tab. 5.1). Surface wind patterns (wind speed and direction) over northern Chile are primarily governed by the South Pacific Anticyclone (SPA) at synoptic spatial-time scales (see §3.1). At local scales, the effect of the SPA is still significant across coastal areas. However, as discussed by Muñoz et al. (2013), over inland desert regions, the surface windspeed is primarily modulated by topography (Fig. 5.1), with higher windspeeds over the relatively flat areas of the central desert.

The four different datasets produce broadly similar patterns of wind speeds (Fig. 5.1). Over the ocean the wind speed spatial distribution and magnitude match relatively closely in WRF341I and ERA5, with the higher resolution RegCM4-CL09 show similar features but with additional fine scale details. Although RegCM-SAM44 simulates this same pattern polewards of 23°S, to the North the wind speeds are damped in comparison to by up to 3 ms^{-1} (Fig. 5.1).

Some large variation in wind speed from the four datasets is seen over land (Fig. 5.1). In relatively flat inland desert areas between 20 and 24 °S, the three models and the ERA5 reanalysis reproduce similar wind speeds between 1 and 3 ms^{-1}. The finer RegCM4-CL09 simulates a confined region with significantly higher velocities to the North of Calama – something which is smeared out in the coarser RegCM4-SAM44 dataset. For this area of complex topography RegCM4-CL09 simulates wind speeds as strong as at the top of the Andes.

Overall, the spatial distribution of wind speeds seen in the ERA5 over the Northern Atacama region (18-24°S) agrees with the modelled datasets presented here (Fig. 5.1). Differences emerge as one heads up into the Andes. Although resolution clearly affects the spatial pattern of wind speed, all models simulate relatively higher values in the Andes, especially over the Altiplano (Andean region at 18-20°S), where altitudes reach a mean of 3,800 m above sea level (Fig. 5.1). This is less evident in WRF341I, but still the model reproduces higher wind speeds associated with easterly wind anomalies in the middle and upper troposphere, which favour moisture transport from the east (Vuille, 1999). Intense dust storms have been described over this area (Gaiero et al., 2013). This pattern is only weakly seen in the ERA5 reanalysis and few differences in wind speed magnitude are observable between the Andean region and the central desert (Fig. 5.1d).

Over the Southern region of the Atacama Desert (24-28°S), where complex topography predominates, the three regional climate models show higher velocities above the Andes (bottom right of Fig. 5.1a,b,c). This pattern is not seen in ERA5, which seems less sensitive to the differences in topography and altitude.

The performance of models in surface wind speed simulation was assessed

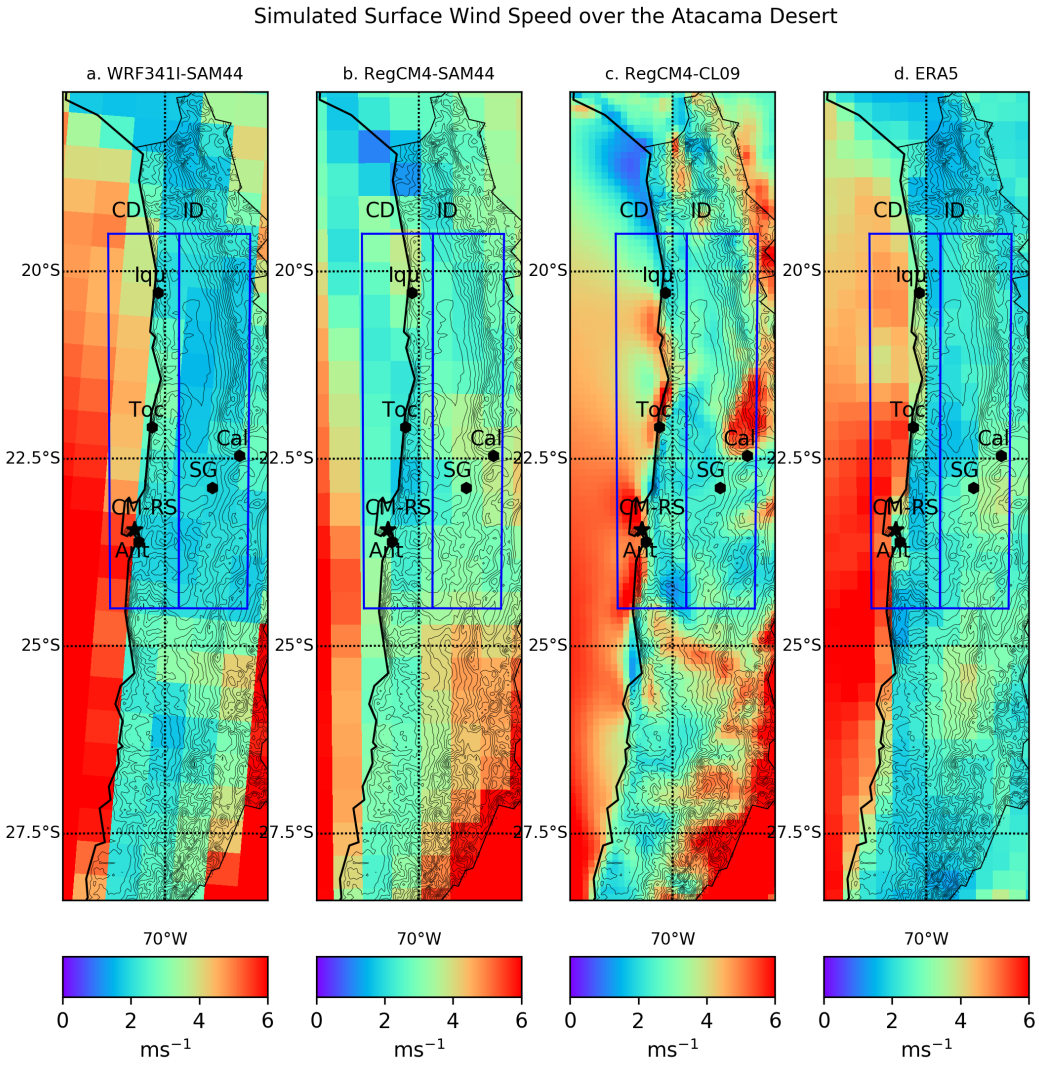

Figure 5.1: Decadal mean (2010-2019) of the surface wind speed computed from (a) WRF341I-SAM44, (b) RegCM4-SAM44, (c) RegCM4-CL09, and (d) the ERA5 Reanalysis. The black star denotes the location of the Cerro Moreno radiosonde site (CM-RS). Black dots depicts the SINCA ground monitoring sites at Antofagasta (Ant), Tocopilla (Toc), Iquique (Iqu), Sierra Gorda (SG) and Calama (Cal). Black contour lines represent topography at 250 m vertical resolution.

against observational records from Cerro Moreno (Antofagasta, coast) and Calama (inland) sites belonging to the DMC network (Fig. 5.2). These sites were chosen because they have more wind speed observations than those available from the SINCA sites (Tab. 5.2). At both locations, the four products underestimate monthly means of wind speed (Fig. 5.2). At the coastal site of Cerro Moreno, the observa-

tional record depicts consistent wind of 3.6 ms^{-1} (25-75% range of 3.4–3.9 ms^{-1}), which is at least 1 ms^{-1} faster than all the products. In this area, all models capture the monthly variations in wind speed, with r values greater than 0.5, except for RegCM4-SAM44 whose r value was 0.37. The higher resolution version of this same model (RegCM4-CL09) both correlates better with the observations (r=0.55) and produces wind speeds closer to those observed. Although WRF341I-SAM44 preforms best of the 3 RCMs on monthly correlations, it underestimates the mean wind speed the most. ERA5 reproduces well both the interquartile amplitude and variability (r=0.65), but has systematically simulated 1 ms^{-1} slower than observations. Over this area, the wind pattern is directly modulated by the SPA, occasional low-pressure systems intrusions and the sea-land flow (see §3.1). As the role of topography is less predominant is reasonable to expect that models perform reasonably well. Indeed, over the ocean region of the coast of Antofagasta, the CMIP5 dataset has been found to behave with a certain agreement, and no significant differences have been found between coarse and fine resolution climate models (Oyarzún and Brierley, 2019). Despite this, when compared with a single ground monitoring site directly governed by boundary layer effects, the local topography can play a crucial role. The disagreement between models and the observational dataset does not necessarily indicate poor model performance at larger spatial scales. In addition, this coastal site (Antofagasta) is located in a land-ocean transition where several coastal phenomena take place, such as convective transport of moisture. These processes are parameterised within the model at multi-kilometre horizontal scale. Hence, their local effect is not dynamically computed.

Over the inland region of Calama, the complex topography provides an additional challenge for modelling performance. In fact, none of the three climate models (WRF341l-SAM44, RegCM-SAM44 and RegCM-CL-09) captured surface wind speed variability (Fig. 5.2). In contrast, ERA5 reproduced a similar spread of wind speeds (an interquartile range of 0.7 ms^{-1}) to observations, but with a robust offset in magnitude. The ERA5 wind speeds exhibit an r-value that is considerably lower to that computed for Cerro Moreno (r=0.39). The horizontal resolution of

ERA5 is still coarse for local analyses in the complex topography of Calama, it provides a finer-scale output than WRF341I-SAM44 and RegCM-SAM44 (Tab. 5.2). The even finer output from the 10-km resolution RegCM-CL09 might suffer from the resolution-related uncertainties of its forcing ERA-Interim dataset.

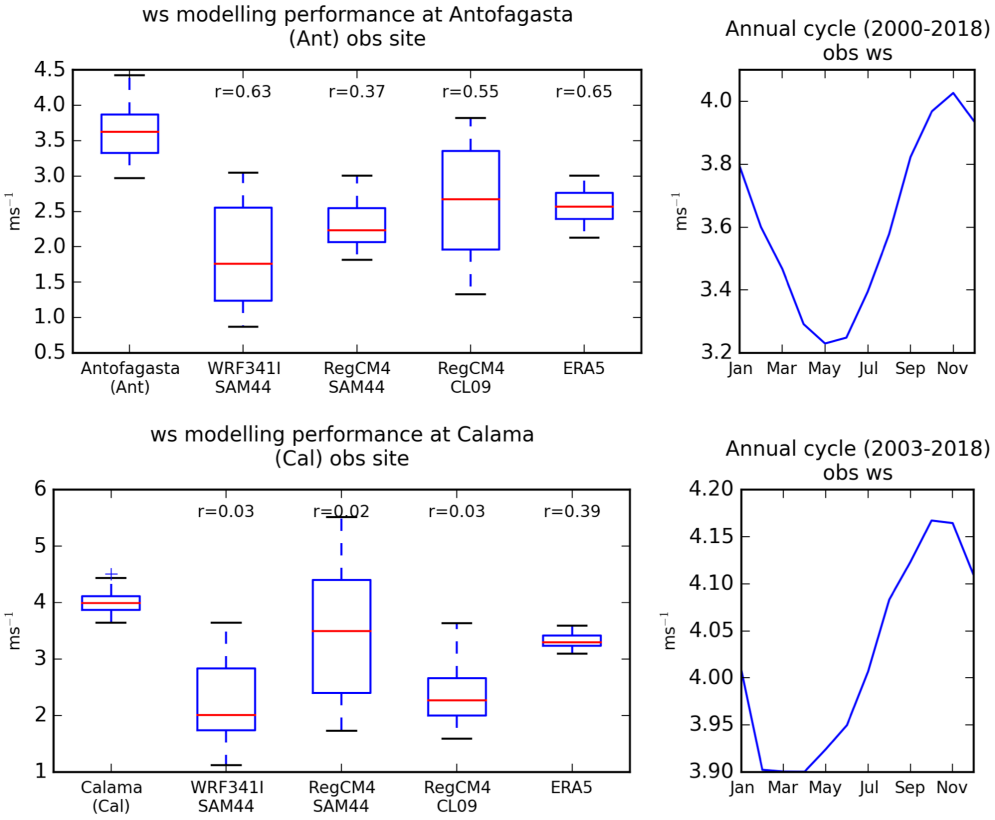

Figure 5.2: Surface wind speed at Cerro Moreno, Antofagasta (upper) and Calama (bottom). Blue boxes depict the 25–75 percentiles of the dataset, and the horizontal red line depict the median. The observed annual cycle computed from monthly means of surface wind speed at each site are shown in the right hand panels. The r-value represents the Pearson coefficient computed for linear correlation between each model's daily mean of wind speed and the Antofagasta (upper) and Calama (bottom) dataset..

The other variable needed to calculate the ventilation coefficient is the boundary layer height (BLH). As described in §5.1.1, non-local PBL schemes in climate models are more appropriate for the simulation of wind shear turbulence under stable conditions in comparison to local PBL schemes (Xie et al., 2012). The four gridded products used comprise a non-local PBL scheme for BLH computation

(Fig. 5.3).

The WRF341I-SAM44 model comprises the Yonsei University (YSU, Hong et al. (2006)) non-local closure PBL scheme in which the BLH is computed based on the formulation of a bulk Richardson number between the surface and the height of the PBL. In the YSU scheme, a critical bulk Richardson number equal to zero determines the minimum flux level. As discussed by (Hong et al., 2006), this scheme has been found suitable for both real-time forecasting and transient climate simulations due to an improved convective processes representation within the PBL, including a more realistic turbulence intensity in the mixing layer, in comparison to its previous version (Hong and Pan, 1996).

Regarding RegCM4-CL09 and RegCM4-SAM44, both configurations comprise the Holtslag et al. (1990) non-local PBL scheme, in which the BLH is calculated by an iteration procedure employing a bulk critical Richardson number formulation. Then a non-local vertical profile of eddy diffusivity for momentum, moisture, and heat is adopted for the layer between the surface and the PBL height (Giorgi et al., 2012).

The ERA5 reanalysis comprises the non-local PBL scheme firstly proposed by Vogelezang and Holtslag (1996), which has been described as a suitable choice for applications on radiosondes, reanalysis and climate model outcomes (Seidel et al., 2012). Similar to WRF341I-SAM44, RegCM4-CL09 and RegCM4-CL44, the BLH is computed based on a bulk Richardson number. The surface frictional effects are ignored since the friction velocity is unknown in radiosonde data. Also, near-surface winds at 2m height are set to zero because radiosonde data do not comprise winds close to the surface. Considering the above, the BLH is defined as the lowest level at which the bulk Richardson number equals a critical value of 0.25. As argued by Seidel et al. (2012), this is suitable for both convective and stable planetary boundary layers.

Fig. 5.3 reveals substantial discrepancies between the four gridded datasets in their simulation of decadal mean boundary layer height (2010-2019). WRF341I-SAM44 and ERA5 simulate shallow boundary layers across the Atacama Desert,

ranging in between a few meters up to 700 *m* above ground level, with the highest values towards the Andes especailly over Calama (Cal) and Sierra Gorda (SG) (Fig. 5.3a,d). RegCM4 simulates considerably higher boundary layers at both resolutions, with values up to 1,500 m above the ground over the Atacama. Again higher values tend to be located towards the Andes, although most of the middle desert exhibits decadal means greater than 1,000 m above the ground (Fig. 5.3b,c). Some differences between the RegCM4 resolutions are observable along the coastline between Iquique (Iqu) and Antofagasta (Ant), yet both are substantially higher than those computed by WRF341I and ERA5 over the same area.

The elevated boundary layers in RegCM4 seem to be linked to a persistent systematic warm bias seen over the Atacama region (Bozkurt et al., 2019). This is attributed to the complexities of simulating land surface and radiative processes and has been reported for other regions in earlier versions of RegCM (such as the 3.5°C warm bias reported by Marcella and Eltahir, 2012, over Southwest Asia). As reported by Bozkurt et al. (2019), in the 0.09°resolution RegCM4 model (RegCM4-CL09) over Northern Chile, the warm bias ranges between +2 and +5°C, with a mean for the Atacama Desert of about +4°C. The coarser 0.44°resolution model (RegCM4-SAM44) reproduces a warm bias of about +2°C, similar to those of forcing reanalysis ERA-Interim. Larger bias from the finer model (RegCM4-CL09) does not necessarily imply a poor representation of temperature patterns and surface fluxes. Indeed, as pointed out by Bozkurt et al. (2019), RegCM4-CL09 reproduced a closer variability and magnitude estimation of evaporation fluxes over the area compared to observations. It also better represents the temperature inter-annual variability.

All products show a boundary layer that is roughly half the height over the coastal desert (Fig. 5.4) as that over inland desert areas (Fig. 5.5) – consistent with Fig. 5.3. The amplitude of the seasonal cycle does not scale proportionally between them, suggesting this is closer to an annual mean offset. RegCM4-SAM44 and RegCM4-CL-09 simulate a TILH over the inland desert of 1200 *m* above the ground (compared to 600 *m* near the coast). This higher inland value provide a

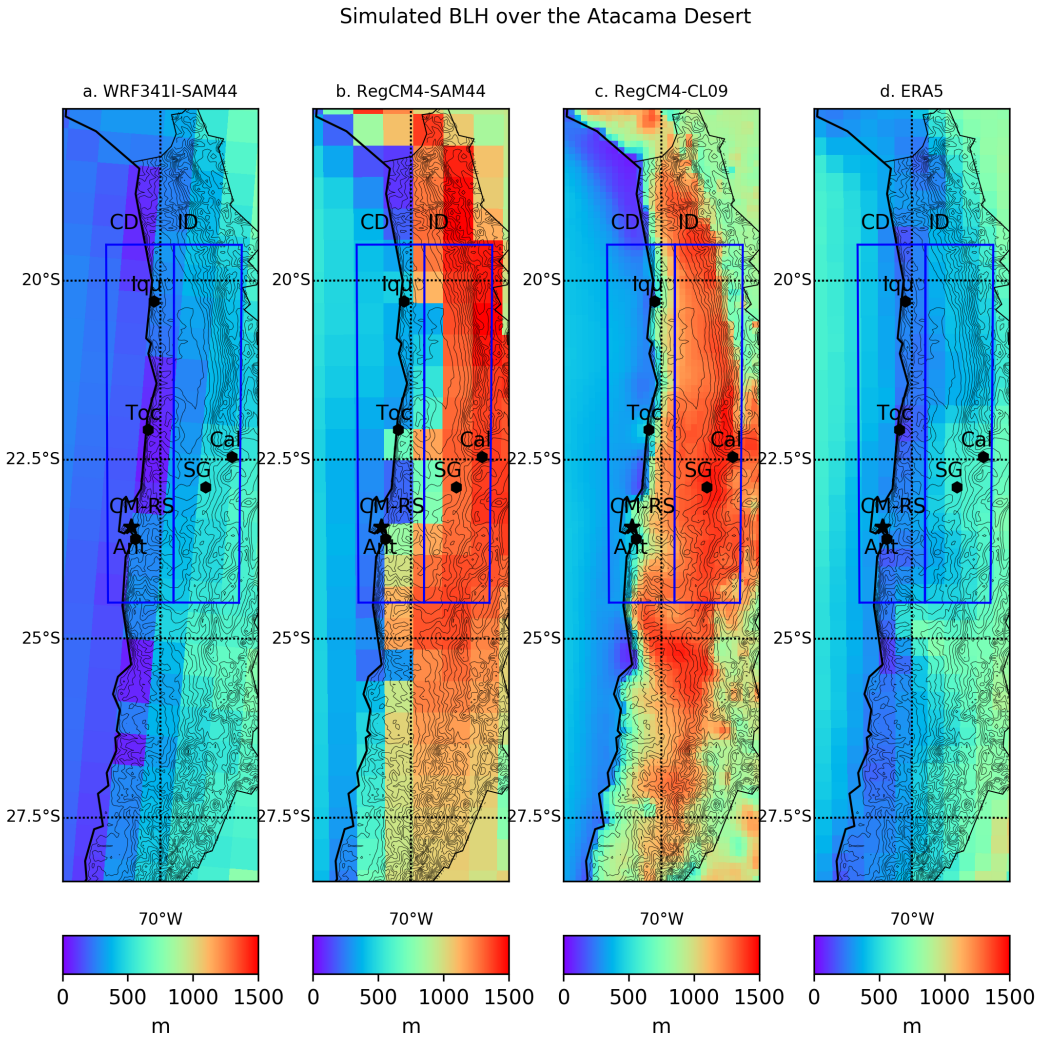

Figure 5.3: Decadal mean (2010-2019) of the Boundary Layer Height (BLH in metres) computed from (a) WRF341I-SAM44, (b) RegCM4-SAM44, (c) RegCM4-CL09, and (d) ERA5. The black star denotes the location of the Cerro Moreno radiosonde site (CM-RS). Black dots depicts the SINCA ground monitoring sites at Antofagasta (Ant), Tocopilla (Toc), Iquique (Iqu), Sierra Gorda (SG) and Calama (Cal). Black contour lines represent topography at 250 m vertical resolution

much closer fit to the observations, although it seems unlikely that the CM site really samples the inland conditions. The deeper boundary layer inland observed in the four datasets is naturally expected because of extremely high solar radiation exposure throughout the day over the desert.

When analysing the area-averaged time series of BLH of computed for the coastal and inland areas (Fig. 5.3), the four gridded datasets reproduce a similar

seasonality than the one computed for the Cerro Moreno radiosonde (see §3.2). The simulated boundary layer is taller in summertime and its height drops in altitude in wintertime (Figs 5.4 and 5.5). The observed TILH exhibits a remarkable decreasing trend from about 1,500 m height in 1981 to 1,300 m height in 2010 (Fig. 5.4). The monthly anomalies are with respect to a climatology calculated over the entire validation period (1981-2010) and shows interannual variability as well as the downward trend (Figs. 5.4). This decline has been reported by Schulz et al. (2011), who linked it to an observed cooling of the sea surface over the Humboldt coastal region since the mid-1970s (Falvey and Garreaud, 2009; Schulz et al., 2011). This ocean cooling is captured by CMIP5 global climate models and arises from intensified upwelling in the upper ocean layers during last decades (Oyarzún and Brierley, 2019). The three regional models (WRF241I, RegCM4-SAM44 and RegCM4-CL09) simulate this boundary layer shallowing, albeit with a weaker trend than observations for the coastal desert area (Fig. 5.4) although the magnitude of decline over the inland area (Fig. 5.5). On the other hand, ERA5 does not capture this decline, perhaps suggesting a need for dynamically downscaling the coastal local meteorology to capture the phenomenon.

The four datasets all show a zonal gradient in the ventilation coefficient (Fig. 5.6), exhibiting higher VC over the inland area (ID) compared to the coastal area (CD). The magnitudes differ considerably (Fig. 5.6), which is to be expected given the substantial differences in the simulated BLH (Fig. 5.3). RegCM4-SAM44 and RegCM4-CL09 simulate higher VC values than WRF341I-SAM44 and the ERA5 reanalysis, whose patterns over land are visually similar. It is relevant to note that despite the discrepancies in magnitude, most of the area remains below the threshold of 6,000 $m^2 s^{-1}$ (Holzworth, 1972) – although that was daily threshold, rather than an annual mean.

Although the BLH primarily controls the ventilation coefficient magnitude, the spatial distribution of VC (Fig. 5.6) seems to be governed by the topography-modulated wind patterns over land (Fig. 5.1). One such example is the higher VC values over Calama and the exceptional higher values over the mountainous

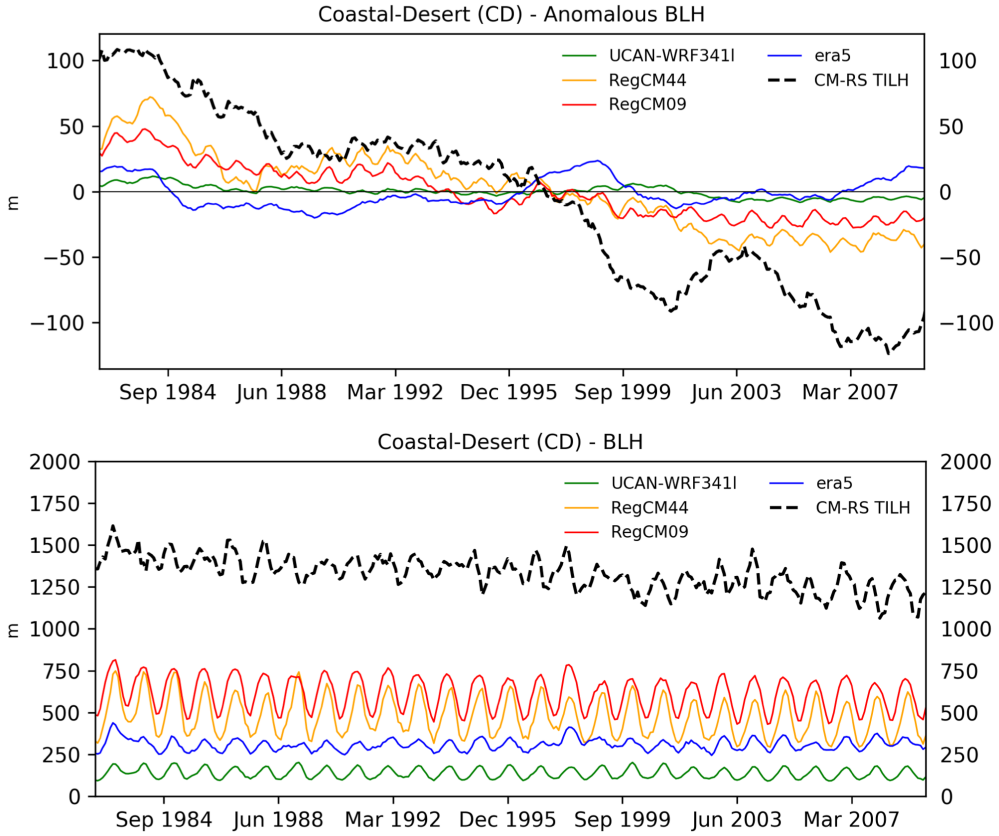

Figure 5.4: Area averaged time series of observational (dotted black line) and simulated boundary layer height from gridded datasets for the coastal desert (CD) area. Upper: anomalies computed with respect to the climatological cycle (averaged over 1981-2010). Bottom: absolute-value time series. Intra seasonal cycle has been removed, preserving seasonality..

Eastern land from 25°S to the South. On the other hand, all datasets reproduce lower atmospheric ventilation along the coast due to the low BLH. Then, VC increases off the shore due to the significant rise of wind speed over the ocean, despite similar boundary layer heights.

A ventilation coefficient can be computed from the Cerro Moreno radiosonde observations combined with and the surface wind speed measurements from Antofagasta (Figs. 5.7 and 5.8). This record shows a strong decline during the last decades, which is driven by the observed decline of BLH (Figs. 5.4). The observed trend in VC is roughly an order of magnitude larger than that seen in any of the products.

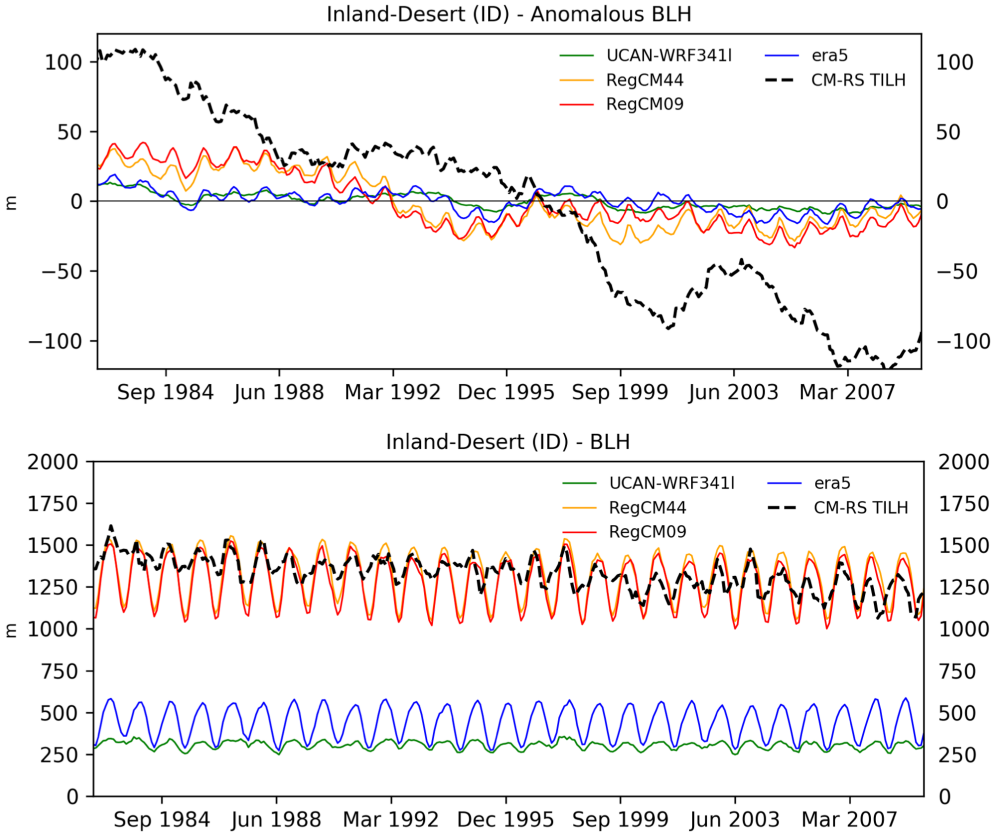

Figure 5.5: Area averaged time series of observational (dotted black line) and simulated boundary layer height from gridded datasets for the inland desert (ID) area. Upper: anomalies computed with respect to the climatological cycle (averaged over 1981-2010). Bottom: absolute-value time series. Intra seasonal cycle has been removed, preserving seasonality..

In the coastal desert area (CD), all three regional models simulate a decline in VC (Figs. 5.7). This decline is weaker in WRF341I-SAM44 than in RegCM4-SAM44 and RegCM4-CL09, because of its shallower boundary layer (Fig. 5.4). Interestingly, ERA5 does not exhibit a reduction in VC, even showing a small increase in VC towards the end of the evaluation period during the 2000s (Fig. 5.7). Over the inland desert (ID, Fig. 5.8), RegCM4-SAM44 and RegCM4-CL09 shows a long-term trend anomalous VC of similar magnitude to those over the CD area (Fig. 5.7), ranging from about +300 to -150 $m^2 s^{-1}$.However, in ID both RegCM-SAM44 and RegCM-CL09 are reproduced with a similar magnitude to the observations, which overlaps towards the ends of the period of analysis. The ventilation coefficient is

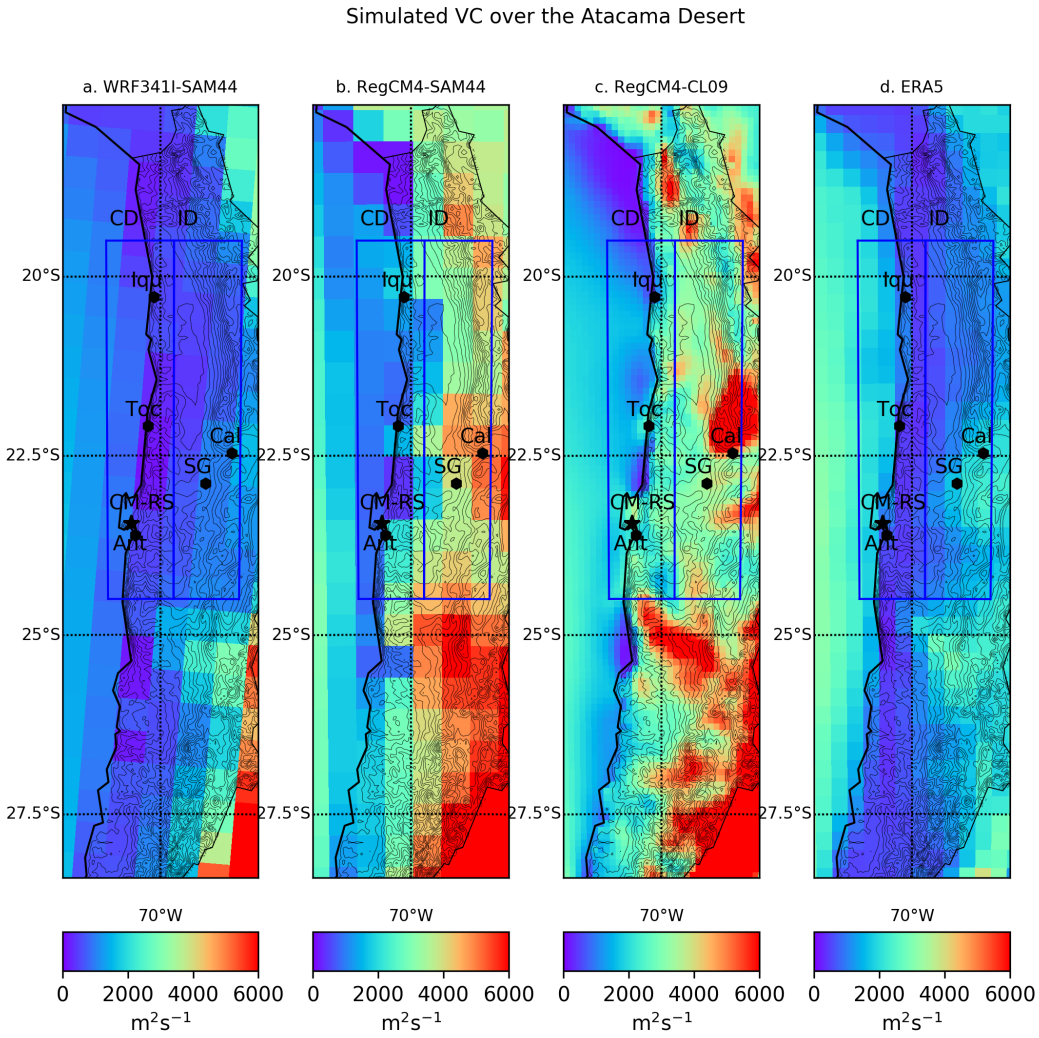

Figure 5.6: Decadal mean (2010-2019) of the Ventilation Coefficient (VC) computed from (a) WRF341I-SAM44, (b) RegCM4-SAM44, (c) RegCM4-CL09 and (d) ERA5. The black star denotes the location of the Cerro Moreno radiosonde site(CM-RS). Black dots depcits the SINCA ground monitoring sites at Antofagasta (Ant), Tocopilla (Toc), Iquique (Iqu), Sierra Gorda (SG) and Calama (Cal). Blue rectangles corresponds to the Coastal Desert (CD) and Inland Desert (ID) areas..

lower in all data products and regions than calculated from the observations. The observed mean VC of 5000 m^2s^{-1} is still over 1000 m^2s^{-1} higher than the highest simulated mean value (RegCM4-SAM44 inland; Fig. 5.8).

Observed VC and simulated VC calculated from RegCM4-SAM44 and RegCM4-CL09 exhibit a clear seasonal pattern across the Atacama with more intense ventilation during summer and lower in winter (Figs. 5.7 and 5.8, bottom).

This is expected because of the annual cycle of both wind speed and BLH. This seasonality signal is weaker in ERA5 and WRF341I-SAM44. However, in the inland desert (Fig. 5.8, bottom), ERA5 reproduces a clear seasonality matching a less defined annual cycle of RegCM4-SAM44 and RegCM4-CL09. On the contrary, WRF341I-SAM44 exhibits the opposite behaviour, with more ventilated conditions in winter.

The observed VC experiences seasonal exceedence of the 6,000 m^2s^{-1} threshold through the period, although the amount of these reduce dramatically after 1997 (Fig. 5.7) with the exception of the 1980s decade. According to the above and considering Holzworth (1972) criterion, the Atacama desert land is prone to prevailing unvented conditions, at least at a regional scale. Daily values of VC and their assessment against Holzworth (1972) threshold are discussed in the following subsections. For the four gridded datasets, VC remains below the 6,000 m^2s^{-1} threshold through the period. This suggests that an absolute threshold is not appropriate across the various data sources and relative thresholds must be defined for each product.

5.4 Particulate Matter and Atmospheric Ventilation Relationships

Particulate matter concentrations depend on several natural and anthropogenic factors (Chapter 3). Therefore, it is unrealistic to expect strong linear relationships between particulate concentration and the ventilation coefficient. Exploring the relationship between these parameters nonetheless provides insights into the natural factors influencing air pollutants concentrations (Zhao et al., 2011a).

Ground-based observations of PM_{10} and $PM_{2.5}$ from five sites (Tab. 5.2) were converted to monthly averages and correlated with the observed and modelled VC. At all locations, observed VC exhibits a negative relationship with $PM_{2.5}$ (Fig. 5.9) and PM_{10} (Fig. 5.10). These relationships can be summarised by correlation statistics, and results for both observed and simulated VC, boundary layer height and wind speed are presented in Tab. 5.4.

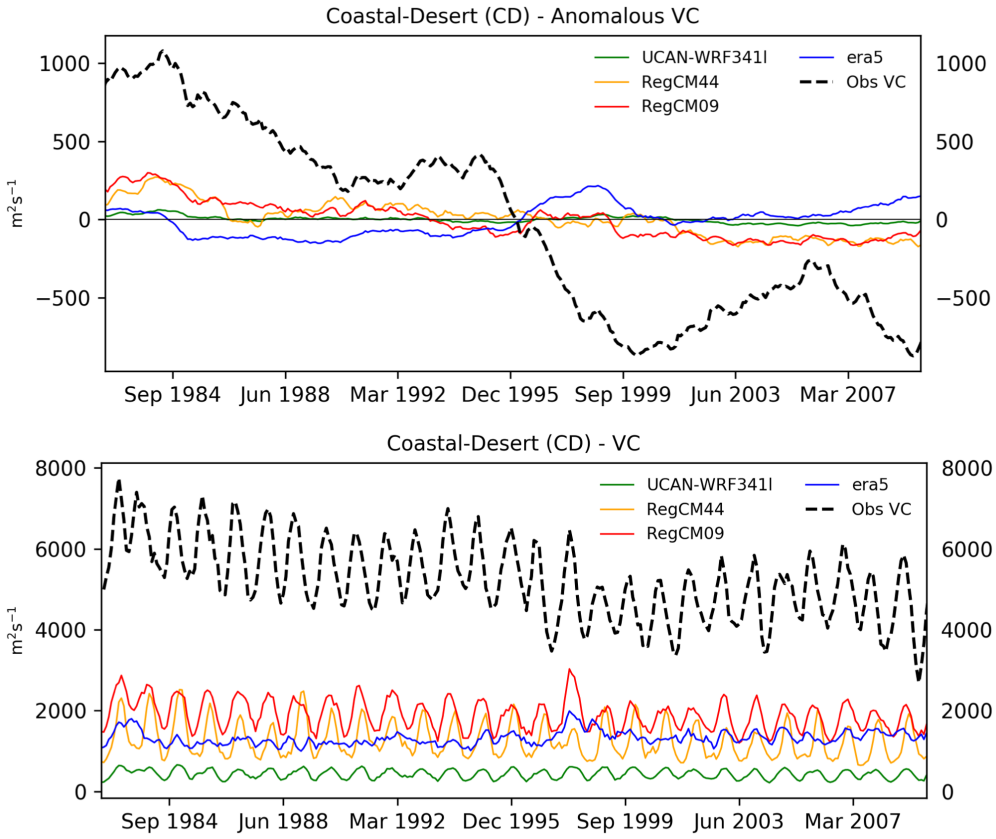

Figure 5.7: Temporal variation in ventilation coefficient (VC). Area averages over the coastal desert area (CD) of simulated VC are shown for four gridded datasets (colours), along with observations from near Antofagasta (dotted black line). Upper panel: anomalies computed with respect to a climatological cycle computed over entire period of analysis 1981-2010. Bottom panel: absolute-value time series with a smoothing applied.

The observed VC from Antofagasta shows a negative relationship with $PM_{2.5}$ (Fig. 5.9) at all five sites selected. The strong relationships at both Tocopilla and Calama are worthy of note. These are some of the most complete records and cover both inland and coastal conditions. This indicates at the seasonal cycle and long term trend over a broad area and influenced by the varying meteorological conditions. Both coastal and inland sites are exposed to substantive anthropogenic emissions, including urban transport, coal power plants (Toc), and open-pit mining operations (Cal) (see details of relevant emission sources in §3.3). As previously discussed, although Antofagasta, Calama and Sierra Gorda present higher VC, all

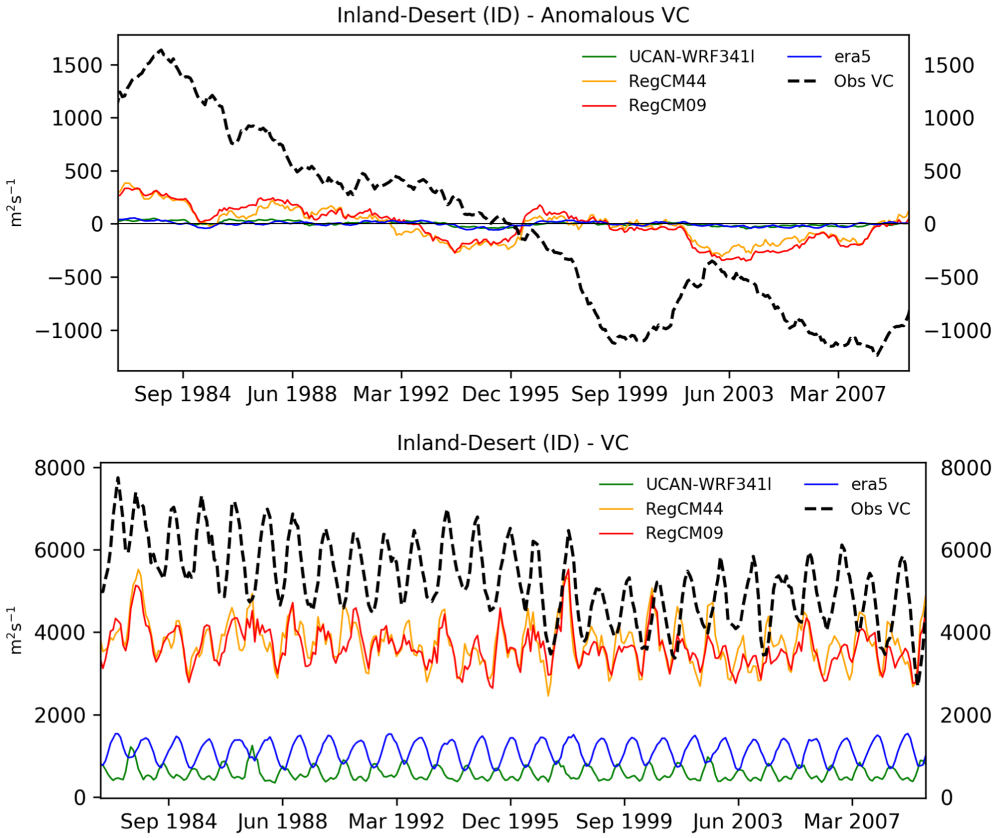

Figure 5.8: Temporal variation in ventilation coefficient (VC). Area averages over the inland desert area (ID) of simulated VC are shown for four gridded datasets (colours), along with observations from near Antofagasta (dotted black line). Upper panel: anomalies computed with respect to a climatological cycle computed over entire period of analysis 1981-2010. Bottom panel: absolute-value time series with a smoothing applied.

the locations are under persistent unvented conditions ($< 6{,}000\ m^2 s^{-1}$). This a conservative assumption, since along the coast, the TILH caps and modulates the BLH (Schulz et al., 2011). Regarding the inland sites (SG and Cal), although the nature of the BLH and temperature inversion layer formation over the inland desert derives from local radiative effects, the marine "trade-wind" TILH still exerts an effect on the inland BLH variability and the generalised stable atmospheric conditions of the region.

Some interesting differences are seen in the relationship of PM_{10} concentrations to ventilation (Fig. 5.10) compared to those of $PM_{2.5}$ – although an in-

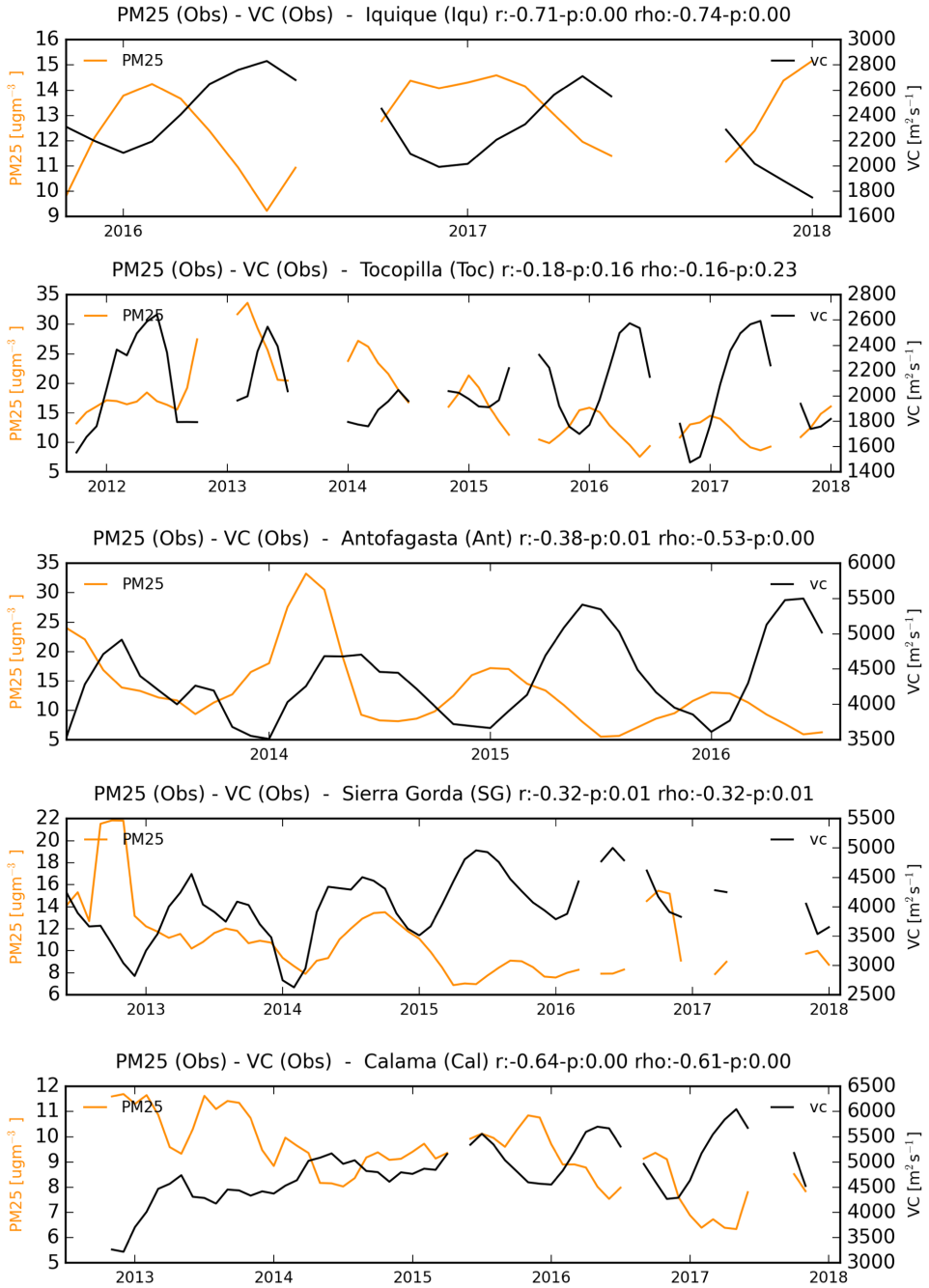

Figure 5.9: Comparison between monthly-mean observed time series of ventilation coefficient with $PM_{2.5}$ for Iquique, Tocopilla, Antofagasta, Sierra Gorda and Calama. The gaps in the plots occur where there is a lack of $PM_{2.5}$ data in those periods. This also means that the horizontal and vertical axes are the same between the panels..

verse relationship still exists at all four sites (Iquique has no PM_{10} measurements). Tocopilla and Antofagasta, both coastal sites, present considerably high correlations between VC and PM_{10} (r values equal to 0.61 and 0.72 respectively). These are stronger than $PM_{2.5}$ relationships at both sites, which makes sense given their stronger potential incidence of in-situ anthropogenic sources that add noise to the unrelated meteorological conditions. However, PM_{10} variability tends to be modulated by atmospheric ventilation, because it relates to both emission and transport of coarse particles in these coastal areas, such as marine aerosols and mineral dust. Conversely, PM_{10} in Calama correlates more weakly with VC ($r = 0.36$) in comparison with $PM_{2.5}$ ($r = 0.64$). In this location, the anthropogenic emissions of coarse PM are substantial, because of the operation of the open-pit mines of Chuquicamata and Mansa Mina located to the north of the City. Although the mines operate throughout the year, the intensity of the operations and hence emissions (say through local transport on unpaved roads) responds to external factors such as the global price of copper. A similar effect is observed in Sierra Gorda, although the impact is less severe. To truly assess the relative natural and anthropogenic contributions implied by these relationships, chemical transport modelling would need to be performed. Nonetheless the results here presented are reasonable and align with the corresponding nature of the emissions in each location.

A close look at Tab. 5.4 reveals significant agreement and discrepancies between the correlations computed from observed VC and the gridded datasets. The observed estimate of the depth boundary layer (technically the temperature inversion level height, TILH) shows higher correlations with PM concentrations than VC for most instances. This reveals a considerable effect of the boundary layer modulating both PM_{10} and $PM_{2.5}$ levels at both coastal and inland locations and the effect of wind speed variations do not matter (except for Iquique). This is of particular significance due to the observed decline of the TILH observed during the last decade. This trend is expected to continue, as inferred by the increasing coastal upwelling intensity at the ocean surface simulated from CMIP5 during the 21st Century and the modelled coastal upwelling and BLH trends from the UKESM1 model

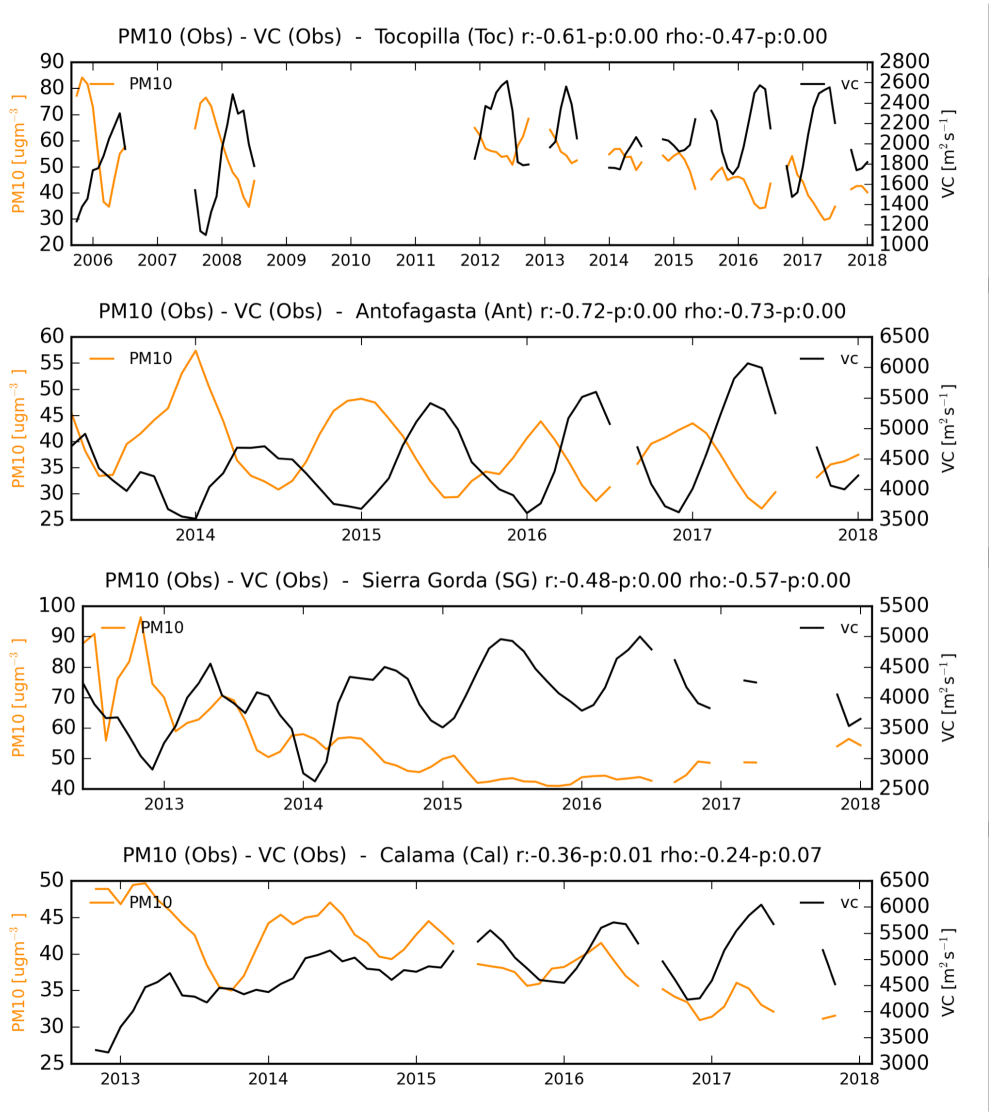

Figure 5.10: Comparison between monthly-mean observed time series of ventilation coefficient with PM_{10} for Tocopilla, Antofagasta, Sierra Gorda and Calama. The gaps in the plots occur where there is a lack of $PM_{2.5}$ data in those periods. This also means that the horizontal and vertical axes are the same between the panels..

contributing to CMIP6 discussed in Chapter 6. A particularly strong correlation is observed in Sierra Gorda, where the PM_{10} relationship with the TILH is much higher ($r = -0.74$), than with the ventilation coefficient ($r = -0.48$).

Table 5.4: Linear correlation between observed VC,TILH and surface wind speed (ws), and modelled VC,BLH and surface wind (ws) speed with observed $PM_{2.5}$ and PM_{10} in Iquique (Iqu), Tocopilla (Toc), Antofagasta (Ant),Sierra Gorda (SG) and Calama (Cal). The results are presented for Observed VC, whose case BLH is given by the TILH, and the gridded datasets RegCM-SAM44, RegCM4-CL09 and ERA5. WRF341I-SAM44 has not been considered due to there was no enough collocation data between the modelling and observational dates to perform monthly-basis correlations (5.1 and 5.2). Also, because of the same, RegCM4-SAM44 and RegCM4-CL09 were not considered for analyses in Iquique

Site	Obs			Reg44			Reg09			ERA5		
	VC	TILH	ws	VC	BLH	ws	VC	BLH	ws	VC	BLH	ws
$PM_{2.5}$												
Iqu	-0.71	-0.47	-0.71	-	-	-	-	-	-	-0.86	-0.84	-0.90
Toc	-0.18	-0.54	0.18	0.38	0.24	0.35	0.24	0.25	0.18	0.11	0.11	0.10
Ant	-0.38	-0.49	-0.13	-0.61	-0.61	-0.46	-0.61	-0.61	-0.61	-0.55	-0.56	-0.52
SG	-0.32	-0.62	0.10	-0.63	0.24	-0.55	-0.67	0.11	-0.58	-0.21	0.00	-0.44
Cal	-0.64	-0.66	-0.43	-0.24	-0.09	-0.16	-0.41	-0.17	-0.24	-0.05	0.02	-0.27
PM_{10}												
Iqu	-	-	-	-	-	-	-	-	-	-	-	-
Toc	-0.61	-0.64	-0.13	0.08	0.0	0.14	-0.08	-0.13	-0.02	0.0	0.13	-0.12
Ant	-0.72	-0.61	-0.56	-0.74	-0.80	-0.45	-0.77	-0.82	-0.74	-0.63	-0.61	-0.64
SG	-0.48	-0.74	-0.04	-0.22	0.22	-0.23	-0.32	0.17	-0.29	-0.11	-0.10	0.01
Cal	-0.36	-0.51	0.00	0.54	-0.14	0.49	0.48	-0.28	0.58	-0.02	-0.10	0.22

Regarding simulated VC, mixing results are observed. In the coastal sites of Iquique and Antofagasta, the gridded datasets reproduce an even higher correlation in comparison with observed VC. Unlike the last one, gridded data suggest a significant effect of both BLH and ws on PM variability. The opposite is the case of inland sites (Sierra Gorda and Calama) and the coastal city of Tocopilla. This is expected when analysing Fig. 5.2 (bottom), which shows an almost null correlation between modelled and observed ws at Calama. Although there is some agreement between the modelled VC correlations and the observed ones at these locations, there are significant discrepancies regarding their constituents components (BLH and ws). This might be associated with the difficulties of the gridded products to capture their variability at such complex terrain.

5.5 Atmospheric Stagnation and Particulate Matter Events

This section aims to understand the role that atmospheric stagnation plays, defined as ASI (Wang and Angell, 1999), on PM_{10}-$PM_{2.5}$ observed events. First, wind speed at 500 hPa records (ws500) from the Cerro Moreno radiosonde dataset are contrasted against the four gridded products used in this Chapter (WRF341I-SAM44, RegCM4-SAM44, RegCM4-CL09 and ERA5). This is to provide confidence in computing, for all sites, an observational ASI using mid-tropospheric winds from the radiosonde records (Cerro Moreno). The above, along with assessing models performance for computing modelled ASI. Then, observed ASI is discussed, followed by the analysis by the spatial distribution of stagnation over northern Chile from the four gridded products. Finally, ASI and PM links during PM_{10} and $PM_{2.5}$ events are discussed along with prevailing atmospheric ventilation (VC) conditions.

5.5.1 Mid-tropospheric wind from Cerro Moreno and gridded products

The mid-troposheric wind speed is one of the variables needed to compute ASI (Wang and Angell, 1999). Therefore is sensible to assess the fidelity of this variable in the four products, to see if it can account for the variation in simulated ASI seen above. The four datasets satisfactory simulate both magnitude and variability of the mid-tropospheric wind speeds over Antofagasta (Fig. 5.11), as compared to the profiles observed at nearby Cerro Moreno. Additional comparison between these observations simulated wind speed over Calama shows that, as expected, ws500 preserves its magnitude across the area of interest (Fig. 5.11).

The radiosonde observations from Cerro Moreno at 500 hPa are representative of the whole area, given the consistency demonstrated in the four products. These records correspond to morning measurement at 8 or 9 am local time. However, because of the near absence of a daily cycle of ws500 above the boundary layer and the governing topography, this is of little consequence.

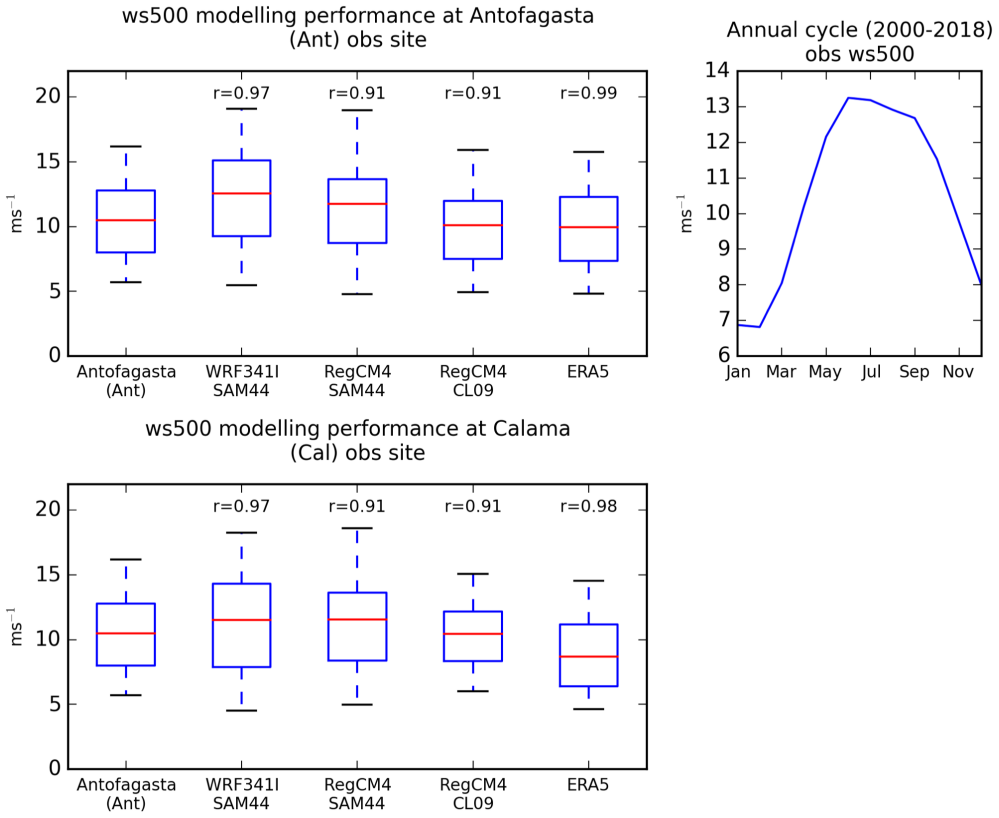

Figure 5.11: Left: Model performance of wind speed at 500 *hPa* (ws500) height in contrast to observational records at Cerro Moreno (labelled as Antofagasta (Ant)). The upper plot shows the modelled ws500 over Antofagasta, and the bottom plot shows the modelled ws500 over Calama. Blue boxes depict the interquartile data. The horizontal red line depicts the median. Right: climatological annual cycle wind speed at 500 *hPa* observed at Cerro Moreno..

5.5.2 Observed ASI

Table. 5.5 summarises observed stagnation computed with ws500 records from Cerro Moreno and surface wind speed measured at each location. Tocopilla presents the highest number of stagnant days (1,756), corresponding to 62.7% of the period of record. The above due to a predominance of days when surface wind speed meet the Wang and Angell (1999) criterion ($ws < 3.2ms^{-1}$). It is interesting to note that Antofagasta, located 180 km south of Tocopilla, presents considerably lower stagnant days (18.8% of the total). Both correspond to coastal cities directly exposed to the SPA. The above difference is driven by the higher amount of days in Tocopilla

when surface wind speed met the criterion for ASI, which suggest that local factors, such as topography or built-environment interferences, might be impacting (reducing) local wind speeds in Tocopilla. Another factor to consider is the zonal location, which is discussed in the next Section.

Regarding inland desert locations, whereas Sierra Gorda presents a similar stagnant days frequency than Antofagasta (18.8% of the total.), Calama presents a considerable low number of stagnant days (2.6%). This is mainly because of the reduced amount of days meeting the Wang and Angell (1999) criterion for surface wind speed (259 days out of 4,392).

Table 5.5: Observed stagnation computed from Cerro Moreno ws500 data and surface wind speed for Tocopilla (Toc), Antofagasta (Ant), Sierra Gorda (SG) and Calama (Cal). Surface wind speed in Tocopilla and Sierra Gorda has been obtained from the SINCA database. For Antofagasta and Calama, the DMC sites in each location have been used (they offer a more extended monitoring period). The second column summarises the number of days (wind speed daily average) when the Wang and Angell (1999) criterion is met. Similarly, the third column summarises the number of days (ws500 measure in each day) when the Wang and Angell (1999) criterion for ws500 is met. Stg days refers to the number of stagnant days observed (ASI=1) during the monitoring period (Period), an % corresponds to the percentage of days out of the total (Total records) that are stagnant.

Site	$ws < 3.2ms^{-1}$ [days]	$ws500 < 13.0ms^{-1}$ [days]	Stg. days	%	Total records	Period
Toc	2,679	1,850	1,756	62.7	2,801	Dec2005-Sep2018
Ant	1,822	4,225	1,187	18.8	6,330	Jan2000-Sep2018
SG	579	1,254	344	17.8	1,930	Sep2012-Sep2018
Cal	259	3,251	127	2.6	4,932	Feb2003-Sep2018

5.5.3 ASI spatial distribution

The Air Stagnation Index (ASI) has been computed for all the four data products (Tab. 5.1). The Wang and Angell (1999) thresholds were used (Section 5.1.3) and the number of days per year averaged over the period 1981-2010 (Fig. 5.12).

Most of Northern Chile presents a significant amount of stagnation episodes (henceforth 'stagnant days'), in agreement with the prevailing unvented conditions over the Atacama. Although some spatial discrepancies are observed between the different datasets, (potentially linked to differences in spatial resolution), there is

a consistent pattern of higher frequency of stagnant events at the lower latitudes of the Atacama, with a reducing amount towards the South (Fig. 5.12). The semi-permanent stagnant conditions in the Northern Atacama are highly influenced by the hyper-aridity and virtual absence of rainfall. Although the pattern is also evidenced from ERA5 (Fig. 5.12d), this reanalysed dataset reproduces considerably more stagnant days. Some areas between 18 and 20°S experience an average of over 300 stagnant days per year in ERA5.

At the 2 inland sites (Sierra Gorda and Calama) all the datasets suggest between 100 to 180 stagnant days per year on average (Fig. 5.12). Greater variability is shown in the coastal locations, likely due to the models' different horizontal resolution and their representation of the ocean-land boundary. WRF341-SAM44 and RegCM4-CL09 simulate 130 and 190 stagnant days per year at Iquique respectively, whereas RegCM4-SAM44 and ERA5 suggest less than 50 stagnant days per year. In the case of Tocopilla, both coarser models (WRF341I-SAM44 and RegCM4-SAM44) simulate about 90 stagnant days per year, whereas RegCM4-CL09 and ERA5 show lower figures of about 30 and 60 stagnant days, respectively (Fig. 5.12). Finally, Antofagasta presents a higher stagnation than its coastal counterparts in all datasets with both WRF341I-SAM44 (120 days), RegCM4-SAM44 (100 days) suggesting stagnation persists for more than a whole season on average. Despite the variations between the different datasets, the results suggesting that a substantial region of the Atacama desert experience over 4 months of stagnant conditions per year fit with the findings of Horton et al. (2014) for Northern Hemisphere dry subtropical regions.

5.5.4 ASI and PM levels

Fig. 5.13 presents an observational analysis between the ASI and PM ($PM_{2.5}$ and PM_{10}) for Tocopilla, Sierra Gorda, Antofagasta and Calama. It also includes the ventilation coefficient, in order to explore the intersection with stagnation. In Fig. 5.13, days where the Wang and Angell (1999) thresholds for ASI index were met are coloured red, whilst other days are shown in black.

Stagnant days in all locations take place under unventilated conditions (as also

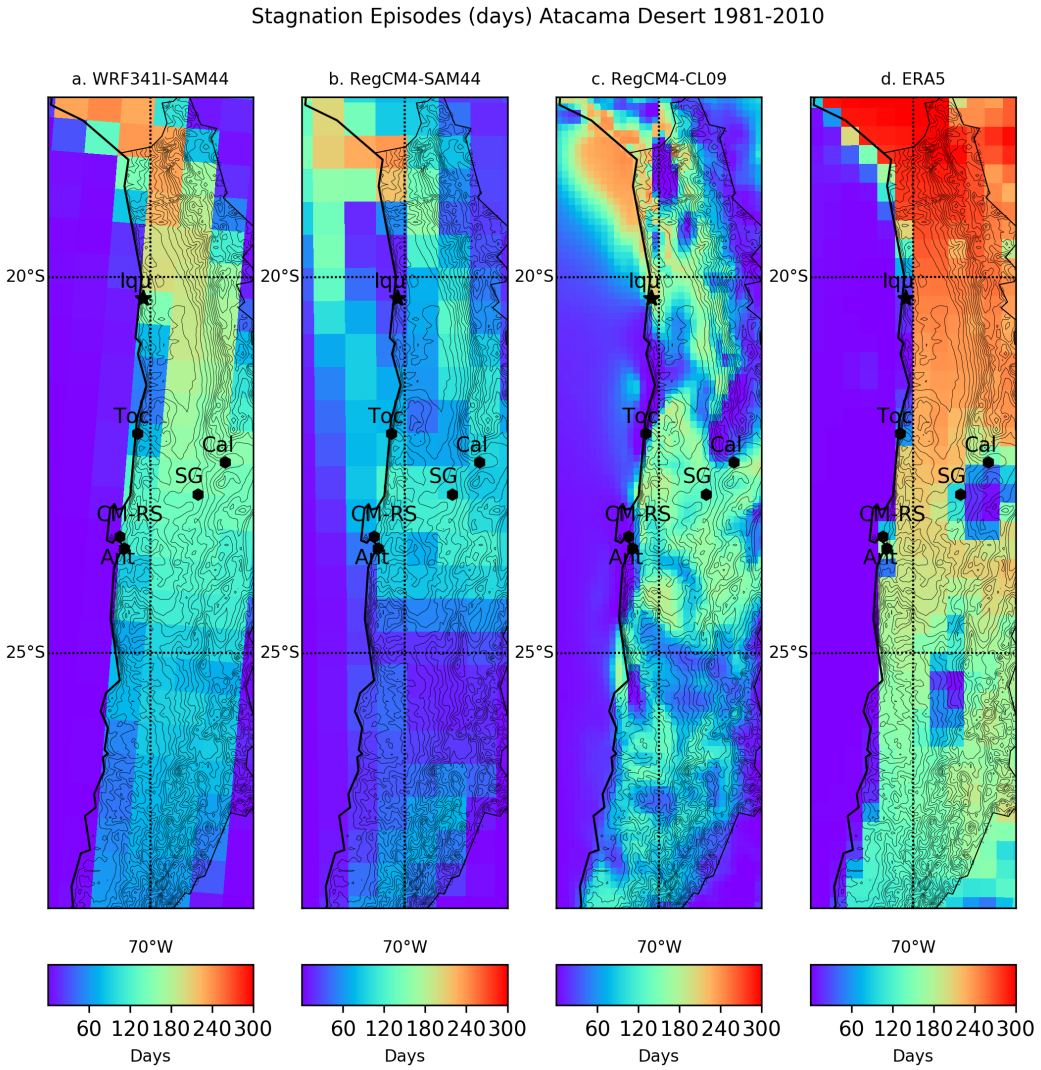

Figure 5.12: Stagnant episodes estimated according to the thresholds defined by Wang and Angell (1999) for ASI index computation. ASI was computed from WRF341I-SAM44 (a), RegCM4-SAM44 (b), RegCM4-CL09 (c), and ERA5 (d). The black star denotes the location of the Cerro Moreno radiosonde site (CM-RS). Black dots depicts the SINCA ground monitoring sites at Antofagasta (Ant), Tocopilla (Toc), Iquique (Iqu), Sierra Gorda (SG) and Calama (Cal).

found by Trail et al., 2013), with only 6 days across all sites and all PM variables that occur with a VC above the threshold of $6,000 m^2 s^{-1}$. In fact, as summarised in Tab. 5.6 for both $PM_{2.5}$ and PM_{10} over 99% of total stagnant days observed in every site took place in days with a VC value lower than 6,000 $m^2 s^{-1}$, (black horizontal lines in Fig. 5.13). It is also important to note that 72.4% of all days

in Calama fall below the unventilated threshold, and 97% in Tocopilla (Tab. 5.6). As discussed in §5.5.2, Calama seems somewhat of an outlier amongst the four sites, as is experiences a much lower number of stagnant days (Fig. 5.13d and Tab. 5.6). Also, $PM_{2.5}$ presents no extreme values, as daily mean, which as discussed in Chapter 3 is reasonable to observe due to the predominance of coarse particulate matter anthropogenic sources in the area.

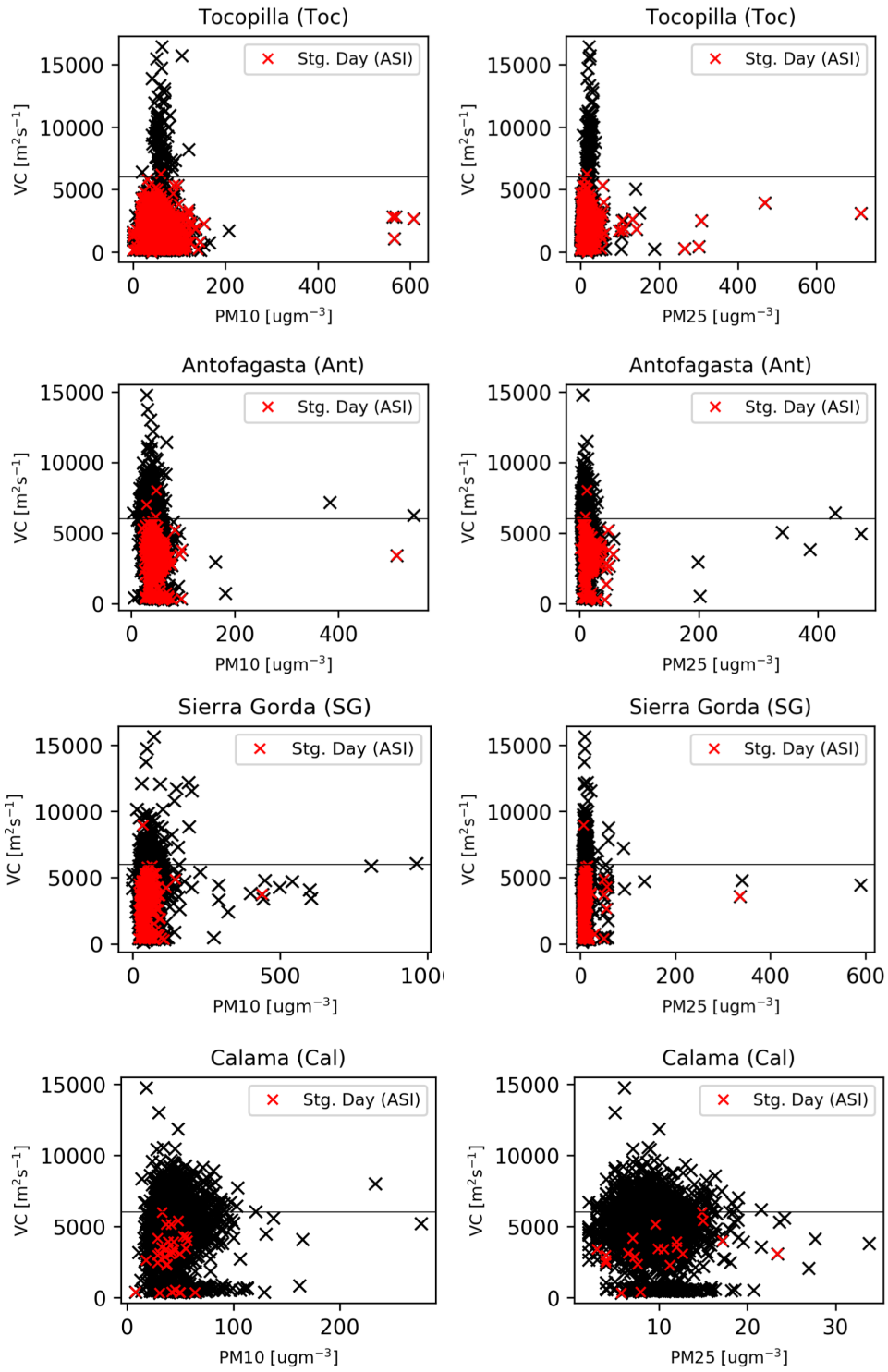

Figure 5.13: Daily observations of PM_{10}-$PM_{2.5}$ and ventilation coefficient. Each day is represented by a cross that is coloured red if it is stagnant according to the ASI definition, and black otherwise. Horizontal black lines denote the threshold $VC = 6,000 m^2 s^{-1}$. Note the different horizontal scales, which vary in relation to each sites particular matter observations. Iquique has not been included as this site does not measure PM_{10}.

Table 5.6: ASI and VC relationships for $PM_{2.5}$ and PM_{10} datasets. Data (days) correspond to the total length of the dataset containing VC, ASI and PM_{10}-$PM_{2.5}$. This varies between PM_{10} and $PM_{2.5}$, with PM_{10} records usually being longer. than $PM_{2.5}$. $VC < 6{,}000 m^2 s^{-1}$: number of days that meet this condition out of the total data. *Stg. days*: number of stagnant days as defined by the ASI index. *Stg. days & VC* $< 6{,}000 m^2 s^{-1}$: number of days that are both stagnant and unventilated.

Site	data (days)	$VC < 6{,}000 m^2 s^{-1}$	Stg. days	Stg. days & $VC < 6{,}000 m^2 s^{-1}$
$PM_{2.5}$				
Toc	2,086	2,006 (96.2%)	1,237	1,236 (99.9%)
Ant	1,286	1,056 (82.1%)	229	227 (99.1%)
SG	1,890	1,679 (88.8%)	332	331 (99.7%)
Cal	2,449	1,833 (74.8%)	31	31 (100.0%)
PM_{10}				
Toc	2,737	2,656 (97.0%)	1,676	1,675 (99.9%)
Ant	2,182	1,770 (81.1%)	384	381 (99.2%)
SG	1,907	1,695 (88.9%)	337	336 (99.7%)
Cal	1,828	1,323 (72.4%)	21	21 (100%)

The occurrence of PM events depends on location, and although all extreme events have taken place under the Holzworth (1972) limit, these do not necessarily occur under stagnant conditions as defined by ASI. In fact, only at Tocopilla (Fig. 5.13a) is an evident pattern of extreme events during stagnant days and unvented conditions observed for both $PM_{2.5}$ and PM_{10}. In this location, similar to the pollution events described by Dawson et al. (2014) in Birmingham (Alabama), extreme PM_{10} and $PM_{2.5}$ events ($> 200 \mu g m^{-3}$) took place in the presence of stagnation and low temperature inversion heights.

5.6 Statistical modelling of particulate matter events

Three experiments (Tab. 5.3) were carried out in order to understand the variables and their respective weights linked to extreme PM events. These were defined as being above 80th percentile (p80) of the $PM_{2.5}$ and PM_{10} datasets, which corresponds to 16 and 46 $\mu g m^{-3}$ respectively. Both values are within the "latent" range of the annual mean Chilean standard of each pollutant. As described in §3.4, "latent" non-attainment means that the air pollutant concentration lies between 80 and 100% of the threshold value, which corresponds to $15 - (<) 20 \mu g m^{-3}$ for $PM_{2.5}$ and

$40-(<)50\mu gm^{-3}$ for PM_{10}. All of the logistic models use surface meteorology as inputs. These are combined with the ventilation coefficient in experiment 1 (Tabs 5.7), combined with the ventilation coefficient and ASI in experiment 2 (Tab. 5.8, or just used by themselves (Tab. 5.9). The coefficients associated with each input variable are determined using a subset of the available data, and then evaluated against the data that was left out (§5.6).

Each of the 3 experiments are evaluated through skill-scores developed for logical data. 'Accuracy' measures the number of cases, either true or false (PM event or non-event) estimated, it means the ratio between the observations predicted correctly and the total of observations. 'Precision' measures the performance of the model for predicting true cases (PM events), which means the ratio between true values predicted correctly and the total of true values predicted (either correct or not). 'Recall' indicates the quantity of actual true values that the model is able to identify, which means the ratio between true values predicted correctly and the total of true values in the observational dataset. The final measure used is the area under the receiver operating characteristic (ROC) curve (AUC-ROC) (§5.6). An AUC-ROC equal to 0.5 indicates difficulties for discrimination, whereas a value equal to 1 indicates perfect class discrimination. The actual ROC curves are presented in Fig. 5.14. Tabs. 5.7, 5.8 and 5.9 summarise the model results for each experiment. To illustrate the performance of the experiment, Confusion matrices are presented in Fig. 5.15. These explicitly shown true and false positives and true and false negatives predicted by each model on the testing dataset (25% of the total).

Experiments 1 and 2 (Figs. 5.7 and 5.8) produce a better prediction than the experiment using solely meteorological variables (Tab. 5.9). Although the PM_{10} and $PM_{2.5}$ models derived using just relative humidity, surface temperature and atmospheric pressure nonetheless demonstrates some skill. In all three experiments, better predictions are found for $PM_{2.5}$ than PM_{10}.

AUC-ROC values are greater than 0.8 in all models incorporating the ventilation coefficient, and slightly higher still once ASI is also included (c.f. Tab. 5.8 with Tab. 5.7). It is also noticeable that the normalised coefficients of VC and sur-

face temperature are considerably larger, and both negatives. On the other hand, the ASI coefficient is positive, but its magnitude is smaller. This agrees with the results for extremely large PM events ($> 200 \mu gm^{-3}$) shown in Fig. 5.13 where large PM events predominantly occur under unvented conditions without clear trends regarding stagnation. This strengthens the argument that both $PM_{2.5}$ and PM_{10} events in Antofagasta are linked to a decrease in surface temperature under unventilated conditions not only for very large events, but also for mild events above 16 and 46 μgm^{-3} as a daily mean of $PM_{2.5}$ and PM_{10}, respectively. The model for experiment 1 was able to predict 241 true positive values for PM_{10} and 266 true positives for $PM_{2.5}$ (Fig. 5.15). On the other hand, the models predicted 84 false PM_{10} events and 64 false PM25 events. This leads to an accuracy of 0.74 and 0.78 for PM_{10} and $PM_{2.5}$ events prediction, respectively (Tab. 5.7). In the case of experiment 2 (Fig. 5.15 c and d), the model predicted 231 true positive values for PM_{10} and 271 true positives for $PM_{2.5}$. On the other hand, the models predicted 94 false PM_{10} events and 59 false PM25 events. These differences with experiment 2 suggest that experiment 1 better predicted PM_{10} events, whereas experiment 2 better predicted $PM_{2.5}$ events. However, this difference is relatively small, as observed in the recall values in Tabs. 5.7 and 5.8.

Table 5.7: Logistic Regression Statistics for Experiment 1 (exp1).

Feature Exp1	Coef PM_{10}	Coef $PM_{2.5}$
RH	0.86	-0.64
T	-3.06	-5.63
AP	0.72	-0.24
VC	-5.23	-5.51
wd E	1.07	1.87
wd S	0.22	0.95
wd W	0.77	2.04
wday	1.37	2.39
wend	0.69	2.47
PM ev (μgm^{-3})	46.0	16.0
AUC-ROC	0.82	0.85
accuracy	0.74	0.78
precision	0.74	0.77
recall	0.74	0.81
Total Data	1592	1572

Table 5.8: Logistic Regression Statistics for Experiment 2 (exp2).

Feature Exp2	Coef PM_{10}	Coef $PM_{2.5}$
RH	1.14	-0.88
T	-3.74	-6.20
AP	0.48	-0.67
VC	-3.76	-4.65
ASI	1.13	0.78
wd E	0.72	1.72
wd S	0.13	1.06
wd W	0.71	2.07
wday	1.11	2.45
wend	0.44	2.40
PM ev (μgm^{-3})	46.0	16.0
AUC-ROC	0.82	0.87
accuracy	0.74	0.79
precision	0.76	0.79
recall	0.71	0.82
Total Data	1592	1572

In experiment 3, the model performance led to lower values of accuracy, precision and recall (Tab. 5.9) compared to the previous two experiments. The above is related to the lack of predicting variables characterising atmospheric ventilation. In this scenario, where wind speed and BLH are not considered, surface temperature

arises as the most significant variable associated with $PM_{2.5}$ and PM_{10} events. However, this presumably relates to being temperature a proxy for the seasonal cycle. As indicated by the AUC-ROC values (0.71-0.79) for experiment 3 in comparison with experiment 2, when including VC and ASI as predicting variables, the models gain the ability to predict about 10 to 15% more true positive or true negatives values (correct PM events and correct PM non-events).

Table 5.9: Logistic Regression Statistics for Experiment 3 (exp3).

Feature Exp3	Coef PM_{10}	Coef $PM_{2.5}$
RH	0.32	-0.54
T	-4.09	-6.68
AP	-0.54	-1.49
wd E	1.72	2.16
wd S	0.18	0.84
wd W	0.51	1.64
wday	1.50	2.27
wend	0.92	2.37
PM ev (μgm^{-3})	46.0	16.0
AUC-ROC	0.71	0.79
accuracy	0.67	0.71
precision	0.67	0.70
recall	0.66	0.74
Total Data	1592	1572

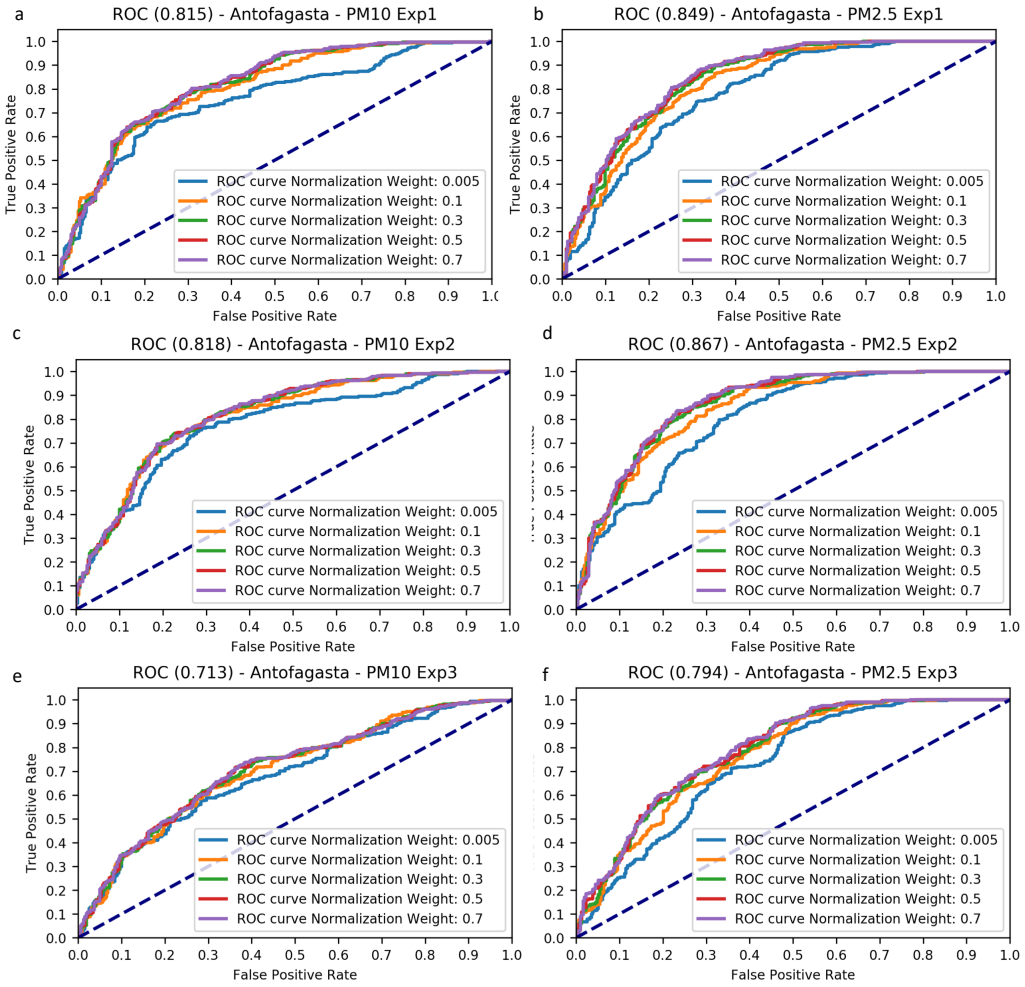

Figure 5.14: ROC curves for normalisation weights (regularisation method) 0.005, 0.1, 0.3, 0.5 and 0.7, for experiments 1, 2 and 3. AUC-ROC value in caption corresponds to the normalisation weight 0.7 which in all cases was the highest AUC-ROC value..

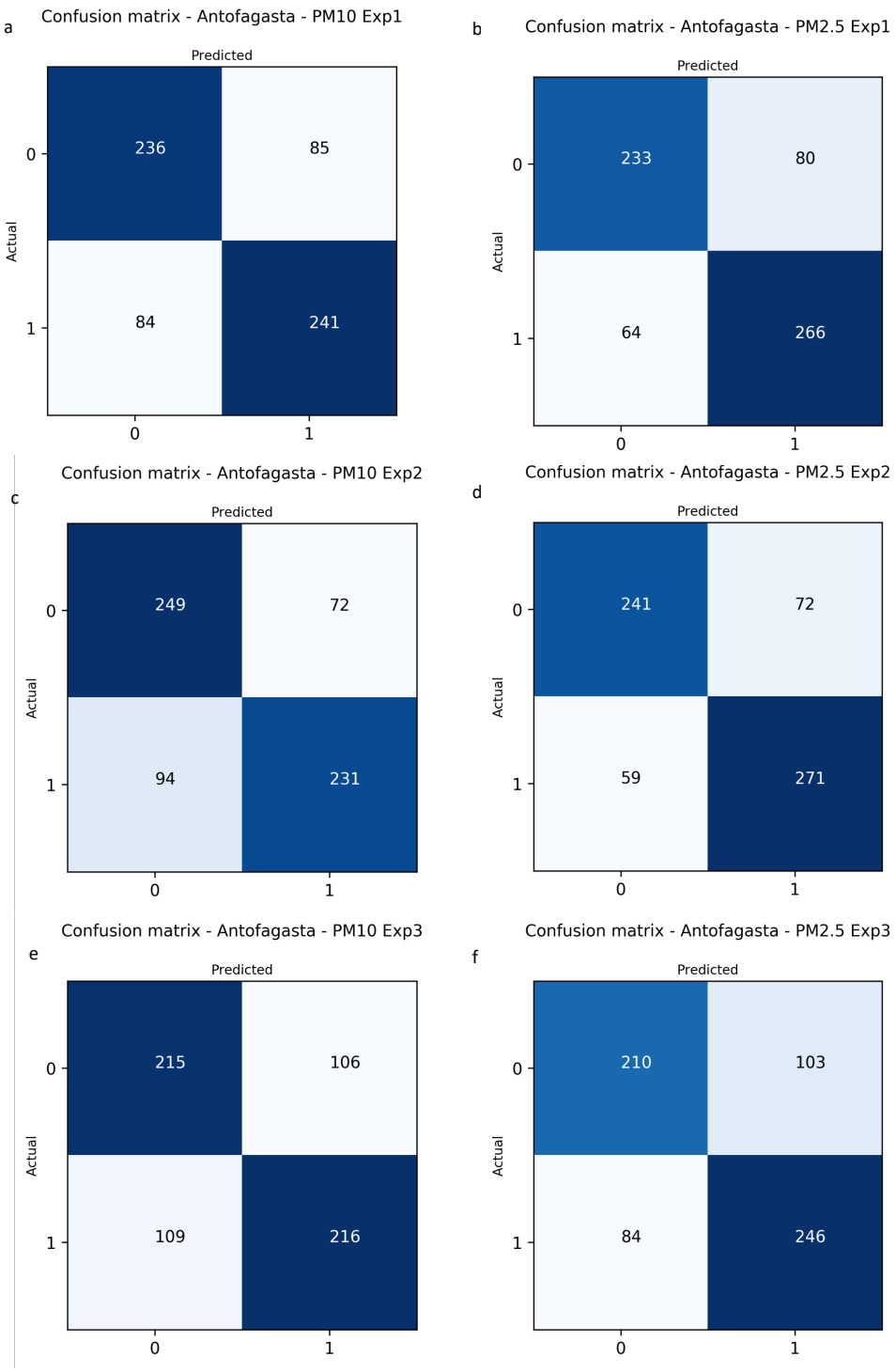

Figure 5.15: Confusion Matrices for Experiments 1, 2 and 3.

A sensitivity test was carried out over a range of PM thresholds ranging from the 60th percentile to the 95th percentile, using the best performing set-up (exper-

iment 2, which includes VC and ASI). The model performance improves as the threshold becomes higher (Tab. 5.10), for example the AUC-ROC increases from 0.75 (60%ile) to 0.87 (for the 95%ile). It is notable that the coefficient for ASI varies little between during these sensitivity tests. However, the parameter for VC doubles in magnitude, suggesting an increasing role as the PM_{10} events become more extreme. Another interesting lessons from this sensitivity test, is that the weekday and weekend variables show a reduced role as the threshold increases (Tab. 5.10) - reaching an equilibrium . This suggests that the potential emissions associated with economic activity, such as anthropogenic traffic emissions, plays a role in determining above-average pollution events, but less so for the extreme ones.

Table 5.10: Sensitivity test for experiment 2. Target: PM_{10} events.

Perct.	PM_{10} (μgm^{-3})	AUC-ROC	Precision	Coef wday	Coef wend	wday/ wend ratio	VC	ASI
60	38.1	0.75	0.71	0.84	0.16	5.3	-2.77	1.4
65	40.0	0.78	0.74	0.71	0.02	35.5	-2.94	1.17
70	42.0	0.77	0.72	1.02	0.29	3.5	-3.7	1.1
75	43.7	0.79	0.77	1.14	0.52	2.2	-4.09	1.07
80	46.0	0.82	0.74	1.11	0.44	2.5	-3.76	1.13
85	49.0	0.83	0.76	1.28	0.71	1.8	-4.18	1.21
90	52.8	0.85	0.74	1.32	0.93	1.4	-5.87	1.13
95	59.6	0.87	0.78	0.85	0.55	1.5	-6.35	1.01

These results contribute to an understanding of both PM variability and the characterisation of events, either mild or extreme. This understanding could have direct implications on local policies and their link with public health, where the prediction of events plays a crucial role. The understanding of the PM variability allows for better targeting of mitigation measures, potential adopting an approach where major emitters are asked to curtail operations if certain meteorological conditions are forecast. The simple, logistic models were able to predict at least 70% of PM events highlighting the potential for more sophisticated air-quality modelling approaches around Antofagasta.

5.7 Summary

Atmospheric ventilation was explored through the ventilation coefficient (VC) in northern Chile from observational, modelled and reanalysed datasets. Consistently, all gridded datasets (WRF341lI-SAM44, RegCM4-SAM44, RegCM4-CL09, and ERA5) reproduce mostly unvented conditions ($VC = 6,000 m^2 s^{-1}$) across the Atacama Desert, which reaches minimum ventilation during wintertime when the boundary layer height (BLH) is lower. On the other hand, during spring and summer, atmospheric ventilation increases due to the higher BLH and the increased wind speed modulated by an intensification of the South Pacific Anticyclone (SPA). The four gridded products analysed reproduce higher VC over inland areas, which is primarily explained by a higher BLH computed over the interior of the Atacama. In particular, RegCM4-SAM44 and RegCM4-CL09 reproduce a considerably higher BLH, and hence VC, linked to a systematic positive temperature bias in RegCM4 over northern Chile.

Regarding the temperature inversion layer height (TILH) along the coast, a decreasing trend is computed from the observational radiosonde data for 1991-2010. This decline is also reproduced for BLH by the four gridded dataset over both the coast and over the inland desert. particularly RegCM4-SAM44 and RegCM4-CL09 reproduce VC in a similar magnitude than the observations (around $4,000 m^2 s^{-1}$).

Respect the role that atmospheric ventilation plays on PM variability, low to high Pearson values were computed between observed $PM_{2.5}$ and observed VC. In particular, high correlations were obtained in Iquique (r=-0.71) and Calama (r=-0.64). Similarly, low to high correlations were computed between PM_{10} and VC. The higher relationships were found in Tocopilla (r=-0.61) and Antofagasta (r=-0.72).

Both PM_{10} and $PM_{2.5}$ events occur mostly under unvented conditions. However, stagnation (ASI) does not arise as a determinant factor during PM events. The exception for the above is Tocopilla, where extreme events of both PM_{10} and $PM_{2.5}$ occur during unvented and stagnant days.

A logistic model comprising VC, ASI , and a set of meteorological variables,

was set up for predicting PM_{10} and $PM_{2.5}$ events in the city of Antofagasta. At least 70% of PM events were successfully predicted, and VC emerged as the most significant predictor in the three experiments performed. ASI significance was considerably lower. This model represents a low-cost initiative for predicting PM events in other cities like Antofagasta where predictions services are not available.

Other potential explanatory variables not included in this study, such as natural emissions or a more sophisticated proxy for anthropogenic emissions, might be expected to result in more accurate predictions in the logistic model. Having built a skilful logistic model, a sensible next step would be to feed it with future trends of modelled meteorological data (such as RCMs outcomes) in order to project the occurrence of events. This would complement analyses based on Earth System Models (ESMs), an example of which is conducted at a coarser spatial and temporal scale in Chapter 6.

Chapter 6

Regional Climate Change and Future Particulate Matter over Northern Chile

Global environmental change is modifying the concentration and composition of pollutants in the atmosphere, which is exacerbated by the extreme sensitivity of air pollution to weather (Fiore et al. (2015); Von Schneidemesser et al. (2015)), atmospheric ventilation and stagnation (Kassomenos et al., 1995; Zhao et al., 2011a). However, the sign of these impacts and their magnitude at a given location depends on both natural and anthropogenic forcings which co-exist at different spatial and time scales (see Chapter 3). Natural forcings comprise changes in climate, synoptic meteorology and natural emissions, such as mineral dust or sea salt, and feedbacks between these forcings and air pollution usually take place in both directions. Indeed, air pollutants can directly impact local weather and long-term climate. Therefore, the understanding of air quality phenomena at local scales is essential for targeting both local air quality policies and climate change mitigation and adaptation strategies.

The Atacama Desert produces an estimate of 35-55 x $10^6 t$ per year of mineral dust directly emitted to the atmosphere (Zender et al., 2003), representing about 2.3-2.6% of the global mineral dust production (Ginoux et al., 2004; Tanaka and Chiba, 2006) (See Chapter 4). A factor to consider is that Particulate Matter (PM)

emissions can impact over a larger area than covered by the local legislation, where the emission sources are located (Fiore et al., 2015). Also, air quality and climate change policies are usually set by separate bodies, and the mitigation of one is not necessarily beneficial for the mitigation of the other (Maione et al., 2016). For example, whereas the global effort of decreasing SO_2 emissions has direct benefits for human health, this reduction prevents it masking greenhouse gas induced warming (Bedsworth, 2011). Nonetheless, drastic measures to mitigate climate change through cutting fossil fuels consumption, certainly represent an opportunity to improve local air quality levels West et al. (2004); Thambiran and Diab (2011). Therefore, whereas climate change policy should consider local air quality standards, the future changes of air quality meteorology may force additional mitigation efforts for meet air quality standards. The above is called the climate penalty (Junkermann et al., 2011; Bedsworth, 2011).

As described in Chapter 3, major climate controls on the Atacama Desert, governing its extreme arid environment and the atmospheric stability of the region, are the South Pacific Anticyclone (SPA), atmospheric moisture, the persistent Temperature Inversion Layer along the Northern Chilean coast, and the Humboldt coastal upwelling system. The dynamic interconnection between these factors is crucial for particulate matter dispersion. The SPA dynamically modulates winds patterns. The coastal upwelling and their effect on Sea Surface Temperature (SST) - along with the Hadley Cell zonal subsidence - contributed to a persistent Temperature Inversion Layer (TIL) along the Atacama latitudes (see §3.1). Both wind patterns and Temperature Inversion Layer Height (TILH) are the main drivers of atmospheric ventilation (Kassomenos et al., 1995). Therefore, there is a strong connection between the major climate drivers of the Atacama Desert and pollutants dispersal in the region. In this section, the main climate and ocean drivers of the Atacama Desert are explored under climate change for a set of Shared Socioeconomic Pathways (SSP) scenarios.

This chapter introduces the connection between climate change and air pollution, including policy implications. Then, the Humboldt coastal upwelling system is discussed in terms of the available literature and its representation in previous

modelling experiments. The third section presents the UK Earth System Model (UKESM1-0-LL), SSP scenarios and the dataset explored in the following sections. The fourth section analyses future regional warming of the Atacama Desert, followed by the study of future vertical stability over Northern Chile in section 5. Finally, projections on future Particulate Matter concentrations over the Atacama Desert are discussed, followed by a summary of the main findings of the chapter.

Elements of this chapter were taken from the article titled 'The future of coastal upwelling in the Humboldt current from model projections' published in Climate Dynamics in 2019 by Damián Oyarzún Valenzuela and Chris M. Brierley (cited as Oyarzún and Brierley (2019)). The paper explored ocean upwelling intensity at different depths in the Humboldt system through the analysis of the upward ocean mass transport variable included in some models contributing to the Coupled Model Intercomparison Project Phase 5 (CMIP5). Its relationship with wind stress and ocean stratification was analysed throughout the Historical experiment (1850-2005) and the Representative Concentration Pathways 8.5 (RCP8.5) climate change scenario (2006-2100). As a complement to this peer-reviewed article, the section Vertical Stability over Northern Chile explores coastal upwelling in the Humboldt system from UKESM1-0-LL. Elements in common are the literature review on coastal upwelling and the methods for studying the upward ocean mass transport variable. Also, the results from UKESM1-0-LL are discussed in the context of the previous results reported in Oyarzún and Brierley (2019).

6.1 Climate Change and Air Pollution

The interaction of air pollutants with the climate in the atmosphere depends on their composition. Whereas some pollutants tend to cool the atmosphere, others lead to warming. Indeed, Fiore et al. (2015) highlighted the interaction of PM with solar radiation and its significant role as a precursor of climate change. However, the effects of aerosols radiation-interactions depend on particles composition. Predominantly, aerosol particles scatter solar radiation (Watson, 2002). As a result, the atmosphere cools due to the short-wave radiation sent back to space interrupting

its path to the surface, what is called the ”aerosol direct effect” (Fiore et al., 2015) (Fig. 6.1). However, whereas this cooling process takes place, constituents of PM such as black carbon (BC), brown carbon (BrC), and mineral dust absorb the solar short-wave radiation, which leads to warming of the atmosphere (aerosol semi-direct effect) (Ramanathan and Feng, 2009; Fiore et al., 2015). The absorption of solar radiation by aerosols can modify the atmospheric temperature profile leading to a temperature inversion layer. As a result, a stable atmosphere and unfavourable ventilation conditions for air pollutants are created (Ackerman et al., 2000; Fiore et al., 2015) (see §3.1). Natural and anthropogenic aerosols act as cloud condensation nuclei (CCN) and cloud ice nuclei (IN) leading to an enhanced number of droplets. Both liquid and crystals droplets modify clouds albedo, making them more reflective (first indirect effect) (Twomey, 1977; Ramanathan and Feng, 2009; Fiore et al., 2015) and increasing their lifetime (aerosols second indirect effect) (Albrecht, 1989; Fiore et al., 2015) (Fig. 6.1). The cooling effects of aerosols have also been linked to decreasing evaporation rates from the land surface, and leading to a weakening of the hydrological cycle at different scales (Ramanathan and Feng, 2009).

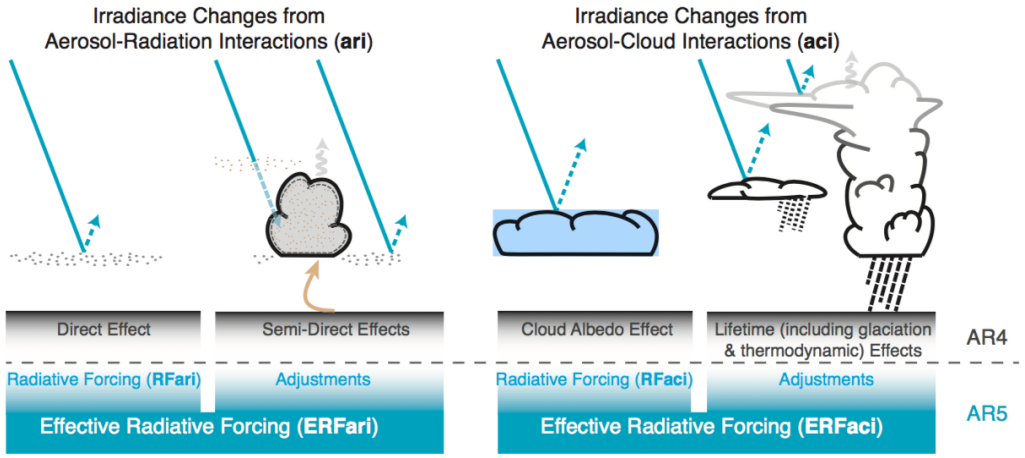

Figure 6.1: Aerosol–radiation (ari) and aerosol–cloud interactions (aci). Blue arrows depict solar radiation and grey arrows terrestrial radiation. (Boucher et al., 2013).

The study of long-term changes in the climate system on air quality has mainly been developed around the understanding of potential changes on air quality mete-

orology. In this regard, future atmospheric ventilation and frequency of stagnation events have been inferred from climate change experiments at local and regional scales. Horton et al. (2014) computed the Air Stagnation Index (ASI), used in Chapter 5, from the CMIP5 dataset in order to analyse the response of stagnations events under global warming at a global scale. The study concluded that the frequency of stagnations events would increase over roughly 55% of the populated areas around the globe, with the highest increases in the tropics and subtropics where stagnation days may rise by 40 days per year. This might result in increasing unfavourable conditions for air quality in populated areas under climate change. Precipitation is a key component for ASI computation, and its seasonality at a regional scale is fundamental to understand long-term climate impacts on PM (Dawson et al., 2014). However, modelled ASI carries a significant uncertainty due to the poor simulation of precipitation, especially in some rainy regions (Horton et al., 2012). With a similar approach, an earlier study by Tai et al. (2012) analysed atmospheric ventilation and air quality meteorology over North America from 15 GCMs contributing to CMIP3. They found that changes on the dominant meteorological modes will lead to an annual mean increase by 0.1 μgm^{-3} of $PM_{2.5}$ over the eastern United States by the year 2050. These results were aligned with those previously reported by Leung and Jr. (2005) based on the Penn State/NCAR Mesoscale Model (MM5). The authors found decreasing trends of atmospheric ventilation along with increasing stagnation conditions across the Midwest USA.

Results at regional and local scales have been reported from the application of regional climate models, such as the Weather Research and Forecasting (WRF) model (Trail et al., 2013; Zhao et al., 2011a). Zhao et al. (2011a) applied WRF at 4 km spatial resolution to analyse future air quality by 2047-2053 in comparison to a baseline in 2000-2006 in California, USA. Air pollution episodes would be closely connected to stagnation events and ventilation conditions given by wind speed, sea breeze intensity and the planetary boundary layer height (PBLH). Whereas better ventilation conditions in the coast of Los Angeles County are expected during summer, in the San Joaquin Valley, stronger stagnation and pollution events are

projected for both summer and winter seasons (Zhao et al., 2011a). Also, aerosols and climate interaction at local scales have been explored using coupled RCM and Chemical Transport Models (CTM) schemes. For instance, Yang et al. (2012) studied the interaction of aerosols with precipitation and stratocumulus cloud systems in Southern Peru and Northern Chile using WRF-Chem in a domain of 9 km horizontal grid spacing. Nonetheless, increasing horizontal resolution does not necessarily guarantee a better model performance. The above because it depends on the location, seasonality, parametrisation schemes and boundary conditions (Rojas, 2006; Flato et al., 2013b; Walther et al., 2013).

The first attempts to analyse and quantify the relationship between potential warming of the atmosphere and heat-absorbing gases dates from the end of the 20th century (Arrhenius, 1896). Since then, until mid-1970s, global warming was strictly linked to CO_2 concentrations in the atmosphere. Since the 1970's other anthropogenic air pollutants emissions, such as O_3, NO_x and CO, have progressively been recognised as greenhouse forcing. However, only during the last decades, air pollution from large urban areas has been accepted of playing a significant role in the atmospheric radiative balance due to the large transport of gases and airborne particles (aerosols) through continents and oceans. Indeed, satellite data reveals that air pollutants can travel trans-oceanic and trans-continent distances within a week (Ramanathan and Feng, 2009). Although the large-scale transport of aerosols is a direct threat to human (Samoli et al., 2011), the interaction of airborne particles in the atmosphere may lead to positive (warming) or negative (cooling) radiative forcing depending on their composition, as mentioned earlier. The radiative forcing for the major PM components, namely sulfate, nitrate, black carbon (BC) and organic carbon (OC), varies in magnitude and sign (Fig. 6.2).

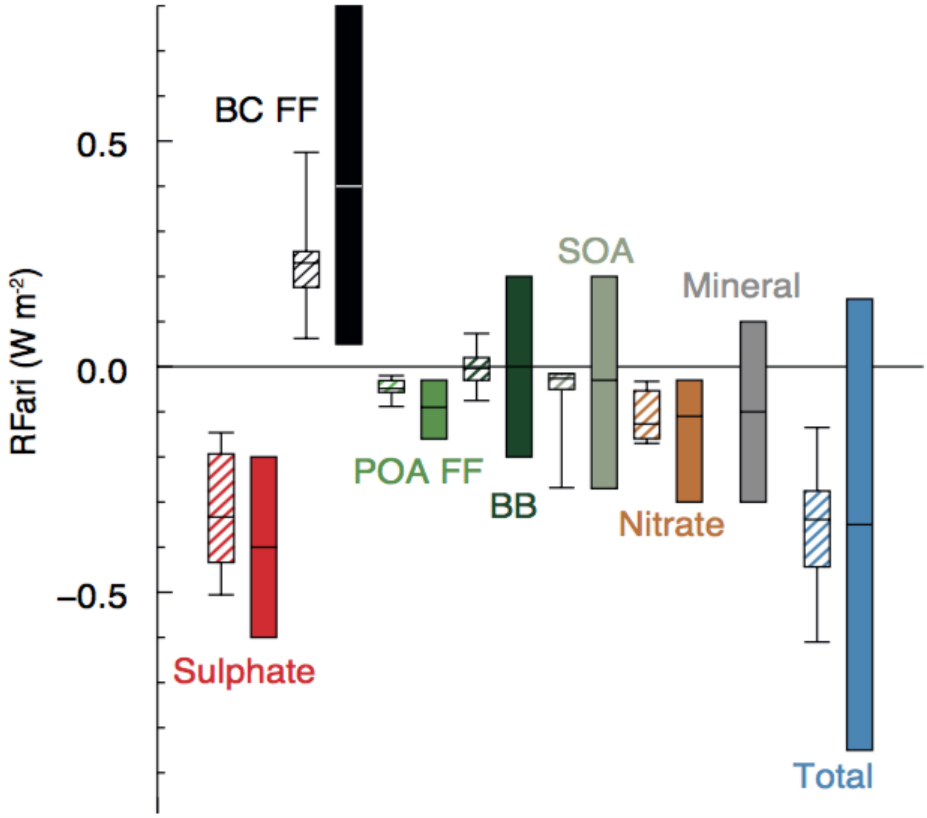

Figure 6.2: Aerosols radiative forcing, annual mean (top of the atmosphere); Black Carbon (CC), Primary and Secondary Organic Aerosols (POA-SOA), Mineral aerosols, biomass burning (BB), Nitrate and Sulphate (Boucher et al., 2013).

Sulfate from SO_2 oxidation is dominant in cloud-albedo interactions being the major cooling contributor for the net aerosol radiative forcing (RF) with a radiative forcing due to aerosol-radiation interaction (RFari) estimated in -0.4 Wm^{-2} with an uncertainty range of -0.6 to -0.2 Wm^{-2} (Myhre et al., 2013). The effective RF (ERF) for sulfate considering radiative (ERFari) and clouds (ERFaci) interactions have been estimated by -0.98 Wm^{-2}, representing about 85% of the overall forcing from aerosols (Zelinka et al., 2014). Similar to sulphate, nitrate from NO_x oxidation also has a negative RFari, estimated in -0.11 Wm^{-2} (Boucher et al., 2013) (Fig. 6.2). Sulfate and nitrate are closely connected due to the common dependence on ammonia. Therefore, although nitrate RFari is relatively small, a decrease of SO_2 concentration could lead to an increase of nitrate due to the higher availability of ammonia in the atmosphere, which tends to favour sulphate particles formation over

nitrate aerosols (Bauer et al., 2007). However, this interaction is complex because of the differences in seasonal patterns, regional spatial variability and particles composition (Fiore et al., 2015).

Organic carbon has a RF estimated by -0.12 Wm^{-2} (Boucher et al., 2013), this considering both primary sources and secondary formation. OC has been observed as a predominant component in high PM pollution events. In fact, Wang et al. (2015b) analysed high concentrations of $PM_{2.5}$ during a drought episode in summer in the southern United States. Based on surface observations and a chemical transport modelling (CTM - GEOS-Chem), they attributed most of the $PM_{2.5}$ concentrations to OC from wildfires. Another carbonaceous component of aerosols is the so-called Brown Carbon (BrC), which is originated from organic matter combustion, and characterised by absorbing components leading to atmospheric warming. However, this is commonly ignored in models (Fiore et al., 2015). Wang et al. (2014) estimated an RF for BrC of -0.11 Wm^{-2} based on absorption optical depth and observational data, and suggest BrC as an absorbent component of OC rather than of BC. BC has a positive radiative forcing (RFari) estimated in +0.64 Wm^{-2}, which comprises anthropogenic fossil and biofuel emissions (+0.40 Wm^{-2}) (Boucher et al., 2013), biomass burning and the albedo effect by deposition on snow and ice surfaces (+0.24 Wm^{-2}) (Myhre et al., 2013). BC has been tied to a decrease in precipitation (Fiore et al., 2015). For instance, Bollasina et al. (2011) found robust connections between large BC anthropogenic emissions and the decrease of precipitations during the Asian monsoon in the second half of the 20^{th} Century.

Estimations of aerosol radiative forcing mainly rely on General Circulation Models (GCM), and Chemistry-Transport Models (CTM) which simulate aerosols abundances based on prescribed aerosols emissions. Although direct observations of aerosols started in the 1960s, most of the long-trend time series of observed aerosol abundance date from the late 1980's (Fiore et al., 2015). The preindustrial abundance of particles has partially been inferred by ice cores (Ruppel et al., 2014; Zdanowicz et al., 2015) and sediments cores (Husain et al., 2008), but these estimations are scarce (Carslaw et al., 2013). These have mainly been obtained from

remote cores, difficult to link to aerosols abundance close to the emission sources (Fiore et al., 2015) or to large-scale concentrations and transport.

An additional challenge for the study of climate change and airborne particles connections is the differentiation between natural and anthropogenic contributions to the total mineral dust load. Anthropocene contributions are primarily associated with agriculture and human influence on erosive soils, where mineral dust is available (Bellouin et al., 2020). The anthropogenic contribution to the global mineral dust load has been estimated by 25%, ranging from 8% in North Africa to 75% in Australia (Ginoux et al., 2012).

As reported in Fig. 6.2, the mineral dust RFari ranges between -0.3 and +0.1 Wm^{-2}, comprising both natural and anthropogenic particles (Boucher et al., 2013). The contribution of anthropogenic aerosols to the mineral dust RF is highly uncertain (Mahowald et al., 2009; Bellouin et al., 2020). The above is because natural and anthropogenic sources of mineral dust are usually coexisting close to each other, being hard to differentiate between them (Mahowald et al., 2009). The negative mean value of RFari (-0.1 Wm^{-2}), presented in Fig. 6.2, comprises the compensating effect of both short-wave scattering (negative feedback; cooling) and long-wave absorption (positive feedback; warming) from the different constituent species of anthropogenic mineral dust (Bellouin et al., 2020).

6.2 The Humboldt Coastal Upwelling System

The eastern boundaries of the Pacific and Atlantic Oceans at subtropical latitudes encompass large areas of coastal upwelling (Sydeman et al., 2014). This upwelling activity is characterized by a relatively shallow vertical transport of mass of water sourced from about 300 m depth (Talley et al., 2011), which is dynamically independent from the ocean gyres systems governing subtropical ocean circulation. An offshore Ekman transport forced by equatorward upwelling-favorable winds has been long accepted as the main driver of the greatest eastern coastal upwelling systems on the Earth (Sverdrup, 1938). The offshore surface transport is replaced by water upwelled from depth (Bakun, 1990; Neelin, 2011; Bakun et al., 2010) leading

to the emergence of cold, nutrient-rich waters at the surface (Bakun, 1990; Warwick and Marjorie, 2001; Diffenbaugh et al., 2003; Bakun et al., 2010; Sydeman et al., 2014; Bakun et al., 2015) (Fig. 6.3). As these systems play a significant role for marine life and hence the fishing industry, variations of coastal upwelling intensity have direct ecological and economic impacts (Vecchi et al., 2006; Bakun et al., 2010; Sydeman et al., 2014; Rykaczewski et al., 2015).

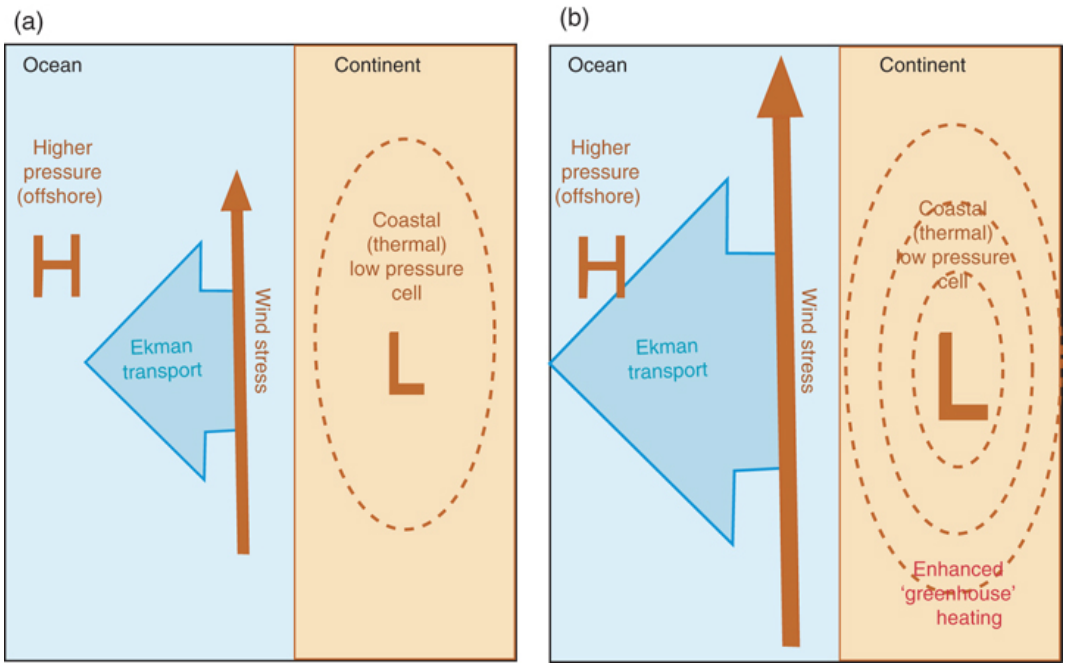

Figure 6.3: Global warming would lead to an intensification of coastal upwelling due to exacerbation of the Ekman transport. As stated by Bakun (1990), this would be explained by an increase of the pressure gradient between the coastland (thermal) low-pressure and the higher surface pressure over the ocean (Bakun et al., 2010).

As described in Chapter 3, the extremely arid conditions of the Atacama Desert are the result of several land-climate-ocean processes taking place at different time and spatial scales. In addition to the zonal forcing given by its location under the subsidence system of the Hadley cell (Houston and Hartley, 2003; Sträter et al., 2010; Muñoz et al., 2011; Schulz et al., 2011), the subtropical anticyclone of the Southeast Pacific leads to a constant southerly airflow. This drives the active coastal upwelling of the Humboldt current along the Northern Chilean and Southern Peruvian coasts. This upwelling system is the most productive system in the world

(Daneri et al., 2000; Bakun et al., 2010; Taylor et al., 2008; Garreaud and Falvey, 2009; Oerder et al., 2015) and provides between 15 to 20% of the world's fish extraction (Sherman and Hempel, 2008).

Because of the Humboldt coastal upwelling, surface waters in the Southeast margin of the Pacific Ocean exhibit a remarkable pattern of cold temperatures in comparison to its zonal mean (Schulz et al., 2011). Both the stable subsidence system (zonal forcing) and the persistent cold sea surface water along the coast (ocean forcing) lead to strong atmospheric stability and the formation of the very persistent temperature inversion layer (TIL) described in §3.1 and §3.2, which inhibits convection and hence precipitation (Houston and Hartley, 2003; Sträter et al., 2010; Muñoz et al., 2011; Schulz et al., 2011).

Although the importance of coastal upwelling systems is widely recognised, their future behaviour is still uncertain (Bakun et al., 2010). The so-called Bakun (1990) hypothesis, based on observational wind data from ship records during the second half of the 20th Century, expects an intensification of coastal upwelling in the Major coastal upwelling systems along the subtropical zones as global warming increases. The mechanism for this is a seasonal strengthening during the warm season of upwelling-favorable winds along-shore, due to an increasing atmospheric pressure gradient driven by a large-scale exacerbation of the land-sea thermal contrast. Sydeman et al. (2014) applied logistic regression methods on observational data from the 20th Century in order to analyse upwelling-favourable wind intensification, in terms of velocity, during the warm season. In accordance with the Bakun (1990) hypothesis, with the exception of the Iberian system, they observed an intensification of wind stress during the warm season in all the major coastal upwelling systems on the planet. This result is similar to other studies based on observed data and modelling outcomes throughout the 20th Century arguing a potential strengthening of upwelling-favourable winds in coastal upwelling areas under future climate change (Cane, 1997; Diffenbaugh et al., 2003; Garreaud and Falvey, 2009).

Belmadani et al. (2013) suggested an intensification of upwelling-favourable winds due to the supported evidence of the expansion of the Hadley cell subsidence

system (Mitas and Clement, 2005; Lu et al., 2007; Garfinkel et al., 2015), and a poleward expansion and intensification of the South Pacific subtropical anticyclone (Li et al., 2013b; Rykaczewski et al., 2015; Aguirre et al., 2019). The above leads to a pronounced increasing trend of wind stress, especially at higher latitudes of the upwelling systems (Belmadani et al., 2013; Aguirre et al., 2019). This phenomenon was consistently observed for the Humboldt system across 13 climate-ocean coupled GCMs contributing to CMIP5 and distinctive seasonalities were identified for the lower and higher latitudes of the Humboldt (Oyarzún and Brierley, 2019). The poleward shift of the the subtropical anticyclone during summer has been associated to an stronger coastal upwelling off the coast of central Chile with almost null activity in winter. Also, observational evidence support that the mentioned migration of the anticyclone under warming and its effect enhancing coastal upwelling would be leading to an exceptional cooling and increase of sea water salinity in the surface 80 m depth layer along the coast of central Chile (Schneider et al., 2017). Several studies have identified this intensification of the upwelling-favorable winds throughout the warm season in the Southern Hemisphere (Bakun et al., 2010; Belmadani et al., 2013; Sydeman et al., 2014; Rykaczewski et al., 2015). Based on 15 global climate models contributing to CMIP3, Garreaud and Falvey (2009) suggested a strengthening of the upwelling-favourable winds in the Humboldt system at the end of the 21st Century. A similar trend has also been reported by in climate model simulations in CMIP5 (Rykaczewski et al., 2015; Wang et al., 2015a). However, different spatial patterns of this intensification were found during the warm season. Whereas wind speeds increase in the southern region of the Humboldt, a weakening of upwelling-favorable winds during summertime is projected nearer the Equator.

A debate about a possible weakening of the Humboldt system during the last Century and future projections has also taken place. Whereas some early studies argued possible errors in wind estimation methods and the equipment used for direct measurements (Peterson and Hasse, 1987; Ramage, 1987; Wright, 1988; Cardone et al., 1990), other research based on observed data and modelling outcomes (Hsieh

and Boer, 1992; Clarke and Lebedev, 1996; Vecchi et al., 2006) directly suggest a potential decline of the Humboldt upwelling system.

6.2.1 Coastal Upwelling in Modelling experiments

Some relevant processes related to coastal upwelling are not fully represented in AOGCMs, because of model resolution (Boville and Gent, 1998; Mote and Mantua, 2002; Burroughs, 2007; Palmer, 2014). For instance, the inaccurate representation of marine stratus clouds in models may lead to errors in wind stress simulations (Mote and Mantua, 2002). In the ocean, mesoscale eddies have a direct effect on water properties and the local current dynamics on a spatial-scale smaller than regular AOGCM ocean grids (Griffies, 2004; Flato et al., 2013a). In addition, because of the interaction with complex mixing processes, the estimation of mesoscale eddies in boundary regions is especially hard (Griffies, 2004).

Different spatial resolutions in couple climate-ocean models, such as AOGCMs, have led to substantially different (and even contradictory) outcomes. The studies by Hsieh and Boer (1992) and Mitchell et al. (1990) based on wind velocity and pressure gradient outcomes suggested a weakening of the major coastal upwelling systems. However, differences have been obtained as the spatial resolution of GCM has improved. While the spatial resolution in the model used by Hsieh and Boer (1992) was 3.75° (roughly 300 to 400 km), Mote and Mantua (2002) based on two GCMs (CSM and HadCM3) with resolution of about 200 km reported no significant variations of wind stress for the EBCS. Nonetheless, recent studies based on modelling approaches at finer resolutions do not necessarily suggest an opposite trend to earlier models. Indeed Vecchi et al. (2006), based on a single GCM (GFDL CM2.1) with a resolution of 2.0° latitude and 2.5° longitude, suggest a potential decline of the Humboldt upwelling system. On the other hand, the 23 coupled GCMs from the CMIP3 dataset with varying resolutions between 0.3° and 5.0° reported mixed results for the Humboldt system without a clear trend (Wang et al., 2010). However, as Miranda et al. (2012) pointed out, there is still a scarcity of coastal upwelling studies based on modelling approaches and the apparently opposing results from models with different resolutions might be partly explained

by the scale of analysis rather than being contradictory projections (Bakun et al., 2010).

6.2.2 Wind Stress and Upward Ocean Mass Transport

There is consensus regarding the role of wind stress as a main driver of coastal upwelling. Therefore, modelling and observational data-based approaches developed to date have mainly been focused on upwelling-favorable wind pattern analyses. Different approaches to conceptualize wind stress in climate models have been adopted. Studies have considered surface wind velocity (Garreaud and Falvey, 2009; Echevin et al., 2011; Sydeman et al., 2014), a combination of wind stress and the Ekman mass transport (Aravena et al., 2014), surface atmospheric pressure gradients as a proxy for winds stress (Clarke and Lebedev, 1996; Vecchi et al., 2006) and also time-averaged eastward (u) and northward (v) velocity components of wind (Yelland and Taylor, 1996; Mote and Mantua, 2002; Bakun et al., 2010; Varela et al., 2015).

As upwelling dynamic is hard to measure in the field, there are not enough data from observations and most of the upwelling phenomenon has been inferred from Global Circulation Models (Talley et al., 2011) or indirect estimations from climate-ocean variables, such as wind stress patterns. In addition, upwelling-related ocean variables such as the sea surface temperature (SST) do not necessarily represent a proper proxy for temporal changes of coastal upwelling (Lorenzo et al., 2005; Chen et al., 2012). Lorenzo et al. (2005) reported positive correlations of upwelling-favorable wind intensity and SST in the California upwelling system. This apparently unexpected relationship was suggested to have arisen from a large-scale heat flux from atmosphere-ocean interactions. Indeed, SST is not only affected by ocean upwelling but also depends on other complex ocean-atmosphere interactions (McCabe et al., 2015; Tim et al., 2015; Schneider et al., 2017).

The upward ocean mass transport variable (kg s^{-1}), described in the following section, and whose name on the Earth System Grid Federation (ESGF) is wmo, represents a direct output from models which can be used as a measure of upwelling activity. This was included in some of the AOGCMs contributing to CMIP5 and the

UKESM1 model contributing to CMIP6. As Griffies et al. (2010) stated, this is an adequate indicator for analysis in part because other physical variables such as vertical velocity can be also derived from it. Despite above, and considering the fact that earlier models contributing to CMIP3 only computed vertical velocity, there is a scarcity in studies of upwelling based on the upward ocean mass transport variable and its relationship with other climate-ocean variables related to coastal upwelling. A study by Xu et al. (2014) in the Southeast Atlantic Ocean incorporated analysis of the upward ocean mass transport, but the main focus was sea-surface temperature biases rather than exploring upwelling.

6.3 UKESM1 Dataset for Climate Change Exploration over the Atacama Desert

Outcomes from the UKESM1 model described in Section 2.5.2 were used for a range of climate change scenarios. This section first described the Shared Socioeconomic Pathways (SSPs) climate change experiments explored in this chapter, followed by the description of the datasets from UKESM1 used.

6.3.1 The Shared Socioeconomic Pathways (SSP)

The Shared Socioeconomic Pathways (SSPs) were developed as the framework of future climate change scenarios. These were used in the IPCC AR5 report but independent of the forcing Representative Concentration Pathways (RCPs) experiments. For CMIP6, SSPs are associated with a radiative forcing scenario. The main goal of Shared Socioeconomic Pathways (SSPs) is to facilitate integrated analysis of the simulated climate change impacts along with vulnerability, mitigation and adaptation strategies (Riahi et al., 2017). In this sense, the challenge for future scenarios formulation is the need for providing both a reasonable description of alternative future climates and a consistent range of possible socioeconomic pathways. As research suggests, an adequate formulation of potential socioeconomic developments might be essential for adaptation and mitigation plans (Field et al., 2014; Riahi et al., 2017).

Five narratives are the core for SSPs scenarios formulation; sustainable development (SSP1), middle-of-the-road development (SSP2), regional rivalry (SSP3), inequality (SSP4), and fossil-fueled development (SSP5). As discussed in Section 3.4 and briefly in previous subsections of this chapter, climate change policies and air quality control are not always aligned. Therefore, mitigation efforts of one of them do not guarantee a positive impact on the other. SSPs formulation addresses this issue by defining socioeconomic scenarios that represent alternative or combined efforts for both climate change and air quality policies.

According to the above, the main components for SSPs developing are the narratives (storylines), scenario drivers (population, urbanisation and GDP), baseline scenarios, mitigation scenarios, country projections and Integrated Assessment Modelling (IAM) outcomes (Riahi et al., 2017). The SSP1 proposes a gradual shift to a sustainable world, including demographic transition associated with educational and health investments, and a well-being-based economic growth. Also, society behaviour tends to lower material and energy consumption, and a reduction in inequality globally. SSP3 involves an increasing nationalism, focused on domestic issues rather than a global joint pathway. Population growth is high in the developing world, local food and energy security is a priority, and the achievement of global environmental goals declines. Inequality persists and intensifies in some regions. Finally, SSP5 proposes a world of intense fossil fuel extraction and consumption, and a high-demand energy lifestyle. There is a rapid technological and economic progress and significant investments in education, health and the promotion for human and social capital. Global population still increases during the next decades under the SSP5 but declines towards the end of the century (Riahi et al., 2017; Rao et al., 2017). As results of the above, some environmental issues are successfully managed, and air pollution is noticeably controlled. This last consideration proposes an interesting paradox in line with the insights reported by previous studies (West et al., 2004; Bedsworth, 2011; Thambiran and Diab, 2011; Maione et al., 2016). A world based on intensive extraction of fossil fuels (SSP5) but strong pollution control, might result in a moderate or even no increase of air pollution

levels. However, a partially fossil-dependant world (SSP3), prioritising domestic issues and weaker pollution controls might lead to significant worsening of air pollution levels.

In this study, UKESM1 data from SSP126, SSP370 and SSP585 are analysed. The SSP126 scenario corresponds to the SSP1 sustainability socio-economic family with a nominal 2.6 Wm^{-2} radiative forcing level by 2100. The second experiment explored in this study, the SSP370, corresponds to a medium-high regional rivalry reference experiment with a nominal 7.0 Wm^{-2} radiative forcing level by 2100. Finally, the SSP585 is a high reference scenario from the SSP5 socio-economic family in the context of a high fossil-fuel-based world, with a nominal 8.5 Wm^{-2} radiative forcing level by 2100 (Meinshausen et al., 2019).

6.3.2 UKESM1 Dataset

Historical and future climate change over the Atacama desert region was explored from modelling outcomes from UKESM1, described in Chapter 2. These variables were analysed throughout the Historical and the SSP126, SSP370, and SSP585 experiments (1850-2100). It is important to state that the three SSPs scenarios share the same Historical simulation, and only the ensemble member r1i1p1f2 was used. Additionally, future Particular Matter (PM_{10} and $PM_{2.5}$) concentrations were explored based on the aerosols species outcomes computed in the aerosol scheme in UKESM1.

The following Table 6.1 summarises the gridded datasets and experiments analysed in the present chapter, and Table 6.2 details the climate and ocean variables considered.

Table 6.1: Gridded Datasets used in this Chapter.

Modelling Dataset	Institution	Horizontal Resolution (°Lat x °Lon)	Experiments	Reference
UKESM1	U.K.'s Met Office and Natural Environment Research Council (NERC)	1.25 x 1.875 (land and atm.) - 1, 1/4 and 1/12° at the Equator (ocean)	Historical (1850-2014), SSP126, SSP370, SSP585 (2015-2100)	Sellar et al. (2019)
ERA5 Reanalysis	European Centre for Medium-Range Weather Forecasts (ECMWF)	31km x 31km (atm.)	(1980-2018)	Copernicus (2017)

Table 6.2: Gridded and Observed Climate and Ocean Variables. *DMC: Antofagasta ground observational site, administrated by the Chile's Meteorological Service (DMC), 1950-2018. For full description see Chapter 2. **CMRS: Radiosounding launching site (once a day at 12:00 UTC) in Cerro Moreno Antofagasta, 1973-2018. Dataset administrated by the University of Wyoming. For full description see Chapter 2. BC: Black carbon, POM: Particulate Organic Matter, ap: atmospheric profile, op: oceanic profile, Freq: output time-frequency

Dataset	Variable Name	Acronym	Unit	Freq
UKESM1	Air temperature	ta (ap)	K	mon
	Surface air temperature	tas	K	mon
	Specific humidity	hus (ap)	ratio	mon
	Relative humidity	hur (ap)	%	mon
	Surface pressure	ps	Pa	mon
	Eastward near-surface wind	uas	ms^{-1}	mon
	Northward near-surface wind	uas	ms^{-1}	mon
	Planetary boundary layer hight	zmla	m	day
	Surface meridional wind stress	tauvo	Nm^{-2}	mon
	Sea water potential temperature	thetao (op)	C	mon
	Upward ocean mass transport	wmo (op)	kgs^{-1}	mon
	PM_{10} sea salt concentration	-	gm^{-3}	mon
	PM_{10} BC aerosol concetration	-	μgm^{-3}	mon
	PM_{10} sulphate aerosol concentration	-	μgm^{-3}	mon
	PM_{10} POM aerosol concentration	-	μgm^{-3}	mon
	PM_{10} dust aerosol concentration	-	μgm^{-3}	mon
	PM_{10} total concentration	-	μgm^{-3}	mon
	$PM_{2.5}$ sea salt concentration	-	μgm^{-3}	mon
	$PM_{2.5}$ BC aerosol concentration	-	μgm^{-3}	mon
	$PM_{2.5}$ sulphate aerosol concentration	-	μgm^{-3}	mon
	$PM_{2.5}$ POM aerosol concentration	-	μgm^{-3}	mon
	$PM_{2.5}$ dust aerosol concentration	-	μgm^{-3}	mon
	$PM_{2.5}$ total concentration	-	μgm^{-3}	mon
WRF341I	Eastward Near-Surface Wind	uas	ms^{-1}	day
	Northward Near-Surface Wind	vas	ms^{-1}	day
	Height of Boundary Layer	zmla	m	day
ERA5	Surface Air Temperature	tas	K	hor
DMC*	Surface Air Temperature	tas	K	-
CMRS**	Air temperature	ta (ap)	K	hor

Gridded data were analysed for the Atacama desert region, hereafter the Atacama region, which is defined as the area in Northern Chile between 18°S - 27°S latitude and 68°W - 73°W longitude, which is highlighted in map plots. For time series computation of atmospheric gridded variables from UKESM1, the areacella vari-

able was used for normalised area-average calculations. In the case of the oceanic gridded variables from UKESM1 (wmo, tauvo, thetao), the region studied corresponds to the Northern Humboldt ocean region described in Oyarzún and Brierley (2019), i.e 16°S - 28°S latitude and from the coastline until 75°W longitude. Over this region, weighted area-averaged time series were computed using the areacello variable from the UKESM1 dataset.

For atmospheric stratification analyses, the environmental lapse rate (ELR) was computed from the UKESM1 temperature dataset. As described by Tiwary and Colls (2010), ELR corresponds to the lapse rate observed over a region in a given time. When this value is lower than the dry adiabatic lapse rate (DALR, 9.8 °C km^{-1}), the atmosphere is usually stable. However, the same air mass could be unstable depending on its content of liquid water. A saturated air mass can convect if the saturated adiabatic lapse rate (SALR) declines under the ELR. Therefore, computing the environmental lapse rate is a direct measure of atmospheric stability. According to the above, a linear regression ($T = f(h)$) was fit for every atmospheric column on the modelling grid cell in the Atacama region, in order to computed the rate (slope) of temperature change by height.

For coastal upwelling analyses, as described in Oyarzún and Brierley (2019), surface meridional wind stress (tauvo) on the upper level of the ocean grid was used as a simplification of the resultant wind stress given the coastal geometry along with the Northern Region of the Humboldt system. Additionally, atmospheric and ocean stratification were analysed through the air and seawater potential temperature profiles, respectively. Upwelling was explored for five different depths: 30, 50, 100, 150 and 300 m. The estimation of upward transport (wmo) is based on the formulation by Adcroft and Hallberg (2006) and summarised by Griffies et al. (2010) as follows:

$$V^s = \rho w^s dxdy \tag{6.1}$$

V^s is the vertical mass transport at s-surface, ρ is the *in situ* or reference density, w^s is the surface flux in the vertical coordinate and $dxdy$ represents the area

of the grid cell. In the terrain following models, the upward mass of water transport is computed by mass-volume conservation whereas in isopycnal models this is computed by the physics of the mass of water across an isopycnal coordinate.

PM_{10} and $PM_{2.5}$ concentrations gridded data were obtained from the Met Office (Turnock et al., 2020). These were inferred from the direct outcomes of the aerosols species in UKESM1: sea salt aerosols, BC aerosol, sulphate aerosol, POM aerosols and dust aerosol. Particulate Matter concentrations were requested as direct output for all CMIP6 contributing models. However, dealing with model ensembles for PM exploration is strongly limited by the inconsistency between the different aerosols schemes across the models. Therefore, PM atmospheric concentrations were calculated based on the individual component mixing ratio of the species aforementioned. Although this is an approximation, it provides a consistent approach (Turnock et al., 2020) which will allow comparing the results reported in this Chapter with other modelling results from the CMIP6 dataset.

6.4 Regional Warming over Northern Chile

This section focuses on the analysis of surface temperature trends from UKESM1 which are discussed in the context of the regional warming previously reported in the IPCC AR5 report. Also, the temperature bias of UKESM1 in the region is explored. Then, future impacts on the moisture content of the atmosphere, specifically specific and relative humidity, are analysed.

6.4.1 Surface Temperature Projections

The projected warming over the Atacama region was computed for the SSP126, SSP370 and SSP585 scenarios in UKESM1 (Fig 6.4). For the Atacama Desert region UKESM1 projects increasing temperatures by 2.4°C under the SSP126, 4.7 °C under the SSP370 and 5.6 °C under the SSP585 scenario in 2071-2100, relative to 1986-2005. The three experiments simulate increasing trends similar their respective global mean (Fig. 6.4). Values from the SSP585 experiment are in a similar order of magnitude than the one computed from the CMIP5 dataset for the extreme climate change scenario RCP8.5, reported in the IPCC AR5, Chapter 12 (Collins

et al., 2013) (Fig 6.5). The spatial distribution for the anomalies for the three experiments is presented in Fig 6.6. The change signal is stronger in the land than the ocean, and a particularly high strong signal is observed at the top of the Andes in the Chilean-Argentinean frontier along Northern Chile, similar to available modelling evidence (Byrne and Ogorman, 2013; Sherwood and Fu, 2014; Berg et al., 2016; Chadwick et al., 2016).

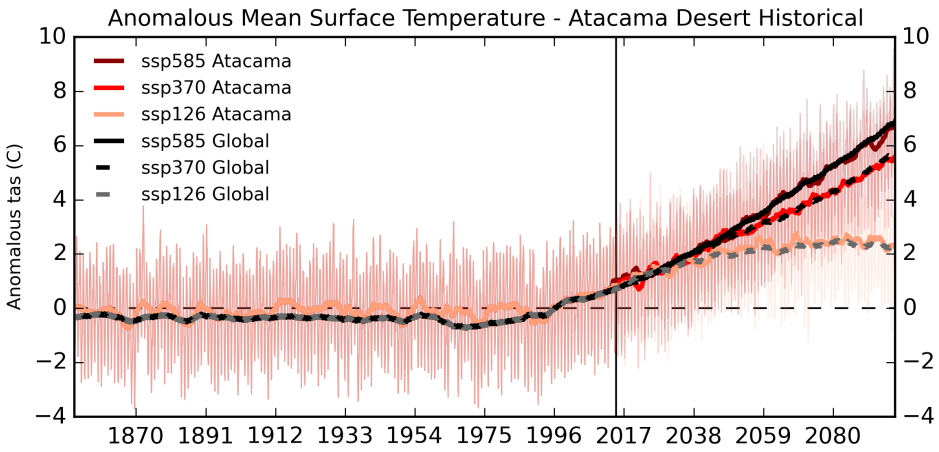

Figure 6.4: Anomalous surface temperature simulated by UKESM1 for the Atacama region under the SSP126, SSP370 and SSP585 scenarios compared with global anomalies for the same experiments. Anomalies with respect to 1986-2005. Solid and dashed lines correspond to the low-pass filtered time series with seasonal and inter-annual cycles removed.

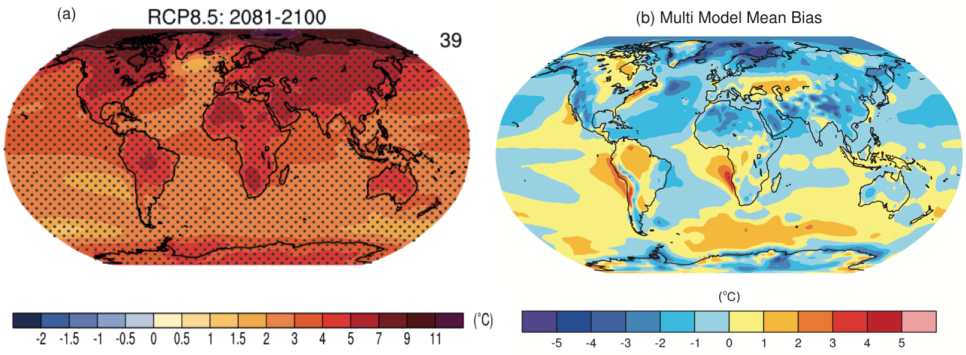

Figure 6.5: a) CMIP5 ensemble mean (39 models) of the climate change signal for surface temperature. Anomalies for 2081-2100 with respect to 1986-2005. Stippling indicates regions where the change is greater than two standard deviation of the internal variability. Taken from Collins et al. (2013). b) Surface temperature bias between the CMIP5 ensemble mean and ERA-Interim ECMWF reanalysis (Dee et al., 2011), 1980-2005. Taken from IPCC AR5, Chapter 9 (Flato et al., 2013a) .

The Fifth Assessment Report of the Intergovernmental Panel on Climate Change IPCC AR5, in its Chapter 9 Evaluation of Climate Models (Flato et al., 2013a), reported a distinctive global pattern for global surface temperature (2 m) bias between the CMIP5 ensemble mean and the ERA-Interim ECMWF reanalysis (Fig 6.5). With the exception of some regions in Eastern North America and Eastern Europe-Western Asia, most of the Northern Hemisphere presents a negative bias exacerbated towards the Arctic. On the other hand, in the Southern Hemisphere with the exception of some regions over Australia, Antarctica and the Western Pacific and Atlantic Oceans, a significant portion of sea and land surface presents a positive bias. This is strongly exacerbated over the Humboldt and Benguela coastal upwelling systems off the coasts of western South America and Africa, respectively. Specifically, over Northern Chile and the Humboldt region a temperature bias until 5 or > 5 ° were computed from the CMIP5 dataset (Fig 6.5). As Flato et al. (2013a) argued, for most of the globe, a bias within +/-2°C was computed. However, significant higher bias was computed for regions such as the North Atlantic ice edge, Himalayas and the Humboldt and Benguela upwelling systems.

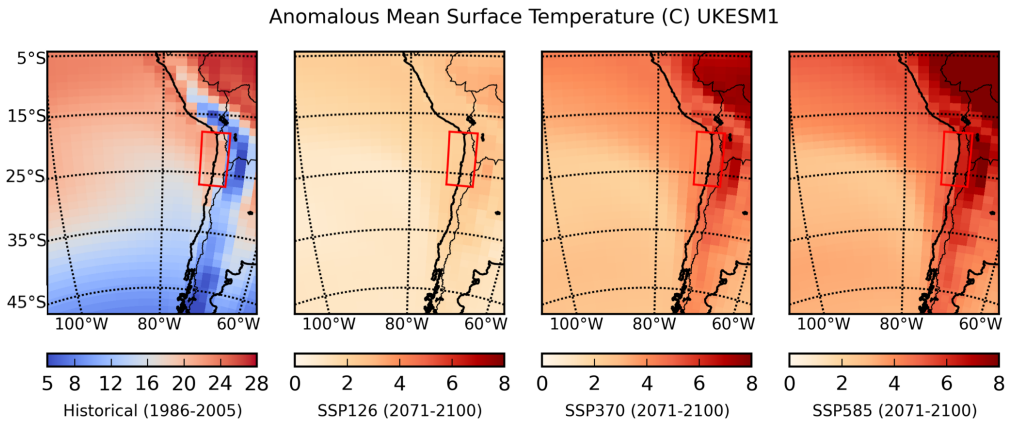

Figure 6.6: Historical and anomalous surface temperature simulated by UKESM1 under the SSP126, SSP370 and SSP585. Anomalies computed for 2071-2100 with respect to 1986-2005. Red box: Atacama region.

From UKESM1 surface temperature outcomes, the UKESM1 temperature bias was calculated with respect to the Fifth generation of ECMWF atmospheric reanalyses of the global climate ERA5 dataset (Copernicus, 2017). Fig. 6.7 (upper) present the correlation between UKESM1 and ERA5 area average surface temperature mean for the Atacama region (18°S and 27°S latitude, 68°S and 73°S longitude) and the modelled grid-cell over the Antofagasta ground observational site (-23.60°S,-70.39°W) administrated by the Chilean Meteorological Service (Dirección Meteorológica de Chile, DMC). The same figure (bottom) shows the seasonal cycle for the bias computed for both areas. At a regional scale (a) there is a high correlation (0.87) between UKESM1 and ERA5, whereas between UKESM1 and the observed data DMC (b) a moderate (0.45) correlation was found. The above is reasonable as both UKESM1 and ERA5 capture the synoptic variability of climate forcers over the Atacama, and the computed bias remain constant at inter-annual time-scales. Although a positive correlation exists between the model and the observational data from Antofagasta, the last is influenced for both the local coastal topography and the urban heat island from the city, located next to the monitoring site. As noticed from the scatter plots, both ERA5 and the observed temperatures are higher than those simulated for UKESM1. This positive bias is consistent with what was reported by Flato et al. (2013a) for the region.

The Humboldt upwelling system has an strong influence on both surface temperature and atmospheric stability in the region. As described in Oyarzún and Brierley (2019) and in §6.2, this northern region of the Humboldt system exhibits a marked seasonality with two peaks during the austral autumn and spring, with almost null upwelling activity (or even negative), during summer. When plotting the UKESM1 bias seasonality, similar behaviour is observed (Fig. 6.7, bottom). During summer, the positive surface temperature bias lies within the to 2°C, similarly magnitude to that reported for most of the globe in Flato et al. (2013a). However, when coastal upwelling activity reaches its peak, the bias with respect to the surface temperature observed at the coastal monitoring site at Antofagasta reaches until 6°C during autumn and spring (Fig. 6.7,d). This supports the argument of the misrepresentation in models of the large effect of coastal upwelling on the local SST, modulating not only its magnitude but also its role in setting the high atmospheric stability governing the climate of the Atacama desert.

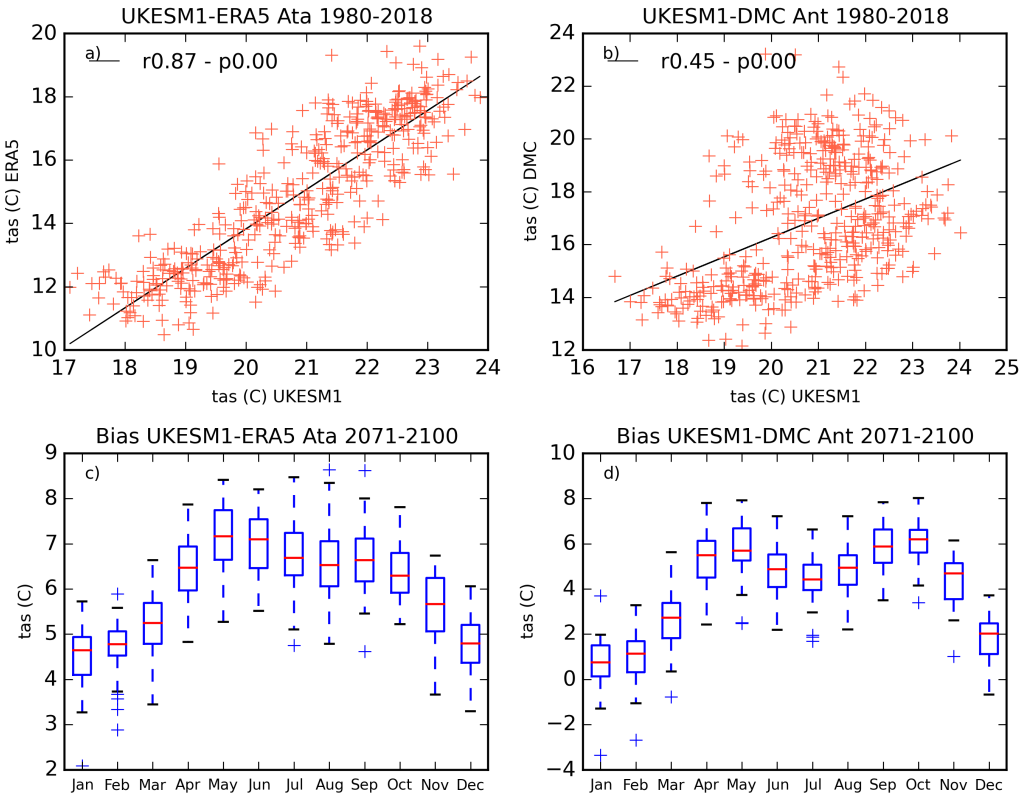

Figure 6.7: upper: linear correlation in 1980-2018 between UKESM1 surface temperature and a) ERA5 reanalysis (Atacama region) and b) observed surface temperature records from the Antofagasta ground monitoring site (modelling cell over the site location). Bottom: seasonal cycle of surface temperature bias between UKESM1 and c) ERA5 and d) surface temperature records from the Antofagasta site.

A significant factor to consider is the substantially higher climate sensitivity computed in CMIP6 models in comparison with their CMIP5 counterparts (Zelinka et al., 2020). Climate sensitivity has been defined by convention as the global mean surface temperature response to a hypothetical CO_2 doubling, which was earlier reported in the range between 1.5 and 4.5 °C (Wainwright and Mulligan, 2013; Zelinka et al., 2020) and recently estimated between 2.0-5.7°C, and 2.3-4.7 °C with 5-95% confidence range (Sherwood et al., 2020). As summarised by Zelinka et al. (2020), the climate sensitivity computed from 27 models contributing to CMIP6 simulate a figure between 1.8 and 5.6 °C, with almost the half of them exceeding 4.5 °C. This increase has been attributed to higher positive clouds feedbacks due to

a decreasing low clouds surface at extratropical latitudes, and its consequent effects on decreasing albedo. The above along with a weaker increase of cloud water content as response to increasing warming. On the other hand, non-cloud feedbacks do not show significant changes. As described in §3.1, the presence of the low clouds deck along the coast of Northern Chile responds to the Hadley Cell subsidence and the quasi-permanent atmospheric stability governing the region, which is also driven by the Humboldt upwelling and SST patterns. Zelinka et al. (2020) proposes an increase in liquid condensate fraction as a possible explanation, but it is still unclear the exact underlying mechanism controlling the strengthened of the cloud feedback in the currently available CMIP6 outcomes (Cesana et al., 2019; Zelinka et al., 2020). Therefore, validation studies based on observations should provide more evidence in the near future, along with the analyses from the entire CMIP6 dataset once available. The above might be especially relevant in regions such as the Western margin of South America where a strong surface temperature bias is reported, and a persistent low cloud deck takes place.

6.4.2 Atmospheric Moisture Projections

Increasing moisture in the air leads to a decrease in air density, promoting instability. As instability enhances atmospheric dispersion, increasing humidity has been linked to decreasing air pollution levels (Tiwary and Colls, 2010). Water cycle studies over a given region usually involve precipitation analyses, which is also a direct input for computing atmospheric stagnation (Wang and Angell, 1999; Horton et al., 2014). However, as the hyper-arid climate of Atacama desert experiences almost no precipitation (Quade et al., 2008; Schulz et al., 2011; Sträter et al., 2010) exploring humidity patterns represents a reasonable approach for exploring the water cycle in the area.

Historical specific and relative humidity present a relatively similar pattern over the Atacama Region (Fig 6.8, middle and bottom). Both exhibit a decreasing trend at the lower troposphere throughout the 20^{th} Century (bottom level in Fig 6.8), which is consistent with decreasing SST trends historically observed in coastal upwelling regions, and also consistent with reported surface trends observed for

low and mid-latitude land regions during the last decades (Simmons et al., 2010; Willett et al., 2014). This decreasing trend continues for both specific and relative humidity during the 21st Century (SSP585), although the reduction is much stronger in surface specific humidity. This surface consistency does not happen aloft, where the two variables show completely opposite behaviour for the tropospheric layer between 950 and 750 hPa.

A progressive and increasing land-ocean contrast is simulated in the SSP126, SSP370 and SSP585 climate change experiments (Fig 6.8, upper panel). Whereas specific humidity is projected to increase over the South Pacific Anticyclone (SPA) region, as expected due to increasing SST, a decreasing trend is simulated over the Atacama Desert not only at the surface but across the atmospheric profile until about 400 hPa (Fig 6.8, middle panel). This result is consistent with the land-ocean contrast described by the global patterns of evaporation change rates reported by Chadwick et al. (2016), who projected decreasing evaporation rates for the Atacama region. As Byrne and O'Gorman (2018) pointed out, climate models predict a decline of relative humidity on land with a relatively unchanged signal over oceans. However, the authors reported increasing trends of specific humidity over land, opposite to the UKESM1 projection presented in Fig 6.8 (middle). In the study, the researchers theorise a connection between SST increase and specific humidity over land, which is particularly strong at low latitudes. However, the anomalous area averages computed by Byrne and O'Gorman (2018) are not representative of the Atacama region, which is governed by the atmospheric subsidence, and the Humboldt coastal upwelling system driving an opposite observed trend of SST.

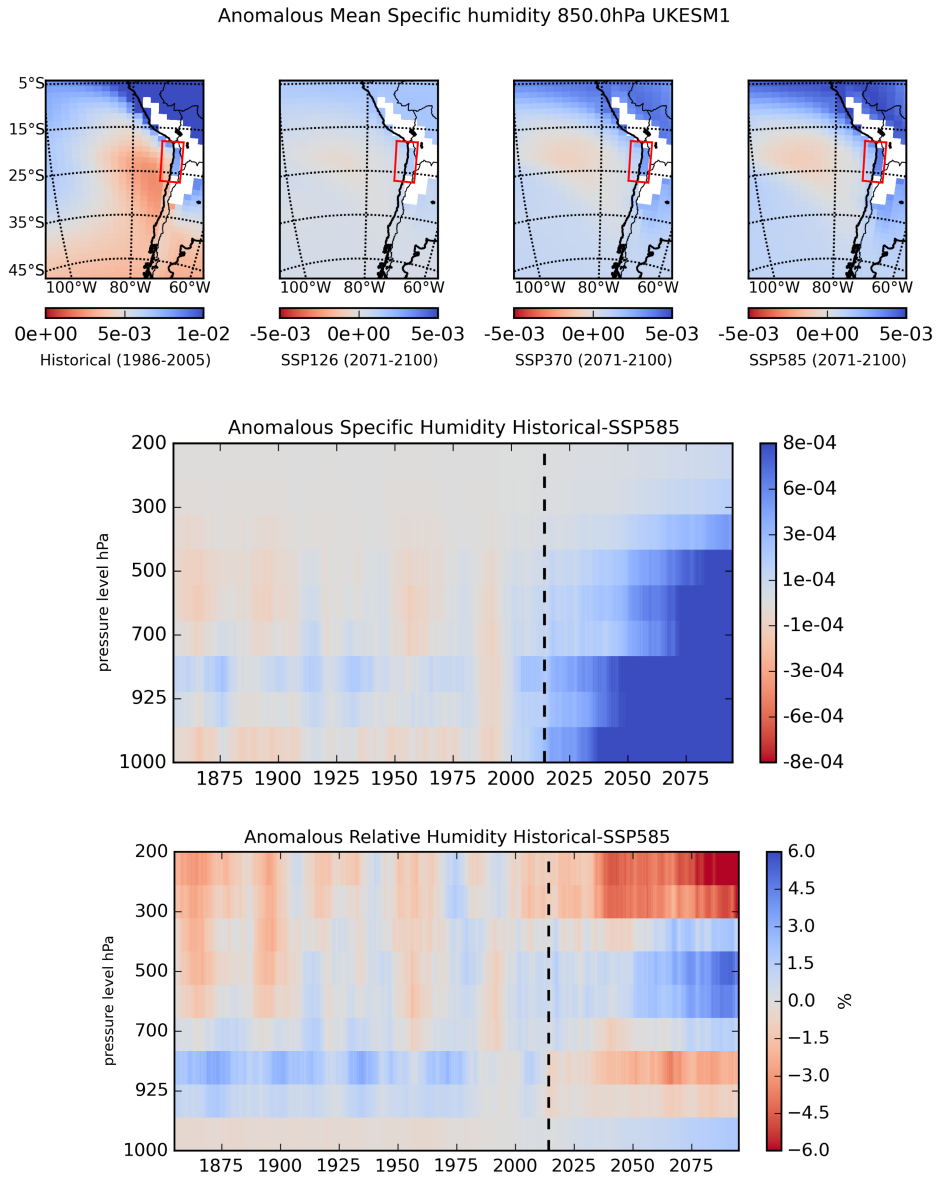

Figure 6.8: Humidity anomalies computed for 2071-2100 with respect to 1986-2005. Upper: Historical and anomalous specific humidity simulated by UKESM1 under the SSP126, SSP370 and SSP585. Red box: Atacama region. White continental regions depict land at 850 hPa. Middle: atmospheric profile of anomalous specific humidity as area-average of the Atacama region box. Bottom: atmospheric profile of anomalous relative humidity as area-average of the Atacama region box. Black vertical dashed lines depict the end of the Historical experiment.

6.5 Atmospheric Stability in Northern Chile

Atmospheric stability is explored through the analysis of the major factors setting the stable conditions over the region (see §3.1). First, the South Pacific Anticyclone is studied along with its role in controlling regional wind patterns. Second, atmospheric stratification is explored along with future trends of the Atmospheric Boundary Layer Height. Finally, the future of the Humboldt coastal upwelling is discussed as well as its connection with ocean stratification.

6.5.1 The South Pacific Anticyclone under Climate Change

The South Pacific Anticyclone (SPA) is the primary driver of winds patterns along the coast of Central and Northern Chile. Its seasonality, analysed below, directly modulates the intensity of both zonal and meridional wind components, which on land are locally modified by topography. Therefore, as described in Chapter 5, SPA seasonality set the annual variability of atmospheric ventilation. In order to explore future changes on the SPA expansion and intensity, surface air pressure fields from UKESM1 were explored throughout the 20th and 21st Centuries. Fig 6.9 depicts the spatial change of the SPA in 2071-2100 relative to 1986-2005. The SPA occurs further southward during the austral summer reaching slightly higher surface pressure at its centre of about 1023.5 hPa in comparison with 1023.2 hPa in winter, as mean value for 1986-2005. Also, in summer the SPA shifts westward from an average latitude of -91°W to about -98°W longitude at its centre point, which results in a decrease of the surface pressure over the Atacama Desert region. This seasonal behaviour prevails in the simulated trends for the SSP126, SSP370 and SSP 585 experiments. However, an extension and intensification of the SPA are simulated to take place during both seasons, as represented by the surface pressure anomalies computed for 2071-2100 (Fig 6.9). Specifically, under the SSP585 scenario, when the climate change signal is stronger, the SPA centre point would reach 1025.1 hPa at -29°S latitude in the austral winter, while in summer the SPA centre would reach 1025.4 hPa at -37°S latitude as the monthly average for 2071-2100.

Since high-pressure systems are associated with enhanced atmospheric stagnation and a decline of ventilation, Anticyclone forcing has been found correlated

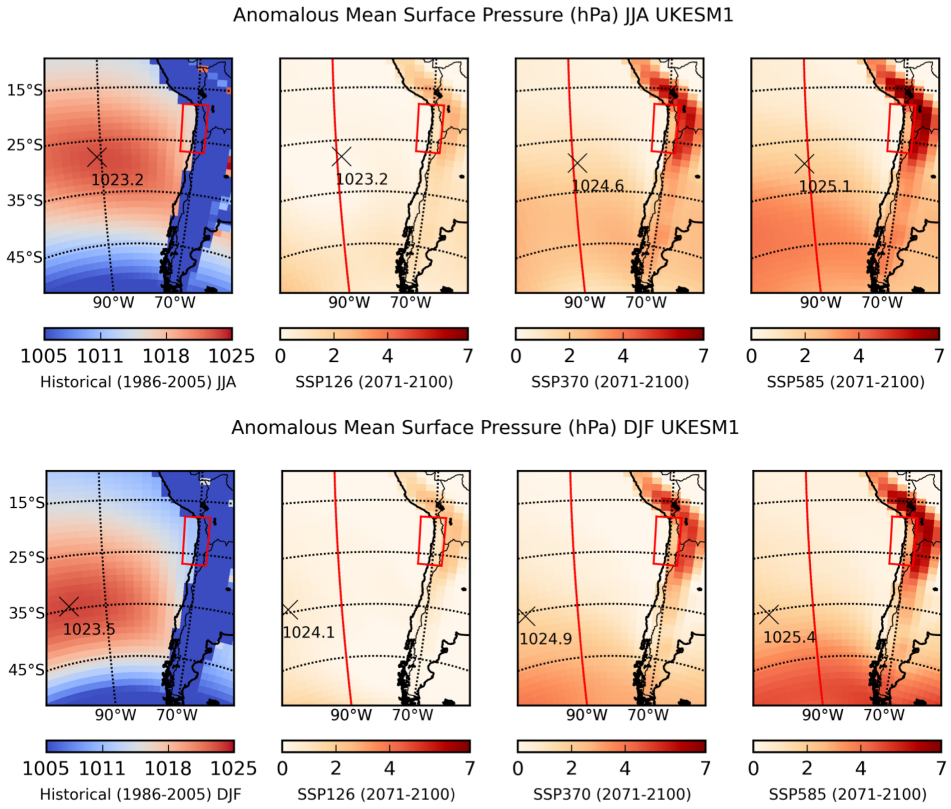

Figure 6.9: Surface pressure anomalies simulated by UKESM1 for 2071-2100 with respect to 1986-2005 for the Historical and under the SSP126, SSP370 and SSP585 scenarios in winter (upper) and summer(bottom). Red meridians corresponds to -90°W longitude for which the SPA transects in 6.10 were computed. Crosses depicts the centre of the SPA calculated as maximum surface pressure period mean under the Historical and each SSP scenario. Red box: Atacama region.

with a worsening of air quality (Buchholz et al., 2010; Tiwary and Colls, 2010; Vallero, 2014; Grundstrom et al., 2015). For the Atacama Desert area, an increase of surface pressure is projected in both summer and winter (Fig 6.9), with annual mean anomalies up to 0.5, 1.2 and 1.5 hPa in 2071-2100 under the SSP126, SSP370

and SSP585, respectively, in comparison with 1986-2005 values.

The expansion of the SPA is depicted in Fig 6.10 taken as meridional reference -90 °W (red meridian in Fig 6.9). Whereas the Northern margin of the SPA is projected to remain almost constant during the Historical and the three SSP experiments, the Southern edge displaces progressively reaching 1022 hPa threshold at about -44°S latitude under the fossil-fuel-intense world experiment SSP585 by the end of the 21st Century. Under the SSP126 and SSP370 scenarios, this surface pressure is reached at about -40 and -41 °S latitude, respectively. As observable in Fig 6.10, and according with the SPA seasonality captured by UKESM1 throughout the 20th and 21st Centuries (Fig Fig 6.9), the maximum latitudinal surface pressure computed for the -90 °W (black crosses) profile progressively shift southward in the three experiments analysed.

Changes in the SPA will necessarily drive changes on winds patters along the western edged of Southern South America. As SPA exhibits a marked seasonal cycle, wind patterns are also expected to respond seasonally to climate change. Fig 6.11 presents the historical wind magnitude (1986-2005) and future anomalies (2071-2100) for the eastern and northern near-surface wind components during winter. Similarly, summertime changes are presented in Fig 6.12. In winter, meridional winds along the Chilean coastline reach their maximum at lower latitudes than in summer, due to the position of the SPA closer to the Equator. This behaviour is progressively exacerbated under the three SSPs experiment analysed. In winter the maximum anomalies of northern near-surface winds are simulated around -35 °S latitude whereas in summer these migrate towards higher latitudes until about -40 °S latitude, consistent with the SPA seasonality. As observed in leftmost maps in Figures 6.11 and 6.12, the zonal component of winds over the ocean is highly influenced by the latitudinal edges of the SPA, which in turn reproduce higher positive anomalies over the land in the Atacama region in both seasons. As described in Section 3.1 based on substantial literature (Houston and Hartley, 2003; Sträter et al., 2010; Muñoz et al., 2011; Schulz et al., 2011), wind over the Atacama desert are dominated by a strong sea-land zonal component, positive (eastward) in day-time

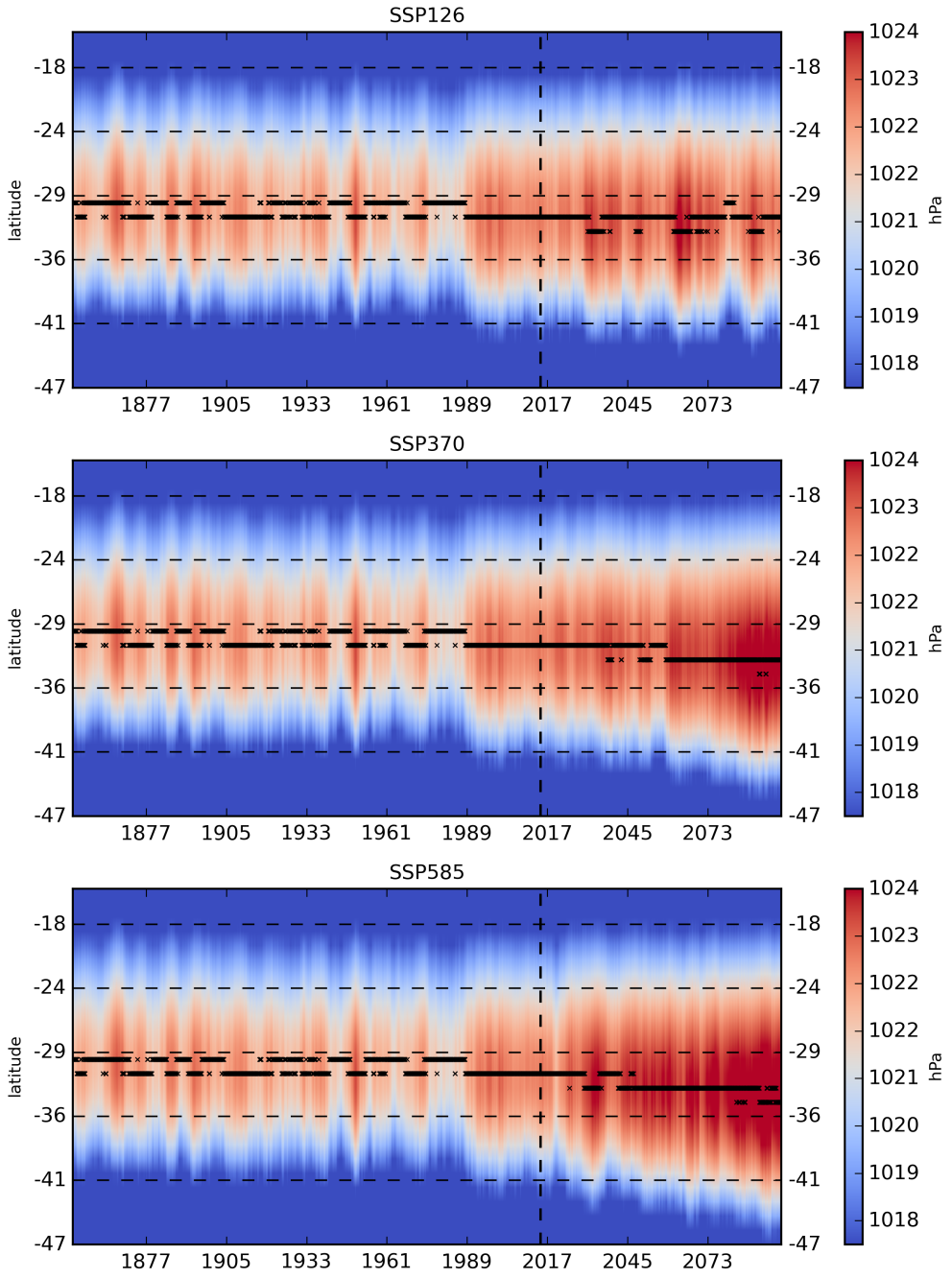

Figure 6.10: Surface pressure longitudinal transects calculated at -90°W longitude throughout the Historical and SSP126 (upper), SSP370 (middle) and SSP585 (bottom) experiments. Black vertical dashed lines depict the end of the Historical experiment. Black crosses represent the latitude of the maximum surface pressure monthly mean for each month in 1850-2100.

and negative (westward) in nigh-time. The daily cycle is dominated by the land-ocean gradient of atmospheric pressure and radiative responses, but wind intensity

at synoptic scales is strongly dependant on the SPA (Garreaud and Falvey, 2009).

Figure 6.13 presents the resultant wind speed and its transient climate signal as area-average for the Atacama region. As reported in previous literature (Rykaczewski and Checkley, 2008; Wang et al., 2010; Aguirre et al., 2019), wind speed over Northern Chile is expected to increase for the three SSPs scenarios. Also, its seasonality is consistent with the changes previously described for both wind components. A strong wind speed seasonality is simulated with peaks in May and October. A similar seasonal influence is projected for the climate change signal. It will reach its maximum in wintertime when SPA intensification is closer to the Atacama, and minimum in summer when the change seems to be less sensitive to the SPA. As will be discussed in the following subsections, this seasonality is consistent with northward wind stress annual cycle. Thus, same seasonality is exhibited by the coastal upwelling at these latitudes, the so-called Northern Humboldt region (Oyarzún and Brierley, 2019).

6.5.2 Atmospheric Stratification and the Planetary Boundary Layer

Ocean stratification due to increasing warming has been widely discussed in terms of its impact on marine ecosystems, ocean circulation (Roemmich and McGowan, 1995; Sigman et al., 2004; Chhak and Di Lorenzo, 2007; Capotondi et al., 2012; Vincent et al., 2014; Nummelin et al., 2016), and its connection with coastal upwelling (Oyarzún and Brierley, 2019). However, there is a scarcity of studies analysing atmospheric stratification and its links with other atmospheric phenomena such as BLH trends and surface pressure patterns. In this sense, the study of atmospheric stratification and its connection with major climate drivers governing the hyper-arid climatology of the Atacama region has received scant attention. Existing studies have focused on the characterisation of the temperature inversion layer based on radiosonde data (Rutllant et al., 2003; Schulz et al., 2011; Rutllant et al., 2013) and the analysis of land-ocean temperature contrasts Falvey and Garreaud (2009) along the coast of Northern Chile.

A more stratified and stable atmosphere might lead to adverse conditions for

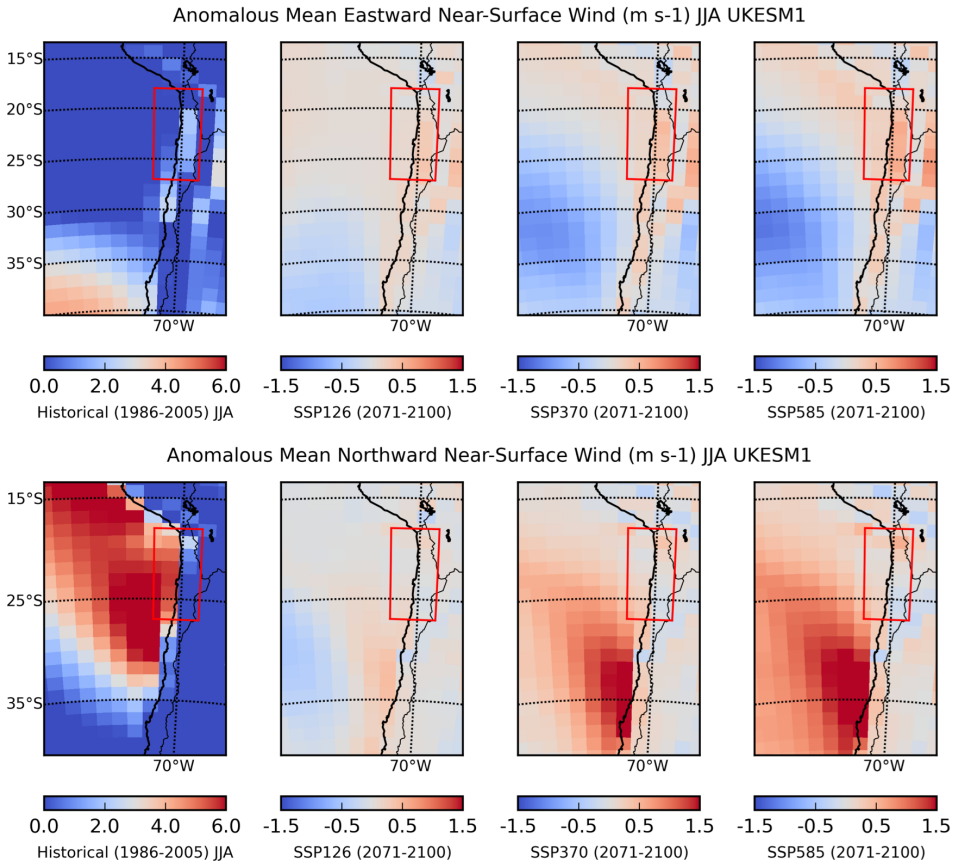

Figure 6.11: Eastward near-surface wind anomalies simulated by UKESM1 for 2071-2100 with respect to 1986-2005 for the Historical and under the SSP126, SSP370 and SSP585 scenarios in winter (upper) and summer(bottom). Red box: Atacama region.

pollutants dispersion, as opposed to unstable or neutral states where pollutants disperse and dilute under stronger mixing and convection (Tiwary and Colls, 2010). Additionally, a worst-case scenario for atmospheric stability is usually given by the presence of a temperature inversion layer, whose base-height usually coincides with the deep of the Boundary Layer height (BLH) (Garrat, 1992; Tiwary and Colls, 2010; Schulz et al., 2011). UKESM1 suggests an increased stratification of the Tro-

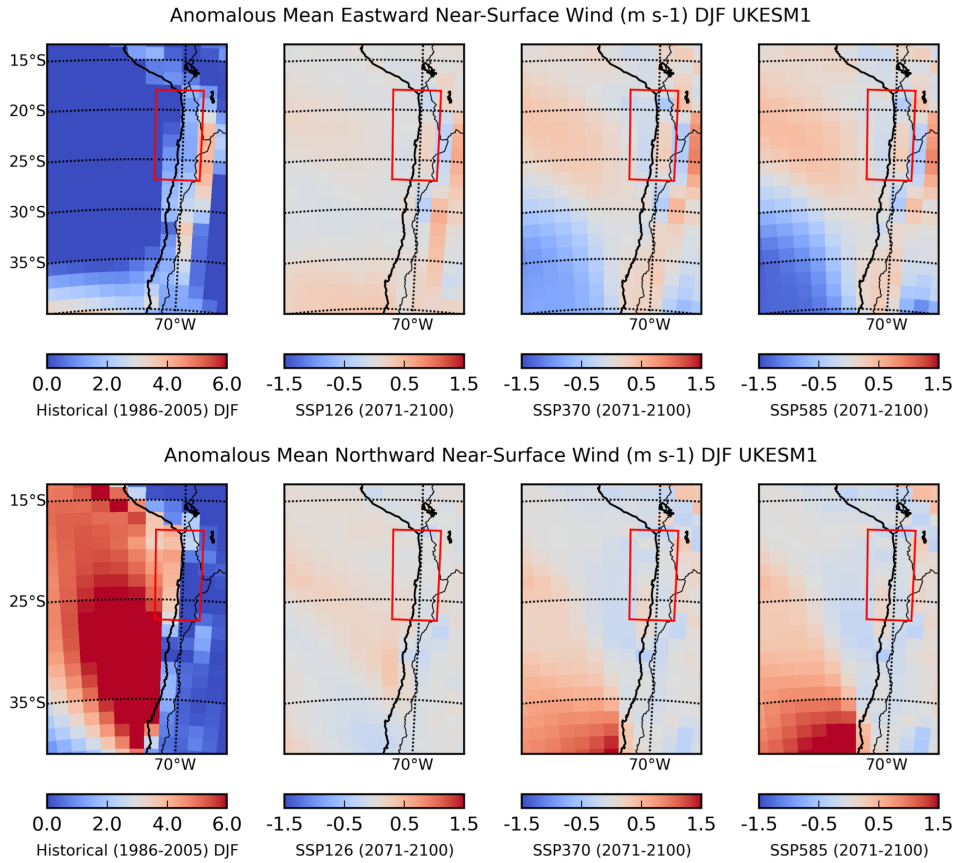

Figure 6.12: Northward near-surface wind anomalies simulated by UKESM1 for 2071-2100 with respect to 1986-2005 for the Historical and under the SSP126, SSP370 and SSP585 scenarios in winter (upper) and summer(bottom). Red box: Atacama region.

posphere throughout the 20th and 21st Centuries, which is especially pronounced from the the mid-21st Century under the SSP370 and SSP585 scenarios (Fig. 6.14). During the SSP126, although stratification would arise as results of moderate global warming, this would remain mostly constant since the 2050s. In Fig. 6.14, it is noticeable the continuous increase of air temperature in the entire tropospheric profile as anomalies have been computed with respect to 1871-1900. However, since the

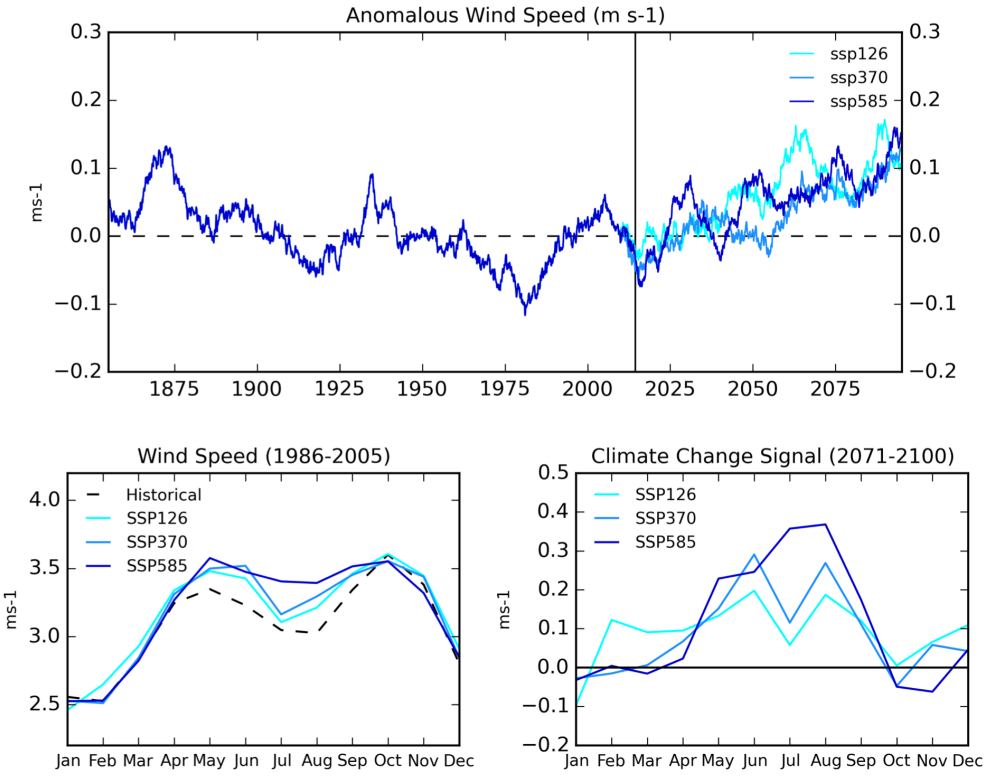

Figure 6.13: Anomalous wind speed simulated by UKESM1 throughout the Historical and SSP126, SSP370 and SSP585 scenarios. Anomalies computed with respect to 1986-2005. Bottom left: seasonal cycle for 1986-2005. Bottom right: Climate change signal in 2071-2100 with respect to 1986-2005.

present (dashed vertical black line) increasing temperature across the entire profile is projected to rise substantially. During the SSP585, air temperature would rise over 6 degrees from 950 hPa up to the top of the Troposphere towards the end of the Century. At higher altitudes, from around 500 hPa, the temperature might experience that increment since the mid-century. The decreasing observed SST trend reported for the area (Falvey and Garreaud, 2009) is not reproduced by UKESM1 simulations. Indeed, as argued by the authors, models have historically had difficul-

ties reproducing the cooling of the sea surface over coastal upwelling regions.

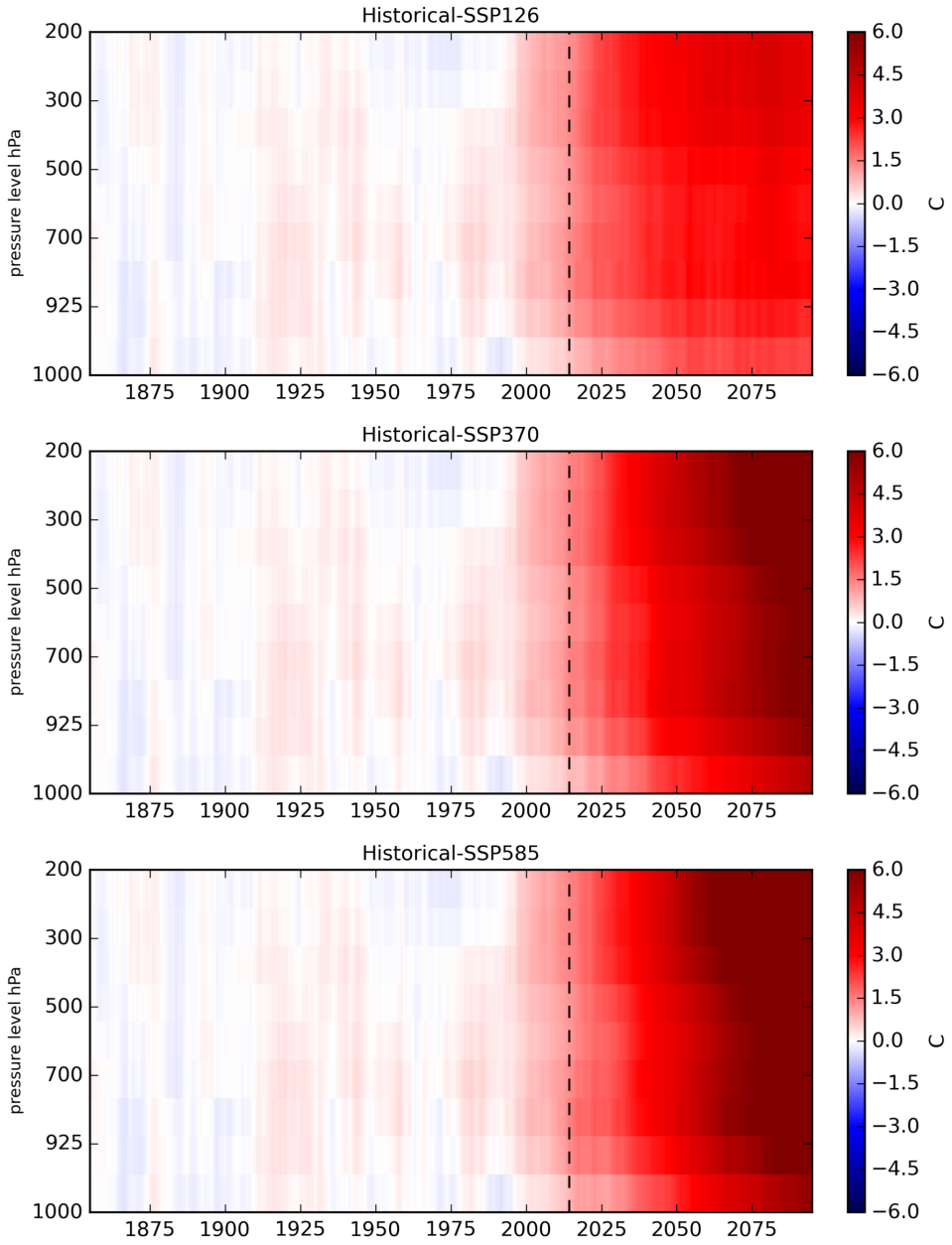

Figure 6.14: Atmospheric temperature stratification. Atmospheric profiles of anomalous air temperature. Anomalies computed as area-average of the Atacama region box for 2071-2100 with respect to 1871-1900 throughout the Historical and a) SSP126, b)SSP370 and c) SSP585 scenario. Black vertical dashed lines depict the end of the Historical experiment.

When plotting boundary layer projections over the Atacama region, a substantial decline is simulated throughout the 20th Century, and during the 21st Century under the SSP585 (Fig 6.15). BLH seasonality is consistent with the seasonality computed for the Temperature Inversion Layer (TILH) from the observational radiosounding dataset in Cerro Moreno Antofagasta (-23.65°S latitude, see §3.2). It exhibits a defined annual cycle with high layer depth during summer and lower in winter (Fig 6.15).

Modelled BLH seems to decline consistently along with increasing stratification during the SSP585 experiment (-39 m in 2071-2100). Although BLH also decreases during the Historical experiment (1850-2014), stratification change is not visually detectable in this period. The decreasing signal of BLH is also detected for the TILH computed from the coastal radiosonde observations (Fig 6.16, upper). However, TILH changes are one order of magnitude higher, which is expected as these are instant measurements recorded once a day at 12:00 UTC. This reduction in the TILH base was also reported in a previous study by Schulz et al. (2011). The authors attributed the observed negative trend to the sea surface cooling previously reported by Falvey and Garreaud (2009) for the Humboldt region.

In order to understand atmospheric stratification and a potential connection with BLH decline, the environmental lapse rate (ELR) was computed from UKESM1 vertical temperature data (see Methods subsection). The results are plotted along with the BLH time series under the SSP585 scenario in Fig 6.16. The temperature lapse rate did not exhibit substantial changes until the 1990's decade when an abrupt decline begins and extents during the 21st Century. Despite that BLH also declined, the connection between both seems to depend on the time scale of the analysis. BLH exhibits an opposite seasonal cycle than the lapse rate. In summer, the boundary layer base is higher, whereas lower lapse rates take place. Therefore, negative correlations are computed at annual time scales. On the other hand, when computing decadal or inter-annual time scale correlations (after removing the seasonal cycle), positive values are obtained. Although enhanced warming is expected to lead a reduction in lapse rates, their final effect on atmospheric sta-

bility will depend on the saturated lapse rates values. In the case of the Atacama, it seems reasonable to interpret that a decline of lapse rates would lead to increased stability since saturated air masses rarely form. Also, the atmosphere tends to be stable under dry conditions (Marshall and Plumb, 2008).

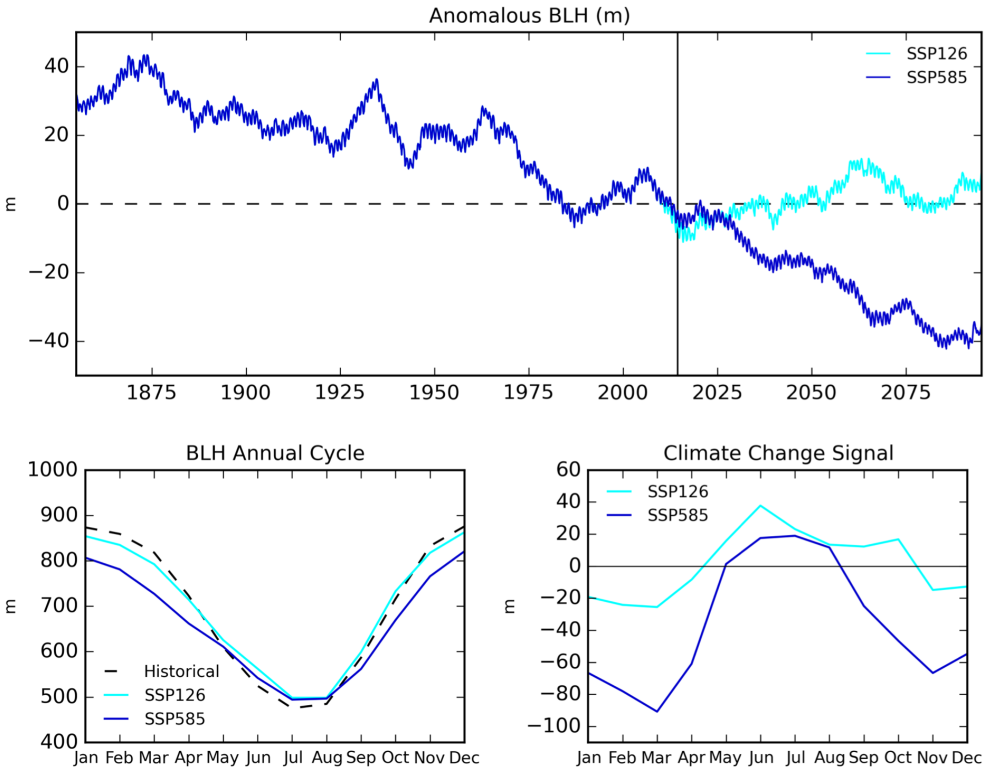

Figure 6.15: Anomalous Boundary Layer height (BLH) simulated by UKESM1 and computed as area-average of the Atacama region throughout the Historical and SSP126, SSP370 and SSP585 scenarios. Anomalies computed with respect to 1986-2005. Bottom left: seasonal cycle for 1986-2005. Bottom right: Climate change signal in 2071-2100 with respect to 1986-2005.

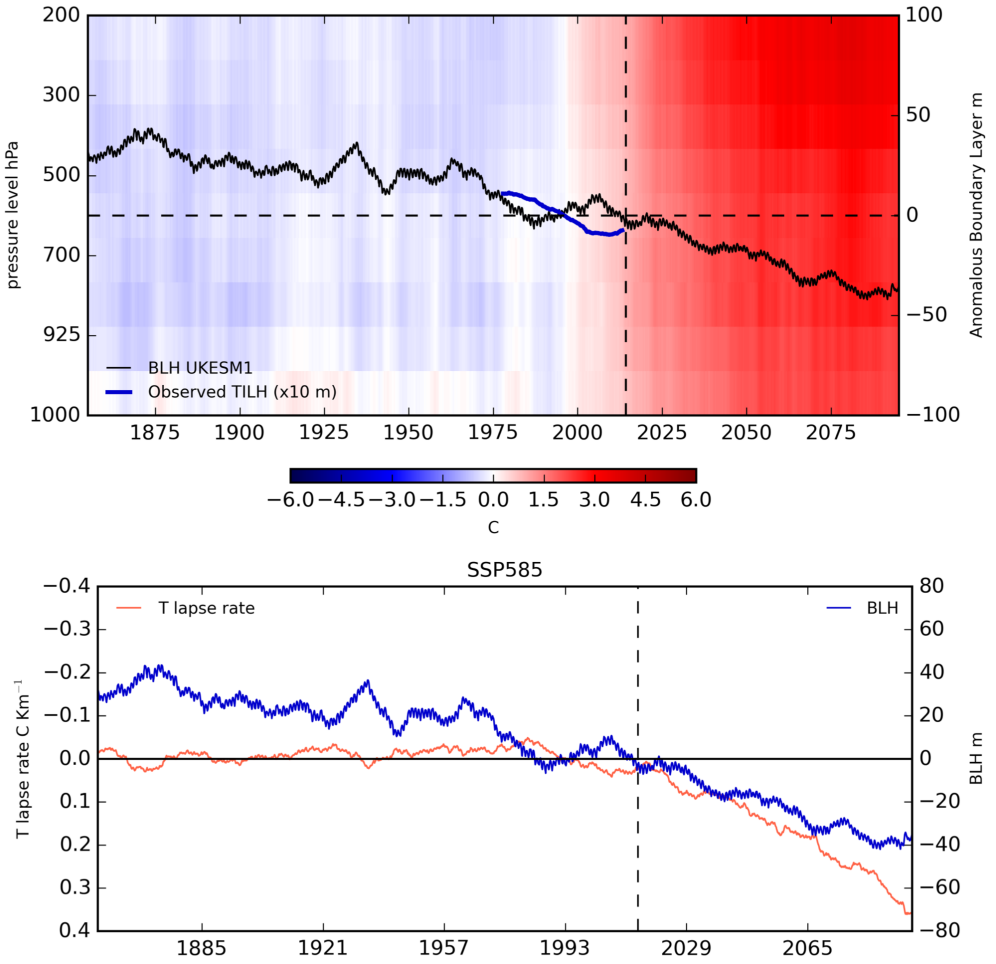

Figure 6.16: Upper: atmospheric temperature stratification. Atmospheric profile of anomalous air temperature. Anomalies computed as area-average of the Atacama region box for 2071-2100 with respect to 1986-2005 throughout the Historical and SSP585 scenario. Black vertical dashed lines depict the end of the Historical experiment. Black solid line corresponds to anomalous BLH timeserie simulated by UKESM1 and computed as area-average of the Atacama region for 2071-2100 with respect to 1986-2005 throughout the Historical and SSP585 scenario. Blue line corresponds to the anomalous Temperature Inversion Layer Height (scaled by a factor of 0.1) for the same period, calculated from air temperature data observed at Cerro Moreno radiosonde site in Antofagasta (see §3.2). Bottom: Blue line depicts anomalous BLH presented in upper plot. Orange solid line corresponds to the anomalous temperature lapse rate computed as area-average of the individual grid cell rates calculated over the Atacama Region.

The global spatial distribution of the BLH change under the SSP585 scenario

is presented in Fig 6.17. Globally, apart from the oceans, large regions where BLH is projected to decline are Southern South America, including the Atacama region, Eastern USA, the Saharan region, and the subtropical latitudes in Asia. Areas exposed to both coastal upwelling and Anticyclones coincide with depicting decreasing trends, such as California (Western North America), Atacama (Western South America), Benguela (Western Southern Africa) and Canary (Western Northern Africa and Southwest Europe), the so-called Eastern Boundary Current Systems (EBCS). A strong negative correlation was found in the Atacama region between monthly mean surface air pressure, dominated by the SPA, and BLH (r=0.81). Indeed, BLH is higher, when the Anticyclone migrates southward, and lower surface pressures take place. Although it is not possible to establish causality, a plausible explanation is that the increase of BLH during summer seems to respond to both a decrease of the temperature lapse rate, typical of a warmer atmosphere and a decrease in surface pressure associated to the migration of the SPA to the south. At longer time scales during the 21st Century, a pronounced expansion and intensification of the SPA would lead to a decline of BLH, along with a decline in temperature lapse rate promoting atmospheric stability. The above, in addition to the observed decline of SST on promoting atmospheric stability (Falvey and Garreaud, 2009).

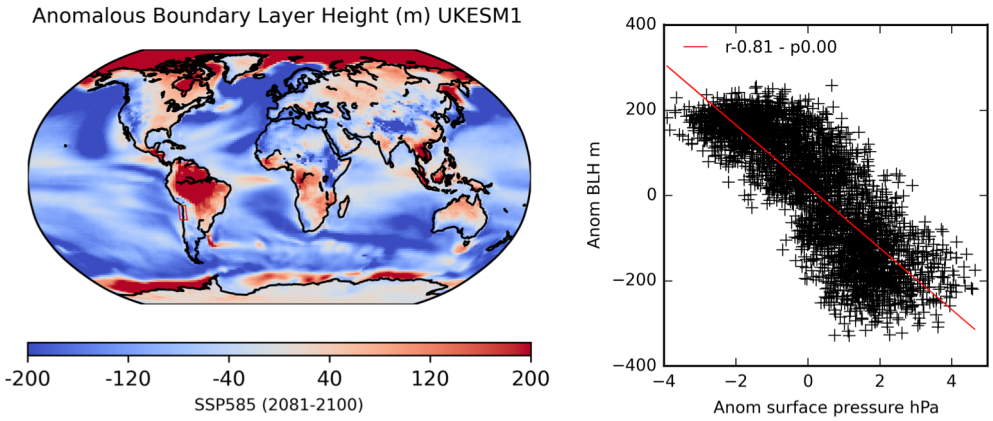

Figure 6.17: Global anomalous BLH mean SSP585. Right: global anomalous BLH mean for 2081-2100 with respect to 1986-2005 under the SSP585 scenario. Left: linear correlation between anomalous surface pressure and BLH in the Atacama region for 1850-2100 throughout the Historical and SSP585 scenarios.

6.5.3 Ocean Forcing: the Humboldt Upwelling System

The traditional approach to analyse future trends of coastal upwelling activity has relied on wind patters studies. On the Northern Humboldt region, off the coast of the Atacama Desert, the CMIP5 ensemble projects increasing wind stress, which will force increasing upwelling activity at the surface layers of the ocean (Oyarzún and Brierley, 2019) (Fig 6.18). However, the historical influence of wind stress on deeper ocean layers until 300 m depth, is expected to decline during the 21st Century under the RCP8.5 experiment. In fact, a disconnection at about 100 m depth is observed, and coastal upwelling below this starts to decline. Prior to Oyarzún and Brierley (2019), the research community attributed increasing trends at all depths based on wind stress patterns. In order to complement this analysis, and the connection of this phenomenon with ocean stratification described in Oyarzún and Brierley (2019), the UKESM1 outcomes of the upward ocean mass transport describing upwelling are presented in Fig 6.19.

Similar to the CMIP5 ensemble under the RCP8.5 (Fig 6.18), UKESM1 reproduces a decline in upwelling intensity during the three SSP scenarios analysed, and it simulates the disconnection between wind stress and upwelling at shallower waters, about 50 m depth. This is consistent across the SSPs and can be attributed to the fact of increasing wind stress, which not exhibits significant differences between the different experiments. This difference with the CMIP5-based analysis might be partially explained since the study reported in Oyarzún and Brierley (2019) focused in an active upwelling season (spring), in order to make it comparable with the Southern Humboldt region, also covered in that study. Unlike higher latitudes, the Humboldt exhibits almost persistent activity throughout the year which peaks in autumn and spring (Fig 6.20). Hence, the entire annual dataset is reported here. Although the general response of upwelling to climate change is captured in the Three SSPs, particularly more severe declines are simulated for the SSP370 and SSP585 by depth. Whereas similar to SSP126 no significant change is expected at 50 m depth, at 300 m depth upwelling is projected to decline until -4 $x10^{-4} kgs^{-1}m^{-2}$ towards the end of the 21st Century under the SSP585.

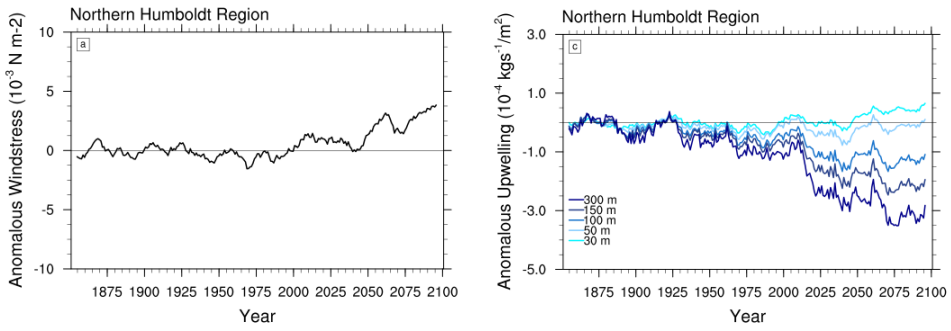

Figure 6.18: CMIP5 (13 models) Ensemble mean time series of anomalies for wind stress (left) and coastal upwelling (right) at 30, 50, 100, 150 and 300 m depth for the Northern Humboldt area in spring season (Sep-Nov). Anomalies computed with respect to 1871-1900 (Oyarzún and Brierley, 2019).

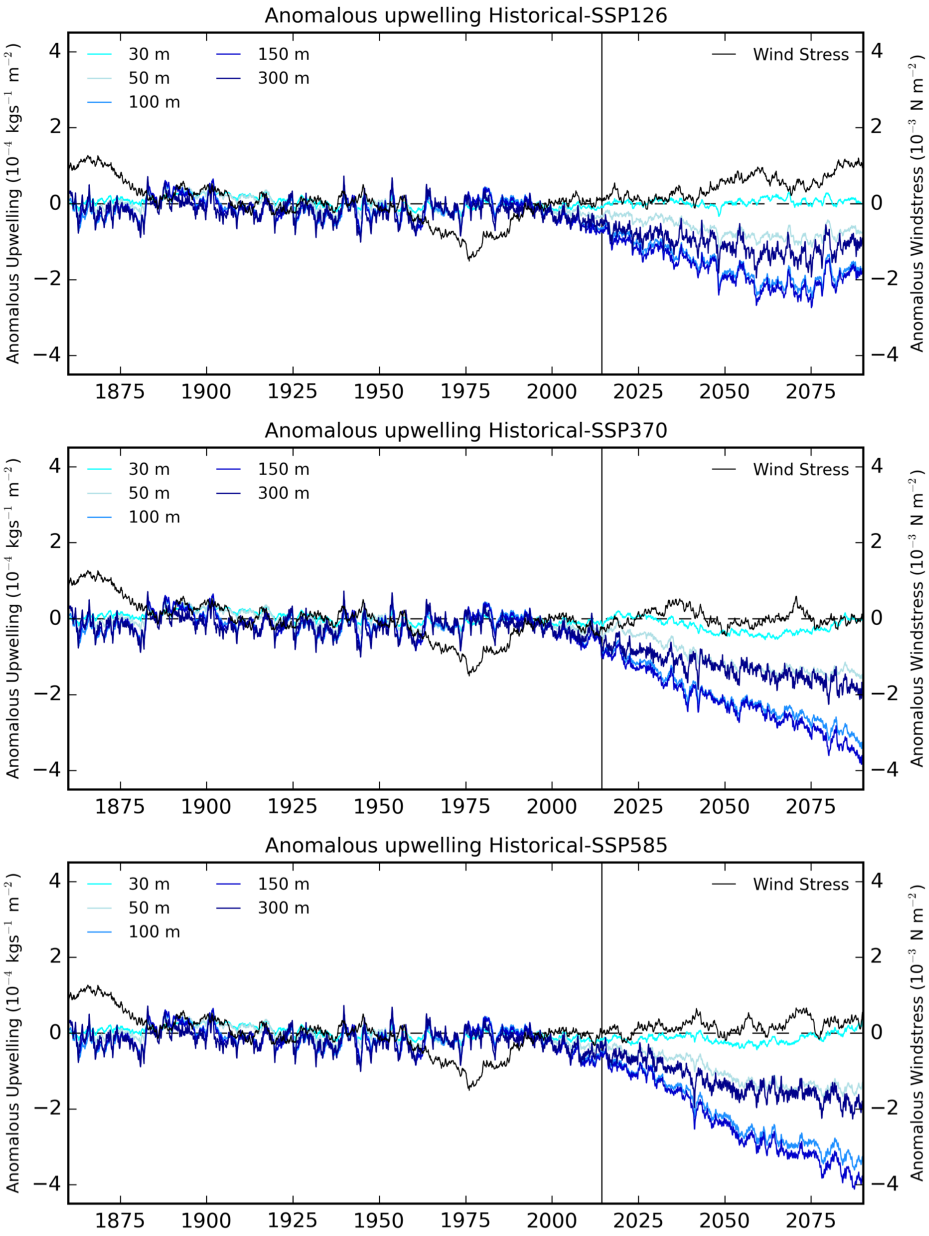

Figure 6.19: UKESM1 time series of anomalies for wind stress (black line, right y-axis) and coastal upwelling (left y-axis) at 30, 50, 100, 150 and 300 m depth for the Northern Humboldt area throughout the Historical and SSP126 (upper), SSP370 (middle) and SSP585 (bottom) experiments.

The disconnection between wind stress and coastal upwelling relies on a opposite forcing, ocean stratification, which interrupt the vertical flow (Lorenzo et al.,

2005; Oyarzún and Brierley, 2019). The intensification of ocean stratification is consistent with the decline of upwelling by depth (Fig 6.21). Maximum temperature increases are simulated at shallow levels until about 100 m depth, where the disconnection takes place, and the anomalous increasing warming is especially intense until about 300 m, similar depth from which waters are sourced in coastal systems (Talley et al., 2011).

The stratification of the climate system simulated by UKESM1 under the SSP585 is illustrated in Fig 6.22. As discussed before, SST decline due to surface upwelling activity has not been successfully reproduced in global models. However, cool seawater episodes conducing to a cooling of the lower Troposphere are simulated during the Historical experiment. The effects of this heat interchange are directly related to atmospheric stability and constitute a major driver of the climate of the Region. The stratification of both atmosphere and ocean are already modifying ocean upwelling intensity and might also be playing a fundamental role in the simulated decline of the BLH over northern Chile.

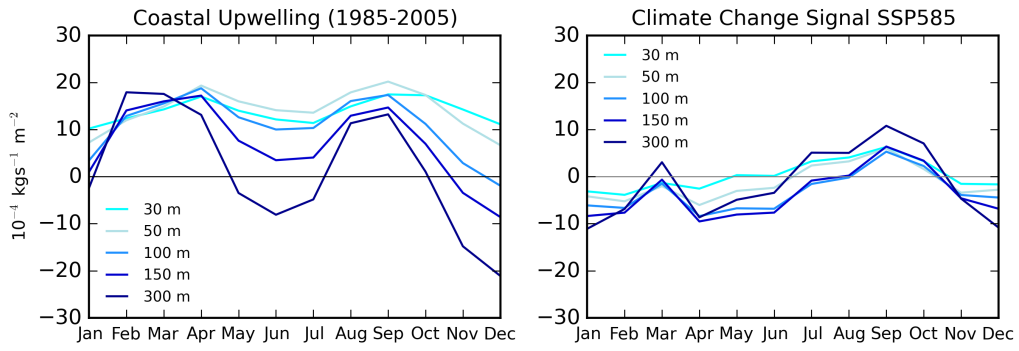

Figure 6.20: UKESM1 seasonal cycle of coastal upwelling at 30, 50, 100, 150, and 300 m depth for the Historical period (1985-2005) (left) and the climate change signal (right) in terms of absolute values computed for 2071-2100 with respect to 1986-2005. .

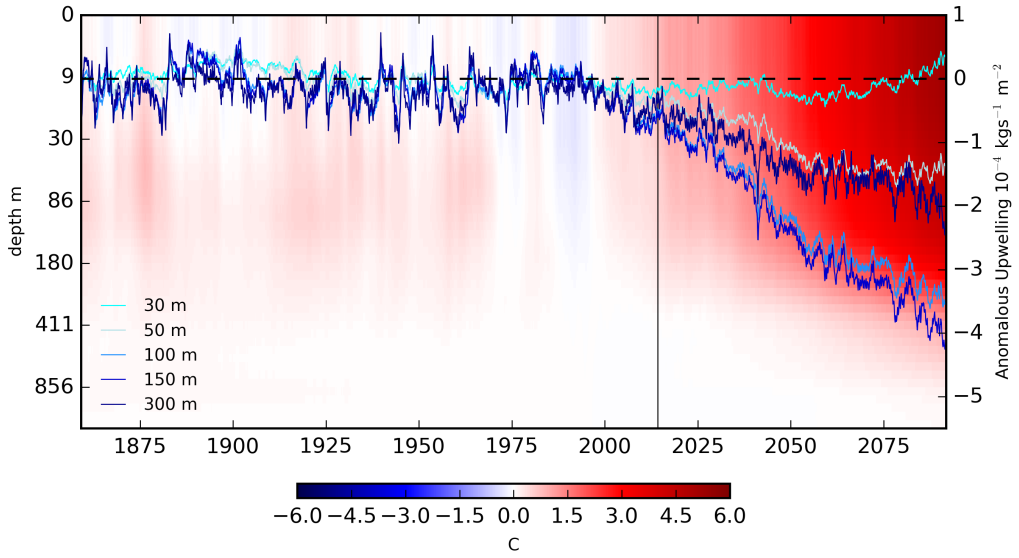

Figure 6.21: UKESM1 ocean temperature stratification under Historical and SSP585 scenarios. Atmospheric profiles of anomalous sea water potential temperature. Anomalies computed as area-average of the Northern Humboldt region for 2071-2100 with respect to 1871-1900 throughout the Historical and a) SSP126, b)SSP370 and c) SSP585 scenario. Black vertical dashed lines depict the end of the Historical experiment. Time series correspond to coastal upwelling under the Historical and SSP585 scenarios as plotted in Fig. 6.19 (bottom).

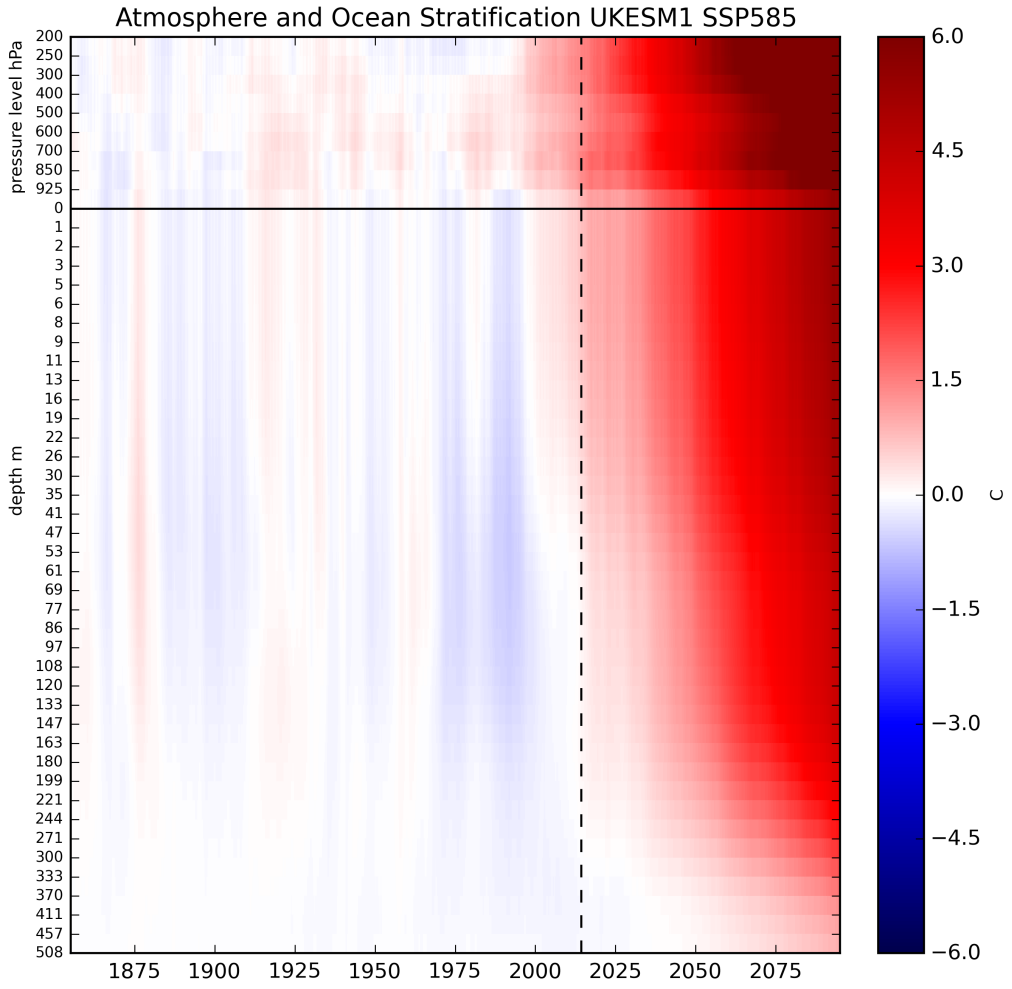

Figure 6.22: UKESM1 climate system temperature stratification. Atacama desert - Northern Humboldt region. Units in y-axis have been preserved for consistency with the rest of the analyses. Atmospheric (hPa) and oceanic (m) vertical levels have been plotted raw to contrast vertical resolutions between the atmospheric and oceanic grids in UKESM1.

6.6 Future Particulate Matter in the Atacama Desert

As described in section 6.3.4, PM_{10} and $PM_{2.5}$ were inferred from the individual aerosol species concentrations computed in the UKESM1 aerosol scheme. Additionally, coarse particulate matter (CPM or PM_{coarse}), or the coarse fraction of PM_{10}, was calculated as the difference between PM_{10} and $PM_{2.5}$ concentrations. In an area of important natural dust activity, PM_{coarse} is a useful indicator of the

dust fraction of PM_{10}. The projected total PM_{10} and $PM_{2.5}$ concentrations exhibit a similar trend for both the Historical and SSPs experiments, as area average in the Atacama region (Fig 6.23, a and b). During the 20th Century both are simulated to have increased progressively until the mid-century. Followed by a dramatic increase since the 1950s, which peaks during the 1990s and rapidly decline at the end of the Century.

An approach to identify the driver of this abrupt rise of PM concentrations is the exploration of the aerosols species trends (Fig 6.23, d and e). For both PM_{10} and $PM_{2.5}$, most the aerosols species exhibit little change during the 20th Century. However, sulphur aerosols concentration pushed PM levels up dramatically during the second half of the 20th. In order to explore the nature of this sulphur aerosol rise, the anthropogenic sulphur emissions dataset from the Community Emissions Data System (CEDS) contributing to CMIP6 (Hoesly et al., 2018) was analysed. Similar to UKESM1 outcomes, Fig 6.24 depicts the area-average time series of sulphur emissions by sector for the Atacama region. For this area, the industrial and energy sector present emissions three orders of magnitude higher with respect to the other sectors (plotted at the right y-axis in Fig 6.24). This is explained by the intrinsic nature of the Desert, an area with lower population density and almost no agriculture. As reported by Lamarque et al. (2010) and Hoesly et al. (2018), after the second world war the emission of anthropogenic SO_2 and other air pollutants boosted globally. Unlike other emissions such as NO_x or CO, Latin America exhibited a decrease of SO_2 emissions towards the end of the Century. For the Atacama (Fig 6.24, upper), this is mainly explained by emissions from the industrial sector. When looking at the spatial distribution of the industrial sulphur emissions during the past Century (Fig 6.24, bottom), an increase of emissions are recognisable on the Atacama Desert (red box), and the trends of PM_{10} and $PM_{2.5}$ concentrations illustrated in Fig 6.23 (a and b) are clearly represented. An abrupt increase of emissions is depicted in 1971-2000 with a subsequent decline in 2001-2014. It is noticeable the similar trend over the mining region of Southern Peru. However, over this area, no decline is observed after the peak in 1971-2000. On other regions of South America, such

as eastern Argentina, a consistent rise of the emissions is observed.

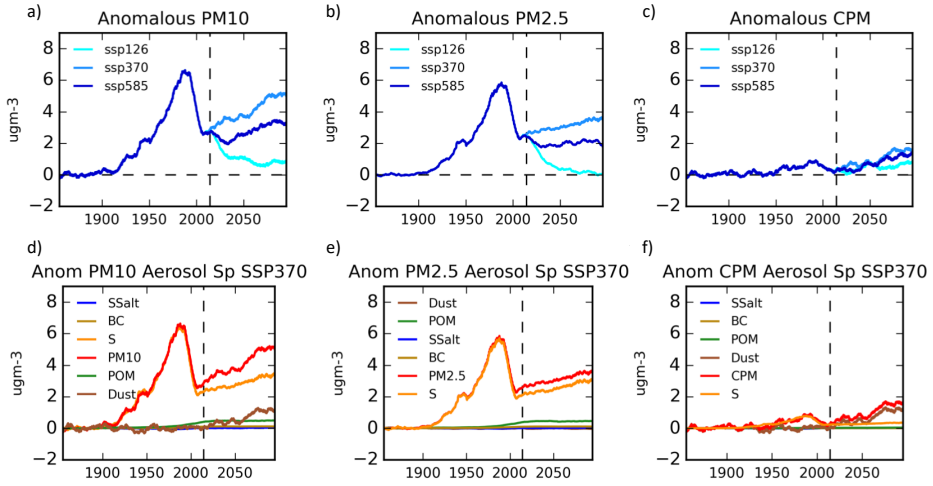

Figure 6.23: Upper: PM_{10} (a), $PM_{2.5}$ (b) and Coarse Particulate Matter (CPM) (c) time series as area-average of the Atacama region, inferred from aerosol species simulation in the UKESM1 aerosol scheme. Historical and SSP126, SSP370 and SSP585 scenarios. Bottom: time series of aerosols species as area-average of the Atacama region throughout the Historical and SSP370 scenario.

Global inventories present some degree of uncertainty with respect to local emissions. In South America, most of the effort is on characterising GHG emission to meet international commitments. However, there is a scarcity of domestic air pollution inventories, especially in remote areas (Huneeus et al., 2020). Despite the above, the previous analysis is consistent with the national mining and energy history in Chile during the 20^{th} Century. This region, similarly to the South of Peru, has historically had a mining culture focused on the extraction of copper, iron and gold reserves across the Desert (see §3.3). Therefore, sulphur emissions, especially sulfur dioxide, are monitored by the industry and the government (Ruiz-Rudolph et al., 2016). Mining activity and the operation of the coal- and oil-fired power plants increased rapidly since the 1950s. Therefore, significant emissions of sulphur species seem coherent, at least their simulated trend. An important inflexion point in Chilean regulation during the decade of the 1990s was the enactment of the Chilean ”law on general bases of the environment” in 1994 (MINSEGPRES, 1994).

This normative body was the beginning for the enactment of specific legislation on emission and air quality levels of concentration, including sulphur dioxide. It led to an increment in innovation and emission control technology to reduce emissions. As this corresponds to a national policy, its effects on decreasing sulphur emissions by 2001-2014, are noticed across the entire Country (Fig 6.24, bottom).

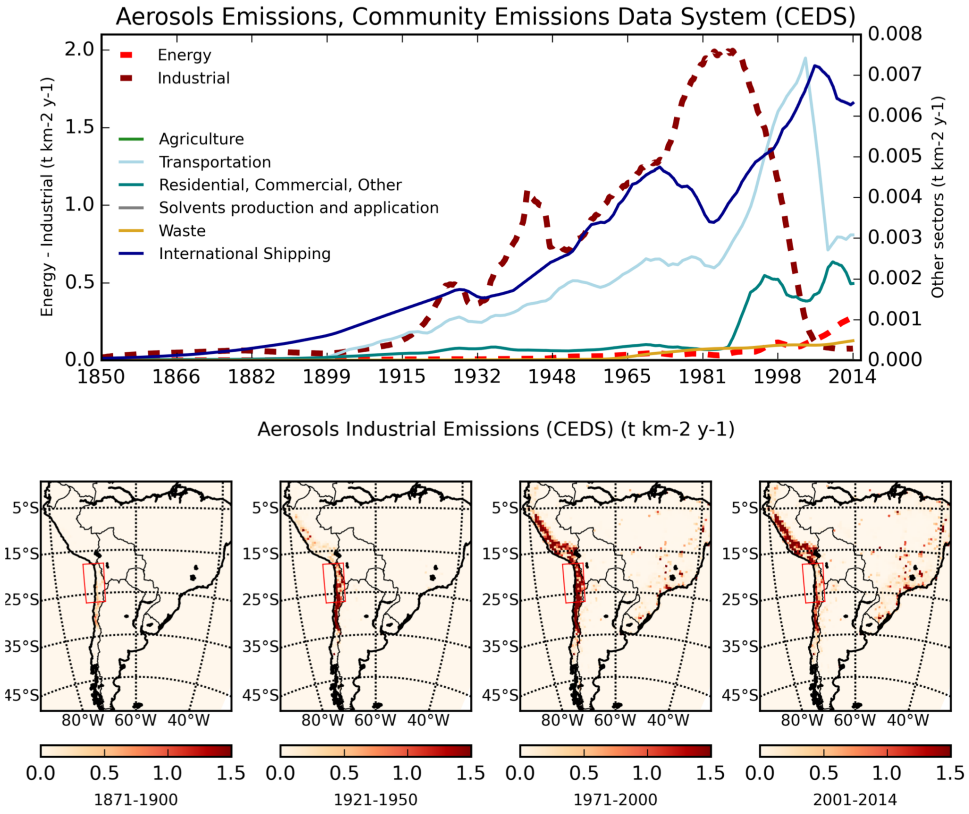

Figure 6.24: Upper: time series for the historical period of anthropogenic aerosols emissions. Computed for the Atacama region from the Community Emission Data System (CEDS) emission inventory. Bottom: Sulphur aerosol emissions during four 30-year period. Red box: Atacama region.

Future PM concentrations strongly depend on the modelling scenario. Their formulation propose not only GHG emissions patterns but also air quality control strategies which are independent of the efforts on fighting climate change. Indeed, under the SSP370 experiment, PM_{10} is projected to rise by 5.0 μm^{-3} as monthly mean for the period 2071- 2100 with respect to 1871-1900 (Fig 6.23, a). This is pri-

marily attributed to sulphur aerosols emission, and in less extent to dust emissions (Fig 6.23, d). This is consistent with the results by Chadwick et al. (2016) discussed in subsection Atmospheric Moisture Projections. The cooling effects of certain aerosols, such as sulphur compounds, have been associated with decreasing evaporation rates over the land surface, debilitating the hydrological cycle (Ramanathan and Feng, 2009). Under the SSP585, a weaker increase is projected for the same period (3.2 μgm^{-3}). The more abrupt rise under SSP370 occurs due to the absence of emissions control plans. Therefore, even under a slightly favourable scenario in terms of climate change mitigation, failing in air pollution control exacerbate significantly PM_{10} projections. This has recently highlighted by sensitivity studies that emphasise the role of emission controls driving future air quality (Cholakian et al., 2019). Similar discrepancies between aerosols projections under the SSP370 and SSP585 have been found for other regions on the globe (Turnock et al., 2020). As warned by Maione et al. (2016), this contradictory behaviour put in evidence the relevance of deploying a consistent mitigation plan for climate change and air quality as a whole. On the other hand, although a slight increase by 0.8 μgm^{-3} is projected under the SSP126 for 2071- 2100 with respect to 1871-1900, a declining trend is projected under the SSP126 during the 20^{th}. This reflects the potential results under the existence of more cohesive mitigation plans comprising both climate change and air pollution strategies.

Regarding PM25, a similar trend of PM_{10} is projected, but slightly weaker (Fig 6.23, b). Under the SSP370, a rise by 3.5 μgm^{-3} is projected for the same period of reference, whereas for the SSP585 and increment by 2.0 μgm^{-3} is simulated. On the other hand, and similar than PM_{10}, a consistent decline is projected under the SSP126 scenario, reaching almost zero net emission at the end of the 20^{th} Century in comparison with 1871-1900 (0.2 μgm^{-3}). Unlike PM_{10}, dust emissions are not relevant for $PM_{2.5}$ concentrations (Fig 6.23, e), as they contribute mainly to the coarse fraction of PM_{10} (Fig 6.23, c and f). As presented in Chapter 4, increasing Aerosol Optical Depth (AOD) observations from MODIS satellite data are strongly correlated with eastward zonal winds. UKESM1 projects a rise of eastward near-

surface wind over the Atacama (Figures 6.12 and 6.11), which in future might lead a progressive rise of dust production. As presented in Figure 6.23 (a and b), the coarse fraction of PM_{10} during the 20^{th} Century was very small, meaning that most of the PM_{10} corresponded to fine $PM_{2.5}$ particles. However, under the three future experiments analysed, PM_{coarse} is expected to increase due to a climate forcing, unlike the anthropogenic signal behind the other aerosols species computation. As described in Section 2.5.2, in UKESM1 all anthropogenic emissions are prescribed from global inventories. However, natural aerosols emissions, such as mineral dust, are dynamically computed due to the full coupling of ESM components. In particular, mineral dust is independently computed through the CLASSIC dust scheme (Bellouin et al., 2011b). Therefore, a plausible reason for the increasing trend simulated for PM_{coarse} might be the consistent increase of wind speed simulated throughout the three SSPs analysed (Fig. 6.13), consistent with the observed connection of dust and zonal wind discussed in §4.5.

6.7 Summary

This chapter explored historical and future simulations over Western South America under three climate change scenarios (SSP126, SSP370 and SSP585) from the UK Earth System Model Version I (UKESM1). Regional warming was explored through temperature and atmospheric moisture projections, whereas atmospheric stability was examined by analysing the South Pacific Anticyclone (SPA), atmospheric stratification and the planetary boundary layer. Then, the ocean forcing was studied by the analysis of the Humboldt coastal upwelling system. Finally, future PM_{10} and $PM_{2.5}$ trends were explored.

UKESM1 reveals a poleward extension and intensification of the South Pacific Anticyclone (SPA) during the austral summertime. This trend is projected to intensify during the 21^{st} Century under the three experiments analysed (SSP126, SSP370 and SSP585). The expansion and intensification of the SPA enhance equatorward surface winds, which promote the strengthening of westward upwelling favourable winds. Also, increasing atmospheric stratification is proposed to be linked to a de-

creasing trend of the BLH, which is projected to decline during the 21 ^{srt} Century. Increasing coastal upwelling induces a decline of SST and promotes atmospheric stability. However, upwelling intensity is projected to decline at about 100 m ocean depth. The above because of the increasing ocean stratification and disconnection of the surface wind stress forcing.

UKESM1 reveals a pronounced peak of PM_{10} and $PM_{2.5}$ that took place over northern Chile during 1970-2000. This is associated with an abrupt peak of SO_2 industrial emissions. At the end of the 1990s, these extremely high PM concentrations declined, coinciding with the enactment of the Chilean law on general bases of the environment.

Future trends of PM_{10} and $PM_{2.5}$ are highly sensitive to the mitigation measurements adopted by each experiment. An increasing trend is projected under the SSP370 and SSP385. This is more pronounced under the SSP370 experiment because of a relaxing in control measurements, along with an increase of SO_2 emissions and, in less magnitude, an increase of mineral dust emissions. These results highlight the impact that future mitigation plans would have on PM_{10} and $PM_{2.5}$ concentrations over northern Chile and suggest the need to computing a climate penalty for northern Chile.

Chapter 7

Discussion and Conclusion

This chapter summarises the findings and results from the previous chapters, discusses their contribution, places them in context, and answers the four research questions stated in §1.3. Then the limitations of the work are then discussed, followed by suggestions for future research and the implications of the research beyond academia. Finally, overall conclusions are presented.

7.1 Research questions and key findings

The Atacama Desert is one of the driest environments on Earth, in fact, it is the driest desert in the world. A quasi-permanent temperature inversion layer (TILH) along the northern Chilean coast, capped by the Hadley cell subsidence, promotes strong atmospheric stability, which is also enhanced by the Humboldt coastal upwelling activity and the anomalously cold sea surface temperature. These along with the rainshadow effect of the Andes Cordillera, promote exceptionally arid conditions with almost no precipitations.

Despite these particular geographical conditions and the fact that it contains about 1.5 million people, it has received scarce attention in terms of both anthropogenic and natural emissions of air pollutants and their relationships with the governing climate and meteorology. According to the Chilean emissions and transfer registry (RETC) database, the mining and coal-and oil-based energy production industries have led, and continue to dominate, significant emissions of particulate matter (PM_{10} and $PM_{2.5}$) and gases (NO_x and SO_2) (§3.3). As described in

§3.4, observational air quality data from the SINCA network provide evidence that nine sites measuring PM_{10} exceeded WHO annual mean guidelines for PM_{10} (20 μgm^{-3}) and five out of the twelve sites measuring $PM_{2.5}$ exceed the WHO annual mean guidelines for $PM_{2.5}$ (10 μgm^{-3}). However, an almost opposite scenario is observed when comparing against Chilean standards. Only one site measuring PM_{10} exceeded the Chilean threshold for the annual mean (50 μgm^{-3}), and none of the twelve sites measuring $PM_{2.5}$ exceeded the Chilean standard for this pollutant (20 μgm^{-3}). This highlights the importance of revising local air quality policy and ensuring their agreement with international guidelines. These features of the Atacama Desert environment motivated the four research questions proposed in §1.3, which are analysed along with the key findings from the previous chapters in the following subsections.

7.1.1 Natural mineral dust and atmospheric ventilation as natural forcers

The dust cycle in the Atacama Desert has remained unexplored prior to this work, despite being an area with historical problems of particulate matter concentrations. Previous global or continental scale studies suggested maximum dust production in northern Chile during summer (Ginoux et al., 2012; Martins et al., 2017) and estimates have placed the contribution of the Atacama Desert to global load at 2.3-2.6%(Zender et al., 2003; Ginoux et al., 2004; Tanaka and Chiba, 2006). However, there is scarce evidence in the literature regarding mineral dust sources, their variability and the frequency of dust events. This lack of understanding motivated the satellite-based mineral dust study presented in Chapter 4 and the formulation of research question 1: what is the geographical and temporal distribution of mineral dust and its sources in the Atacama Desert?. The AOD retrievals from MCD19A2 MODIS datasets, which corresponds to Terra (morning) and Aqua (afternoon) retrieval post-processed with the MAIAC algorithm (Lyapustin et al., 2011a,c) showed a better agreement with the AERONET site in Arica, in comparison with the Deep Blue (MOD04L2 and MYD04L2) products during the period of analysis, 2010-2020 (§4.3). Based on the analysis of AOD and Angstrom exponent

(α) data, two areas located in the northern and southern margins of the Antofagasta region were identified as dominant mineral dust sources. These show relatively high AOD values (up to 0.25, as a decadal mean in summer and spring) and very low α values (< 0.5 as a decadal mean in summer and spring) (§4.3). At a seasonal time scale, no significant differences were computed between Aqua and Terra retrievals. Mineral dust events across these zones, which take place preferably in summer and spring, registered AOD values up to 0.7. Relative seasonal thresholds were used to define an event. Particularly in the active season (summertime), the episodes registered AOD over 0.20 for Terra retrievals and 0.22 for Aqua retrievals. In both areas identified as mineral dust sources in the Antofagasta Region, an increasing trend of mineral dust events during summertime was identified during Aqua retrievals. Also in both regions, the frequency of events increased from about 5 in 2010 up to over 12 in 2017-2019 (§4.3). A positive correlation with surface wind speed computed from the ERA5 reanalysis was found. However, the underlying mechanisms behind this notorious increasing trend require further attention. The understanding of the mineral dust cycle refers to a major natural source of PM across northern Chile. Therefore, its understanding provides insight into the potential role of this natural source on air quality levels across the region. Future research in this regard is discussed in the following section.

The prevailing stable conditions along the coast of the Atacama Desert, as well as the predominance of the quasi-permanent temperature inversion layer (TILH) along the coast, motivated research question 2, as listed in §1.3: What role do local atmospheric conditions play in episodes of dangerous particulate matter levels in the Atacama Desert?. The approach chosen for answering this question involved two families of data; observational and modelled (§5.2). Despite the evidence for intense anthropogenic and natural emissions, a relationship between the observed ventilation coefficient (VC, Kassomenos et al. (1995)) and PM_{10}-$PM_{2.5}$ levels was found (§5.4). The four gridded datasets explored for computing gridded VC (WRF341I-SAM44, RegCM-SAM44, RegCM-CL09 and ERA5) reasonably reproduced VC and PM relationships, particularly on the coastal cities of Iquique and

Antofagasta. Most of the high-concentration episodes of PM_{10} and $PM_{2.5}$ (daily mean greater than 100 μgm^{-3} in both cases) in the cities of Antofagasta, Tocopilla, Sierra Gorda and Calama took place during unvented days when the VC daily mean was lower than the threshold of 6,000 μgm^{-3}, as defined by Holzworth (1972). On the contrary, the atmospheric stagnation index (ASI, Wang and Angell (1999)), which omits the boundary layer height (BLH) effect, does not seem to contribute to the occurrence of PM episodes (§5.5). These results highlight the role that plays the temperature inversion layer height (TILH) on PM_{10} and $PM_{2.5}$ variability in northern Chile.

A logistic model purely based on atmospheric variables for the city of Antofagasta predicted PM_{10} events (daily means) reasonable well with 0.74 of accuracy and $PM_{2.5}$ events with 0.78 of accuracy (§5.6). The threshold for the definition of events was defined as 80^{th} percentile of the daily mean observations. These concentration values lied on the "latent" range of both PM_{10} (CONAMA, 1998) and $PM_{2.5}$ (MMA, 2011) Chilean standards. As described in both normative bodies, the "latent" range corresponds to that between 80 and 100% of the standard value. This means that the predicted events correspond to PM levels that relate, potentially, to exceedances of the annual mean standard. As expected, in all experiments, VC adopted a negative sign, which resulted in the most significant factor contributing to the model. Under an uncertain climate change scenario and future anthropogenic emissions, it is reasonable to consider the potential need of computing a climate penalty for PM levels in northern Chile. If the observed decreasing trend of the TILH (§5.3), and consequently of the BLH, above the region intensifies during the 21^{st} Century, additional mitigation efforts might be needed in order to meet air quality standards. Future research in this regard is also discussed in the following section.

7.1.2 The future of the Atacama Desert

In order to answer the third research question proposed in §1.3 - What are the mechanisms by which the climate of the hyper-arid environment in Northern Chile is projected to change over the coming century? - the governing climatic factors con-

trolling the Atacama Desert were analysed by the UKESM1 model contributing to CMIP6.

The decreasing trend of the BLH described in §5.3, was also reproduced by the UKESM1 model, as presented in §6.5.2. The intensification of atmospheric temperature stratification is leading to a decreasing BLH in the lower troposphere over the Atacama. Similarly, an increasing temperature stratification of the eastern South Pacific Ocean (§6.5.3) is triggering a decline of coastal upwelling (upward water mass flow) at about 100 m depth (and deeper). The consequences of a decline of the BLH on PM levels over northern Chile is unknown and has not been previously reported. This is complemented with changes in wind patterns, directly associated with the seasonal variability of the South Pacific Anticyclone (SPA). Currently, the SPA extends poleward and intensifies during the austral summertime. As UKESM1 reveals, and in agreement with evidence from the literature, this behaviour is being enhanced as a result of climate change for the three experiments explored (SSP126, SSP370 and SSP585) (§6.5). This intensification of the SPA enhances equatorward surface winds, which trigger two fundamental processes that indirectly promote particulate matter concentrations over northern Chile. First, an intensification of westward upwelling favourable winds, which lead to increasing coastal upwelling intensity in the surface layer of the ocean (in contrast with the decreasing intensity by depth, due to stratification)(§6.5.3). The enhanced upwelling activity at the ocean surface promotes decreasing sea surface temperature (SST), which in turn partially promotes the governing atmospheric stability and scarcity of precipitations. Second, an intensification of the southwest inflow toward the Atacama modulates seasonal and daily cycles of winds patterns, as described by Muñoz et al. (2013) and Rutllant et al. (2013), especially in summer afternoons. This intensification of wind, along with a higher BLH (and coastal TILH), explains the increased ventilation in summer and unvented conditions in winter, as computed from the surface and upper air observational records, modelled outcomes and reanalysed data in §5.3. Following the understanding of the ocean-climate factors that governs the hyper-arid climate of northern Chile and their potential affectation under climate

change, the fourth research question proposed - How would mineral dust, PM_{10} and $PM_{2.5}$ atmospheric concentrations respond under these future climate changes? - was addressed by exploring PM_{10} and $PM_{2.5}$ trends from UKESM1 and the input emission inventory data in UKESM1; the community emission data system (CEDS) emission inventory. According to CEDS, SO_2 emissions from the industry sector have historically (20^{th} Century) modulated PM_{10} and $PM_{2.5}$ concentrations over northern Chile (§6.6). A dramatic peak of SO_2 emissions was computed between the years 1970 and 2000, which coincides with the intensification of copper exploitation in northern Chile. Similarly, this peak was also reproduced over southern Peru. However, whereas an evident decline of the emissions is observed in Chile after the 1990s, in Peru the increasing trend remained during the 2000s. This decline of SO_2 emissions in Chile coincides with enactment in 1994 of the Chilean "law on general bases of the environment" (MINSEGPRES, 1994), which forces industries to control their gaseous (including SO_2) and particulate matter emissions, and submit detailed environmental impact assessments, including appropriate mitigation plans.

The future trends of PM_{10} and $PM_{2.5}$ computed from UKESM1 are highly dependant on the emission scheme adopted in each experiment analysed (SSP126, SSP370 and SSP585). As discussed in §6.6, a decline during the 21^{st} Century is projected under the SSP126 due to mitigation plans covering both GHG and air pollutant emissions. However, an increase of PM_{10} and $PM_{2.5}$ is projected under the SSP370 and SSP585 scenarios. In a world with high GHG emissions but significant air quality control measures (SSP585), a weaker increase is simulated in comparison to a world whose development sustains lower GHG emissions but uncontrolled air quality emissions (SSP370). Under the SSP370 experiment, an abrupt increase of both PM_{10} and $PM_{2.5}$ concentrations is projected. This is primarily associated with an increase in SO_2 emissions over northern Chile as well as a sustained increase in mineral dust emissions. These results, along with the observed effect of the Chilean environmental legislation during the1990s on SO_2 emissions, highlight the significant impact that future mitigation plans will have on PM_{10} and $PM_{2.5}$ levels.

This supposes a major challenge for adopting joint mitigation strategies considering air quality and climate change, in agreement with international standards relying on a common reference for protecting human health, the environment and promoting sustainable development. The above would contribute to avoiding disagreements on qualifying air quality levels and the consequent mitigation actions triggered from this classification, as shown for northern Chile by the contrast between Chilean and WHO standards (§3.4).

The increase in mineral dust emissions projected by UKESM1 seems reasonable due to the increased wind speeds projected over the central latitudes of the Atacama (about 23°S), which are associated with the intensification and expansion of the SPA. However, it is not clear if UKESM1 is adequately reproducing local mineral dust production. Additionally, these results highlight the high sensitivity of PM projections from UKESM1 to the prescribed emission inventory. The impact of the decreasing trend of BLH on PM_{10} and $PM_{2.5}$ trends is not evident, although it seems reasonable to postulate that a decline in BLH might enhance PM concentration levels, especially in the absence of appropriate mitigation measures. This assumption represents a valuable starting hypothesis for future research.

7.2 Limitations

The complexity of the geography of northern Chile imposes a significant challenge for both observational and modelling datasets. However, the ground level and upper air observational datasets used in this research have provided a good frequency of data and time framework for the study.

Surface observations correspond to local data restricted by local conditions. The significance of this impact depends on the location. Wind patterns data at coastal sites are suitable for explaining local scales patterns and their links with synoptic climate drivers, such as SPA variability. However, in inland desert areas, the topography restricts winds patterns to local conditions. Therefore, observational analysis of air quality and atmospheric ventilation was restricted to each monitoring site. Increasing the monitoring effort in the SINCA and DMC networks and incor-

porating additional launching sites for upper air observation in inland areas would significantly improve the analysis.

Regarding satellite observations, the aerosols retrievals analysed were used at their best quality as defined by MODIS. However, this led to a lower amount of valid data for the mineral dust characterisation. Also, due to the persistent morning stratocumulus deck along the coast, satellite retrievals cannot reproduce reliable data on coastal boundaries, where mineral dust activity can also occur. Similarly, Deep Blue products (MOD04L2 and MYD04L2), which provided the angstrom exponent data (α) suffer from a significant lack of data on the Andes Cordillera. Although the scarce literature on mineral dust activity over Northern Chile has previously suggested a potential for dust production predominantly in the central region of the Desert, potential dust sources located in the Andes Cordillera might be missed. However, the top of the Andes is dominated by very complex topography and high roughness that suggest that intense dust production is unlikely.

The modelling datasets used, including regional climate models, reanalysed data, and earth system simulations, are state of the art for exploring the climate system at global and regional scales and, according to products resolution, at a local scale. However, models suffer from multiple sources of uncertainty given partially by the parameterised processes not dynamically simulated. For the study area, two relevant factors especially contribute to uncertainty in the models; convective transport under the TILH along the coast and the complex topography of the inland desert areas. These uncertainties directly impact BLH and wind pattern simulations. The use of observational datasets contrasting with modelling results helped to deal and understand these limitations.

Finally, climate change scenarios have been explored based on prescribed global anthropogenic emission inventories in UKESM1. Even though the results contribute significantly to the understanding of an unexplored region in terms of future air quality trends under a range of climate change experiments, a refined method might consider modelling PM using local emission inventories, such as the Emissions and Transfer Registry (RETC in Spanish) (§3.3). However, this would

require re-running UKESM1 for the four experiments studied, which is out of scope of this study. Finally, a more robust result would have been achieved by using an ensemble of models contributing to CMIP6. However, the focus was on exploring the multiple elements of the climate system, concluding with future trends of PM. Significant extra resources are required if multiple models are used due to the different aerosols schemes across the ensemble members. Future research in this regards is proposed in the following section.

7.3 Reflections for future research and practice

The mineral dust cycle in northern Chile had not previously been explored. Therefore, this research first focused on understanding the dust cycle, source areas and their variability. However, this knowledge indicates future research opportunities in several aspects. A first approach is to further understand the connection between aerosols retrievals from satellite sensors and particulate matter levels, which requires devoted atmospheric chemistry modelling of the vertical distribution of aerosols. A satellite-based tool for air quality prediction would provide PM concentrations in isolated areas where there is a lack of monitoring, complementing the observational database of SINCA. A second element that deserves further study is applying the knowledge gained on the dust cycle in order to validate future mineral dust simulations over northern Chile. In particular, the fine resolution (1 km) of the MCD19A2 product and its good data availability allow the development of a suitable dataset for validating models on complex terrain. This study is also expandable to a continental scale for South America due to the lack of mineral dust studies in the region, where Patagonia and central Argentina are also important sources of mineral dust that had not been yet characterised in the literature.

Mineral dust is an aspect of concern for the solar energy industry, which has grown dramatically in northern Chile over recent years. Chemical transport simulations validated with satellite-derived mineral dust products might represent a robust basis for developing dust forecasting and compute their effects on soiling and direct normal irradiance (DNI). Both are crucial elements for the productivity of photo-

voltaic panels.

Regarding air quality forecasting for policy purposes, it is important to highlight that there is no operational forecasting tool in Chile. The logistic model proposed for PM_{10} and $PM_{2.5}$ represents an opportunity for developing a low-cost solution suitable for PM prediction. The expansion of this tool for predicting PM or other pollutants variability might require adding independent variables so far no considered. For instance, council-level emissions from RETC could be incorporated to strengthen forecasts along with modelled or reanalysed BLH data in areas with a lack of upper-air observations. This work would require the expansion of both ground level and upper air observations across the Desert.

In terms of policy implications, in addition to the development of a PM forecasting tool, based on the observed and projected decline of the BLH, the estimation of a climate penalty for PM_{10} and $PM_{2.5}$ would be of significant value. However, this should be done at smaller spatial scales, removing possible uncertainties from local environmental factors, such as topography and its effect on the local wind patterns. Although the decline of BLH seems robust from observations and models, wind patterns require local-scale characterisation to adequately test their impact on ventilation under decreasing BLH trends.

The results presented here on climate change impacts across northern Chile and the southeast Pacific Ocean have been based on one model (UKESM1). A natural next step would be to expand the analysis considering an ensemble of models contributing to CMIP6, with a focus on atmospheric stability and PM levels across northern Chile. Among other relevant elements of the climate dynamics of the region, the above would imply an analysis of BLH trends from multiple ensemble members and PM_{10}-$PM_{2.5}$ data from simulations. However, the latter would imply a critical challenge because of the differences in aerosols schemes among models. This study could also be expanded to other areas in central and southern Chile, and potentially across South America. Also, future simulations based on the RETC emission inventory would be beneficial for analysing future air quality trends. Finally, future research might comprise studying the Humboldt coastal

upwelling system from the CMIP6 ensemble members in order to compare with the results reported by (Oyarzún and Brierley, 2019) based on the CMIP5 dataset. Expanding the study to other eastern boundary upwelling systems would also be a valuable contribution to the field.

7.4 Conclusion

This research was situated in northern Chile, an area of complex geography where a range of natural forces promote the dominating hyper-arid environment and coexist with anthropogenic forcings that promote high PM_{10} and $PM_{2.5}$ concentrations. The study has provided novel knowledge that serves as a source of understanding for fundamental and unexplored processes in the Atacama Desert, which have direct implications for public health and future policy design.

Understanding the mineral dust cycle is the basis for mineral dust forecasting and its operational applications on air quality and solar power generation. Similarly, the role of the variability of the temperature inversion layer height on air pollution, either PM or gaseous compounds, remained unexplored, despite the history of the Atacama of intense anthropogenic intervention. These results strongly suggest the study of a climate penalty in northern Chile regarding PM emissions. This is reinforced by the future projections of PM_{10} and $PM_{2.5}$ concentrations from UKESM1, which provide evidence of the high sensitivity of future air quality to mitigation plans. The above, along with a projected intensification of the major drivers of the hyper-arid climate and stable atmospheric conditions of the Atacama Desert during the 21st Century.

Appendix

National Air Quality Information System of Chile (SINCA) - Ministry of Environment (MMA)

					Air Quality										
ID	Station	Region	Started	Finished	PM10	PM2.5	CO	O3	Nox	NO	NO2	SO2	CY	Pb	As
1	Arica	Arica y Parinacota	27/11/2013	working		X									
2	Alto hospicio	Tarapaca	17/12/2015	working		X									
3	Antofagasta	Antofagasta	01/06/2013	working	X	X									
4	Playa Blanca	Antofagasta	01/09/2007	30/12/2009	X										
5	Rendic	Antofagasta	02/01/2006	30/12/2009	X								X	X	X
6	Sur	Antofagasta	01/01/2000	30/12/2009	X							X			X
7	Chiu Chiu	Antofagasta	01/05/2008	30/12/2009	X							X			X
8	Colegio Pedro vergara Geller	Antofagasta	01/12/2012	working	X	X									
9	Complejo Deportivo 23 de Marzo	Antofagasta	01/12/2012	working	X	X									
10	Estacion Centro	Antofagasta	07/11/2012	working	X	X		X	X	X	X	X	X		
11	Hospital el Cobre	Antofagasta	05/01/2002	30/12/2009	X							X			X
12	Servicio Médico Legal	Antofagasta	12/04/2008	30/12/2009	X							X			X
13	Aukahuasi	Antofagasta	02/01/2000	30/12/2009	X							X			X
14	San Jose	Antofagasta	02/01/2000	30/04/2008	X		X					X			
15	Villa Caspana	Antofagasta	02/01/2000	06/04/2008	X							X			
16	Hospital	Antofagasta	01/01/2000	31/12/2009	X										
17	Iglesia	Antofagasta	01/01/2000	31/12/2009	X										
18	Compañía de Bomberos	Antofagasta	01/01/2000	31/12/2009	X		X	X	X	X	X				
19	Ferrocarriles	Antofagasta	01/01/2000	30/12/2009	X			X			X	X			
20	Jardin Infantil Integra	Antofagasta	12/04/2002	16/10/2009	X				X	X	X				
21	Sierra Gorda	Antofagasta	11/09/2012	13/12/2016	X	X									
22	Paposo	Antofagasta	29/02/2000	24/12/2009	X		X	X	X	X	X	X			
23	Punto de Máximo Impacto	Antofagasta	29/02/2000	24/12/2009	X		X	X	X	X	X	X			
24	Bomberos	Antofagasta	01/03/2009	13/12/2016		X									
25	Gendarmería	Antofagasta	21/07/2011	working	X	X									
26	Gobernación	Antofagasta	01/06/2004	working	X							X			
27	Escuela E-10	Antofagasta	03/01/2000	working	X	X	X	X	X	X	X	X			
28	Centro	Antofagasta	01/03/2004	04/04/2007								X			
29	Escuela E-12	Antofagasta	12/06/2004	13/02/2006	X							X			
30	Escuela Gabriela Mistral	Antofagasta	12/06/2004	13/02/2006								X			
31	Sur	Antofagasta	01/03/2004	04/04/2007	X							X			
32	Copiapo Civica	Atacama	18/10/2013	working	X	X									
33	Copiapo	Atacama	01/02/1999	31/03/2009	X							X			
34	Los Volcanes	Atacama	01/01/2003	30/12/2003	X							X			
35	Paipote	Atacama	01/02/1999	31/03/2009	X							X			
36	San Fernando	Atacama	01/02/1999	31/03/2009	X							X			
37	CAP	Atacama	04/09/2002	28/11/2010	X							X			
38	Cine Inca	Atacama	-	-											
39	Doña Ines	Atacama	14/01/1999	28/11/2010	X							X			
40	Intelec	Atacama	-	-											
41	SM6 Parcela Buena Esperanza	Atacama	01/01/2002	working								X			
42	SM7 Los Loros	Atacama	01/01/2002	working								X			
43	SM8 Freirina	Atacama	01/01/2002	working								X			
44	Huasco Sivica	Atacama	01/06/2014	working		X									
45	EME F	Atacama	01/02/2001	30/12/2010	X	X				X	X	X			
46	EME M	Atacama	01/02/2001	30/12/2010	X					X	X	X			
47	EME ME	Atacama	01/02/2002	27/02/2002								X			
48	SM1 Vertedero	Atacama	01/01/2002	working								X			
49	SM2 Quinta La Rosa	Atacama	01/01/2002	working								X			
50	SM3 Compañía	Atacama	01/01/2002	working								X			
51	SM4 Carretera km 40	Atacama	01/01/2002	working								X			
52	SM5 Parcela 5 El Pino	Atacama	01/01/2002	working								X			
53	Pabellón	Atacama	01/01/1994	30/04/2009								X			
54	Tierra Amarilla	Atacama	01/02/1999	31/03/2009	X							X			
55	Coquimbo	Coquimbo	10/12/2013	working		X									
56	La Serena	Coquimbo	11/12/2013	working		X									

Figure A1: Details of the air quality monitoring records of the National Air Quality Information System of Chile (SINCA). The length of the records and the variables measured are shown.

National Air Quality Information System of Chile (SINCA) - Ministry of Environment (MMA)

			Meteorology								
ID	Station	Region	Started	Finished	SR (W/M2) 3 m	AP (mbar) 2 m	pr (mm) 2 m	RH (%) 3 m	T (ºC) 3 m	wd (deg) 10 m	ws (m/s) 10 m
1	Arica	Arica y Parinacota									
2	Alto hospicio	Tarapaca	16/02/2016	working	X			X	X	X	X
3	Antofagasta	Antofagasta									
4	Playa Blanca	Antofagasta	01/01/2009	31/12/2009						X	X
5	Rendic	Antofagasta	01/01/2009	31/12/2009						X	X
6	Sur	Antofagasta									
7	Chiu Chiu	Antofagasta	31/01/2004	working	X	X		X	X	X	X
8	Colegio Pedro vergara Geller	Antofagasta	30/11/2012	working				X	X	X	X
9	Complejo Deportivo 23 de Marzo	Antofagasta	18/10/2012	working				X	X	X	X
10	Estacion Centro	Antofagasta	19/10/2012	working				X	X	X	X
11	Hospital el Cobre	Antofagasta	08/01/2003	working	X	X	X	X	X	X	X
12	Servicio Médico Legal	Antofagasta									
13	Aukahuasi	Antofagasta									
14	San Jose	Antofagasta	31/12/2002	31/12/2008		X	X		X	X	X
15	Villa Caspana	Antofagasta									
16	Hospital	Antofagasta									
17	Iglesia	Antofagasta									
18	Compañía de Bomberos	Antofagasta									
19	Ferrocarriles	Antofagasta									
20	Jardin Infantil Integra	Antofagasta									
21	Sierra Gorda	Antofagasta	10/09/2012	13/12/2016					X	X	X
22	Paposo	Antofagasta									
23	Punto de Máximo Impacto	Antofagasta	01/01/2009	31/12/2009	X	X	X	X	X	X	X
24	Bomberos	Antofagasta									
25	Gendarmería	Antofagasta	20/07/2011	working	X	X		X	X	X	X
26	Gobernación	Antofagasta	01/01/2007	30/11/2007							X
27	Escuela E-10	Antofagasta	31/12/2005	working	X	X		X	X	X	X
28	Centro	Antofagasta	31/12/2007	31/12/2008						X	X
29	Escuela E-12	Antofagasta									
30	Escuela Gabriela Mistral	Antofagasta									
31	Sur	Antofagasta									
32	Copiapo Civica	Atacama									
33	Copiapo	Atacama	01/01/2009	31/12/2009						X	X
34	Los Volcanes	Atacama									
35	Paipote	Atacama	01/01/2009	31/12/2009						X	X
36	San Fernando	Atacama	01/01/2009	31/12/2009						X	X
37	CAP	Atacama	31/12/2008	30/11/2010	X	X	X	X	X	X	X
38	Cine Inca	Atacama									
39	Doña Ines	Atacama	31/12/2008	30/11/2010	X	X	X	X	X	X	X
40	Intelec	Atacama									
41	SM6 Parcela Buena Esperanza	Atacama									
42	SM7 Los Loros	Atacama									
43	SM8 Freirina	Atacama	01/01/2003	31/12/2008						X	X
44	Huasco Sivica	Atacama	06/04/2016	working	X			X	X	X	X
45	EME F	Atacama									
46	EME M	Atacama									
47	EME ME	Atacama	01/01/2003	31/12/2009	X	X	X	X	X	X	X
48	SM1 Vertedero	Atacama									
49	SM2 Quinta La Rosa	Atacama									
50	SM3 Compañía	Atacama									
51	SM4 Carretera km 40	Atacama	01/01/2002	working						X	X
52	SM5 Parcela 5 El Pino	Atacama									
53	Pabellón	Atacama									
54	Tierra Amarilla	Atacama	01/01/2009	31/12/2009						X	X
55	Coquimbo	Coquimbo	09/04/2016	working	X			X	X	X	X
56	La Serena	Coquimbo	08/04/2016	working	X			X	X	X	X

Figure A2: Details of the meteorological monitoring records of the National Air Quality Information System of Chile (SINCA). The length of the records and the variables measured are shown.

Bibliography

Ackerman, A. S., Toon, O. B., Stevens, D. E., Heymsfield, A. J., Ramanathan, V., and Welton, E. J.: Reduction of tropical cloudiness by soot, Science, 288, 1042–1047, 2000.

Adcroft, A. and Hallberg, R.: On methods for solving the oceanic equations of motion in generalized vertical coordinates, Ocean Modelling, 11, 224–233, 2006.

Aguirre, C., Rojas, M., Garreaud, R. D., and Rahn, D. A.: Role of synoptic activity on projected changes in upwelling-favourable winds at the ocean's eastern boundaries, npj Climate and Atmospheric Science, 2, 1–7, 2019.

Al-Saadi, J., Szykman, J., Pierce, R. B., Kittaka, C., Neil, D., Chu, D. A., Remer, L., Gumley, L., Prins, E., Weinstock, L., et al.: Improving national air quality forecasts with satellite aerosol observations, Bulletin of the American Meteorological Society, 86, 1249–1262, 2005.

Albrecht, B. A.: Aerosols, Cloud Microphysics, and Fractional Cloudiness, Science, 245, 1227–1230, 1989.

Alfaro, S. C., Flores-Aqueveque, V., Foret, G., Caquineau, S., Vargas, G., and Rutllant, J. A.: A simple model accounting for the uptake, transport, and deposition of wind-eroded mineral particles in the hyperarid coastal Atacama Desert of northern Chile, Earth Surface Processes and Landforms, 36, 923–932, 2011.

Altaratz, O., Bar-Or, R., Wollner, U., and Koren, I.: Relative humidity and its effect on aerosol optical depth in the vicinity of convective clouds, Environmental Research Letters, 8, 034 025, 2013.

Anderson, J. O., Thundiyil, J. G., and Stolbach, A.: Clearing the air: a review of the effects of particulate matter air pollution on human health, Journal of medical toxicology, 8, 166–175, 2012.

Anderson, T., Spall, S., Yool, A., Cipollini, P., Challenor, P., and Fasham, M.: Global fields of sea surface dimethylsulfide predicted from chlorophyll, nutrients and light, Journal of Marine Systems, 30, 1–20, 2001.

Anderson, T. L., Charlson, R. J., Winker, D. M., Ogren, J. A., and Holmén, K.: Mesoscale variations of tropospheric aerosols, Journal of the Atmospheric Sciences, 60, 119–136, 2003.

Ångström, A.: On the atmospheric transmission of sun radiation and on dust in the air, Geografiska Annaler, 11, 156–166, 1929.

Appelhans, T., Sturman, A., and Zawar-Reza, P.: Synoptic and climatological controls of particulate matter pollution in a Southern Hemisphere coastal city, International Journal of Climatology, 33, 463–479, 2013.

Aravena, G., Broitman, B., and Stenseth, N. C.: Twelve Years of Change in Coastal Upwelling along the Central-Northern Coast of Chile: Spatially Heterogeneous Responses to Climatic Variability, Plos One, 9, 2014.

Archibald, A. T., O'Connor, F. M., Abraham, N. L., Archer-Nicholls, S., Chipperfield, M. P., Dalvi, M., Folberth, G. A., Dennison, F., Dhomse, S. S., Griffiths, P. T., et al.: Description and evaluation of the UKCA stratosphere–troposphere chemistry scheme (StratTrop vn 1.0) implemented in UKESM1, Geoscientific Model Development, 13, 1223–1266, 2020.

Arrhenius, S.: On the Influence of Carbonic Acid in the Air upon the Temperature of the Ground, Philosophical Magazine and Journal of Science, 41, 237–276, 1896.

Bahamondez, F.: The energy transition and renewable energy in Chile: Top points for foreign investors, 2020.

Bakun, A.: Global Climate Change and Intensification of Coastal Ocean Upwelling, Science, 247, 198–201, 1990.

Bakun, A., Field, D. B., Redondo-Rodriguez, A., and Weeks, S. J.: Greenhouse gas upwelling-favorable winds, and the future of coastal ocean upwelling ecosystems, Global Change Biology, 16, 1213–1228, 2010.

Bakun, A., Black, B. A., Bograd, S. J., García-Reyes, M., Miller, A. J., Rykaczewski, R. R., and Sydeman, W. J.: Anticipated Effects of Climate Change on Coastal Upwelling Ecosystems, Current Climate Change Reports, 1, 85–93, 2015.

Balkanski, Y., Schulz, M., Claquin, T., and Guibert, S.: Reevaluation of Mineral aerosol radiative forcings suggests a better agreement with satellite and AERONET data, Atmospheric Chemistry and Physics, 7, 81–95, 2007.

Banerjee, T., Murari, V., Kumar, M., and Raju, M.: Source apportionment of airborne particulates through receptor modeling: Indian scenario, Atmospheric Research, 164, 167–187, 2015.

Barraza, F., Lambert, F., Jorquera, H., Villalobos, A. M., and Gallardo, L.: Temporal evolution of main ambient PM2. 5 sources in Santiago, Chile, from 1998 to 2012, Atmospheric Chemistry and Physics, 2017.

Bauer, S. E., Koch, D., Unger, N., Metzger, S. M., Shindell, D. T., and Streets, D. G.: Nitrate aerosols today and in 2030: a global simulation including aerosols and tropospheric ozone, Atmospheric Chemistry and Physics, 7, 5043–5059, 2007.

Bedsworth, L.: Air quality planning in California's changing climate, Climatic Change, 111, 101–118, doi: 10.1007/s10584-011-0244-0, URL `http://dx.doi.org/10.1007/s10584-011-0244-0`, 2011.

Beljaars, A.: The parametrization of the planetary boundary layer, ECMWF Meteorological Training Course Lecture Series, pp. 1–57, 1992.

Bellouin, N., Collins, W., Culverwell, I., Halloran, P., Hardiman, S., Hinton, T., Jones, C., McDonald, R., McLaren, A., O'Connor, F., et al.: The HadGEM2 family of met office unified model climate configurations, Geoscientific Model Development, 4, 723–757, 2011a.

Bellouin, N., Rae, J., Jones, A., Johnson, C., Haywood, J., and Boucher, O.: Aerosol forcing in the Climate Model Intercomparison Project (CMIP5) simulations by HadGEM2-ES and the role of ammonium nitrate, Journal of Geophysical Research: Atmospheres, 116, 2011b.

Bellouin, N., Quaas, J., Gryspeerdt, E., Kinne, S., Stier, P., Watson-Parris, D., Boucher, O., Carslaw, K. S., Christensen, M., Daniau, A.-L., et al.: Bounding global aerosol radiative forcing of climate change, Reviews of Geophysics, 58, e2019RG000 660, 2020.

Belmadani, A., Echevin, V., Codron, F., Takahashi, K., and Junquas, C.: What dynamics drive future wind scenarios for coastal upwelling off Peru and Chile?, Climate Dynamics, 43, 1893–1914, 2013.

Benkley, C. W. and Schulman, L. L.: Estimating Hourly Mixing Depths from Historical Mteorological Data, Journal of Applied Meteorology, 18, 772–780, 1979.

Berg, A., Findell, K., Lintner, B., Giannini, A., Seneviratne, S. I., Van Den Hurk, B., Lorenz, R., Pitman, A., Hagemann, S., Meier, A., et al.: Land–atmosphere feedbacks amplify aridity increase over land under global warming, Nature Climate Change, 6, 869–874, 2016.

Bilal, M. and Nichol, J. E.: Evaluation of MODIS aerosol retrieval algorithms over the Beijing-Tianjin-Hebei region during low to very high pollution events, Journal of Geophysical Research: Atmospheres, 120, 7941–7957, 2015.

Blanchard, D. C. and Woodcock, A. H.: The production, concentration, and vertical distribution of the sea-salt aerosol, Annals of the New York Academy of Sciences, 338, 330–347, 1980.

Bollasina, M. A., Ming, Y., and Ramaswamy, V.: Anthropogenic Aerosols and the Weakening of the South Asian Summer Monsoon, Science, 334, 502–505, 2011.

Bonan, G. B. and Doney, S. C.: Climate, ecosystems, and planetary futures: The challenge to predict life in Earth system models, Science, 359, 2018.

Boucher, O., Randall, D., Artaxo, P., Bretherton, C., Feingold, G., Forster, P., Kerminen, V.-M., Kondo, Y., Liao, H., Lohmann, U., Rasch, P., Satheesh, S., Stevens, S. S. B., and Zhang, X.: Clouds and Aerosols, Climate Change 2013: The Physical Science Basis. Contribution of Working Group I to the Fifth Assessment Report of the Intergovernmental Panel on Climate Change, Cambridge University Press, Cambridge, United Kingdom and New York, NY, USA, 2013.

Boville, B. A. and Gent, P. R.: The NCAR Climate System Model Version One, Journal of Climate, 11, 1115–1130, 1998.

Bozkurt, D., Rondanelli, R., Garreaud, R., and Arriagada, A.: Impact of warmer eastern tropical Pacific SST on the March 2015 Atacama floods, Monthly Weather Review, 144, 4441–4460, 2016.

Bozkurt, D., Rondanelli, R., Marin, J., and Garreaud, R.: Foehn event triggered by an atmospheric river underlies record-setting temperature along continental Antarctica, Journal of Geophysical Research: Atmospheres, 123, 3871–3892, 2018.

Bozkurt, D., Rojas, M., Boisier, J. P., Rondanelli, R., Garreaud, R., and Gallardo, L.: Dynamical downscaling over the complex terrain of southwest South America: present climate conditions and added value analysis, Climate Dynamics, 53, 6745–6767, 2019.

Buchholz, S., Junk, J., Krein, A., Heinemann, G., and Hoffmann, L.: Air pollution characteristics associated with mesoscale atmospheric patterns in northwest continental Europe, Atmospheric Environment, 44, 5183–5190, 2010.

Burney, J. and Ramanathan, V.: Recent climate and air pollution impacts on Indian agriculture, Proceedings of the National Academy of Sciences, 111, 16 319–16 324, 2014.

Burroughs, W. J.: Climate Change, Cambridge University Press (CUP), 2007.

Byrne, M. P. and Ogorman, P. A.: Land–ocean warming contrast over a wide range of climates: Convective quasi-equilibrium theory and idealized simulations, Journal of Climate, 26, 4000–4016, 2013.

Byrne, M. P. and O'Gorman, P. A.: Trends in continental temperature and humidity directly linked to ocean warming, Proceedings of the National Academy of Sciences, 115, 4863–4868, 2018.

Cane, M. A.: Twentieth-Century Sea Surface Temperature Trends, Science, 275, 957–960, 1997.

Capotondi, A., Alexander, M. A., Bond, N. A., Curchitser, E. N., and Scott, J. D.: Enhanced upper ocean stratification with climate change in the CMIP3 models, Journal of Geophysical Research: Oceans, 117, 2012.

Cardone, V. J., Greenwood, J. G., and Cane, M. A.: On Trends in Historical Marine Wind Data, Journal of Climate, 3, 113–127, 1990.

Carslaw, K., Lee, L., Reddington, C., Pringle, K., Rap, A., Forster, P., Mann, G., Spracklen, D., Woodhouse, M., Regayre, L., et al.: Large contribution of natural aerosols to uncertainty in indirect forcing, Nature, 503, 67, 2013.

Cesana, G. V., Del Genio, A., Ackerman, A. S., Kelley, M., Elsaesser, G. S., Fridlind, A. M., Cheng, Y., and Yao, M.-S.: Evaluating models' response of tropical low clouds to SST forcings using CALIPSO observations, 2019.

Chadwick, R., Good, P., and Willett, K.: A simple moisture advection model of specific humidity change over land in response to SST warming, Journal of Climate, 29, 7613–7632, 2016.

Chen, A., Howl, B., and Sidel, A.: How Aerosols Are Measured: The Science of Deep Blue, 2015.

Chen, F. and Dudhia, J.: Coupling an advanced land surface–hydrology model with the Penn State–NCAR MM5 modeling system. Part I: Model implementation and sensitivity, Monthly weather review, 129, 569–585, 2001.

Chen, J., Li, Z., Lv, M., Wang, Y., Wang, W., Zhang, Y., Wang, H., Yan, X., Sun, Y., and Cribb, M.: Aerosol hygroscopic growth, contributing factors, and impact on haze events in a severely polluted region in northern China, Atmospheric Chemistry and Physics, 19, 1327–1342, 2019.

Chen, Z., Cheng, S., Li, J., Guo, X., Wang, W., and Chen, D.: Relationship between atmospheric pollution processes and synoptic pressure patterns in northern China, Atmospheric Environment, 42, 6078–6087, doi: 10.1016/j.atmosenv.2008.03.043, URL http://dx.doi.org/10.1016/j.atmosenv.2008.03.043, 2008.

Chen, Z., Yan, X.-H., Jo, Y.-H., Jiang, L., and Jiang, Y.: A study of Benguela upwelling system using different upwelling indices derived from remotely sensed data, Continental Shelf Research, 45, 27–33, 2012.

Cheng, C. S., Campbell, M., Li, Q., Li, G., Auld, H., Day, N., Pengelly, D., Gingrich, S., and Yap, D.: A Synoptic Climatological Approach to Assess Climatic Impact on Air Quality in South-central Canada. Part I: Historical Analysis, Water, Air, and Soil Pollution, 182, 131–148, doi: 10.1007/s11270-006-9327-3, URL http://dx.doi.org/10.1007/s11270-006-9327-3, 2007.

Chhak, K. and Di Lorenzo, E.: Decadal variations in the California Current upwelling cells, Geophysical Research Letters, 34, n/a–n/a, doi: 10.1029/2007GL030203, URL http://dx.doi.org/10.1029/2007GL030203, l14604, 2007.

Cholakian, A., Colette, A., Coll, I., Ciarelli, G., and Beekmann, M.: Future climatic

drivers and their effect on PM10 components in Europe and the Mediterranean Sea, Atmospheric Chemistry and Physics, 19, 4459–4484, 2019.

Chudnovsky, A., Tang, C., Lyapustin, A., Wang, Y., Schwartz, J., and Koutrakis, P.: A critical assessment of high resolution aerosol optical depth (AOD) retrievals for fine particulate matter (PM) predictions, Atmospheric Chemistry and Physics Discussions, 13, 14 581–14 611, 2013.

Clark, D., Mercado, L., Sitch, S., Jones, C., Gedney, N., Best, M., Pryor, M., Rooney, G., Essery, R., Blyth, E., et al.: The Joint UK Land Environment Simulator (JULES), model description Part 2: carbon fluxes and vegetation dynamics, Geoscientific Model Development, 4, 701–722, 2011.

Clarke, A. J. and Lebedev, A.: Long-Term Changes in the Equatorial Pacific Trade Winds, Journal of Climate, 9, 1020–1029, 1996.

Collaud Coen, M., Andrews, E., Asmi, A., Baltensperger, U., Bukowiecki, N., Day, D., Fiebig, M., Fjaeraa, A. M., Flentje, H., Hyvärinen, A., Jefferson, A., Jennings, S. G., Kouvarakis, G., Lihavainen, H., Lund Myhre, C., Malm, W. C., Mihapopoulos, N., Molenar, J. V., O'Dowd, C., Ogren, J. A., Schichtel, B. A., Sheridan, P., Virkkula, A., Weingartner, E., Weller, R., and Laj, P.: Aerosol decadal trends – Part 1: In-situ optical measurements at GAW and IMPROVE stations, Atmospheric Chemistry and Physics, 13, 869–894, doi: 10.5194/acp-13-869-2013, URL https://acp.copernicus.org/articles/13/869/2013/, 2013.

Collins, M., Knutti, R., Arblaster, J., Dufresne, J.-L., Fichefet, T., Friedlingstein, P., Gao, X., Gutowski, W. J., Johns, T., Krinner, G., et al.: Long-term climate change: projections, commitments and irreversibility, in: Climate Change 2013-The Physical Science Basis: Contribution of Working Group I to the Fifth Assessment Report of the Intergovernmental Panel on Climate Change, pp. 1029–1136, Cambridge University Press, 2013.

Collins, W. D., Rasch, P. J., Boville, B. A., Hack, J. J., McCaa, J. R., Williamson,

D. L., Kiehl, J. T., Briegleb, B., Bitz, C., Lin, S.-J., et al.: Description of the NCAR community atmosphere model (CAM 3.0), NCAR Tech. Note NCAR/TN-464+ STR, 226, 2004.

CONAMA: D.S 59/1998. Establece norma de calidad primaria para material particulado respirable MP10, en especial de los valores que definen situaciones de emergencia, 1998.

Copernicus, C. C. S.: ERA5: Fifth generation of ECMWF atmospheric reanalyses of the global climate, Copernicus Climate Change Service Climate Data Store (CDS), URL https://cds.climate.copernicus.eu/cdsapp#!/home, 2017.

Cordero, R., Damiani, A., Laroze, D., Macdonell, S., Jorquera, J., Sepúlveda, E., Feron, S., Llanillo, P., Labbe, F., Carrasco, J., et al.: Effects of soiling on photovoltaic (PV) modules in the Atacama Desert, Scientific reports, 8, 1–14, 2018.

CORDEX: CORDEX domains for model integrations, 2015.

Crumeyrolle, S., Chen, G., Ziemba, L., Beyersdorf, A., Thornhill, L., Winstead, E., Moore, R. H., Shook, M. A., Hudgins, C., and Anderson, B. E.: Factors that influence surface $PM_{2.5}$ values inferred from satellite observations: perspective gained for the US Baltimore–Washington metropolitan area during DISCOVER-AQ, Atmospheric Chemistry and Physics, 14, 2139–2153, doi: 10.5194/acp-14-2139-2014, URL https://acp.copernicus.org/articles/14/2139/2014/, 2014.

Daneri, G., Dellarossa, V., Quiñones, R., Jacob, B., Montero, P., and Ulloa, O.: Primary production and community respiration in the Humboldt Current System off Chile and associated oceanic areas, Marine Ecology Progress Series, 197, 41–49, 2000.

Dawson, J. P., Bloomer, B. J., Winner, D. A., and Weaver, C. P.: Understanding the Meteorological Drivers of U.S. Particulate Matter Concentrations in a Changing Climate, Bulletin of the American Meteorological Society, 95, 521–532,

doi: 10.1175/bams-d-12-00181.1, URL http://dx.doi.org/10.1175/BAMS-D-12-00181.1, 2014.

Deardorff, J. W.: Parameterization of the planetary boundary layer for use in general circulation models, Monthly Weather Review, 100, 93–106, 1972.

Dee, D. P., Uppala, S. M., Simmons, A., Berrisford, P., Poli, P., Kobayashi, S., Andrae, U., Balmaseda, M., Balsamo, G., Bauer, d. P., et al.: The ERA-Interim reanalysis: Configuration and performance of the data assimilation system, Quarterly Journal of the royal meteorological society, 137, 553–597, 2011.

Di, Q., Kloog, I., Koutrakis, P., Lyapustin, A., Wang, Y., and Schwartz, J.: Assessing PM2. 5 exposures with high spatiotemporal resolution across the continental United States, Environmental science & technology, 50, 4712–4721, 2016.

Di Nicolantonio, W., Cacciari, A., and Tomasi, C.: Particulate matter at surface: Northern Italy monitoring based on satellite remote sensing, meteorological fields, and in-situ samplings, IEEE Journal of Selected Topics in Applied Earth Observations and Remote Sensing, 2, 284–292, 2009.

Díaz-Robles, L., Saavedra, H., Schiappacasse, L., Cereceda-Balic, F., Cereceda, F., and Santa, T. F.: The Air Quality in Chile, EM, pp. 28–33, 2011.

Dickerson, R. R., Kondragunta, S., Stenchikov, G., Civerolo, K. L., Doddridge, B. G., and Holben, B. N.: The Impact of Aerosols on Solar Ultraviolet Radiation and Photochemical Smog, Science, 278, 827–830, 1997.

Dickinson, R. E.: Biosphere atmosphere transfer scheme (BATS) version 1e as coupled to the NCAR community climate model, NCAR Tech. Note TH-387+ STR, 1993.

Diffenbaugh, N. S., Snyder, M. A., and Sloan, L. C.: Could CO2-induced land-cover feedbacks alter near-shore upwelling regimes?, Proceedings of the National Academy of Sciences, 101, 27–32, 2003.

Dore, C., Murrells, T., Passant, N., Hobson, M., Thistlethwaite, G., Wagner, A., Li, Y., Bush, T., King, K., Norris, J., et al.: UK emissions of air pollutants 1970 to 2006, AEA Energy & Environment, Harwell, Oxfordshire, 2008.

Dreher, K. L. and Costa, D. L.: SYSTEMIC HEALTH EFFECTS OF AMBIENT AIR PARTICULATE MATTER EXPOSURE, Journal of Toxicology and Environmental Health, Part A, 1491–1492, 2002.

Du, Y., Xu, X., Chu, M., Guo, Y., and Wang, J.: Air particulate matter and cardiovascular disease: the epidemiological, biomedical and clinical evidence, Journal of thoracic disease, 8, E8, 2016.

Dubovik, O., Holben, B., Eck, T. F., Smirnov, A., Kaufman, Y. J., King, M. D., Tanré, D., and Slutsker, I.: Variability of absorption and optical properties of key aerosol types observed in worldwide locations, Journal of the atmospheric sciences, 59, 590–608, 2002.

Ealo, M., Alastuey, A., Ripoll, A., Pérez, N., Minguillón, M. C., Querol, X., and Pandolfi, M.: Detection of Saharan dust and biomass burning events using near-real-time intensive aerosol optical properties in the north-western Mediterranean, 2016.

Echevin, V., Goubanova, K., Belmadani, A., and Dewitte, B.: Sensitivity of the Humboldt Current system to global warming: a downscaling experiment of the IPSL-CM4 model, Climate Dynamics, 38, 761–774, 2011.

Eck, T. F., Holben, B., Reid, J., Dubovik, O., Smirnov, A., O'neill, N., Slutsker, I., and Kinne, S.: Wavelength dependence of the optical depth of biomass burning, urban, and desert dust aerosols, Journal of Geophysical Research: Atmospheres, 104, 31 333–31 349, 1999.

El-Shobokshy, M. S. and Hussein, F. M.: Degradation of photovoltaic cell performance due to dust deposition on to its surface, Renewable energy, 3, 585–590, 1993.

Energy: Chile Investment in the Energy Sector, 2020.

Engelstaedter, S. and Washington, R.: Atmospheric controls on the annual cycle of North African dust, Journal of Geophysical Research, 112, 2007.

Falvey, M. and Garreaud, R. D.: Regional cooling in a warming world: Recent temperature trends in the southeast Pacific and along the west coast of subtropical South America (1979–2006), Journal of Geophysical Research: Atmospheres, 114, 2009.

Field, C. B., Barros, V. R., Mastrandrea, M. D., Mach, K. J., Abdrabo, M. A.-K., Adger, W. N., Anokhin, Y. A., Anisimov, O. A., Arent, D. J., Barnett, J., et al.: Summary for Policy Makers: Working group 11 contribution to the fifth assessment report of the Intergovernmental panel on Climate Change, 2014.

Fiore, A. M., Naik, V., and Leibensperger, E. M.: Air Quality and Climate Connections, Journal of the Air and Waste Management Association, 65, 645–685, doi: 10.1080/10962247.2015.1040526, URL http://dx.doi.org/10.1080/10962247.2015.1040526, 2015.

Fitzgerald, J. W.: Approximation formulas for the equilibrium size of an aerosol particle as a function of its dry size and composition and the ambient relative humidity, Journal of Applied Meteorology and Climatology, 14, 1044–1049, 1975.

Flato, G., Marotzke, J., Abiodun, B., Braconnot, P., Chou, S. C., Collins, W., Cox, P., Driouech, F., Emori, S., Eyring, V., Forest, C., Gleckler, P., Guilyardi, E., Jakob, C., Kattsov, V., Reason, C., and Rummukainen, M.: Evaluation of Climate Models. In: Climate Change 2013: The Physical Science Basis. Contribution of Working Group I to the Fifth Assessment Report of the Intergovernmental Panel on Climate Change, Cambridge University Press, Cambridge, United Kingdom and New York, NY, USA, 2013a.

Flato, G., Marotzke, J., Abiodun, B., Braconnot, P., Chou, S. C., Collins, W. J., Cox, P., Driouech, F., Emori, S., Eyring, V., et al.: Evaluation of Climate Models.

In: Climate Change 2013: The Physical Science Basis. Contribution of Working Group I to the Fifth Assessment Report of the Intergovernmental Panel on Climate Change, Climate Change 2013, 5, 741–866, 2013b.

Florence, D. L., Hountondji, Y.-C., Henry, S., and Ozer, P.: What do we know about effects of desert dust on air quality and human health in West Africa compared to other regions?, Science of The Total Environment, 409, 1–8, doi: 10.1016/j.scitotenv.2010.09.025, URL `http://dx.doi.org/10.1016/j.scitotenv.2010.09.025`, 2010.

Flores-Aqueveque, V., Alfaro, S., Muñoz, R., Rutllant, J. A., Caquineau, S., Le Roux, J. P., and Vargas, G.: Aeolian erosion and sand transport over the Mejillones Pampa in the coastal Atacama Desert of northern Chile, Geomorphology, 120, 312–325, 2010.

Flores-Aqueveque, V., Caquineau, S., Alfaro, S., Valdes, J., and Vargas, G.: Using Image-Based Size Analysis For Determining the Size Distribution and Flux of Eolian Particles Sampled In Coastal Northern Chile (23S), Journal of Sedimentary Research, 84, 238–244, 2014.

Fritsch, J. and Chappell, C.: Numerical prediction of convectively driven mesoscale pressure systems. Part I: Convective parameterization, Journal of Atmospheric Sciences, 37, 1722–1733, 1980.

Fuenzalida, H. A., Sánchez, R., and Garreaud, R. D.: A climatology of cutoff lows in the Southern Hemisphere, Journal of Geophysical Research: Atmospheres, 110, 2005.

Gaiero, D. M., Simonella, L., Gassó, S., Gili, S., Stein, A., Sosa, P., Becchio, R., Arce, J., and Marelli, H.: Ground/satellite observations and atmospheric modeling of dust storms originating in the high Puna-Altiplano deserts (South America): Implications for the interpretation of paleo-climatic archives, Journal of Geophysical Research: Atmospheres, 118, 3817–3831, 2013.

Gallardo, L., Olivares, G., Langner, J., and Aarhus, B.: Coastal lows and sulfur air pollution in Central Chile, Atmospheric Environment, 36, 3829–3841, 2002.

Garfinkel, C. I., Waugh, D. W., and Polvani, L. M.: Recent Hadley cell expansion: The role of internal atmospheric variability in reconciling modeled and observed trends, Geophysical Research Letters, 42, 10–824, 2015.

Garrat, J.: The atmospheric boundary layer, Cambridge University Pres, 1992.

Garreaud, R. and Muñoz, R. C.: The low-level jet off the west coast of subtropical South America: Structure and variability, Monthly Weather Review, 133, 2246–2261, 2005.

Garreaud, R. and Rutllant, J.: Análisis meteorológico de los aluviones de Antofagasta y Santiago de Chile en el periodo 1991-1993, Atmósfera, 9, 251–271, 1996.

Garreaud, R., Rutllant, J., and Fuenzalida, H.: Coastal lows along the subtropical west coast of South America: Mean structure and evolution, Monthly Weather Review, 130, 75–88, 2002.

Garreaud, R., Vuille, M., and Clement, A. C.: The climate of the Altiplano: observed current conditions and mechanisms of past changes, Palaeogeography, palaeoclimatology, palaeoecology, 194, 5–22, 2003.

Garreaud, R. D. and Falvey, M.: The coastal winds off western subtropical South America in future climate scenarios, International Journal of Climatology, 29, 543–554, 2009.

Gil, G. M. V., Cunha, R. B. A., Di Santo, S. G., Monaro, R. M., Costa, F. F., and Sguarezi Filho, A. J.: Photovoltaic energy in South America: Current state and grid regulation for large-scale and distributed photovoltaic systems, Renewable Energy, 162, 1307–1320, 2020.

Giles, D. M., Sinyuk, A., Sorokin, M. G., Schafer, J. S., Smirnov, A., Slutsker, I., Eck, T. F., Holben, B. N., Lewis, J. R., Campbell, J. R., et al.: Advancements in

the Aerosol Robotic Network (AERONET) Version 3 database–automated near-real-time quality control algorithm with improved cloud screening for Sun photometer aerosol optical depth (AOD) measurements, Atmospheric Measurement Techniques, 12, 169–209, 2019.

Ginoux, P., Chin, M., Tegen, I., Prospero, J. M., Holben, B., Dubovik, O., and Lin, S.-J.: Sources and distributions of dust aerosols simulated with the GOCART model, Journal of Geophysical Research, 106, 20 255–20 273, 2001.

Ginoux, P., Prospero, J., Torres, O., and Chin, M.: Long-term simulation of global dust distribution with the GOCART model: correlation with North Atlantic Oscillation, Environmental Modelling and Software, 19, 113–128, doi: 10.1016/s1364-8152(03)00114-2, URL `http://dx.doi.org/10.1016/S1364-8152(03)00114-2`, 2004.

Ginoux, P., Prospero, J. M., Gill, T. E., Hsu, N. C., and Zhao, M.: Global-scale attribution of anthropogenic and natural dust sources and their emission rates based on MODIS Deep Blue aerosol products, Reviews of Geophysics, 50, 2012.

Giorgi, F.: Thirty years of regional climate modeling: where are we and where are we going next?, Journal of Geophysical Research: Atmospheres, 124, 5696–5723, 2019.

Giorgi, F., Marinucci, M. R., and Bates, G. T.: Development of a second-generation regional climate model (RegCM2). Part I: Boundary-layer and radiative transfer processes, Monthly Weather Review, 121, 2794–2813, 1993.

Giorgi, F., Coppola, E., Solmon, F., Mariotti, L., Sylla, M., Bi, X., Elguindi, N., Diro, G., Nair, V., Giuliani, G., et al.: RegCM4: model description and preliminary tests over multiple CORDEX domains, Climate Research, 52, 7–29, 2012.

Giorgi, F., Torma, C., Coppola, E., Ban, N., Schär, C., and Somot, S.: Enhanced summer convective rainfall at Alpine high elevations in response to climate warming, Nature Geoscience, 9, 584–589, 2016.

Gonzáles, M., Orozco, C., Pérez, A., Gonzales, N., Rodriguez, F., and Alfayate, J.: Contaminación ambiental: una visión desde la química, 2011.

Goossens, D., Offer, Z. Y., and Zangvil, A.: Wind tunnel experiments and field investigations of eolian dust deposition on photovoltaic solar collectors, Solar energy, 50, 75–84, 1993.

Gowers, A., Miller, B., and Stedman, J.: Estimating local mortality burdens associated with particulate air pollution, Centre for Radiation, Chemical and Environmental Hazards, Public Health England, 2014.

Gramsch, E., Cereceda-Balic, F., Oyola, P., and Von Baer, D.: Examination of pollution trends in Santiago de Chile with cluster analysis of PM10 and ozone data, Atmospheric environment, 40, 5464–5475, 2006.

Grassi, B., Redaelli, G., and Visconti, G.: Arctic sea ice reduction and extreme climate events over the Mediterranean region, Journal of Climate, 26, 10 101–10 110, 2013.

Grell, G. A.: Prognostic evaluation of assumptions used by cumulus parameterizations, Monthly weather review, 121, 764–787, 1993.

Grell, G. A., Dudhia, J., Stauffer, D. R., et al.: A description of the fifth-generation Penn State/NCAR mesoscale model (MM5), 1994.

Griffies, S., Adcroft, A. J., Aiki, H., Balaji, V., Bentson, M., Bryana, F., Danabasoglu, G., Denvil, S., England, H. D. M., Gregorya, J., Hallberg, R. W., Legg, S., Martin, T., McDougall, T., Pirani, A., Schmidt, G., Stevens, D., Taylor, K. E., and Tsujino, H.: Sampling Physical Ocean Fields in WCRP CMIP5 Simulations. CLIVAR Working Group for Ocean Model Development (WGOMD) Committee on CMIP5 Ocean Model Output WCRP, Informal Rep. 3/2009, 137, 55, 2010.

Griffies, S. M.: Fundamentals of ocean climate models, Princeton University Press, 2004.

Grundstrom, M., Tang, L., Hallquist, M., Nguyen, H., Chen, D., and Pleijel, H.: Influence of atmospheric circulation patterns on urban air quality during the winter, Atmospheric Pollution Research, 6, 278–285, 2015.

Gupta, V., Sharma, M., Pachauri, R. K., and Babu, K. D.: Comprehensive review on effect of dust on solar photovoltaic system and mitigation techniques, Solar Energy, 191, 596–622, 2019.

Hammond, R., Srinivasan, D., Harris, A., Whitfield, K., and Wohlgemuth, J.: Effects of soiling on PV module and radiometer performance, in: Conference Record of the Twenty Sixth IEEE Photovoltaic Specialists Conference-1997, pp. 1121–1124, IEEE, 1997.

Hannay, C., Williamson, D. L., Hack, J. J., Kiehl, J. T., Olson, J. G., Klein, S. A., Bretherton, C. S., and Köhler, M.: Evaluation of forecasted southeast Pacific stratocumulus in the NCAR, GFDL, and ECMWF models, Journal of Climate, 22, 2871–2889, 2009.

Harper, A. B., Cox, P. M., Friedlingstein, P., Wiltshire, A. J., Jones, C. D., Sitch, S., Mercado, L. M., Groenendijk, M., Robertson, E., Kattge, J., et al.: Improved representation of plant functional types and physiology in the Joint UK Land Environment Simulator (JULES v4. 2) using plant trait information, Geoscientific Model Development, 9, 2415–2440, 2016.

Harper, A. B., Wiltshire, A. J., Cox, P. M., Friedlingstein, P., Jones, C. D., Mercado, L. M., Sitch, S., Williams, K., and Duran-Rojas, C.: Vegetation distribution and terrestrial carbon cycle in a carbon cycle configuration of JULES4. 6 with new plant functional types, 2018.

Haywood, J. M., Osborne, S. R., Francis, P. N., Keil, A., Formenti, P., Andreae, M. O., and Kaye, P. H.: The mean physical and optical properties of regional haze dominated by biomass burning aerosol measured from the C-130 aircraft during SAFARI 2000, Journal of Geophysical Research: Atmospheres, 108, 2003.

He, Q., Gu, Y., and Zhang, M.: Spatiotemporal trends of PM2. 5 concentrations in central China from 2003 to 2018 based on MAIAC-derived high-resolution data, Environment International, 137, 105 536, 2020.

Heavens, N. G., Ward, D. S., and Natalie, M.: Studying and projecting climate change with earth system models, Nature Education Knowledge, 4, 4, 2013.

Henriquez, A., Osses, A., Gallardo, L., and Resquin, M. D.: Analysis and optimal design of air quality monitoring networks using a variational approach, Tellus B: Chemical and Physical Meteorology, 67, 25 385, 2015.

Hoesly, R. M., Smith, S. J., Feng, L., Klimont, Z., Janssens-Maenhout, G., Pitkanen, T., Seibert, J. J., Vu, L., Andres, R. J., Bolt, R. M., et al.: Historical (1750-2014) anthropogenic emissions of reactive gases and aerosols from the Community Emission Data System (CEDS), Geoscientific Model Development, 11, 369–408, 2018.

Holben, B. N., Eck, T. F., Slutsker, I. a., Tanre, D., Buis, J., Setzer, A., Vermote, E., Reagan, J. A., Kaufman, Y., Nakajima, T., et al.: AERONET A federated instrument network and data archive for aerosol characterization, Remote sensing of environment, 66, 1–16, 1998.

Holtslag, A. and Boville, B.: Local versus nonlocal boundary-layer diffusion in a global climate model, Journal of climate, 6, 1825–1842, 1993.

Holtslag, A., De Bruijn, E., and Pan, H.: A high resolution air mass transformation model for short-range weather forecasting, Monthly Weather Review, 118, 1561–1575, 1990.

Holzworth, G. C.: Mixing Depths, Wind Speeds and Air Pollution Potential for Selected Locations in the United States, Journal of Applied Meteorology, 6, 1039–1044, 1967.

Holzworth, G. C.: Mixing heights, wind speeds, and potential for urban air pollution throughout the contiguous United States, US Government Printing Office, 1972.

Hong, S.-Y. and Pan, H.-L.: Nonlocal boundary layer vertical diffusion in a medium-range forecast model, Monthly weather review, 124, 2322–2339, 1996.

Hong, S.-Y., Noh, Y., and Dudhia, J.: A new vertical diffusion package with an explicit treatment of entrainment processes, Monthly weather review, 134, 2318–2341, 2006.

Horton, D. E., Harshvardhan, and Diffenbaugh, N. S.: Response of air stagnation frequency to anthropogenically enhanced radiative forcing, Environ Res Lett, 7, doi: 10.1088/1748-9326/7/4/044034, 2012.

Horton, D. E., Skinner, C. B., Singh, D., and Diffenbaugh, N. S.: Occurrence and persistence of future atmospheric stagnation events, Nature Climate Change, 4, 698–703, doi: 10.1038/nclimate2272, URL `http://dx.doi.org/10.1038/NCLIMATE2272`, 2014.

Houston, J. and Hartley, A. J.: The central Andean west-slope rainshadow and its potential contribution to the origin of hyper-aridity in the Atacama Desert, International Journal of Climatology, 23, 1453–1464, 2003.

Hsieh, W. W. and Boer, G. J.: Global climate change and ocean upwelling, Fisheries Oceanography, 1, 333–338, 1992.

Hsu, N., Jeong, M.-J., Bettenhausen, C., Sayer, A., Hansell, R., Seftor, C., Huang, J., and Tsay, S.: Enhanced Deep Blue aerosol retrieval algorithm: The second generation, Journal of Geophysical Research: Atmospheres, 118, doi: 10.1002/jgrd.50712, 2013.

Hsu, N. C., Tsay, S.-C., King, M. D., and Herman, J. R.: Aerosol properties over bright-reflecting source regions, IEEE Transactions on Geoscience and Remote Sensing, 42, 557–569, 2004.

Huang, R., Zhai, X., Ivey, C. E., Friberg, M. D., Hu, X., Liu, Y., Di, Q., Schwartz, J., Mulholland, J. A., and Russell, A. G.: Air pollutant exposure field modeling

using air quality model-data fusion methods and comparison with satellite AOD-derived fields: application over North Carolina, USA, Air Quality, Atmosphere & Health, 11, 11–22, 2018.

Huneeus, N., Schulz, M., Balkanski, Y., Griesfeller, J., Prospero, J., Kinne, S., Bauer, S., Boucher, O., Chin, M., Dentener, F., and et al.: Global dust model intercomparison in AeroCom phase I, Atmospheric Chemistry and Physics, 11, 7781–7816, doi: 10.5194/acp-11-7781-2011, URL http://dx.doi.org/10.5194/acp-11-7781-2011, 2011.

Huneeus, N., van der Gon, H. D., Castesana, P., Menares, C., Granier, C., Granier, L., Alonso, M., de Fatima Andrade, M., Dawidowski, L., Gallardo, L., et al.: Evaluation of anthropogenic air pollutant emission inventories for South America at national and city scale, Atmospheric Environment, p. 117606, 2020.

Husain, L., Khan, A. J., Ahmed, T., Swami, K., Bari, A., Webber, J. S., and Li, J.: Trends in atmospheric elemental carbon concentrations from 1835 to 2005, Journal of Geophysical Research, 113, 2008.

Ichoku, C., Chu, D. A., Mattoo, S., Kaufman, Y. J., Remer, L. A., Tanré, D., Slutsker, I., and Holben, B. N.: A spatio-temporal approach for global validation and analysis of MODIS aerosol products, Geophysical Research Letters, 29, MOD1–1, 2002.

IHME: Global Burden of Disease Collaborative Network. Global Burden of Disease Study 2017 (GBD 2017) Results, 2018.

Incecik, S., Gertler, A., and Kassomenos), P.: Aerosols and air quality, Science of the Total Environment, 488?489, 355, 2014.

INE: National Statistics Institute of Chile (INE), INE, URL http://www.ine.cl/, 2016.

Jackson, J. M., Liu, H., Laszlo, I., Kondragunta, S., Remer, L. A., Huang, J., and

Huang, H.-C.: Suomi-NPP VIIRS aerosol algorithms and data products, Journal of Geophysical Research: Atmospheres, 118, 12–673, 2013.

Jacob, D. J. and Winner, D. A.: Effect of climate change on air quality, Atmospheric Environment, 43, 51–63, doi: 10.1016/j.atmosenv.2008.09.051, URL `http://dx.doi.org/10.1016/j.atmosenv.2008.09.051`, 2009.

Jacobson, M. Z.: A physically-based treatment of elemental carbon optics: Implications for global direct forcing of aerosos, Geophysical Research Letters, 27, 217–220, 2000.

Jeong, M.-J. and Li, Z.: Quality, compatibility, and synergy analyses of global aerosol products derived from the advanced very high resolution radiometer and Total Ozone Mapping Spectrometer, Journal of Geophysical Research: Atmospheres, 110, 2005.

Jethva, H., Torres, O., and Yoshida, Y.: Accuracy assessment of MODIS land aerosol optical thickness algorithms using AERONET measurements over North America., Atmospheric Measurement Techniques, 12, 2019.

Jhun, I., Oyola, P., Moreno, F., Castillo, M. A., and Koutrakis, P.: PM2. 5 mass and species trends in Santiago, Chile, 1998 to 2010: The impact of fuel-related interventions and fuel sales, Journal of the Air & Waste Management Association, 63, 161–169, 2013.

Ji, D., x, Y., Wang, L., Chen, L., Hu, B., Tang, G., Xin, J., Song, T., Wen, T., Sun, Y., and et al.: Analysis of heavy pollution episodes in selected cities of northern China, Atmospheric Environment, 50, 338–348, doi: 10.1016/j.atmosenv.2011.11.053, URL `http://dx.doi.org/10.1016/j.atmosenv.2011.11.053`, 2012.

Jorquera, H. and Barraza, F.: Source apportionment of PM10 and PM2. 5 in a desert region in northern Chile, Science of the Total Environment, 444, 327–335, 2013.

Jorquera, H., Orrego, G., Castro, J., and Vesovic, V.: Trends in air quality and population exposure in Santiago, Chile, 1989–2001, International journal of Environment and Pollution, 22, 507–530, 2004.

Junkermann, W., Vogel, B., and Sutton, M. A.: The climate penalty for clean fossil fuel combustion, Atmospheric Chemistry and Physics, 11, 12 917–12 924, doi: 10.5194/acp-11-12917-2011, URL http://dx.doi.org/10.5194/acp-11-12917-2011, 2011.

Kain, J. S.: The Kain–Fritsch convective parameterization: an update, Journal of applied meteorology, 43, 170–181, 2004.

Kalashnikova, O. V. and Kahn, R. A.: Mineral dust plume evolution over the Atlantic from MISR and MODIS aerosol retrievals, Journal of Geophysical Research: Atmospheres, 113, 2008.

Kaskaoutis, D., Kambezidis, H., Hatzianastassiou, N., Kosmopoulos, P., and Badarinath, K.: Aerosol climatology: dependence of the Angstrom exponent on wavelength over four AERONET sites, 2007.

Kassomenos, P., Kotroni, V., and Kallos, G.: ANALYSIS OF CLIMATOLOGICAL AND AIR QUALITY OBSERVATIONS FROM GREATER ATHENS AREA, Atmospheric Environment, 29, 3671–3688, 1995.

Katragkou, E., García-Díez, M., Vautard, R., Sobolowski, S., Zanis, P., Alexandri, G., Cardoso, R. M., Colette, A., Fernandez, J., Gobiet, A., Goergen, K., Karacostas, T., Knist, S., Mayer, S., Soares, P. M. M., Pytharoulis, I., Tegoulias, I., Tsikerdekis, A., and Jacob, D.: Regional climate hindcast simulations within EURO-CORDEX: evaluation of a WRF multi-physics ensemble, Geoscientific Model Development, 8, 603–618, doi: 10.5194/gmd-8-603-2015, URL https://www.geosci-model-dev.net/8/603/2015/, 2015.

Kaufman, Y., Setzer, A., Ward, D., Tanre, D., Holben, B., Menzel, P., Pereira, M., and Rasmussen, R.: Biomass burning airborne and spaceborne experiment in

the Amazonas (BASE-A), Journal of Geophysical Research: Atmospheres, 97, 14 581–14 599, 1992.

Kavouras, I. G., Koutrakis, P., Cereceda-Balic, F., and Oyola, P.: Source apportionment of PM10 and PM25 in five Chilean cities using factor analysis, Journal of the Air & Waste Management Association, 51, 451–464, 2001.

Kiehl, J., Hack, J., Bonan, G., Boville, B., and Briegleb, B.: Description of the NCAR community climate model (CCM3). Technical Note, Tech. rep., National Center for Atmospheric Research, Boulder, CO (United States, 1996.

Kim, D., Kim, J., Jeong, J., and Choi, M.: Estimation of health benefits from air quality improvement using the MODIS AOD dataset in Seoul, Korea, Environmental research, 173, 452–461, 2019.

Kloog, I., Chudnovsky, A. A., Just, A. C., Nordio, F., Koutrakis, P., Coull, B. A., Lyapustin, A., Wang, Y., and Schwartz, J.: A new hybrid spatio-temporal model for estimating daily multi-year PM2. 5 concentrations across northeastern USA using high resolution aerosol optical depth data, Atmospheric Environment, 95, 581–590, 2014.

Kloog, I., Sorek-Hamer, M., Lyapustin, A., Coull, B., Wang, Y., Just, A. C., Schwartz, J., and Broday, D. M.: Estimating daily PM2. 5 and PM10 across the complex geo-climate region of Israel using MAIAC satellite-based AOD data, Atmospheric Environment, 122, 409–416, 2015.

Konsta, D., Binietoglou, I., Gkikas, A., Solomos, S., Marinou, E., Proestakis, E., Basart, S., García-Pando, C. P., El-Askary, H., and Amiridis, V.: Evaluation of the BSC-DREAM8b regional dust model using the 3D LIVAS-CALIPSO product, Atmospheric environment, 195, 46–62, 2018.

Koren, I., Remer, L. A., Kaufman, Y. J., Rudich, Y., and Martins, J. V.: On the twilight zone between clouds and aerosols, Geophysical Research Letters, 34, 2007.

Kuhlbrodt, T., Jones, C. G., Sellar, A., Storkey, D., Blockley, E., Stringer, M., Hill, R., Graham, T., Ridley, J., Blaker, A., et al.: The low-resolution version of HadGEM3 GC3. 1: Development and evaluation for global climate, Journal of Advances in Modeling Earth Systems, 10, 2865–2888, 2018.

Kumar, M., Raju, M., Singh, R., and Banerjee, T.: Impact of drought and normal monsoon scenarios on aerosol induced radiative forcing and atmospheric heating in Varanasi over middle Indo-Gangetic Plain, Journal of Aerosol Science, 113, 95–107, 2017.

Kuo, C.-Y., Chen, P.-T., Lin, Y.-C., Lin, C.-Y., Chen, H.-H., and Shih, J.-F.: Factors affecting the concentrations of PM10 in central Taiwan, Chemosphere, 70, 1273–1279, doi: 10.1016/j.chemosphere.2007.07.058, URL http://dx.doi.org/10.1016/j.chemosphere.2007.07.058, 2008.

Kyung, S. Y. and Jeong, S. H.: Particulate-matter related respiratory diseases, Tuberculosis and respiratory diseases, 83, 116, 2020.

Lagos, G., Peters, D., Lima, M., and Jara, J. J.: Potential copper production through 2035 in Chile, Mineral Economics, 33, 43–56, 2020.

Lamarque, J.-F., Bond, T. C., Eyring, V., Granier, C., Heil, A., Klimont, Z., Lee, D., Liousse, C., Mieville, A., Owen, B., et al.: Historical (1850–2000) gridded anthropogenic and biomass burning emissions of reactive gases and aerosols: methodology and application, 2010.

Lee, H., Liu, Y., Coull, B., Schwartz, J., and Koutrakis, P.: A novel calibration approach of MODIS AOD data to predict PM 2.5 concentrations., Atmospheric Chemistry & Physics, 11, 2011.

Leibensperger, E. M., Mickley, L. J., and Jacob, D. J.: Sensitivity of US air quality to mid-latitude cyclone frequency and implications of 1980–2006 climate change, Atmospheric Chemistry and Physics, 8, 7075–7086, 2008.

Lesins, G., Chylek, P., and Lohmann, U.: A study of internal and external mixing scenarios and its effect on aerosol optical properties and direct radiative forcing, Journal of Geophysical Research, 107, 2002.

Leung, L. R. and Jr., W. I. G.: Potential regional climate change and implications to U.S. air quality, Geophysical Research Letters, 32, 2005.

Levy, R., Mattoo, S., Munchak, L., Remer, L., Sayer, A., Patadia, F., and Hsu, N.: The Collection 6 MODIS aerosol products over land and ocean, Atmospheric Measurement Techniques, 6, 2989, 2013.

Li, J., Carlson, B. E., and Lacis, A. A.: Application of spectral analysis techniques in the intercomparison of aerosol data: 1. An EOF approach to analyze the spatial-temporal variability of aerosol optical depth using multiple remote sensing data sets, Journal of Geophysical Research: Atmospheres, 118, 8640–8648, 2013a.

Li, J., Carlson, B. E., and Lacis, A. A.: How well do satellite AOD observations represent the spatial and temporal variability of PM2. 5 concentration for the United States?, Atmospheric Environment, 102, 260–273, 2015.

Li, W., Li, L., Ting, M., Deng, Y., Kushnir, Y., Liu, Y., Lu, Y., Wang, C., and Zhang, P.: Intensification of the Southern Hemisphere summertime subtropical anticyclones in a warming climate, Geophysical Research Letters, 40, 5959–5964, 2013b.

Liu, L. and Mishchenko, M. I.: Toward unified satellite climatology of aerosol properties: Direct comparisons of advanced level 2 aerosol products, Journal of Quantitative Spectroscopy and Radiative Transfer, 109, 2376–2385, 2008.

Lorenzo, E. D., Miller, A. J., Schneider, N., and McWilliams, J. C.: The Warming of the California Current System: Dynamics and Ecosystem Implications, Journal of Physical Oceanography, 35, 336–362, 2005.

Lu, J., Vecchi, G. A., and Reichler, T.: Expansion of the Hadley cell under global warming, Geophysical Research Letters, 34, 2007.

Lu, Q., Zheng, J., Ye, S., Shen, X., Yuan, Z., and Yin, S.: Emission trends and source characteristics of SO2, NOx, PM10 and VOCs in the Pearl River Delta region from 2000 to 2009, Atmospheric Environment, 76, 11–20, 2013.

Luo, C., Mahowald, N. M., and del Corral, J.: Sensitivity study of meteorological parameters on mineral aerosol mobilization, transport, and distribution, Journal of Geophysical Research, 108, 2003.

Lyapustin, A., Martonchik, J., Wang, Y., Laszlo, I., and Korkin, S.: Multiangle implementation of atmospheric correction (MAIAC): 1. Radiative transfer basis and look-up tables, Journal of Geophysical Research: Atmospheres, 116, 2011a.

Lyapustin, A., Wang, Y., Hsu, C., Torres, O., Leptoukh, G., Kalashnikova, O., and Korkin, S.: Analysis of MAIAC dust aerosol retrievals from MODIS over North Africa, Atti della Accademia Peloritana dei Pericolanti-Classe di Scienze Fisiche, Matematiche e Naturali, 89, 2011b.

Lyapustin, A., Wang, Y., Laszlo, I., Kahn, R., Korkin, S., Remer, L., Levy, R., and Reid, J.: Multiangle implementation of atmospheric correction (MAIAC): 2. Aerosol algorithm, Journal of Geophysical Research: Atmospheres, 116, 2011c.

Lyapustin, A., Korkin, S., Wang, Y., Quayle, B., and Laszlo, I.: Discrimination of biomass burning smoke and clouds in MAIAC algorithm, Atmospheric Chemistry and Physics, 12, 9679–9686, 2012.

Lyapustin, A., Wang, Y., Korkin, S., and Huang, D.: MODIS Collection 6 MAIAC algorithm., Atmospheric Measurement Techniques, 11, 2018.

Macintyre, H. L., Heaviside, C., Neal, L. S., Agnew, P., Thornes, J., and Vardoulakis, S.: Mortality and emergency hospitalizations associated with atmospheric particulate matter episodes across the UK in spring 2014, Environment international, 97, 108–116, 2016.

Mahowald, N. M., Engelstaedter, S., Luo, C., Sealy, A., Artaxo, P., Benitez-Nelson, C., Bonnet, S., Chen, Y., Chuang, P. Y., Cohen, D. D., et al.: Atmospheric iron deposition: global distribution, variability, and human perturbations, Annual Review of Marine Science, 1, 245–278, 2009.

Maione, M., Fowler, D., Monks, P. S., Reis, S., Rudich, Y., Williams, M. L., and Fuzzi, S.: Air quality and climate change: Designing new win-win policies for Europe, Environment Science and Policy, 65, 48–57, 2016.

Makra, L., Mika, J., Bartzokas, A., Béczi, R., Borsos, E., and Sümeghy, Z.: An objective classification system of air mass types for Szeged, Hungary, with special interest in air pollution levels, Meteorology and Atmospheric Physics, 92, 115–137, doi: 10.1007/s00703-005-0143-x, URL `http://dx.doi.org/10.1007/s00703-005-0143-x`, 2006.

Mann, G., Carslaw, K., Spracklen, D., Ridley, D., Manktelow, P., Chipperfield, M., Pickering, S., and Johnson, C.: Description and evaluation of GLOMAP-mode: A modal global aerosol microphysics model for the UKCA composition-climate model, Geoscientific Model Development, 3, 519, 2010.

Mann, G., Carslaw, K., Ridley, D., Spracklen, D., Pringle, K., Merikanto, J., Korhonen, H., Schwarz, J., Lee, L., Manktelow, P., et al.: Intercomparison of modal and sectional aerosol microphysics representations within the same 3-D global chemical transport model., Atmospheric Chemistry & Physics, 12, 2012.

Manzanas, R., Gutiérrez, J., Fernández, J., Van Meijgaard, E., Calmanti, S., Magariño, M., Cofiño, A., and Herrera, S.: Dynamical and statistical downscaling of seasonal temperature forecasts in Europe: Added value for user applications, Climate Services, 9, 44–56, 2018.

Marcella, M. P. and Eltahir, E. A.: Modeling the summertime climate of Southwest Asia: The role of land surface processes in shaping the climate of semiarid regions, Journal of Climate, 25, 704–719, 2012.

Marshak, A., Platnick, S., Várnai, T., Wen, G., and Cahalan, R. F.: Impact of three-dimensional radiative effects on satellite retrievals of cloud droplet sizes, Journal of Geophysical Research: Atmospheres, 111, 2006.

Marshall, J. and Plumb, R.: Atmosphere, ocean and climate dynamics: an introductory text, Academic Press, 2008.

Marticorena, B. and Bergametti, G.: Modeling the atmospheric dust cycle: 1. Design of a soil-derived dust emission scheme, Journal of Geophysical Research: Atmospheres, 100, 16 415–16 430, 1995.

Marticorena, B., Kardous, M., Bergametti, G., Callot, Y., Chazette, P., Khatteli, H., Le Hégarat-Mascle, S., Maille, M., Rajot, J.-L., Vidal-Madjar, D., et al.: Surface and aerodynamic roughness in arid and semiarid areas and their relation to radar backscatter coefficient, Journal of Geophysical Research: Earth Surface, 111, 2006.

Martins, V. S., Lyapustin, A., de Carvalho, L. A., Barbosa, C. C. F., and Novo, E. M. L. d. M.: Validation of high-resolution MAIAC aerosol product over South America, Journal of Geophysical Research: Atmospheres, 122, 7537–7559, 2017.

Marzban, C.: The ROC curve and the area under it as performance measures, Weather and Forecasting, 19, 1106–1114, 2004.

McCabe, R. M., Hickey, B. M., Dever, E. P., and MacCready, P.: Seasonal Cross-Shelf Flow Structure Upwelling Relaxation, and the Alongshelf Pressure Gradient in the Northern California Current System, J. Phys. Oceanogr., 45, 209–227, 2015.

McGregor, G. R. and Bamzelis, D.: Synoptic Typing and its Application to the Investigation of Weather Air Pollution Relationships, Birmingham, United Kingdom, Theoretical and Applied Climatology, 51, 223–236, 1995.

Meinshausen, M., Nicholls, Z., Lewis, J., Gidden, M. J., Vogel, E., Freund, M., Beyerle, U., Gessner, C., Nauels, A., Bauer, N., et al.: The SSP greenhouse gas

concentrations and their extensions to 2500, Geosci. Model Dev. Discuss, 2019, 1–77, 2019.

Melas, D., Ziomas, I. C., and Zerefos, C. S.: BOUNDARY LAYER DYNAMICS IN AN URBAN COASTAL ENVIRONMENT UNDER SEA BREEZE CONDITIONS, Atmospheric Environment, 29, 3605–3617, 1995.

Mena-Carrasco, M., Oliva, E., Saide, P., Spak, S. N., de la Maza, C., Osses, M., Tolvett, S., Campbell, J. E., Molina, L. T., et al.: Estimating the health benefits from natural gas use in transport and heating in Santiago, Chile, Science of the Total Environment, 429, 257–265, 2012.

Menut, L., Tripathi, O. P., Colette, A., Vautard, R., Flaounas, E., and Bessagnet, B.: Evaluation of regional climate simulations for air quality modelling purposes, Climate Dynamics, 40, 2515–2533, 2013.

Mhawish, A., Banerjee, T., Broday, D. M., Misra, A., and Tripathi, S. N.: Evaluation of MODIS Collection 6 aerosol retrieval algorithms over Indo-Gangetic Plain: Implications of aerosols types and mass loading, Remote sensing of environment, 201, 297–313, 2017.

Mhawish, A., Banerjee, T., Sorek-Hamer, M., Lyapustin, A., Broday, D. M., and Chatfield, R.: Comparison and evaluation of MODIS Multi-angle Implementation of Atmospheric Correction (MAIAC) aerosol product over South Asia, Remote Sensing of Environment, 224, 12–28, 2019.

Mi, W., Li, Z., Xia, X., Holben, B., Levy, R., Zhao, F., Chen, H., and Cribb, M.: Evaluation of the moderate resolution imaging spectroradiometer aerosol products at two aerosol robotic network stations in China, Journal of Geophysical Research: Atmospheres, 112, 2007.

Michel Flores, J., Bar-Or, R., Bluvshtein, N., Abo-Riziq, A., Kostinski, A., Bormann, S., Koren, I., and Rudich, Y.: Absorbing aerosols at high relative humidity: linking hygroscopic growth to optical properties, Atmospheric Chemistry and Physics, 12, 5511–5521, 2012.

Miller, R. L., Tegen, I., and Perlwitz, J.: Surface radiative forcing by soil dust aerosols and the hydrologic cycle, Journal of Geophysical Research, 109, 2004.

Minguillón, M., Querol, X., Baltensperger, U., and Prévôt, A.: Fine and coarse PM composition and sources in rural and urban sites in Switzerland: local or regional pollution?, Science of the Total Environment, 427, 191–202, 2012.

MINSAL, Ministerio de Salud, S. d. S. P.: D.S 138/2005. Establece obligacion de declaran emisiones que indica, 2005.

MINSEGPRES, M. S. G. d. l. P.: Ley 19300, Aprueba Ley sobre Bases generales del Medio Ambiente, 1994.

Miranda, P. M. A., Alves, J. M. R., and Serra, N.: Climate change and upwelling: response of Iberian upwelling to atmospheric forcing in a regional climate scenario, Climate Dynamics, 40, 2813–2824, 2012.

Mitas, C. M. and Clement, A.: Has the Hadley cell been strengthening in recent decades?, Geophysical Research Letters, 32, 2005.

Mitchell, J. F. B., Manabe, S., Meleshko, V., and Tokioka, T., eds.: Equilibrium Climate Change - and its Implications for the Future, Cambridge University Press (CUP), 1990.

MMA: D.S 12/2011. Establece norma primaria de calidad ambiental para material particulado fino respirable MP2,5., 2011.

MMA, M. d. M. A.: Sistema de evaluacion de impacto ambiental, Chile, Ministerio del Medio Ambiente, URL `http://www.sea.gob.cl/`, 2015.

MMA, M. d. M. A. d. C.: Informe Consolidado de Emisiones y Transferencias de Contaminantes. 2005-2016, RETC, Tech. rep., MMA Ministerio de Medio Ambiente de Chile, 2018.

Mohan, S. M.: An overview of particulate dry deposition: measuring methods, deposition velocity and controlling factors, International journal of environmental science and technology, 13, 387–402, 2016.

Molina, A., Falvey, M., and Rondanelli, R.: A solar radiation database for Chile, Scientific reports, 7, 1–11, 2017.

Mote, P. W. and Mantua, N. J.: Coastal upwelling in a warmer future, Geophysical Research Letters, 29, 53–1–53–4, 2002.

Mulcahy, J., Jones, C., Sellar, A., Johnson, B., Boutle, I., Jones, A., Andrews, T., Rumbold, S., Mollard, J., Bellouin, N., et al.: Improved aerosol processes and effective radiative forcing in HadGEM3 and UKESM1, Journal of Advances in Modeling Earth Systems, 10, 2786–2805, 2018.

Mulcahy, J. P., Johnson, C., Jones, C. G., Povey, A. C., Scott, C. E., Sellar, A., Turnock, S. T., Woodhouse, M. T., Abraham, N. L., Andrews, M. B., et al.: Description and evaluation of aerosol in UKESM1 and HadGEM3-GC3. 1 CMIP6 historical simulations, Geoscientific Model Development Discussions, pp. 1–59, 2020.

Muñoz, R. C., Zamora, R. A., and Rutllant, J. A.: The coastal boundary layer at the eastern margin of the southeast Pacific (23.4 S, 70.4 W): Cloudiness-conditioned climatology, Journal of Climate, 24, 1013–1033, 2011.

Muñoz, R. C., Falvey, M. J., Araya, M., and Jacques-Coper, M.: Strong down-valley low-level jets over the Atacama Desert: Observational characterization, Journal of applied meteorology and climatology, 52, 2735–2752, 2013.

Muñoz, R. C., Quintana, J., Falvey, M. J., Rutllant, J. A., and Garreaud, R.: Coastal clouds at the eastern Margin of the southeast Pacific: Climatology and trends, Journal of Climate, 29, 4525–4542, 2016.

Myhre, G., Samset, B. H., Schulz, M., Balkanski, Y., Bauer, S., Berntsen, T. K., Bian, H., Bellouin, N., Chin, M., Diehl, T., and et al.: Radiative forcing of the direct aerosol effect from AeroCom Phase II simulations, Atmospheric Chemistry and Physics, 13, 1853–1877, doi: 10.5194/acp-13-1853-2013, URL `http://dx.doi.org/10.5194/acp-13-1853-2013`, 2013.

Nakajima, T. and Higurashi, A.: A use of two-channel radiances for an aerosol characterization from space, Geophysical Research Letters, 25, 3815–3818, 1998.

Neelin, J.: Climate change and climate modeling, Cambridge University Press, 2011.

Nester, K.: Influence of Sea Breeze Flows on Air Pollution over the Attica Peninsula, Atmospheric Environment, 29, 3655–3670, 1995.

Nordio, F., Kloog, I., Coull, B. A., Chudnovsky, A., Grillo, P., Bertazzi, P. A., Baccarelli, A. A., and Schwartz, J.: Estimating spatio-temporal resolved PM10 aerosol mass concentrations using MODIS satellite data and land use regression over Lombardy, Italy, Atmospheric environment, 74, 227–236, 2013.

Nummelin, A., Ilicak, M., Li, C., and Smedsrud, L. H.: Consequences of future increased Arctic runoff on Arctic Ocean stratification, circulation, and sea ice cover, Journal of Geophysical Research: Oceans, 121, 617–637, 2016.

Oerder, V., Colas, F., Echevin, V., Codron, F., Tam, J., , and Belmadani, A.: Peru-Chile upwelling dynamics under climate change, Journal of Geophysical Research: Oceans, 120, 1152–1172, 2015.

Oh, S.-G., Park, J.-H., Lee, S.-H., and Suh, M.-S.: Assessment of the RegCM4 over East Asia and future precipitation change adapted to the RCP scenarios, Journal of Geophysical Research: Atmospheres, 119, 2913–2927, 2014.

Ortlieb, L.: Eventos El Niño y episodios lluviosos en el desierto de Atacama: el registro de los últimos dos siglos, Bull. Inst. fr. études andines, 24, 519–537, 1995.

Osborne, S., Johnson, B., Haywood, J., Baran, A., Harrison, M., and McConnell, C.: Physical and optical properties of mineral dust aerosol during the Dust and Biomass-burning Experiment, Journal of Geophysical Research: Atmospheres, 113, 2008.

Oyarzún, D. and Brierley, C. M.: The future of coastal upwelling in the Humboldt current from model projections, Climate Dynamics, 52, 599–615, 2019.

Pal, J. S., Small, E. E., and Eltahir, E. A.: Simulation of regional-scale water and energy budgets: Representation of subgrid cloud and precipitation processes within RegCM, Journal of Geophysical Research: Atmospheres, 105, 29 579–29 594, 2000.

Palmer, T.: Climate forecasting: Build high-resolution global climate models, Nature, 515, 338–339, 2014.

Pandithurai, G., Dipu, S., Dani, K., Tiwari, S., Bisht, D., Devara, P., and Pinker, R.: Aerosol radiative forcing during dust events over New Delhi, India, Journal of Geophysical Research: Atmospheres, 113, 2008.

Peterson, E. W. and Hasse, L.: Did the Beaufort Scale or the Wind Climate Change?, Journal of Physical Oceanography, 17, 1071–1074, 1987.

Pielke, R. A., Stocker, R. A., Arritt, R. W., and McNider, R. T.: A procedure to estimate worst-case air quality in complex terrain, Environment international, 17, 559–574, 1991.

Pope, C. A., Burnett, R. T., Thun, M. J., Calle, E. E., Krewski, D., Ito, K., and Thurston, G. D.: Lung Cancer, Cardiopulmonary Mortality, and Long-term Exposure to Fine Particulate Air Pollution, American Medical Association, 287, 1132–1141, 2002.

Prigent, C., Jiménez, C., and Catherinot, J.: Comparison of satellite microwave backscattering (ASCAT) and visible/near-infrared reflectances (PARASOL) for the estimation of aeolian aerodynamic roughness length in arid and semi-arid regions, Atmospheric Measurement Techniques, 5, 2703, 2012.

Pringle, K., Tost, H., Pozzer, A., Pöschl, U., and Lelieveld, J.: Global distribution of the effective aerosol hygroscopicity parameter for CCN activation, Atmos. Chem. Phys, 10, 5241–5255, 2010.

Qin, D., Plattner, G., Tignor, M., Allen, S., Boschung, J., Nauels, A., Xia, Y., Bex, V., Midgley, P., et al.: Climate change 2013: the physical science basis, Contribution of Working Group I to the Fifth Assessment Report of the Intergovernmental Panel on Climate Change (eds TF Stocker et al.), pp. 5–14, 2014.

Quade, J., Rech, J. A., Betancourt, J. L., Latorre, C., Quade, B., Rylander, K. A., and Fisher, T.: Paleowetlands and regional climate change in the central Atacama Desert, northern chile, Quaternary Research, 69, 343–360, doi: 10.1016/j.yqres.2008.01.003, URL http://dx.doi.org/10.1016/j.yqres.2008.01.003, 2008.

Radhi, M., Box, M., Box, G., Mitchell, R., Cohen, D., Stelcer, E., and Keywood, M.: Optical, physical and chemical characteristics of Australian continental aerosols: results from a field experiment., Atmospheric Chemistry & Physics, 10, 2010.

Ramage, C. S.: Secular Change in Reported Surface Wind Speeds over the Ocean, Journal of Climate and Applied Meteorology, 26, 525–528, 1987.

Ramanathan, V. and Feng, Y.: Air pollution, greenhouse gases and climate change: Global and regional perspectives, Atmospheric Environment, 43, 37–50, doi: 10.1016/j.atmosenv.2008.09.063, URL http://dx.doi.org/10.1016/j.atmosenv.2008.09.063, 2009.

Ramanathan, V. and Ramana, M.: Persistent, widespread, and strongly absorbing haze over the Himalayan foothills and the Indo-Gangetic Plains, Pure and Applied Geophysics, 162, 1609–1626, 2005.

Ramanathan, V., Crutzen, P., Kiehl, J., and Rosenfeld, D.: Aerosols, climate, and the hydrological cycle, science, 294, 2119–2124, 2001.

Rao, S., Klimont, Z., Smith, S. J., Van Dingenen, R., Dentener, F., Bouwman, L., Riahi, K., Amann, M., Bodirsky, B. L., van Vuuren, D. P., et al.: Future air pollution in the Shared Socio-economic Pathways, Global Environmental Change, 42, 346–358, 2017.

Ravishankara, A., Dawson, J. P., and Winner, D. A.: New Directions: Adapting air quality management to climate change: A must for planning, Atmospheric Environment, 50, 387–389, doi: 10.1016/j.atmosenv.2011.12.048, URL `http://dx.doi.org/10.1016/j.atmosenv.2011.12.048`, 2012.

Reyers, M., Hamidi, M., and Shao, Y.: Synoptic analysis and simulation of an unusual dust event over the Atacama Desert, Atmospheric Science Letters, 20, e899, 2019.

Riahi, K., Van Vuuren, D. P., Kriegler, E., Edmonds, J., O'neill, B. C., Fujimori, S., Bauer, N., Calvin, K., Dellink, R., Fricko, O., et al.: The shared socioeconomic pathways and their energy, land use, and greenhouse gas emissions implications: an overview, Global Environmental Change, 42, 153–168, 2017.

Ritchie, H. and Roser, M.: Air Pollution, Our World in Data, https://ourworldindata.org/air-pollution, 2017.

Roemmich, D. and McGowan, J.: Climatic Warming and the Decline of Zooplankton in the California Current, Science, 267, 1324–1326, 1995.

Rojas, M.: Multiply nested regional climate simulation for southern South America: Sensitivity to model resolution, Monthly weather review, 134, 2208–2223, 2006.

Rondanelli, R., Molina, A., and Falvey, M.: The Atacama surface solar maximum, Bulletin of the American Meteorological Society, 96, 405–418, 2015.

Ruiz-Rudolph, P., Arias, N., Pardo, S., Meyer, M., Mesías, S., Galleguillos, C., Schiattino, I., and Gutiérrez, L.: Impact of large industrial emission sources on mortality and morbidity in Chile: A small-areas study, Environment International, 92-93, 130–138, 2016.

Ruppel, M. M., Isaksson, I., Ström, J., Beaudon, E., Svensson, J., Pedersen, C. A., and Korhola, A.: Increase in elemental carbon values between 1970 and 2004 observed in a 300-year ice core from Holtedahlfonna (Svalbard), Atmospheric

Chemistry and Physics, 14, 11 447–11 460, doi: 10.5194/acp-14-11447-2014, URL http://dx.doi.org/10.5194/acp-14-11447-2014, 2014.

Russell, P., Bergstrom, R., Shinozuka, Y., Clarke, A., DeCarlo, P., Jimenez, J., Livingston, J., Redemann, J., Dubovik, O., and Strawa, A.: Absorption Angstrom Exponent in AERONET and related data as an indicator of aerosol composition, Atmos. Chem. Phys, 10, 1155–1169, 2010.

Rutllant, J. A., Fuenzalida, H., and Aceituno, P.: Climate dynamics along the arid northern coast of Chile: the 1997–1998 Dinámica del Clima de la Región de Antofagasta (DICLIMA) experiment, Journal of Geophysical Research: Atmospheres, 108, 2003.

Rutllant, J. A., Muñoz, R. C., and Garreaud, R. D.: Meteorological observations on the northern Chilean coast during VOCALS-REx, Atmospheric Chemistry and Physics, 13, 3409–3422, doi: 10.5194/acp-13-3409-2013, URL http://dx.doi.org/10.5194/acp-13-3409-2013, 2013.

Rykaczewski, R. R. and Checkley, D. M.: Influence of ocean winds on the pelagic eco- system in upwelling regions, Proceedings of the National Academy of Sciences, 105, 1965–1970, 2008.

Rykaczewski, R. R., Dunne, J. P., Sydeman, W. J., García-Reyes, M., Black, B. A., and Bograd, S. J.: Poleward displacement of coastal upwelling-favorable winds in the ocean's eastern boundary currents through the 21st century, Geophysical Research Letters, 42, 6424–6431, 2015.

Sacks, J. D., Stanek, L. W., Luben, T. J., Johns, D. O., Buckley, B. J., Brown, J. S., and Ross, M.: Particulate Matter–Induced Health Effects: Who Is Susceptible?, Environmental Health Perspectives, 119, 446–454, doi: 10.1289/ehp.1002255, URL http://dx.doi.org/10.1289/ehp.1002255, 2010.

Salvador, A., Arasa, R., and Codina, B.: Aeolian Dust Forecast in Arid and Semi-arid Regions of Peru and Chile and Their Contribution over Particulate Matter

Concentration, Journal of Geoscience and Environment Protection, 4, 128–152, 2016.

Samoli, E., Kougea, E., Kassomenos, P., Analitis, A., and Katsouyanni, K.: Does the presence of desert dust modify the effect of PM10 on mortality in Athens, Greece?, Science of The Total Environment, 409, 2049–2054, doi: 10.1016/j.scitotenv.2011.02.031, URL `http://dx.doi.org/10.1016/j.scitotenv.2011.02.031`, 2011.

Sarver, T., Al-Qaraghuli, A., and Kazmerski, L. L.: A comprehensive review of the impact of dust on the use of solar energy: History, investigations, results, literature, and mitigation approaches, Renewable and sustainable energy Reviews, 22, 698–733, 2013.

Sassen, K., DeMott, P. J., Prospero, J. M., and Poellot, M. R.: Saharan dust storms and indirect aerosol effects on clouds: CRYSTAL-FACE results, Geophysical Research Letters, 30, 2003.

Sayer, A., Munchak, L., Hsu, N., Levy, R., Bettenhausen, C., and Jeong, M.-J.: MODIS Collection 6 aerosol products: Comparison between Aqua's e-Deep Blue, Dark Target, and ?merged? data sets, and usage recommendations, Journal of Geophysical Research: Atmospheres, 119, 13–965, 2014.

Schäfer, K., Harbusch, A., Emeis, S., Koepke, P., and Wiegner, M.: Correlation of aerosol mass near the ground with aerosol optical depth during two seasons in Munich, Atmospheric Environment, 42, 4036–4046, 2008.

Schneider, W., Donoso, D., Garcés-Vargas, J., and Escribano, R.: Water-column cooling and sea surface salinity increase in the upwelling region off central-south Chile driven by a poleward displacement of the South Pacific High, Progress in oceanography, 151, 38–48, 2017.

Schnelle, K. B.: Atmospheric Diffusion Modeling, in: Encyclopedia of Physical Science and Technology (Third Edition), edited by Meyers, R. A., pp.

679–705, Academic Press, New York, third edition edn., doi: https://doi.org/10.1016/B0-12-227410-5/00036-3, URL https://www.sciencedirect.com/science/article/pii/B0122274105000363, 2003.

Schulz, N., Boisier, J. P., and Aceituno, P.: Climate change along the arid coast of northern Chile, International Journal of Climatology, 32, 1803–1814, doi: 10.1002/joc.2395, URL http://dx.doi.org/10.1002/joc.2395, 2011.

Schuster, G. L., Dubovik, O., and Holben, B. N.: Angstrom exponent and bimodal aerosol size distributions, Journal of Geophysical Research: Atmospheres, 111, 2006.

Seidel, D. J., Zhang, Y., Beljaars, A., Golaz, J.-C., Jacobson, A. R., and Medeiros, B.: Climatology of the planetary boundary layer over the continental United States and Europe, Journal of Geophysical Research: Atmospheres, 117, 2012.

Sellar, A. A., Jones, C. G., Mulcahy, J., Tang, Y., Yool, A., Wiltshire, A., O'connor, F. M., Stringer, M., Hill, R., Palmieri, J., et al.: UKESM1: Description and evaluation of the UK Earth System Model, Journal of Advances in Modeling Earth Systems, 2019.

Shao, Y.: A model for mineral dust emission, Journal of Geophysical Research: Atmospheres, 106, 20 239–20 254, 2001.

Sherman, K. and Hempel, G.: The UNEP Large Marine Ecosystem Report: A perspective on changing conditions in LMEs of the world?s Regional Seas, UNEP Regional Seas Report and Studies, pp. 1–40, 2008.

Sherwood, S. and Fu, Q.: A drier future?, Science, 343, 737–739, 2014.

Sherwood, S., Webb, M. J., Annan, J. D., Armour, K., Forster, P. M., Hargreaves, J. C., Hegerl, G., Klein, S. A., Marvel, K. D., Rohling, E. J., et al.: An assessment of Earth's climate sensitivity using multiple lines of evidence, Reviews of Geophysics, 58, e2019RG000 678, 2020.

Shi, C., Yu, B., Liu, D., Wu, Y., Li, P., Chen, G., and Wang, G.: Effect of high-velocity sand and dust on the performance of crystalline silicon photovoltaic modules, Solar Energy, 206, 390–395, 2020.

Sigman, D. M., Jaccard, S. L., and Haug, G. H.: Polar ocean stratification in a cold climate, Nature, 428, 59–63, 2004.

Simmons, A., Willett, K., Jones, P., Thorne, P., and Dee, D.: Low-frequency variations in surface atmospheric humidity, temperature, and precipitation: Inferences from reanalyses and monthly gridded observational data sets, Journal of Geophysical Research: Atmospheres, 115, 2010.

Singh, N., Murari, V., Kumar, M., Barman, S., and Banerjee, T.: Fine particulates over South Asia: Review and meta-analysis of PM2. 5 source apportionment through receptor model, Environmental Pollution, 223, 121–136, 2017.

Sinyuk, A., Holben, B. N., Eck, T. F., Giles, D. M., Slutsker, I., Korkin, S., Schafer, J. S., Smirnov, A., Sorokin, M., and Lyapustin, A.: The AERONET Version 3 aerosol retrieval algorithm, associated uncertainties and comparisons to Version 2, Atmospheric Measurement Techniques, 13, 3375–3411, 2020.

Skamarock, W., Klemp, J., Dudhia, J., Gill, D., Barker, D., Duda, M., Huang, X., Wang, W., and Powers, J.: A description of the advanced research WRF. ver. 3. NCAR/TN-475+ STR, National Center for Atmospheric Research: Boulder, CO, USA, 2008.

Soni, K., Singh, S., Bano, T., Tanwar, R., and Nath, S.: Wavelength dependence of the aerosol Angstrom exponent and its implications over Delhi, India, Aerosol Science and Technology, 45, 1488–1498, 2011.

Stafoggia, M., Schwartz, J., Badaloni, C., Bellander, T., Alessandrini, E., Cattani, G., De'Donato, F., Gaeta, A., Leone, G., Lyapustin, A., et al.: Estimation of daily PM10 concentrations in Italy (2006–2012) using finely resolved satellite data, land use variables and meteorology, Environment international, 99, 234–244, 2017.

Stohl, A., Aamaas, B., Amann, M., Baker, L., Bellouin, N., Berntsen, T. K., Boucher, O., Cherian, R., Collins, W., Daskalakis, N., et al.: Evaluating the climate and air quality impacts of short-lived pollutants, Atmospheric Chemistry and Physics, 15, 10 529–10 566, 2015.

Storkey, D., Blaker, A. T., Mathiot, P., Megann, A., Aksenov, Y., Blockley, E. W., Calvert, D., Graham, T., Hewitt, H. T., Hyder, P., et al.: UK Global Ocean GO6 and GO7: A traceable hierarchy of model resolutions, Geoscientific Model Development, 11, 3187–3213, 2018.

Sträter, E., Westbeld, A., and Klemm, O.: Pollution in coastal fog at Alto Patache, Northern Chile, Environmental Science and Pollution Research, 17, 1563–1573, doi: 10.1007/s11356-010-0343-x, URL http://dx.doi.org/10.1007/s11356-010-0343-x, 2010.

Stull, R. B.: An introduction to boundary layer meteorology, vol. 13, Springer Science & Business Media, 1988.

Sverdrup, H. U.: On the Process of Upwelling, Journal of Marine Research, 1, 155–164, 1938.

Sydeman, W. J., Garcia-Reyes, M., Schoeman, D. S., Rykaczewski, R. R., Thompson, S. A., Black, B. A., and Bograd, S. J.: Climate change and wind intensification in coastal upwelling ecosystems, Science, 345, 77–80, 2014.

Tai, A. P., Mickley, L. J., and Jacob, D. J.: Correlations between fine particulate matter (PM2.5) and meteorological variables in the United States: Implications for the sensitivity of PM2.5 to climate change, Atmospheric Environment, 44, 3976–3984, doi: 10.1016/j.atmosenv.2010.06.060, URL http://dx.doi.org/10.1016/j.atmosenv.2010.06.060, 2010.

Tai, A. P. K., Mickley, L. J., and Jacob, D. J.: Impact of 2000–2050 climate change on fine particulate matter (PM2.5) air quality inferred from a multi-model analysis of meteorological modes, Atmospheric Chemistry and Physics, 12, 11 329–

11 337, doi: 10.5194/acp-12-11329-2012, URL http://dx.doi.org/10.5194/acp-12-11329-2012, 2012.

Talley, L. D., Pickard, G. L., Emery, W. J., and Swift, J. H.: Descriptive Physical Oceanography: an Introduction. Sixth Edition, Elsevier, 2011.

Tanaka, T. Y. and Chiba, M.: A numerical study of the contributions of dust source regions to the global dust budget, Global and Planetary Change, 52, 88–104, doi: 10.1016/j.gloplacha.2006.02.002, URL http://dx.doi.org/10.1016/j.gloplacha.2006.02.002, 2006.

Tang, C.-H., Coull, B. A., Schwartz, J., Lyapustin, A. I., Di, Q., and Koutrakis, P.: Developing particle emission inventories using remote sensing (PEIRS), Journal of the Air & Waste Management Association, 67, 53–63, 2017.

Tanré, D., Kaufman, Y., Herman, M., and Mattoo, S.: Remote sensing of aerosol properties over oceans using the MODIS/EOS spectral radiances, Journal of Geophysical Research: Atmospheres, 102, 16 971–16 988, 1997.

Tao, M., Chen, L., Wang, Z., Wang, J., Che, H., Xu, X., Wang, W., Tao, J., Zhu, H., and Hou, C.: Evaluation of MODIS Deep Blue aerosol algorithm in desert region of East Asia: ground validation and intercomparison, Journal of Geophysical Research: Atmospheres, 122, 10–357, 2017.

Taylor, M. H., Tam, J., Blaskovic, V., Espinoza, P., Ballón, R. M., Wosnitza-Mendo, C., Arguelles, J., Díaz, E., Purca, S., Ochoa, N., Ayón, P., Goya, E., Gutiérrez, D., Quipuzcoa, L., and Wolff, M.: Trophic modeling of the Northern Humboldt Current Ecosystem Part II: Elucidating ecosystem dynamics from 1995 to 2004 with a focus on the impact of ENSO, Progress in Oceanography, 79, 366–378, 2008.

Tegen, I. and Fung, I.: Modeling of mineral dust in the atmosphere: Sources, transport, and optical thickness, Journal of Geophysical Research, 99, 22 897, doi: 10.1029/94jd01928, URL http://dx.doi.org/10.1029/94JD01928, 1994.

Tegen, I., Harrison, S. P., Kohfeld, K., Prentice, I. C., Coe, M., and Heimann, M.: Impact of vegetation and preferential source areas on global dust aerosol: Results from a model study, Journal of Geophysical Research: Atmospheres, 107, AAC–14, 2002.

Thambiran, T. and Diab, R. D.: Air quality and climate change co-benefits for the industrial sector in Durban, South Africa, Energy Policy, 39, 6658–6666, 2011.

Tim, N., Zorita, E., and Hunicke, B.: Decadal variability and trends of the Benguela upwelling system as simulated in a high-resolution ocean simulation, Ocean Science, 11, 483–502, 2015.

Tiwary, A. and Colls, J.: Air pollution: measurement, modelling and mitigation, Taylor and Francis, 3rd edn., 2010.

Toro, R., Campos, C., Molina, C., Leiva-Guzmán, M. A., et al.: Accuracy and reliability of Chile's National Air Quality Information System for measuring particulate matter: Beta attenuation monitoring issue, Environment international, 82, 101–109, 2015.

Trail, M., Tsimpidi, A., Liu, P., Tsigaridis, K., Hu, Y., Nenes, A., and Russell, A.: Downscaling a global climate model to simulate climate change over the US and the implication on regional and urban air quality, Geoscientific Model Development, 6, 1429–1445, 2013.

Turnock, S., Allen, R., Andrews, M., Bauer, S., Emmons, L., Horowitz, L., et al.: Historical and future changes in air pollutants from CMIP6 models, Atmospheric Chemistry and Physics Discussions, pp. 1–40, 2020.

Twigg, M. M., Di Marco, C. F., Leeson, S., van Dijk, N., Jones, M. R., Leith, I. D., Morrison, E., Coyle, M., Proost, R., Peeters, A. N. M., Lemon, E., Frelink, T., Braban, C. F., Nemitz, E., and Cape, J. N.: Water soluble aerosols and gases at a UK background site – Part 1: Controls of $PM_{2.5}$ and PM_{10} aerosol composition, Atmospheric Chemistry and Physics, 15, 8131–8145, doi: 10.5194/

acp-15-8131-2015, URL https://acp.copernicus.org/articles/15/8131/2015/, 2015.

Twomey, S.: The Influence of Pollution on the Shortwave Albedo of Clouds, Journal of the Atmospheric Sciences, 34, 1977.

Valenzuela, A., Olmo, F., Lyamani, H., Antón, M., Titos, G., Cazorla, A., and Alados-Arboledas, L.: Aerosol scattering and absorption Angström exponents as indicators of dust and dust-free days over Granada (Spain), Atmospheric Research, 154, 1–13, 2015.

Vallero, D. A.: Fundamentals of air pollution, Academic press, 2014.

Van Donkelaar, A., Martin, R. V., Brauer, M., Kahn, R., Levy, R., Verduzco, C., and Villeneuve, P. J.: Global estimates of ambient fine particulate matter concentrations from satellite-based aerosol optical depth: development and application, Environmental health perspectives, 118, 847–855, 2010.

van Marle, M. J. E., Kloster, S., Magi, B. I., Marlon, J. R., Daniau, A.-L., Field, R. D., Arneth, A., Forrest, M., Hantson, S., Kehrwald, N. M., Knorr, W., Lasslop, G., Li, F., Mangeon, S., Yue, C., Kaiser, J. W., and van der Werf, G. R.: Historic global biomass burning emissions for CMIP6 (BB4CMIP) based on merging satellite observations with proxies and fire models (1750–2015), Geoscientific Model Development, 10, 3329–3357, doi: 10.5194/gmd-10-3329-2017, 2017.

Varela, R., Álvarez, I., Santos, F., deCastro, M., and Gómez-Gesteira, M.: Has upwelling strengthened along worldwide coasts over 1982?2010?, Scientific Reports, 5, 2015.

Varutbangkul, V., Brechtel, F., Bahreini, R., Ng, N., Keywood, M., Kroll, J., Flagan, R., Seinfeld, J., Lee, A., and Goldstein, A.: Hygroscopicity of secondary organic aerosols formed by oxidation of cycloalkenes, monoterpenes, sesquiterpenes, and related compounds, Atmospheric Chemistry and Physics, 6, 2367–2388, 2006.

Vecchi, G. A., Soden, B. J., Wittenberg, A. T., Held, I. M., Leetmaa, A., and Harrison, M. J.: Weakening of tropical Pacific atmospheric circulation due to anthropogenic forcing, Nature, 441, 73–76, 2006.

Vincent, E. M., Emanuel, K. A., Lengaigne, M., Vialard, J., and Madec, G.: Influence of upper ocean stratification interannual variability on tropical cyclones, Journal of Advances in Modeling Earth Systems, 6, 680–699, 2014.

Vogelezang, D. and Holtslag, A. A.: Evaluation and model impacts of alternative boundary-layer height formulations, Boundary-Layer Meteorology, 81, 245–269, 1996.

Vohra, K., Vodonos, A., Schwartz, J., Marais, E. A., Sulprizio, M. P., and Mickley, L. J.: Global mortality from outdoor fine particle pollution generated by fossil fuel combustion: Results from GEOS-Chem, Environmental Research, 195, 110 754, 2021.

Von Schneidemesser, E., Monks, P. S., Allan, J. D., Bruhwiler, L., Forster, P., Fowler, D., Lauer, A., Morgan, W. T., Paasonen, P., Righi, M., et al.: Chemistry and the linkages between air quality and climate change, Chemical reviews, 115, 3856–3897, 2015.

Vuille, M.: Atmospheric circulation over the Bolivian Altiplano during dry and wet periods and extreme phases of the Southern Oscillation, International Journal of Climatology: A Journal of the Royal Meteorological Society, 19, 1579–1600, 1999.

Vuille, M. and Ammann, C.: Regional snowfall patterns in the high, arid Andes, Climatic change, 36, 413–423, 1997.

Wainwright, J. and Mulligan, M., eds.: Environmental modelling: finding simplicity in complexity, John Wiley and Sons, Ltd, 2nd edn., 2013.

Walters, D., Baran, A. J., Boutle, I., Brooks, M., Earnshaw, P., Edwards, J., Furtado, K., Hill, P., Lock, A., Manners, J., et al.: The Met Office Unified Model global at-

mosphere 7.0/7.1 and JULES global land 7.0 configurations, Geoscientific Model Development, 12, 1909–1963, 2019.

Walther, A., x, J.-H., Nikulin, G., Jones, C., and Chen, D.: Evaluation of the warm season diurnal cycle of precipitation over Sweden simulated by the Rossby Centre regional climate model RCA3, Atmospheric research, 119, 131–139, 2013.

Wang, D., Gouhier, T. C., Menge, B. A., and Ganguly, A. R.: Intensification and spatial homogenization of coastal upwelling under climate change, Nature, 518, 390–394, 2015a.

Wang, J., Xia, X., Wang, P., and Christopher, S. A.: Diurnal variability of dust aerosol optical thickness and Angström exponent over dust source regions in China, Geophysical research letters, 31, 2004.

Wang, J. X. and Angell, J. K.: Air Stagnation Climatology for the United States (1948-1998), NOAA/Air Resources Laboratory ATLAS, 1, 1999.

Wang, M., Overland, J. E., and Bond, N. A.: Climate projections for selected large marine ecosystems, Journal of Marine Systems, 79, 258–266, 2010.

Wang, X., Heald, C. L., Ridley, D. A., Schwarz, J. P., Spackman, J. R., Perring, A. E., Coe, H., Liu, D., and Clarke, A. D.: Exploiting simultaneous observational constraints on mass and absorption to estimate the global direct radiative forcing of black carbon and brown carbon, Atmospheric Chemistry and Physics, 14, 10 989–11 010, doi: 10.5194/acp-14-10989-2014, URL http://dx.doi.org/10.5194/acp-14-10989-2014, 2014.

Wang, Y., Xie, Y., Cai, L., Dong, W., Zhang, Q., and Zhang, L.: Impact of the 2011 Southern U.S. Drought on Ground-Level Fine Aerosol Concentration in Summertime*, Journal of the Atmospheric Sciences, 72, 1075–1093, doi: 10.1175/jas-d-14-0197.1, URL http://dx.doi.org/10.1175/JAS-D-14-0197.1, 2015b.

Warwick, G. and Marjorie, R.: Joachim of Fiore in Eastern Europe, Oxford University Press (OUP), 2001.

Watson, J. G.: Visibility: Science and Regulation, Journal of the Air and Waste Management Association, 52, 628–713, doi: 10.1080/10473289.2002.10470813, URL http://dx.doi.org/10.1080/10473289.2002.10470813, 2002.

Werner, M., Tegen, I., Harrison, S. P., Kohfeld, K. E., Prentice, I. C., Balkanski, Y., Rodhe, H., and Roelandt, C.: Seasonal and interannual variability of the mineral dust cycle under present and glacial climate conditions, Journal of Geophysical Research, 107, 2002.

West, J., P, O., I, L., J, M., and A, F.: Co-control of urban air pollutants and greenhouse gases in Mexico City, Environment Science and Technology, 38, 3474–3481, 2004.

WHO: WHO. Air quality guidelines for particulate matter, ozone, nitrogen dioxide and sulphur dioxide. Global update 2005, Summary of Risk Assessment, 2006.

WHO: Ambient (outdoor) air quality and health, World Health Organization, URL https://www.who.int/en/news-room/fact-sheets/detail/ambient-(outdoor)-air-quality-and-health, 2018.

Willett, K., Dunn, R., Thorne, P., Bell, S., De Podesta, M., Parker, D., Jones, P., and Williams Jr, C.: HadISDH land surface multi-variable humidity and temperature record for climate monitoring, Climate of the Past, 10, 2014.

Williams, K., Copsey, D., Blockley, E., Bodas-Salcedo, A., Calvert, D., Comer, R., Davis, P., Graham, T., Hewitt, H., Hill, R., et al.: The Met Office global coupled model 3.0 and 3.1 (GC3. 0 and GC3. 1) configurations, Journal of Advances in Modeling Earth Systems, 10, 357–380, 2018.

Wright, P. B.: On the reality of climatic changes in wind over the Pacific, Journal of Climatology, 8, 521–527, 1988.

Xie, B., Fung, J. C., Chan, A., and Lau, A.: Evaluation of nonlocal and local planetary boundary layer schemes in the WRF model, Journal of Geophysical Research: Atmospheres, 117, 2012.

Xu, Y.: Evaluation of mineral dust aerosol optical depth and related components from the CHIMERE-DUST model using satellite remote sensing and ground-based observations, Atmospheric Environment, 191, 395–413, 2018.

Xu, Z., Chang, P., Richter, I., Kim, W., and Tang, G.: Diagnosing southeast tropical Atlantic SST and ocean circulation biases in the CMIP5 ensemble, Climate Dynamics, 43, 3123–3145, 2014.

Xue-Jie, G., Mei-Li, W., and Giorgi, F.: Climate change over China in the 21st century as simulated by BCC_CSM1. 1-RegCM4. 0, Atmospheric and Oceanic Science Letters, 6, 381–386, 2013.

Yang, Q., Gustafson Jr, W., Fast, J., Wang, H., Easter, R., Wang, M., Ghan, S., Berg, L., Leung, L., and Morrison, H.: Impact of natural and anthropogenic aerosols on stratocumulus and precipitation in the Southeast Pacific: a regional modelling study using WRF-Chem, Atmospheric Chemistry and Physics, 12, 8777–8796, 2012.

Yang, S., Wei, Z., Chen, B., and Xu, X.: Influences of atmospheric ventilation on the composition of the upper troposphere and lower stratosphere during the two primary modes of the South Asia high, Meteorology and Atmospheric Physics, pp. 1–12, 2019.

Yelland, M. and Taylor, P. K.: Wind Stress Measurements from the Open Ocean, Journal of Physical Oceanography, 26, 541–558, 1996.

Yool, A., Popova, E., and Anderson, T.: MEDUSA-2.0: an intermediate complexity biogeochemical model of the marine carbon cycle for climate change and ocean acidification studies, Geoscientific Model Development, 6, 1767–1811, 2013.

Zdanowicz, C., Kruemmel, E., Lean, D., Poulain, A., Kinnard, C., Yumvihoze, E., Chen, J., and Hintelmann, H.: Pre-industrial and recent (1970–2010) atmospheric deposition of sulfate and mercury in snow on southern Baffin Island, Arctic Canada, Science of The Total Environment, 509–510, 104–114, 2015.

Zelinka, M. D., Andrews, T., Forster, P. M., and Taylor, K. E.: Quantifying components of aerosol-cloud-radiation interactions in climate models, Journal of Geophysical Research: Atmospheres, 119, 7599–7615, 2014.

Zelinka, M. D., Myers, T. A., McCoy, D. T., Po-Chedley, S., Caldwell, P. M., Ceppi, P., Klein, S. A., and Taylor, K. E.: Causes of higher climate sensitivity in CMIP6 models, Geophysical Research Letters, 2020.

Zender, C. S., Bian, H., and Newman, D.: Mineral Dust Entrainment and Deposition (DEAD) model: Description and 1990s dust climatology, Journal of Geophysical Research, 108, 2003.

Zeng, X., Zhao, M., and Dickinson, R. E.: Intercomparison of bulk aerodynamic algorithms for the computation of sea surface fluxes using TOGA COARE and TAO data, Journal of Climate, 11, 2628–2644, 1998.

Zhang, J., Reid, J. S., and Holben, B. N.: An analysis of potential cloud artifacts in MODIS over ocean aerosol optical thickness products, Geophysical Research Letters, 32, 2005.

Zhang, N., Gao, Z., Liu, Y., and Li, D.: Sensitivity of a global climate model to the critical Richardson number in the boundary layer parameterization, Journal of Geophysical Research: Atmospheres, 120, 3310–3328, 2015.

Zhao, Z., Chen, S.-H., Kleeman, M. J., and Mahmud, A.: The Impact of Climate Change on Air Quality–Related Meteorological Conditions in California. Part II: Present versus Future Time Simulation Analysis, Journal of Climate, 24, 3362–3376, doi: 10.1175/2010jcli3850.1, URL http://dx.doi.org/10.1175/2010JCLI3850.1, 2011a.

Zhao, Z., Chen, S.-H., Kleeman, M. J., Tyree, M., and Cayan, D.: The Impact of Climate Change on Air Quality–Related Meteorological Conditions in California. Part I: Present Time Simulation Analysis, Journal of Climate, 24, 3344–3361, doi: 10.1175/2011jcli3849.1, URL http://dx.doi.org/10.1175/2011JCLI3849.1, 2011b.